



# Identification of Small Molecule Inhibitors of the Kynurenine Pathway

## Dissertation

zur Erlangung des akademischen Grades des  
Doktors der Naturwissenschaften (Dr. rer. nat.)

der Fakultät für Chemie und Chemische Biologie  
an der Technischen Universität Dortmund

## Dissertation

for the achievement of the academic degree of  
Doctor in Natural Sciences (Dr. rer. nat.)

from the faculty of Chemistry and Chemical Biology  
of the Technical University of Dortmund

vorgelegt durch/submitted by

**Lara Jil Dötsch, M.Sc.**

geb./born 12.12.1994 in Bottrop

Dortmund, 17.07.2023



Erstgutachter/ First examiner: Prof. Dr. Dr. h.c. Herbert Waldmann  
Zweitgutachter/ Second examiner: Prof. Dr. Carsten Watzl

Die vorliegende Arbeit wurde im Zeitraum von November 2018 bis Juli 2023 unter Anleitung von Prof. Dr. Dr. h.c. Herbert Waldmann und Dr. Slava Ziegler an der Fakultät für Chemie und Chemische Biologie der Technischen Universität Dortmund und dem Max-Planck-Institut für molekulare Physiologie, Dortmund verfasst.

The work presented in this thesis was performed from November 2018 to July 2023 under the supervision of Prof. Dr. Dr. h.c. Herbert Waldmann and Dr. Slava Ziegler at the Faculty of Chemistry and Chemical Biology at the Technical University of Dortmund and the Max Planck Institute of Molecular Physiology, Dortmund.



*Für meine Eltern Marion & Herbert.*



Ergebnisse dieser Dissertation sind Teil folgender Publikation:

The results presented in this thesis contributed to the following publications:

Davies<sup>+</sup>, C., Dötsch<sup>+</sup>, L., Ciulla, M. G., Hennes, E., Yoshida, K., Gasper, R., Scheel, R., Sievers, S., Strohmann, C., Kumar, K., Ziegler, S. Waldmann, H. "Identification of a Novel Pseudo-Natural Product Type IV IDO1 Inhibitor Chemotype", *Angewandte Chemie International Edition* **2022**, 61(40), e202209374.

<sup>+</sup>Co-Erstautoren – diese Autoren haben zu gleichen Teilen beigetragen.

<sup>+</sup>Co-first authors – these authors contributed equally.





## Table of Contents

1	Kurzzusammenfassung.....	1
2	Abstract .....	2
3	Introduction .....	3
3.1	The Immune System and Cancer.....	3
3.2	Cancer Immunotherapy .....	10
3.3	Identification of Bioactive Small Molecules.....	13
4	Aim of the Thesis .....	19
5	Results.....	20
5.1	Apoxidoles as Novel Type IV IDO1 Inhibitors.....	22
5.2	Epoxykynin sEH Inhibitors as Potent Kyn Pathway Modulators.....	38
6	Discussion .....	70
6.1	Apoxidoles as Novel Type IV IDO1 Inhibitors.....	71
6.2	Epoxykynin sEH Inhibitors as Potent Kyn Pathway Modulators.....	80
7	Conclusion and Future Perspective.....	100
8	Experimental Part .....	102
8.1	Materials and Instruments.....	102
8.2	Cell Biology Methods .....	111
8.3	Molecular Biology, Biochemical and Biophysical Methods .....	122
8.4	Proteomics Methods .....	127
9	References .....	132
10	Abbreviations .....	153
11	Appendix.....	157
11.1	Supplementary Data .....	157
11.2	Acknowledgements.....	176
11.3	Publication List.....	178



### 1 Kurzzusammenfassung

Das Immunsystem fungiert als wirksame Barriere gegen die Tumorentwicklung. Maligne Zellen können sich jedoch der Eliminierung durch das Immunsystem entziehen, indem sie das Immunsystem in der Tumormikroumgebung (TME) verändern. Unter anderem können Krebszellen Immuntoleranz durch die Expression des immunsuppressiven Enzyms Indolamin-2,3-dioxygenase 1 (IDO1) induzieren. IDO1 katalysiert den Abbau der essenziellen Aminosäure Tryptophan (Trp) zu Kynureninen (Kyn) über den Kyn-Stoffwechselweg. Die Modulation des Kyn-Stoffwechsels hat sich in der Vergangenheit als attraktives therapeutisches Ziel in der Immunonkologie erwiesen.

In dieser Arbeit wurden anhand eines zellbasierten Screenings zwei Substanzklassen entdeckt, die den Kyn-Spiegel in Krebszellen bei Stimulation mit dem Zytokin Interferon- $\gamma$  (IFN- $\gamma$ ) auf unterschiedliche Weise senken. Die Apoxidole sind Indol-Tetrahydropyridin-Pseudonaturstoffe (PNPs) und hemmen IDO1 direkt, indem sie apo-IDO1 *in vitro* und in Zellen binden und stabilisieren. Durch die Verdrängung des IDO1-Cofaktors Häm wird das Enzym katalytisch inaktiviert und der Kyn-Spiegel gesenkt. Apo-IDO1-Inhibitoren wie Apoxidole imitieren eine irreversible Hemmung und weisen eine hohe Selektivität für IDO1 gegenüber den beiden anderen Trp-abbauenden Enzymen Tryptophan-2,3-dioxygenase (TDO) und IDO2 auf, was sie zu nützlichen Instrumenten für Studien der Relevanz von IDO1 im Vergleich zu TDO und IDO2 macht.

Die zweite Stoffklasse *N*-substituierter Indole, auch Epoxykynine genannt, modulieren den Kyn-Stoffwechsel auf eine alternative Weise, da sie keine direkten Inhibitoren von IDO1 sind. Stattdessen hemmen Epoxykynine die katalytische Aktivität der C-terminalen Fettsäurehydrolase-Domäne der löslichen Epoxidhydrolase (sEH-H). Als Teil der Arachidonsäure (AA)-Kaskade spielt das hochaktive Enzym sEH-H eine wichtige Rolle bei der Hydrolyse von CYP-Epoxygenase-abgeleiteten Fettsäureepoxiden. Dadurch trägt es zur Regulierung der bioverfügbaren Epoxide bei und steuert eine Vielzahl biologischer Prozesse wie Entzündung, Vasodilatation, Angiogenese, neuropsychiatrischen Erkrankungen und Schmerz. Die in dieser Arbeit erzielten Ergebnisse decken eine funktionelle Verbindung zwischen sEH-H und dem Kyn-Signalweg auf.

Die Entdeckung neuer Hemmstoffe für den Kyn-Signalweg ist von großer Bedeutung, da der bestentwickelte holo-IDO1-Inhibitor Epcadostat kürzlich in klinischen Studien gescheitert ist. Darüber hinaus hat die Entdeckung der Epoxykynine das Verständnis der Interaktion des Kyn-Signalwegs und des AA-Stoffwechsels vertieft. Diese Erkenntnisse könnten neue Strategien für die Entwicklung von Immuntherapien ermöglichen und das Immunsystem stärken, um die krebsbedingte Immuntoleranz zu überwinden.

## 2 Abstract

The immune system functions as an effective barrier against tumor development. However, malignant cells can avoid elimination by the immune system by acquiring certain characteristics that alters the immune system in the tumor microenvironment (TME). For instance, cancer cells can actively induce immune tolerance by expression of the immunosuppressive enzyme indoleamine 2,3-dioxygenase 1 (IDO1). IDO1 expression results in degradation of the essential amino acid tryptophan (Trp) and production of kynurenines (Kyn) *via* the Kyn pathway. Targeting the Kyn pathway has emerged to be an attractive target in immuno-oncology.

In this thesis, two compound classes were discovered through a cell-based screening that reduce Kyn levels in cancer cells upon stimulation with the cytokine interferon- $\gamma$  (IFN- $\gamma$ ) by two distinct mechanisms. The indole-tetrahydropyridine pseudo-natural products (PNPs) called apoxidoles inhibit IDO1 directly by binding and stabilizing apo-IDO1 *in vitro* and in cells. The displacement of the IDO1 cofactor heme catalytically inactivates the enzyme and thereby decreases Kyn levels. Apo-IDO1 inhibitors like apoxidoles mimic irreversible inhibition and have a high selectivity for IDO1 over the two other Trp-catabolizing enzymes tryptophan 2,3-dioxygenase (TDO) and IDO2, thus, being useful tools for the investigation of IDO1's relevance in comparison to TDO and IDO2.

The small molecule class of *N*-substituted indoles called epoxykynins represents an alternative approach to modulate the Kyn pathway by not directly targeting IDO1. Instead, epoxykynin inhibits the catalytic activity of the C-terminal fatty acid hydrolase domain of the soluble epoxide hydrolase (sEH-H). As part of the arachidonic acid (AA) cascade, the highly active enzyme sEH-H plays an important role in the hydrolysis of CYP epoxygenase-derived fatty acid epoxides. Thereby, it contributes to the regulation of bioavailable epoxides and controls a variety of biological processes, such as inflammation, vasodilation, angiogenesis, neuropsychiatries and pain. The results obtained throughout this thesis uncover a functional link between sEH-H and the Kyn pathway.

The discovery of new Kyn pathway inhibitors is in high demand, since the most advanced holo-IDO1 inhibitor epacadostat has recently failed in clinical trials. Additionally, the discovery of epoxykynins has deepened the understanding of the cross-talk between the Kyn pathway and the AA metabolism. These findings might enable novel strategies to design immunotherapies and enhance the host's immune system to overcome cancer-induced immune tolerance.

### 3 Introduction

Cancer is one of the most fatal diseases of recent times and is the second leading cause of death globally<sup>1</sup>. Annually, approximately 20 million people are diagnosed with cancer, leading to approximately 10 million deaths every year<sup>2</sup>. The term cancer refers to abnormal cell growth with the potential to invade other tissues as a result of genetic mutations<sup>3</sup>. As a heterogeneous group of different disease types, cancer can start in almost every organ or tissue of the human body. Due to the demographic change, the cancer burden continues to grow globally. Especially in recent years, the coronavirus disease 2019 (COVID-19) caused delays in the diagnosis and treatment of cancer.

Even though the estimated age-standardized incidence rate (ASR) for Germany has remained the same over the past 25 years (with an ASR of 313.2 per 100,000 citizens in 2020), the annual mortality rate has decreased by approximately 30%<sup>1</sup>. As a country with a strong healthcare system, early detection and quality treatment are available, which significantly improves the survival rates of cancer patients. Additionally, new therapy strategies have been developed, including cancer immunotherapy as a major breakthrough for a number of cancers<sup>4</sup>.

#### 3.1 The Immune System and Cancer

The concept that the immune system functions as effective primary barrier to tumorigenesis and tumor progression has been first proposed in 1909 by Paul Ehrlich<sup>5</sup>. However, at that time it was challenging to experimentally prove this hypothesis because only little was known about the basis of anti-cancer immunity. It took around half a century of controversy to validate and establish this crucial paradigm for immuno-oncology<sup>6-9</sup>. In 1970, the term 'immunological surveillance' was introduced by Sir Macfarlane Burnet<sup>8</sup> and 41 years later, avoiding immune destruction has been recognized as one of the hallmarks of cancer<sup>10</sup>.

##### 3.1.1 Immune Surveillance and Cancer Immunoediting

The immune system has three roles in the prevention of tumors. First, elimination of viral infections to avoid virus-induced tumorigenesis; second, rapid clearance of pathogens and thereby, timely resolution of inflammation that can promote cancer development; third, the identification and elimination of malignant cells by tumor-specific antigens<sup>11</sup>. The latter process refers to immune surveillance.

The immune system consists of innate and adaptive immunity, of which both are involved in the elimination of cancer cells<sup>12</sup>. Key mediators for the clearance of malignant cells are natural killer (NK) cells that belong to the innate immune system and CD8<sup>+</sup> cells or cytotoxic T lymphocytes (CTLs), belonging to the adaptive immunity. The T cell-mediated immune surveillance is a cyclic process representing an interplay between the innate and adaptive

## Introduction

immune compartments, also known as cancer-immunity cycle<sup>13</sup>. It consists of seven steps that can be divided into a priming (step i-iv) and effector phase (step v-vii). Steps associated with the priming phase are heavily dependent on the innate immune system, comprising i) tumor-specific antigen uptake by antigen-presenting cells (APCs) in the tumor, ii) cross-presentation of tumor antigens to T cells by APCs in tumor-draining lymph nodes, iii) priming and activation of naïve T cells by the APCs and iv) trafficking of the activated T cells to the tumor *via* the blood stream. The effector phase is occurring in the tumor, including v) T cell infiltration into the tumor, vi) recognition and vii) elimination of cancer cells by the activated T cells.

Despite this very effective barrier for tumor development, cancers occur in immuno-competent individuals. In addition to immune surveillance, the immune system can also promote carcinogenesis. The immune selection pressure can shape cancer cells to be less immunogenic, to then eventually evade immune surveillance. This refined the immune surveillance hypothesis into 'cancer immunoediting'<sup>14, 15</sup>.

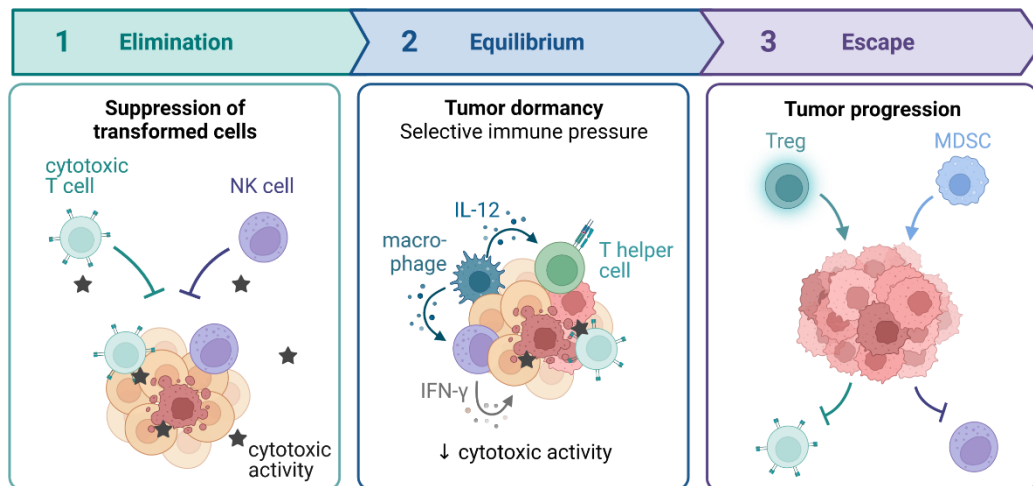


**Figure 1:** The three Es of cancer immunoediting. In the elimination phase, NK cells and CTLs identify and eliminate malignant cells. In the second equilibrium phase, mutations accumulate that make tumor cells resistant to the immune attack, facilitated by tumor-promoting selective immune pressure. Finally, the tumor can escape the immune surveillance and additional tumor cell variants develop. The figure was created with BioRender.com. Stars represent the cytotoxic activity of immune cells. IL-12: interleukin-12, IFN- $\gamma$ : interferon- $\gamma$ , Treg: T regulatory cell, MDSC: myeloid-derived suppressor cell.

The concept of cancer immunoediting emphasizes the duality of the immune system in light of tumorigenesis. It comprises three phases, also known as the three Es of cancer immunoediting (Figure 1)<sup>14</sup>. While the first phase, the so-called elimination phase, represents the classical immune surveillance mainly mediated by NK and cytotoxic T cells, the second and third steps describe the adaption and evasion of malignant cells from the immune system. During the second phase, the immune response within the tumor is remodeled by a positive feedback loop. Tumor-infiltrating macrophages secrete interleukin 12 (IL-12) that stimulates NK cell-mediated production of interferon- $\gamma$  (IFN- $\gamma$ ), which in turn activates macrophages to

## Introduction

produce more IL-12 creating a positive feedback<sup>14</sup>. At the same time, IL-12 initiates the differentiation of naïve CD4<sup>+</sup> T cells into T helper cells (Th1)<sup>16,17</sup> which provide help to cytotoxic T cells<sup>18</sup> and secrete IFN- $\gamma$ <sup>19</sup>. The release of IFN- $\gamma$  can trigger a range of IFN- $\gamma$ -dependent processes, including both tumoricidal and tumorigenic effects<sup>19</sup>. As a result, a proportion of the malignant cells is eliminated, while simultaneously less immunogenic cancer-cell variants arise that avoid immune destruction. During tumor progression, genetic instability and heterogeneity, as well as immune selection facilitate the escape of cancer cells from the immune system in the third phase. Tumor cells can evade the killing by two intrinsic mechanisms, namely avoiding the recognition by immune cells, e.g. by downregulation of tumor-specific antigens, or resisting the immunological killing, e.g. by constitutive activation of anti-apoptotic signaling<sup>14</sup>. The active suppression of cytotoxic immune cells represents a third extrinsic mechanism, e.g. by induction of the expansion of suppressive immune cell types, such as T regulatory (Treg) cells or myeloid-derived suppressor cells (MDSC)<sup>20,21</sup>.

### 3.1.2 The Tumor Microenvironment

Tumors are imprinted by the immune system in which they develop. At the same time, cancer cells shape the so-called tumor microenvironment (TME) to become tolero- and tumorigenic.

The tumor microenvironment (TME) is composed of diverse cell types, soluble factors, the extracellular matrix (ECM) and blood vessels. It constantly evolves, is remarkably adaptable and is thereby actively promoting tumor progression. Its components can be separated into cancer cells, immune cells, stromal cells and non-cellular components (Figure 2)<sup>22</sup>. The densely-packed TME causes low nutrient levels, high amounts of metabolic byproducts, diminished oxygen levels and an acidic pH level in the core of the tumor<sup>23</sup>. Additionally, a multitude of cytokines and growth factors, high levels of ROS and nitric oxide shape the TME<sup>23,24</sup>. This elicits strict regulation of intra-tumoral immune cells.

Cancer cells recruit stromal cells, such as cancer-associated fibroblasts or endothelial cells, to promote angiogenesis, proliferation, invasion, and metastasis<sup>25</sup>. By remodeling the ECM, formation of new blood vessels and production of growth factors and cytokines, stromal cells provide the 'soil' for tumor growth<sup>26,27</sup>. For this reason, a high tumor stroma percentage (TSP) has been associated with poor patient survival<sup>28</sup>.

The interplay between immune cells and cancer cells in the TME is critical to support cancer cell survival. Macrophages and APCs are responsible for tumor-antigen presentation and T cell priming, while NK cells and CTLs eliminate malignant cells with the support of Th cells<sup>11</sup>. Unlike other lymphocytes, B cells only rarely infiltrate the TME and remain at the border of the tumor<sup>22</sup>.

## Introduction

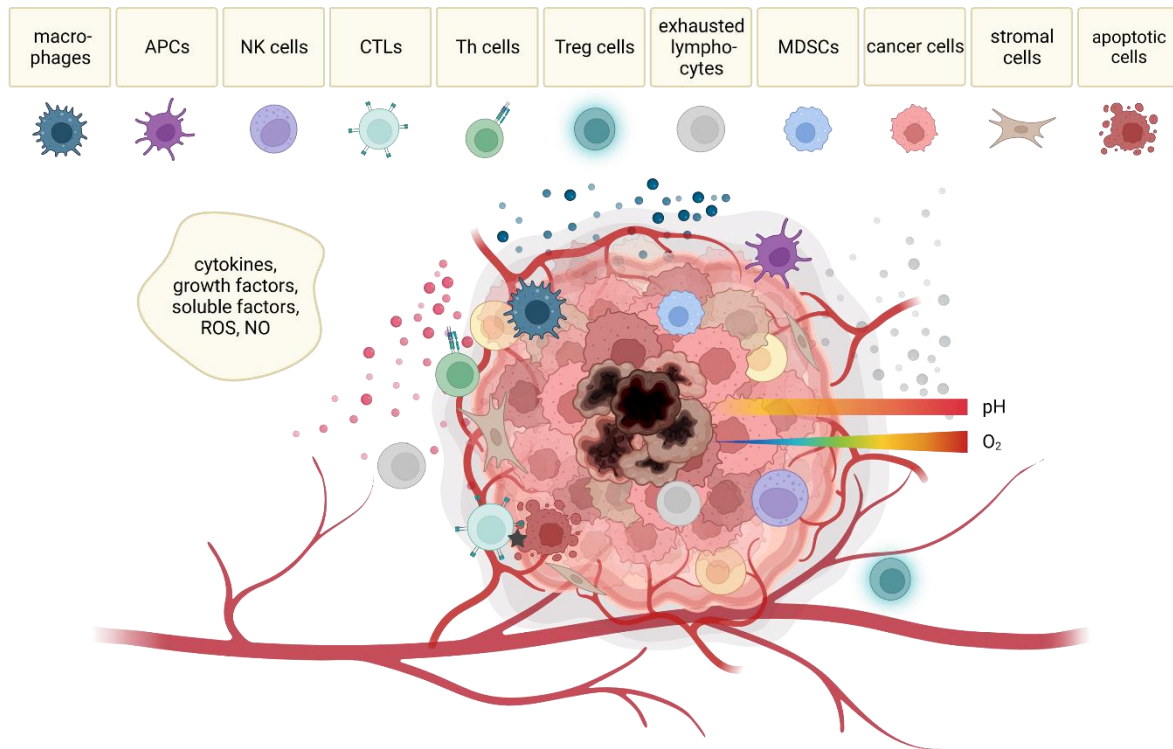


**Figure 2:** The tumor microenvironment (TME). The TME is composed of diverse cell types, soluble factors, the extracellular matrix and blood vessels and actively supports tumor growth. The dense TME is characterized by nutrient, pH and oxygen gradients. The figure was created with BioRender.com. APCs: antigen-presenting cells; NK cells: natural killer cells; CTLs: cytotoxic lymphocytes, Th cells: T helper cells; Treg cells: T regulatory cells; MDSCs: myeloid-derived suppressor cells; ROS: reactive oxygen species.

Besides immune cells that display or enhance cytolytic activities, Treg cells and MDSCs are present in the TME. MDSCs originate from the bone marrow and are able to directly interact with different immune cells. They are generally immuno-suppressive and produce high levels of reactive oxygen species (ROS) and nitric oxide<sup>20</sup>. For instance, they inhibit Th cells that are a source for NK- and CTL-stimulating cytokines<sup>23</sup>. Tregs are defined as a sub-population of CD4<sup>+</sup> cells that is highly responsive to IL-2 and expresses the transcription factor forkhead box p3 (FOXP3)<sup>29</sup>. They induce immune tolerance by secretion of suppressive cytokines, such as transforming growth factor- $\beta$  (TGF- $\beta$ )<sup>30</sup> or IL-10<sup>31</sup>, induction of apoptosis of effector cells by granzyme B<sup>32</sup> and 'reverse signaling' *via* nuclear factor- $\kappa$ B (NF- $\kappa$ B)<sup>33</sup>.

Since the TME is a miscellaneous and multifaceted interplay of different components, therapeutic strategies require specific and efficient targeting of key players of immune suppression. Tryptophan catabolism and the enzyme indoleamine 2,3-dioxygenase 1 (IDO1) serve as attractive targets for reverting immune tolerance.

### 3.1.3 Indoleamine 2,3-dioxygenase 1 and Kynurenine Production

L-Tryptophan (Trp) is an essential amino acid serving as a building block for the biosynthesis of proteins and as a precursor for bioactive molecules<sup>34</sup>. The majority of Trp is catabolized *via* the kynurenine (Kyn) pathway (Figure 3), while a small amount of Trp is metabolized by Trp



## Introduction

hydroxylases<sup>35</sup>. The first and rate-limiting step along the Kyn pathway can be catalyzed by three heme-containing enzymes, namely the two related indoleamine 2,3-dioxygenases (IDO) IDO1 and IDO2 and the unrelated tryptophan 2,3-dioxygenase (TDO)<sup>36</sup>. Whereas TDO and IDO2 expression is mainly limited to the liver, the kidney and APCs, IDO1 is widely expressed throughout the body with high prevalence in immune-privileged tissues<sup>36</sup>. Expression of the *IDO1* gene is upregulated by IFN- $\gamma$ , lipopolysaccharides (LPS), prostaglandin E2 (PGE-2), tumor necrosis factor- $\alpha$  (TNF- $\alpha$ ), TGF- $\beta$  and NF- $\kappa$ B. In contrast, *IDO1* expression is downregulated by IL-4, nitric oxide, IL-6 and the tumor suppressor gene *BIN1*<sup>37-40</sup>.

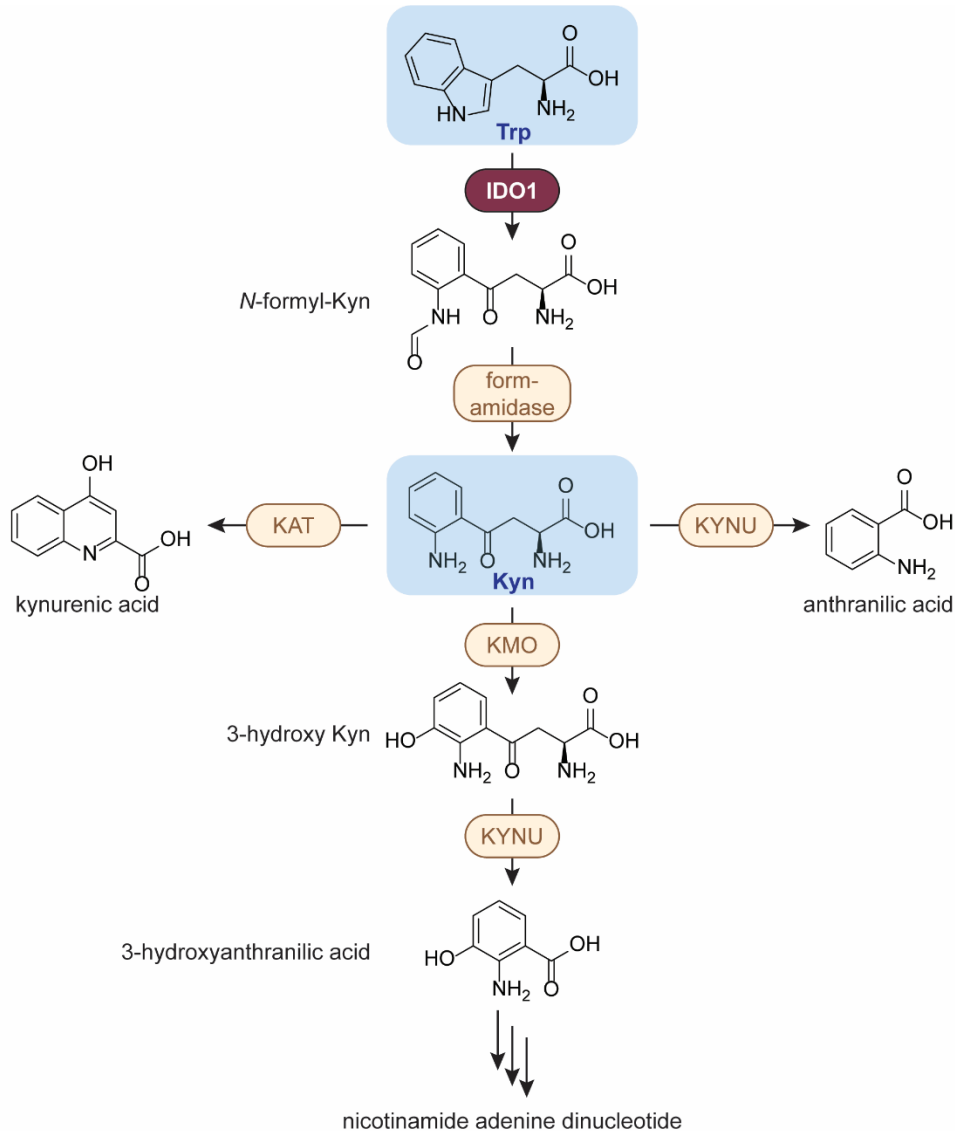


**Figure 3:** The Kyn pathway. KYNU: kynureninase; KAT: Kyn aminotransferase; KMO: Kyn 3-monooxygenase.

The Kyn pathway is initiated by the oxidation of Trp to *N*-formyl-Kyn by IDO1, IDO2 or TDO, which is then rapidly hydrolyzed into Kyn by Kyn formamidase. Kyn can be converted into anthranilic acid, kynurenic acid or 3-hydroxykynurenine by kynureninase (KYNU), Kyn aminotransferase or kynurenine 3-monooxygenase, respectively. KYNU can also act on 3-

## Introduction

hydroxykynurenine to form 3-hydroxyanthranilic acid, which is a precursor for the biosynthesis of nicotinamide adenine dinucleotide<sup>41</sup>. Several diseases are connected to the dysregulation of the Kyn pathway and its catabolites, including neurological disorders<sup>42</sup>, autoimmune conditions<sup>43, 44</sup> and tumorigenesis<sup>45</sup>.

In 1998, David Munn and Andrew Mellor first suggested that IDO1 expression might lead to immune suppression. They proposed that deprivation of the essential amino acid Trp induces T cell anergy and mitotic arrest<sup>46</sup>. Later it was discovered that this process is mediated by elevated levels of uncharged tRNAs, which in turn activate the stress-response general control nonderepressible 2 (GCN2) kinase pathway<sup>47</sup>. Furthermore, GCN2 activation contributes to the differentiation of naïve CD4<sup>+</sup> T cells into Tregs<sup>48</sup>. However, it is not only the starvation of Trp that induces immune tolerance. Additionally, the production of Kyn and downstream metabolites suppresses the immune system. Kyn inhibits the IL-2-induced proliferation and cytolytic activity of NK cells<sup>49</sup> and also promotes the IL-6-induced generation of MDSCs<sup>50</sup>. Moreover, kynurenines act as endogenous agonists of the aryl hydrocarbon receptor (AhR) which is a transcriptional regulator of different cellular processes, including immune response<sup>43</sup>. AhR activation induces T reg differentiation<sup>51</sup> and also generation of tolerogenic IDO<sup>+</sup> dendritic cells (DCs)<sup>52</sup>. Taken together, this leads to IDO1-dependent tolerogenesis in the TME by a Kyn- and IFN- $\gamma$ -based positive feedback loop.

The phenomenon of some proteins having multiple roles within an organism is called 'moonlighting'<sup>53, 54</sup>. Moonlighting proteins include mainly enzymes that perform a secondary function different from catalysis, e.g. transcriptional regulation or conformational folding as a molecular chaperone<sup>54</sup>. IDO1 as a moonlighting protein has additional signaling functions in DCs independent of IFN- $\gamma$  and its catalytic activity (Figure 4)<sup>55</sup>. Stimulation with TGF- $\beta$  induces phosphorylation of two immunoreceptor tyrosine-based inhibitory motifs (ITIMs) T111 and in the small, non-catalytic domain of IDO1 by Src family kinases. The phosphorylated ITIMs serve as anchors for different Src homology region 2 (SH2) domain-containing proteins<sup>56</sup>. Phosphorylated ITIM1 recruits SH2 domain-containing phosphatases 1 and 2 (SHP1 and SHP2) that activate non-canonical NF- $\kappa$ B signaling, resulting in sustained *IDO1* and *TGFB1* gene expression and induction of long-term tolerance<sup>38, 56</sup>. In the presence of the pro-inflammatory IL-6, the expression of suppressor of cytokine signaling 3 (SOCS3) is upregulated which can directly bind to phosphorylated ITIM2 of IDO1 and thereby mark the IDO1-SOCS3 complex for ubiquitination *via* the Elongin-Cullin-SOCS (ECS) E3 ligase complex and subsequent canonical proteasomal degradation<sup>38-40</sup>. Thus, the two ITIMs in IDO1 have distinct roles, contributing either to tolerance or immunity.

## Introduction

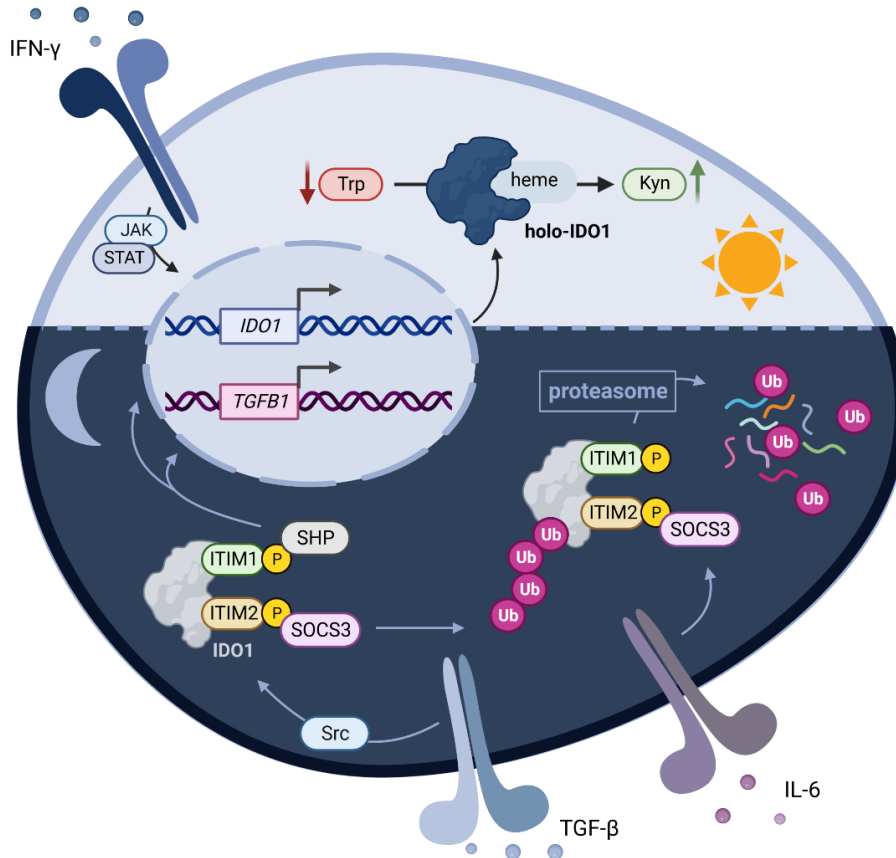


**Figure 4:** The moonlighting protein IDO1. Depending on the TME, IDO1 can take on different roles in DCs. IFN- $\gamma$  stimulation triggers JAK/STAT signaling, promoting IDO1 expression and catalytic activity. Additionally, TGF- $\beta$  mediates the phosphorylation of two immunoreceptor tyrosine-based inhibitory motifs (ITIMs) in IDO1. ITIM1 recruits Src homology region 2 domain-containing phosphatases (SHPs) to activate *IDO1* and *TGFB1* gene expression. In contrast, IL-6 induces upregulation of suppressor of cytokine signaling 3 (SOCS3) which can bind to phosphorylated ITIM2. The IDO1-SOCS3 complex is then ubiquitinated and degraded by the proteasome. The figure was created with BioRender.com. JAK: janus kinase; STAT: signal transducers and activators of transcription; Ub: ubiquitin.

Besides the phosphorylation of the two ITIMs, IDO1 features an N-terminal alanine acetylation and three tyrosine nitrations as posttranslational modifications (PTM)<sup>57</sup>. As for the majority of eukaryotic proteins, the N-terminal methionine is cleaved from the nascent amino acid chain by methionine aminopeptidases and an acetyl group is transferred to the following alanine residue from acetyl-coenzyme A by N-terminal acetyltransferases. This process most likely happens co-translationally for 80-90% of all cytosolic proteins<sup>58</sup>. Depending on the cellular context, this widespread modification has an influence on the half-life, folding, interaction and localization of the mature protein<sup>59</sup>. The exact role of the N-terminal acetylation (Ac/N) of IDO1 remains unknown, but the perhaps most discussed hypothesis is the function of Ac/Ns as degrons according to the Ac/N-end rule<sup>60</sup>. Misfolding or unshielding due to disrupted interactions exposes the Ac/N-degron to the solvent and makes it accessible for Ac/N-specific E3 ligases. By ubiquitination, the protein is marked for proteasomal degradation. In this way, the protein quality and stoichiometric protein levels are regulated<sup>59, 60</sup>.

## Introduction

Nitration of residues Tyr15, Tyr345 and Tyr353 reduces IDO1 catalytic activity<sup>57</sup>. Activated macrophages release nitric oxide and superoxide in response to pathogens or cancer cells, which leads to the rapid formation of peroxynitrite and subsequent nitration of solvent-exposed tyrosines<sup>61, 62</sup>. Compared to tyrosine, 3-nitrotyrosine has a lower  $pK_a$  of the hydroxyl group, is larger and more hydrophobic<sup>63, 64</sup>. This PTM alters the electronic and steric properties of tyrosine residues, may resulting in conformational and functional perturbations<sup>63</sup>.

### 3.2 Cancer Immunotherapy

In the year 1868, the surgeon Wilhelm Busch first reported the regression of a tumor in one of his patients after infection with *Streptococcus* bacteria<sup>65</sup>. 23 years later, the surgical oncologist William Coley developed the first prototypical anti-cancer vaccine called 'Coley's toxin' for inoperable tumors: He cured around 1,000 patients by injection of heat-inactivated *S. pyogenes* and *Serratia marcescens* (at that time termed *Bacillus prodigiosus*) into tumors<sup>66, 67</sup>. Over the next century, the foundation of modern immuno-oncology was laid: Burnet proposed the immune surveillance theory<sup>8</sup>, Jerne, Edelman and Porter contributed to the understanding of antibodies<sup>68-71</sup>, Köhler and Milstein invented the hybridoma technology<sup>72</sup> and many more pivotal discoveries were made in the field<sup>73</sup>. Finally, in 1986, IFN- $\alpha$ 2 was the first cancer immunotherapy to be approved by the US Food and Drug Administration (FDA) for the treatment of hairy cell leukemia<sup>74</sup>.

Today's immunotherapies can generally be divided into passive and active strategies based on their ability to engage the patient's immune system. Passive immunotherapies include tumor-targeting monoclonal antibodies (mAbs), oncolytic viruses and cell-based therapies, while active approaches comprise stimulatory cytokines, cancer vaccines, immune checkpoint inhibitors and small molecules<sup>75</sup>. Among these strategies, especially chimeric antigen receptor (CAR) T cell therapies as cell-based approach and immune checkpoint blockade are considered as breakthroughs<sup>76, 77</sup>.

The CAR T cell approach uses genetically engineered T cells of patients or donors to express CARs against tumor-specific antigens. The resulting CAR T cells are then transferred back into the patient, where they eliminate malignant cells. Limitations for this strategy are the high tumor (antigen) heterogeneity, the suppressive TME and successful trafficking to the tumor<sup>78</sup>. Furthermore, there are frequently occurring severe side effects, such as the cytokine release syndrome (CRS, often used interchangeably with cytokine storm) where large amounts of leukocytes get activated and release cytokines<sup>79</sup>.

To prevent auto-immunity, cells within an organism express co-receptors called immune checkpoints on their surface. When immune cells bind to these receptors, they recognize the presenting cell as 'self' and do not elicit immune response<sup>80</sup>. Thereby, immune checkpoints

## Introduction

act as gatekeepers for the activation of CTLs. Cancer cells can overexpress inhibitory ligands for checkpoints to avoid elimination. Hence, blockade of either the immune checkpoint receptors on the immune cells or the upregulated ligands on the cancer cells can restore anti-cancer immunity<sup>81</sup>. The two most intensively studied checkpoints in relation to cancer are CTL-associated protein 4 (CTLA-4) and programmed cell death protein 1 (PD-1). With ipilimumab against CTLA-4<sup>82</sup> and pembrolizumab against PD-1<sup>83</sup>, the first checkpoint-targeting antibodies were approved by the FDA in 2011 and 2014, respectively. Despite the broad efficacy of checkpoint blockade, this approach encounters similar challenges as CAR T cell therapies. Additionally, acquired resistance to immunotherapy is a phenomenon commonly observed in immune checkpoint inhibition<sup>84</sup>.

While small molecules serve as cutting-edge therapy for targeted cancer treatments, they are underrepresented in immuno-oncology<sup>85</sup>. Yet they offer several advantages compared to biologics: Small molecules can potentially be administered orally, target intracellular components and easily traffic to the TME<sup>86</sup>.

### 3.2.1 Small Molecule Inhibitors of IDO1 and Kyn Production

In 2018, IDO1 has emerged as the eighth-most prominent target in immuno-oncology alongside 416 other targets<sup>85</sup> and its well established enzymology facilitates the development of selective inhibitors. Currently, there are eighteen active trials involving the two small molecule IDO1 inhibitors epacadostat<sup>87</sup> and BMS-986205<sup>88</sup> (Figure 5) as well as the dual IDO1/TDO inhibitor SHR9146<sup>89</sup> and the T-win® vaccine IO102-IO103 against IDO1 and PD-L1 in the clinical trials database<sup>90</sup>. Furthermore, there are completed studies for indoximod<sup>91</sup>, navoximod<sup>92</sup>, NLG802<sup>93</sup>, PF06840003<sup>94</sup>, LY3381916<sup>95</sup>, M4112<sup>96</sup> and KHK2455<sup>97</sup> (Figure 5).

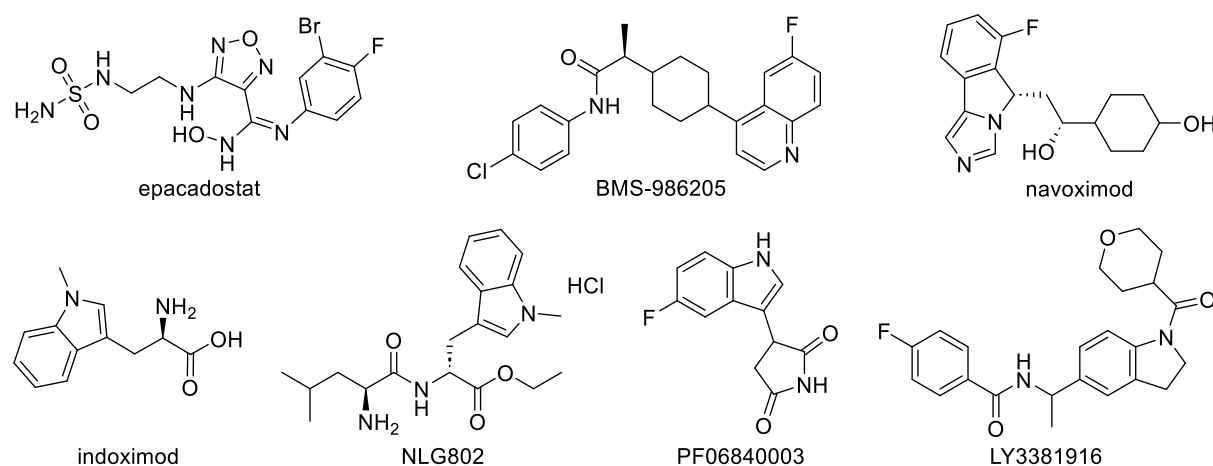


**Figure 5:** Structures of IDO1 and Kyn pathway inhibitors in clinical trials. The structures of SHR9146, M4112 and KHK2455 are not disclosed to public.

Crystal structure analyses and biochemical assays provide valuable insights into the molecular mechanisms of IDO1 inhibitors. Röhrig *et al.*<sup>98</sup> utilized this data to define five

## Introduction

inhibitor types of IDO1: Type I inhibitors bind to oxygen-bound holo-IDO1 in a Trp-competitive manner, type II competes with oxygen for free ferrous holo-IDO1, type III targets free ferric holo-IDO1, type IV binds to apo-IDO1 and type X inhibitors act as redox-cyclers and do not target IDO1 directly. Recent molecular docking and mutagenesis studies revealed that there might be an additional allosteric inhibitory site in the large, catalytic domain of IDO1<sup>99</sup>. Additionally, a first IDO1 proteolysis-targeting chimera (PROTAC) has been developed by linking epacadostat to pomalidomide as ligand of the E3 ligase cereblon<sup>100</sup>. Nevertheless, not only inhibitors targeting IDO1 directly are of interest, but also dual inhibitors, such as navoximod, or small molecules inhibiting other proteins within the Kyn pathway, e.g. indoximod and its prodrug NLG802 (Figure 6).

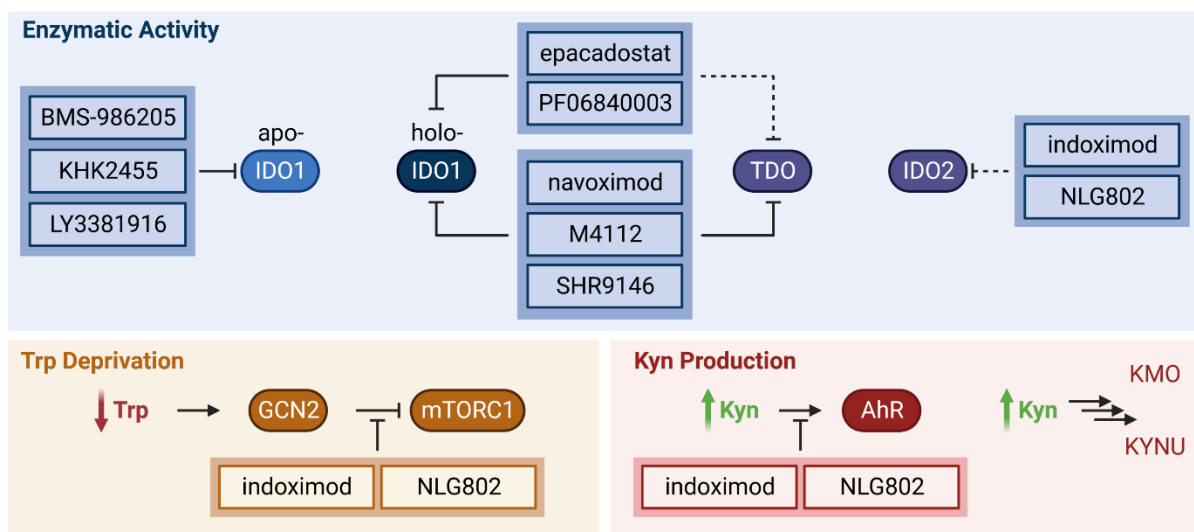


**Figure 6:** Targets of the IDO1 and Kyn pathway inhibitors in clinical trials. BMS-986205, KHK2455 and LY3381916 target apo-IDO1. Epacadostat and PF06840003 inhibit holo-IDO1, with additional weak inhibition of TDO. Navoximod, M4112 and SHR9146 act as dual inhibitors for IDO1 and TDO. Indoximod and its prodrug NLG802 weakly reduce IDO2 activity, but more importantly act directly on the Kyn pathway by blocking of Trp deprivation-induced downregulation of mTORC1 (mammalian target of rapamycin complex 1) and inhibition of Kyn-mediated activation of AhR. The figure was created with BioRender.com.

Preclinical studies have demonstrated that patients benefit from multi-therapy approaches over single-agent treatments. Especially combination of immune checkpoint blockade and IDO1 inhibition emerged as a promising strategy<sup>101</sup>. Thus, Incyte launched several phase III trials investigating its IDO1 inhibitor epacadostat in combination with pembrolizumab or chemotherapy. However, the failure of the ECHO1/KN-252 trial dampened the enthusiasm of the community. The study indicated that combination of epacadostat and pembrolizumab did not improve the progression-free survival of patients with advanced melanoma compared to administration of pembrolizumab alone<sup>102</sup>. The negative outcome resulted in the halt of other ongoing trials involving IDO1 inhibitors. Potential reasons for failure include that the patients were not specifically selected for constitutive IDO1 expression in the tumor, compensatory

## Introduction

expression of TDO and IDO2 or activation of AhR by epacadostat<sup>102-104</sup>. The clinical failure of epacadostat demonstrated that targeting IDO1 directly might not be sufficient to revert immune suppression within the complex TME. Instead, it is vital to study the whole Kyn pathway with its numerous pathway members, regulators and interactors as potential targets. Altered protein or metabolite levels, modulated posttranslational modifications or reshaped interaction networks potentially reduce Kyn production. Additionally, the complex interplay of immune cells has to be considered. Thus, the development of alternative approaches to decrease Kyn levels by not targeting IDO1 directly are crucial to overcome immune tolerance.

Taken together, IDO1 and Kyn pathway inhibition remain relevant and appealing targets in immuno-oncology. The broad understanding of the molecular mechanisms facilitates the discovery of potent inhibitors, as well as the design of adequate research.

### 3.3 Identification of Bioactive Small Molecules

Chemical biology is a highly interdisciplinary and growing field. It applies a chemist's toolbox to answer fundamental biological questions. The value of this discipline has been widely acknowledged, as can be seen from the fact that many Nobel prizes in recent years have been awarded to perfect examples of chemical biology innovations<sup>105</sup>. For instance, Jennifer A. Doudna and Emmanuelle Charpentier have been awarded with the Nobel prize in Chemistry 2020 for the discovery of the CRISPR/Cas9 technology<sup>106</sup> and Carolyn R. Bertozzi, Morten Meldal and K. Barry Sharpless received the Nobel prize in Chemistry 2022 for the development of click chemistry and bioorthogonal chemistry<sup>107</sup>.

The generation of bioactive small molecules for disease-relevant targets is at the heart of chemical biology. Perturbation of biological systems with small molecules has several advantages compared to genetic interventions. Chemical compounds represent rapidly acting molecular entities that can (reversibly) modulate one function of a (multi-) functional protein in a dose-dependent manner. On top of that, they have the potential to disrupt protein-protein interactions (PPIs)<sup>108</sup>. Nevertheless, chemical genetics require bioavailable and selective small molecules<sup>109</sup>. Hence, compounds have to be carefully designed, e.g. with the help of structural biology methods or according to certain criteria. 90% of all orally available compounds in phase II or late-stage clinical trials follow the Lipinski's 'rule of 5'<sup>110, 111</sup>. These parameters outline favorable physicochemical properties for drug-like molecules, namely a molecular weight less than 500 Da, an octanol-water partition coefficient  $\log P$  of less than 5, less than five hydrogen-bond donors and less than ten hydrogen-bond acceptors. Over the past years, natural products (NPs) have made major contributions to drug discovery<sup>112</sup>. However, NPs are often large and highly steric molecules that are difficult to access synthetically. Moreover, NPs or NP-derived compounds only modulate a certain set of their initial biological targets. More easily accessible, structurally diverse small molecule libraries

## Introduction

provide flexibility for the discovery of novel, maybe even so far undruggable targets<sup>113</sup>. Therefore, methods to overcome these limitation have been developed, such as diversity-oriented synthesis (DOS)<sup>114</sup> or biology-oriented synthesis (BIOS)<sup>115</sup>. Nonetheless, these strategies are NP-guided and thus, resulting molecules are limited in chemical space. To address this challenge, the pseudo-NP (PNP) approach combines NP-derived fragments in unprecedented ways not found in nature. Thereby, the resulting compounds inherit bioactivity and cover the chemical space in between approved drugs and NPs<sup>116, 117</sup>. Applying this synthesis strategy, small-molecule libraries for biological testing can be generated.

### 3.3.1 Screening Approaches and Target Identification

Multiple methodologies have been devised to discover bioactive small molecules. Traditional strategies include genetic, target-based and phenotypic screenings<sup>118</sup>. Additionally, computational approaches and target-fishing tools have gained influence over the years, as they became more advanced and are often more cost-efficient than wet-lab experiments<sup>119</sup>.

Between 1999 and 2008, 50 first-in-class small molecules were approved by the FDA, thereof 28 compounds were discovered *via* phenotypic screenings, while only 17 molecules originated from target-centric approaches<sup>120</sup>. In forward chemical genetics, research begins with screening of compound libraries for induction of a phenotypic or physiological change. With the active small molecule in hand, the protein target can be elucidated. Reverse chemical genetics represents the opposite approach, starting from a target protein-of-interest for which binders or modulators are identified in biophysical or biochemical assays. The active compounds are then tested for alterations in physiology (Figure 7)<sup>118</sup>. For target-based methods, the protein target must be carefully selected and relevant to the corresponding disease phenotype, whereas for phenotype-based experiments, a robust screening representing the disease phenotype must be designed. Therefore, the phenotypic 'rule of 3' has been established, namely utilizing a disease-relevant system, employing a physiological stimulus and a downstream readout close to the clinical end point<sup>121</sup>.



## Introduction

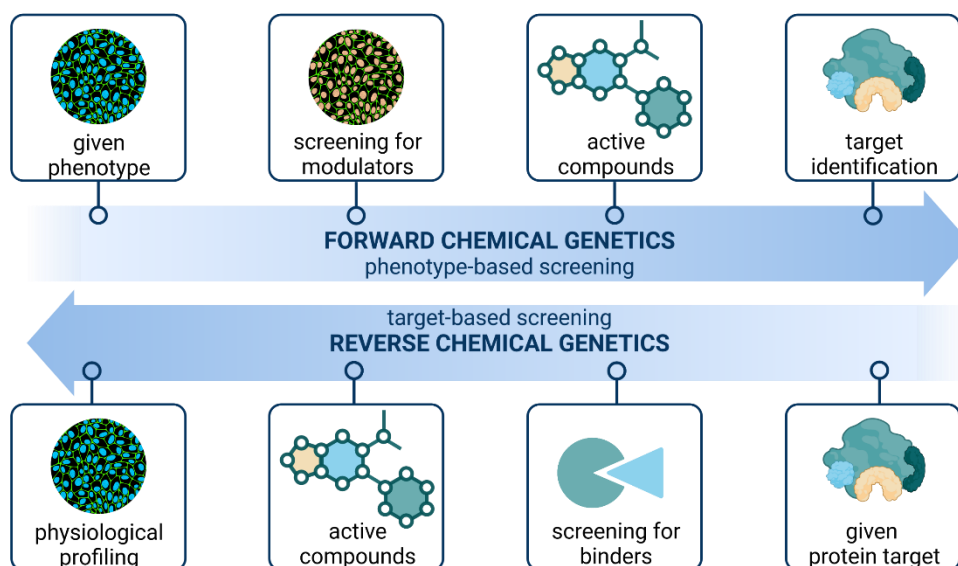


**Figure 7:** Principles of chemical genetics: forward versus reverse chemical genetics. The figure was created with BioRender.com.

In contrast to reverse chemical genetics, where the protein target is known at the earliest stage, the molecular target for the phenotypic change has to be determined in forward chemical genetics. This often proves to be challenging, but understanding the molecular mode of action (MMOA) is essential for clinical translation and safe administration<sup>120</sup>. However, there is no 'one-size-fits-all' strategy for target identification (targetID, Figure 8), since MMOAs are highly miscellaneous and small molecules cannot only modulate proteins, but also carbohydrates, nucleic acids and lipids<sup>122</sup>. Traditionally, the 'one drug, one target' paradigm dominated the pharmaceutical industry<sup>123</sup>. As of now, it is widely accepted that diseases are often multi-factorial conditions and thus, the concepts of polypharmacology and drug repurposing have emerged<sup>124, 125</sup>. Polypharmacologic agents modulate more than one target, but at the same time do not act promiscuously to induce adverse effects<sup>126</sup>. Many renowned drugs fall under these categories, such as aspirin, sildenafil or imatinib<sup>125, 127</sup>. Hence, today's drug discovery not only considers the disease-relevant 'on-target', but also characterizes 'off-targets'. Additionally, multi-targeting ligands are developed by rational target selection and combination of different pharmacophores<sup>128</sup>.

## Introduction

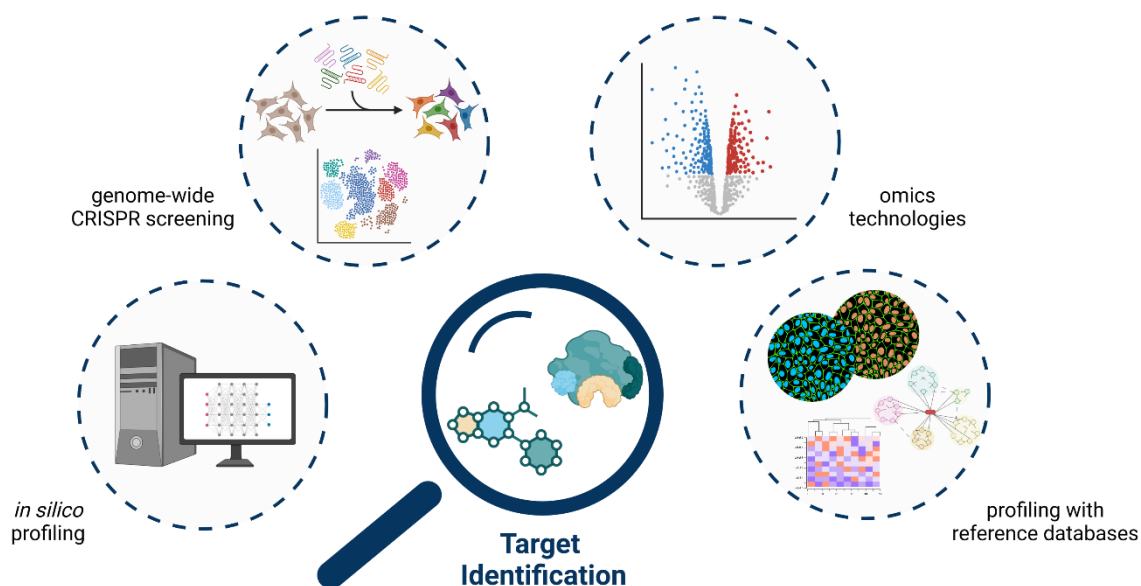


**Figure 8:** Identification of protein targets of small molecules. The figure was created with BioRender.com.

*In silico* profiling has emerged as a powerful tool to computationally identify targets of small molecules beyond wet lab approaches. Common technologies include molecular similarity, machine learning, protein-structure-based dockings and comparison of bioactivity profiles<sup>129</sup>. As of today, there are numerous web-based target prediction tools readily available. Since chemoinformatic techniques are less time- and resource-consuming than experiments, they are frequently used to narrow down and expedite drug discovery projects<sup>130</sup>. Especially with the recent improvements in artificial intelligence, computational profiling is becoming increasingly valuable for targetID. Experimental data can be used to train and validate algorithms, serve as models for molecular dynamics or docking and even provide information on the MMOA of a small molecule<sup>129</sup>.

CRISPR-Cas9 screens aim to identify the relationship of a gene knockout and a phenotypic alteration<sup>129</sup>. SgRNA libraries are used to target coding regions of genes and create loss-of-function mutations and complete protein depletion<sup>131</sup>. In genome-wide or targeted CRISPR screens, a small molecule's target can be identified by positive selection mediated by disruption of the target gene and thereby, resistance to compound treatment<sup>132</sup>. However, in some cases genetic alterations do not always translate into chemical perturbations. Particularly in proteins with multiple functions only one of them might be inhibited by small molecule treatment, while the other functions are not affected. Vice versa, gene editing might not reliably discover the target(s) of multi-target drugs<sup>129</sup>.

Mass spectrometry-based omics technologies have proven to be a powerful tool to analyze biological systems on the gene, transcript, protein, metabolite and lipid level<sup>133</sup>. Especially proteomics gave rise to unprecedented abilities for targetID, since in 2017 856 out of 893

## Introduction

targets of FDA-approved drugs were proteins, with many of them being classified as G protein-coupled receptors, ion channels, kinases, transporters or enzymes<sup>134</sup>. Proteomics can be utilized to study the influence of a compound on protein abundance, modification, localization and interaction. Furthermore, it can give insights into small molecule-target interactions by means of affinity, activity, stability and folding<sup>135</sup>. Some of these methods involve application of chemical probes, such as affinity-based chemoproteomics or photoaffinity labelling. The generation of these functionalized, compound-specific small molecules can be challenging, as they often lose affinity to its target compared to the parental compound<sup>135</sup>. Therefore, techniques without any labelling or probes have been developed, such as thermal proteome profiling (TPP)<sup>136</sup>. TPP represents an advanced proteome-wide version of the cellular thermal shift assay (CETSA)<sup>137</sup> that profiles small molecule-induced alterations in the thermal stability of proteins. In conclusion, technological progress enables high-sensitivity and high-throughput proteome profiling and investigation of single cells and heterogeneous disease-phenotypes. Omics methods will become even more effective in the future with the recent advances in computational processing and artificial intelligence.

Profiling by comparison of experimental data to a reference data set represents a complementary approach to discover bioactive small molecules by serendipity. Morphological profiling in particular has become increasingly relevant in recent years. In contrast to phenotypic screenings, morphological profiling allows for a broader identification of physiological changes not associated with only one particular disease-phenotype<sup>138</sup>. The cell painting assay (CPA)<sup>139, 140</sup> is a widely applicable technology that employs six dyes to stain different cellular compartments. By high-content microscopy and automated-image analysis, 1,716 morphological features can be extracted and used to generate morphological profiles or so-called fingerprints<sup>141, 142</sup>. Clustering of CPA fingerprints and comparison to profiles of annotated drugs can provide meaningful target hypotheses<sup>122, 143-149</sup>. However, many important disease-related cellular processes require a specific stimulus and not all small molecule-dependent perturbations induce a significant morphological change.

Following targetID, the target candidate has to be validated in a disease-related context and optimally, the underlying MMOA is subsequently elucidated.

### 3.3.2 Small Molecule Target Validation

Small molecules often modulate more than one molecular entity. Therefore, it is pivotal to prove that the potential target is associated with alterations in the disease phenotype. Widely used strategies for target validation include genetic methods, such as RNA interference, knockdown and overexpression of certain genes<sup>150, 151</sup> (Figure 9).

## Introduction

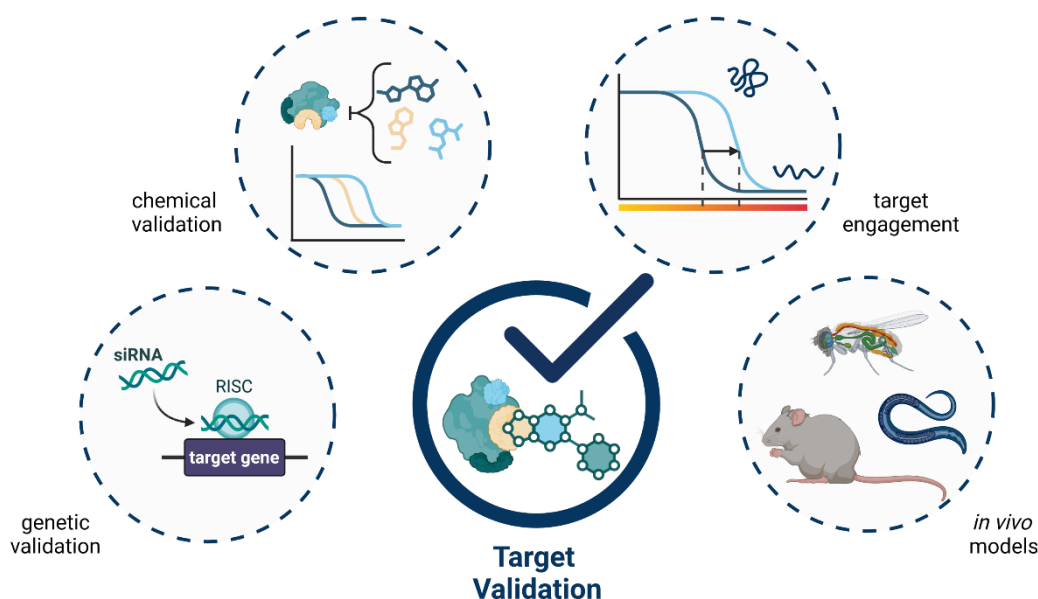


**Figure 9:** Validation of protein targets of small molecules. The figure was created with BioRender.com.

Depletion of a gene or partial downregulation of gene-specific protein expression often phenocopies pharmacological inhibition<sup>150</sup>, whereas overexpression of a small molecule target increases resistance<sup>151</sup>. A disadvantage of genetic approaches is that many genes produce more than one protein isoform that can have distinct functions or localizations. Additionally, small molecule perturbations can induce alterations in post-translational modification that mediate the observed effect<sup>152</sup>.

Chemical validation employs annotated reference compounds that are known to modulate the target candidate<sup>153</sup>. If they have the same physiological effect as the substance under investigation, the probability that they have the same target is high. Ideally, the known modulators are highly selective and provide distinct pharmacophores compared to the studied small molecule. In contrast to genetic approaches, chemical validation also includes non-protein targets. However, a disadvantage of this strategy is the heterogeneity between various modulators of one target and the uncertainty whether the observed effects are 'on-target' or 'off-target'<sup>153</sup>.

Another powerful method for target validation are *in vivo* studies. Animal models that resemble the disease phenotype can give rise to highly significant answers to the underlying biological question. Additionally, animal models provide information about pharmacokinetics, -dynamics and toxicity of the investigated small molecules<sup>154</sup>. Nevertheless, *in vivo* validation is generally more time-consuming, costly and not always translatable to humans<sup>152</sup>.

Taken together, the identification of bioactive small molecules, downstream elucidation of the physiological target and MMOA analysis are at heart of chemical biology. It represents an interdisciplinary research field, in which chemists explore biologically relevant chemical spaces and biologists use the chemical toolbox to address disease-related problems.

## 4 Aim of the Thesis

Immunotherapy is considered a major breakthrough in the treatment of cancer patients. Generally, immunotherapies are well tolerated compared to traditional chemotherapies. For passive strategies, immune molecules are administered to the patient, whereas for active strategies, the patient's immune system is stimulated to induce a response. With the first immunotherapy approved in 1986, diverse approaches have emerged. However, small molecules are heavily underrepresented in the field of immuno-oncology.

Hence, the aim of this thesis was to discover small molecule modulators of the kynurenine pathway. Therefore, a cell-based screening was employed that monitors kynurenine production in cancer cells upon stimulation with the cytokine IFN- $\gamma$ . The kynurenine pathway and its key player indoleamine 2,3-dioxygenase 1 induce immune tolerance in the tumor microenvironment, thereby actively suppressing immune cells and promoting tumor progression. By inhibition of the kynurenine pathway, immune suppression can be reverted and the immune system is enhanced to successfully eliminate malignant cells.

Among several others, the screening assay identified two chemically distinct small molecules that potently reduce cellular kynurenine levels. The structure-activity relationship of these two hit compounds should be explored and the most potent derivatives should be characterized with regard to their molecular mode of action.

These discoveries might give rise to novel insights into the kynurenine pathway and its interaction with other cancer-related pathways. Furthermore, these findings may contribute to better understanding of the tumor microenvironment and open up new opportunities for cancer-targeting therapies.

## Results

### 5 Results

In order to identify modulators of the Kyn pathway upon stimulation with IFN- $\gamma$ , 157,332 compounds were screened by the Compound Management and Screening Center (COMAS) in an automated cell-based assay (Figure 10)<sup>155</sup>. The screening library consisted of 10% in-house synthesized substances and of 90% commercially available compounds and compound libraries. 0.62% of all compounds reduced cellular Kyn levels by 50% at a concentration of 7.1  $\mu$ M without affecting the cell viability (25% threshold) or being pan-assay interference (PAINS) compounds<sup>156-160</sup>. Hit compounds that reduced Kyn levels by more than 70% were subjected to dose-response measurements to determine half-maximal inhibitory concentrations (IC<sub>50</sub>).

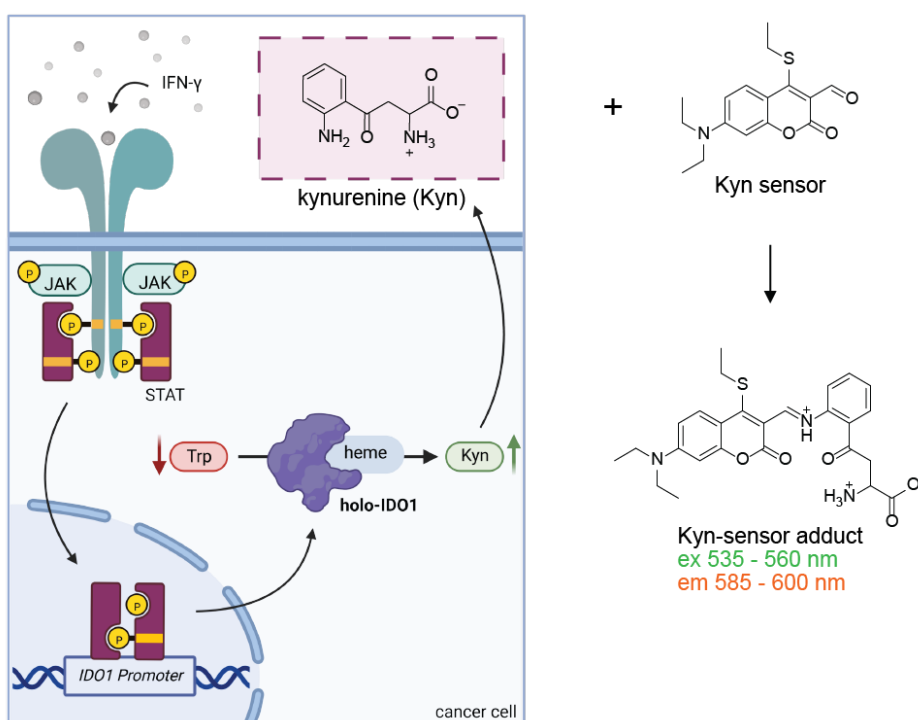


**Figure 10:** Schematic representation of the automated Kyn screening assay in BxPC-3 cells upon treatment with IFN- $\gamma$ , Trp and compounds for 48 h and detection of Kyn levels with a fluorescence-based sensor. Treatment of the cells with IFN- $\gamma$  induces a JAK/STAT signaling cascade, leading to the expression of IDO1. The holo-IDO1 protein converts the supplemented Trp to N-formyl-Kyn which is rapidly hydrolyzed to Kyn under acidic conditions prior to quantification of Kyn levels with the fluorescent Kyn sensor<sup>161</sup>. Figure was created with BioRender.com. ex: excitation; em: emission.

For the screening assay, the human pancreatic cancer cell line BxPC-3 was selected. As for most of the human cell lines, BxPC-3 cells do not express IDO1, but its expression is highly inducible by the cytokine IFN- $\gamma$ <sup>162</sup>. Treatment of the cells with IFN- $\gamma$  and additional Trp over 48 h leads to the expression of IDO1 *via* JAK/STAT signaling and the production of Kyn, which can be detected by a fluorescent coumarin-based sensor (Kyn sensor)<sup>161</sup>. Simultaneous addition of inhibiting small molecules dose-dependently reduces Kyn levels by various mechanisms. With this assay in hand, two compound classes, namely the indole-

## Results

tetrahydropyridine (THP) PNPs apoxidoles and the N-substituted indoles epoxykynins, were identified to potently reduce cellular Kyn levels (Figure 11). The hit molecules were further optimized by means of a structure-activity relationship (SAR) and characterized by in-depth biological analysis.

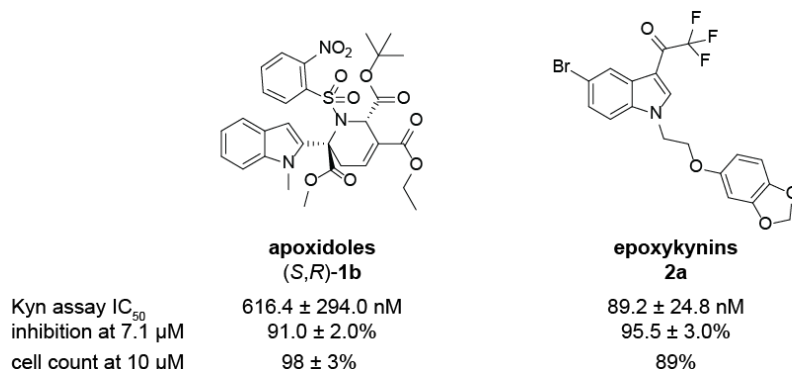


**Figure 11:** Chemical structures of the hit compounds of the indole-tetrahydropyridine apoxidoles and N-substituted indoles epoxykynins. The IC<sub>50</sub> values, inhibition levels (mean ± SD, n≥4) and cell counts (mean ± SD, n≥1) were obtained from the initial screening by COMAS.

The compounds can inhibit cellular Kyn levels *via* different mechanisms (Figure 12). Small molecules can interfere with the stimulus, e.g. blocking the activation of the (IFN-γ) receptor, or alter *IDO1* gene expression or *IDO1* protein expression on both transcriptional or translational levels. After protein expression, *IDO1* might be maintained in the catalytically

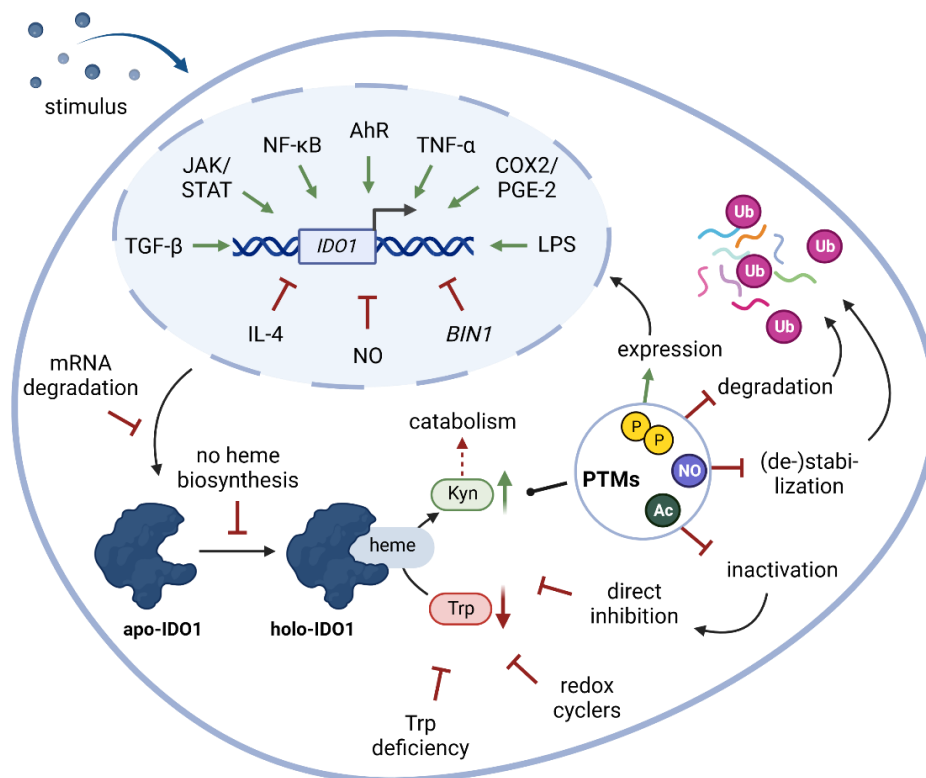


**Figure 12:** Inhibition of the Kyn pathway. AhR: aryl hydrocarbon receptor; *BIN1*: bridging integrator 1; COX2: cyclooxygenase 2; IL-4: interleukin-4; LPS: lipopolysaccharides; NF-κB: nuclear factor-κB; PGE-2: prostaglandin E2; TGF-β: transforming growth factor-β; TNF-α: tumor necrosis factor-α; Ub: ubiquitin.

## Results

inactive apo-form upon compound treatment. Additionally, the catalytic activity of holo-IDO1 might be impaired by direct inhibition, redox cycling compounds or limited availability of Trp. Compound-induced PTMs might as well inactivate IDO1 or accelerate the turnover of IDO1. Lastly, Kyn levels might be reduced by increased consumption of Kyn by downstream catabolism.

The inhibition mechanisms described above are the obvious mechanisms connected to the Kyn pathway. It is highly likely that there are additional ways to reduce cellular Kyn levels beyond these, e.g. through modulation of previously unknown Kyn pathway proteins. In contrast to target-based approaches, a cell-based assay may reveal these unknown inhibitory mechanisms and help to uncover novel MMOAs.

### 5.1 Apoxidoles as Novel Type IV IDO1 Inhibitors

#### 5.1.1 Confirmation of Reduced Cellular Kyn Levels

Hit compound (*S,R*)-**1b** reduced cellular Kyn levels in BxPC-3 cells in the automated HTS Kyn assay with an  $IC_{50}$  of  $616 \pm 294$  nM (Figure 11). To exclude a false-positive hit, the Kyn reduction was tested manually in HeLa and BxPC-3 cells with the Ehrlich reagent (2% *p*-dimethylaminobenzaldehyde (*p*-DMAB) in glacial acetic acid) and HPLC-ESI-MS/MS as orthogonal readouts (Figure 13).

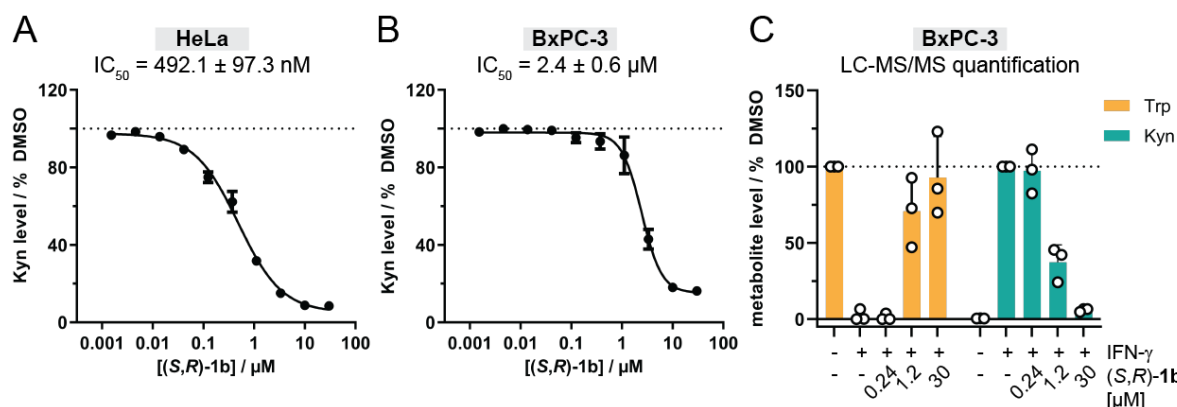


**Figure 13:** Influence of hit compound (*S,R*)-**1b** on cellular Kyn levels. A-B) Determination of Kyn levels in HeLa (A) and BxPC-3 cells (B) upon treatment with IFN- $\gamma$ , Trp and (*S,R*)-**1b** for 48 h and detection of Kyn levels using *para*-dimethylaminobenzaldehyde (*p*-DMAB) (mean  $\pm$  SD,  $n=3$ ). C) Determination of Trp and Kyn levels in BxPC-3 cells upon treatment with IFN- $\gamma$ , Trp and (*S,R*)-**1b** for 48 h and quantification of Trp and Kyn levels with HPLC-ESI-MS/MS (mean  $\pm$  SD,  $n \geq 3$ ).

(*S,R*)-**1b** dose-dependently decreased Kyn levels in HeLa and BxPC-3 cells with  $IC_{50}$  values of  $492.1 \pm 97.3$  nM and  $2.4 \pm 0.6$   $\mu$ M, respectively (Figure 13A-B). Furthermore, HPLC-ESI-MS/MS was used as an orthogonal readout to quantify the levels of Kyn and Trp upon compound treatment. (*S,R*)-**1b** dose-dependently reduced Kyn levels, while in parallel the level of Trp increased (Figure 13C). This result confirmed that (*S,R*)-**1b** inhibited the conversion of Trp to Kyn and with that validated (*S,R*)-**1b** as true positive hit from the Kyn screen.



## Results

### 5.1.1.1 Comparison to Centrocountins

The synthesis of apoxidoles was inspired by the tetrahydroindoloquinolizine centrocountins (Figure 14A). The most potent derivative centrocountin-1 is a strong inhibitor of mitosis (Figure 14B). By targeting centrosomal proteins nucleophosmine and Exportin 1, centrocountin-1 induces mitotic delays, which can already be detected at concentrations of  $1.5 \mu\text{M}$ <sup>163</sup>.

PNPs are derived from NP fragments and may induce different phenotypic changes than the guiding scaffolds<sup>164</sup>. Since aberrant mitosis might contribute to cellular Kyn reduction, the influence of hit compound (*S,R*)-**1b** on microtubules was investigated (Figure 14C). Compared to the DMSO control, nocodazole<sup>165</sup>-treated HeLa cells displayed defects in the tubulin polymerization. In contrast, compound (*S,R*)-**1b** had no effect on microtubule architecture or assembly. Hence, apoxidoles, unlike centrocountins, do not impair mitosis.

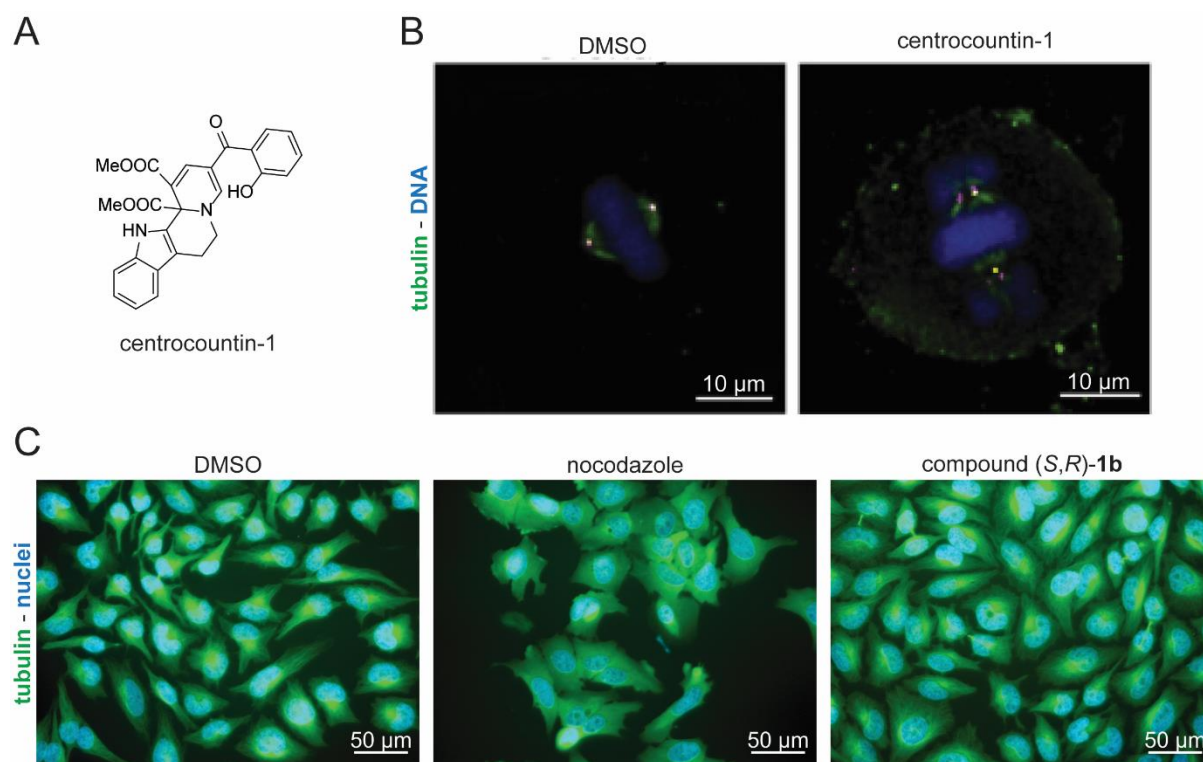


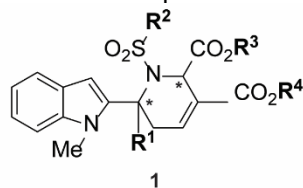
**Figure 14:** Influence of hit compound (*S,R*)-**1b** on mitosis. A) Structure of centrocountin-1 and B) influence on mitosis. HeLa cells were treated with  $25 \mu\text{M}$  centrocountin-1 for 18 h prior to staining for tubulin (green) and DNA (blue). Images are reprinted from Dückert *et al.* 'Natural product-inspired cascade synthesis yields modulators of centrosome integrity'<sup>163</sup>. C) HeLa cells were treated with  $1 \mu\text{M}$  nocodazole or  $10 \mu\text{M}$  compound (*S,R*)-**1b** for 24 h prior to staining for tubulin (green) and nuclei (blue). Images were acquired with the Zeiss Observer Z1 microscope under 63X magnification. Representative images are shown ( $n=2$ ).

### 5.1.1.2 Structure-Activity Relationship of Apoxidoles

Twenty-two chemically diverse derivatives were synthesized by Dr. Caitlin Davies (Max Planck Institute of Molecular Physiology, Department of Chemical Biology) and tested manually for their reduction of cellular Kyn levels in HeLa cells (Table 1) to explore the SAR of the apoxidoles.

## Results

**Table 1:** Structure-activity relationship of the PNP apoxidole compound class (mean  $\pm$  SD, n=3).



entry	compound	R <sup>1</sup>	R <sup>2</sup>	R <sup>3</sup>	R <sup>4</sup>	ee [%]	Configuration	Kyn assay IC <sub>50</sub> [μM]
1	<b>1a<sup>a</sup></b>	CO <sub>2</sub> Me	<i>o</i> -NO <sub>2</sub> -Ph	Et	Et	88	( <i>R,S</i> )	>10
2	<b>1b</b>	CO <sub>2</sub> Me	<i>o</i> -NO <sub>2</sub> -Ph	tBu	Et	75	( <i>S,R</i> )	0.49 $\pm$ 0.10
3	<b>1b<sup>a</sup></b>	CO <sub>2</sub> Me	<i>o</i> -NO <sub>2</sub> -Ph	tBu	Et	76	( <i>R,S</i> )	2.44 $\pm$ 0.56
4	<b>1c</b>	H	<i>o</i> -NO <sub>2</sub> -Ph	tBu	Et	82	( <i>S,R</i> )	1.04 $\pm$ 0.08
5	<b>1d</b> (apoxidole-1)	CO <sub>2</sub> Me	<i>p</i> -Me-Ph	tBu	Et	85	( <i>S,R</i> )	0.07 $\pm$ 0.01
6	<b>1d<sup>a</sup></b>	CO <sub>2</sub> Me	<i>p</i> -Me-Ph	tBu	Et	86	( <i>R,S</i> )	0.28 $\pm$ 0.04
7	<b>1e</b>	H	<i>p</i> -Me-Ph	tBu	Et	86	( <i>S,R</i> )	0.26 $\pm$ 0.05 <sup>d</sup>
8	<b>1f</b>	CO <sub>2</sub> Me	Me	tBu	Et	86	( <i>S,R</i> )	0.08 $\pm$ 0.01
9	<b>1g</b>	CO <sub>2</sub> Me	Ph	tBu	Et	78	( <i>S,R</i> )	0.08 $\pm$ 0.01
10	<b>1h</b>	CO <sub>2</sub> Me	<i>p</i> -Br-Ph	tBu	Et	82	( <i>S,R</i> )	0.43 $\pm$ 0.15
11	<b>1i</b>	CO <sub>2</sub> Me	<i>m</i> -CF <sub>3</sub> -Ph	tBu	Et	84	( <i>S,R</i> )	1.54 $\pm$ 0.41
12	<b>1j</b>	CO <sub>2</sub> Me	<i>p</i> -Me-Ph	Et	tBu	90	( <i>S,R</i> )	0.76 $\pm$ 0.04
13	<b>1k</b>	H	<i>p</i> -F-Ph	tBu	Et	84	( <i>S,R</i> )	0.11 $\pm$ 0.02
14	<b>1l</b>	H	<i>p</i> -Me-Ph	Et	tBu	76	( <i>S,R</i> )	1.63 $\pm$ 0.16
15	<b>1m</b>	CO <sub>2</sub> Me	<i>o</i> -NO <sub>2</sub> -Ph	tBu	Bn	76	( <i>S,R</i> )	1.39 $\pm$ 0.09
16	<b>1m<sup>a</sup></b>	CO <sub>2</sub> Me	<i>o</i> -NO <sub>2</sub> -Ph	tBu	Bn	84	( <i>R,S</i> )	2.88 $\pm$ 0.13
17	<b>1n</b>	CO <sub>2</sub> Me	<i>o</i> -NO <sub>2</sub> -Ph	Et	tBu	86	( <i>S,R</i> )	2.46 $\pm$ 0.29
18	<b>1o</b>	CO <sub>2</sub> Me	<i>o</i> -NO <sub>2</sub> -Ph	Bn	Et	76	( <i>R,S</i> )	7.52 $\pm$ 0.80
19	<b>1p</b>	CO <sub>2</sub> Me	<i>o</i> -NO <sub>2</sub> -Ph	tBu	tBu	90	( <i>S,R</i> )	0.65 $\pm$ 0.08
20	<b>1p<sup>a</sup></b>	CO <sub>2</sub> Me	<i>o</i> -NO <sub>2</sub> -Ph	tBu	tBu	86	( <i>S,R</i> )	0.82 $\pm$ 0.70
21	<b>1q</b>	CO <sub>2</sub> Me	<i>p</i> -Me-Ph	tBu	Bn	87	( <i>S,R</i> )	1.65 $\pm$ 0.23
22	<b>1r</b>	H	<i>o</i> -NO <sub>2</sub> -Ph	tBu	Bn	76	( <i>S,R</i> )	0.89 $\pm$ 0.19
23	<b>1b<sup>b</sup></b>	CO <sub>2</sub> Me	<i>o</i> -NO <sub>2</sub> -Ph	tBu	Et	>99	( <i>S,R</i> )	0.66 $\pm$ 0.05
24	<b>1c<sup>b</sup></b>	H	<i>o</i> -NO <sub>2</sub> -Ph	tBu	Et	>99	( <i>S,R</i> )	0.48 $\pm$ 0.06
25	<b>1d<sup>b</sup></b>	CO <sub>2</sub> Me	<i>p</i> -Me-Ph	tBu	Et	>99	( <i>S,R</i> )	0.047 $\pm$ 0.002
26	<b>1d<sup>ab</sup></b>	CO <sub>2</sub> Me	<i>p</i> -Me-Ph	tBu	Et	>99	( <i>R,S</i> )	3.41 $\pm$ 0.26
27	<b>1o<sup>b</sup></b>	H	<i>p</i> -Me-Ph	tBu	Et	>99	( <i>S,R</i> )	0.16 $\pm$ 0.05
28	<b>1g<sup>bc</sup></b>	CO <sub>2</sub> Me	Ph	tBu	Et	>99	( <i>S,R</i> )	0.09 $\pm$ 0.01

[a] Acquired using (*S,S*)-Et-BPE, [b] Purified on chiral preparative HPLC, IC column, DCM:EtOH(100:2)/*iso*-hexane = 30/70, flow rate = 3 mL min<sup>-1</sup>. [c] Enantiomer purified using DCM:MeOH(100:5)/*iso*-hexane = 30/70. [d] IC<sub>50</sub> value obtained from the automated Kyn Assay.

Interestingly, the enantioenriched analogue derived from the (*S,S*) phosphine catalyst, namely (*R,S*)-**1b**, was substantially less active than the hit compound (*S,R*)-**1b** (Table 1, entries 2-3) with an IC<sub>50</sub> of 2.44  $\pm$  0.56  $\mu$ M. This observed trend was consistent for all (*R,S*) enantiomers when compared to its (*S,R*) enantiomers (Figure 16 and Table 1, compare entries 2 and 3, 5

## Results

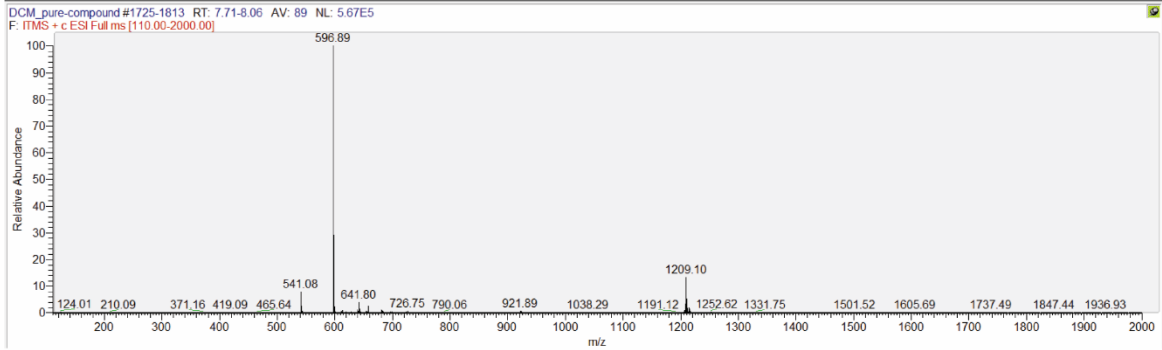
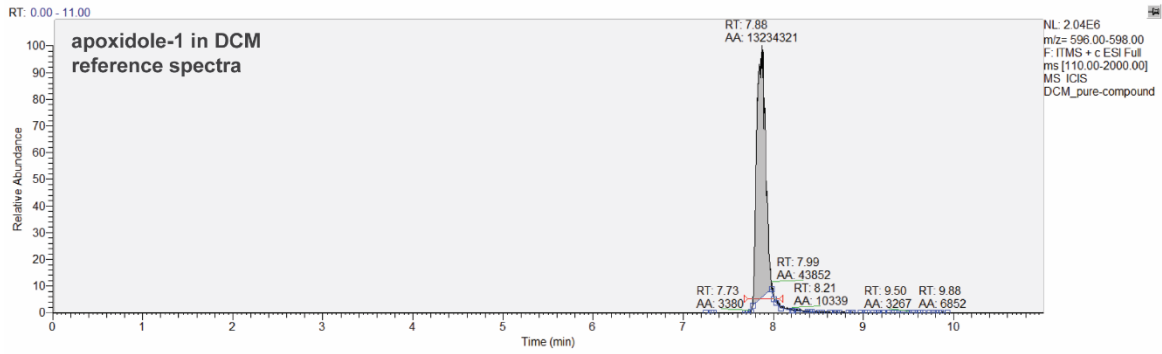
and 6, 15 and 16, 19 and 20). Compounds lacking the methyl ester at R<sup>1</sup> are generally less active than compounds with the stereogenic center in this position (Table 1, entries 2 and 4, 12 and 14, 23 and 24, 25 and 27). For modifications on the sulfonyl group in R<sup>2</sup> position, hydrophobic moieties like methyl, phenyl or tolyl provided sub-micromolar activities (Table 1, entries 5-9). Electron-withdrawing substituents or substituents in *ortho* or *meta* position on the phenyl ring decreased the potency (Table 1, entries 1-4, 10-11, 13). The combination of tert-butyl and ethyl ester in R<sup>3</sup> and R<sup>4</sup> position generally increased the activity, while compounds with larger esters are less potent (Table 1, entries 15-22). Ultimately, enantiopure (*S,R*)-**1d** (Figure 16 and Table 1, entry 25) with methyl, tert-butyl and ethyl esters in R<sup>1</sup>, R<sup>3</sup> and R<sup>4</sup> position, respectively, and a tosyl substituent on the nitrogen of the THP was the most active derivative with an IC<sub>50</sub> value of 46.7 ± 2.4 nM. This analogue was termed apoxidole-1 and was selected for in-depth biological characterization.

### 5.1.1.3 Stability of the Ester Groups

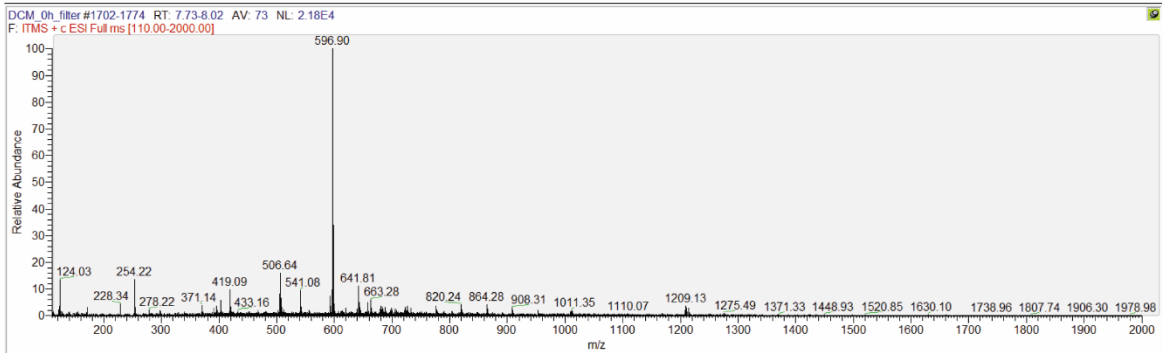
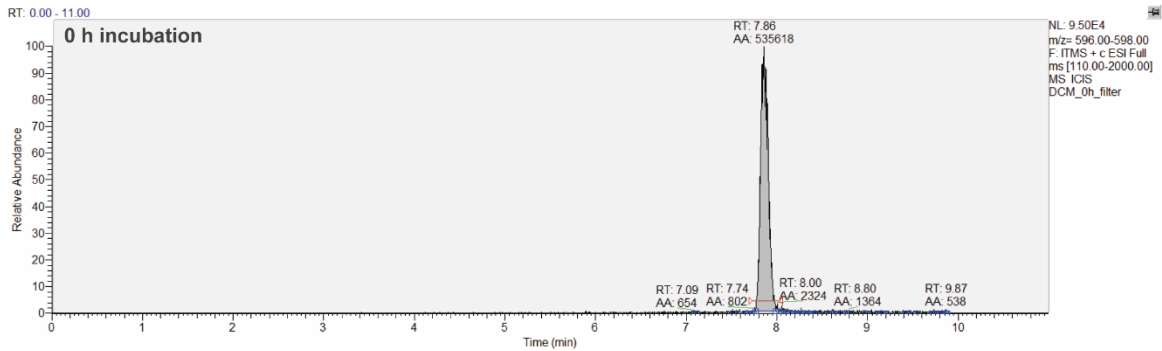
Apoxidole-1 contains three ester groups which might be hydrolyzed by esterases in the cell culture growth medium or cellular environment<sup>166, 167</sup>. Thus, the stability of the esters was evaluated by incubation of apoxidole-1 in serum for up to 48 h (Figure 15). The reference spectrum of apoxidole-1 in dichloromethane (DCM, Figure 15A) showed a peak at a mass-to-charge ratio *m/z* of 596.89, which corresponds to the molecular weight of apoxidole-1 of 596.22 g/mol. The spectra for the initial time point displayed a peak at the same *m/z* ratio (Figure 15B), confirming that apoxidole-1 was successfully extracted from the serum. The obtained results for incubation of up to 48 h (Figure 15C-F) indicate that all esters in apoxidole-1 are stable in serum.

# Results

## A

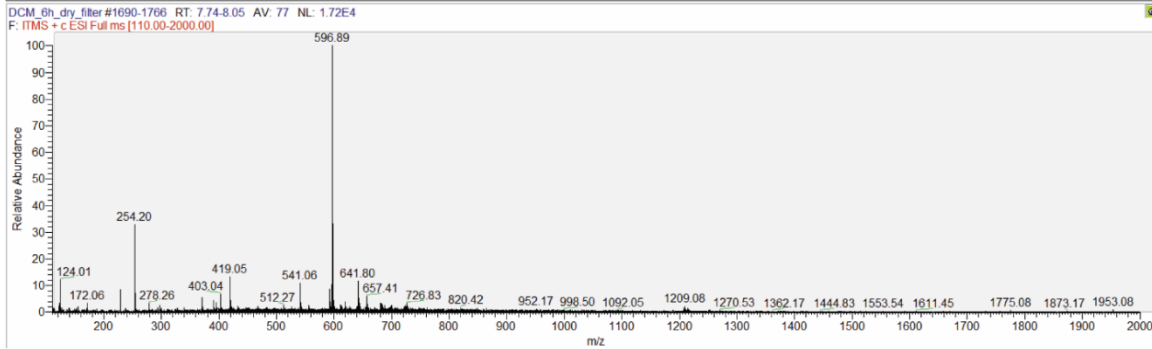
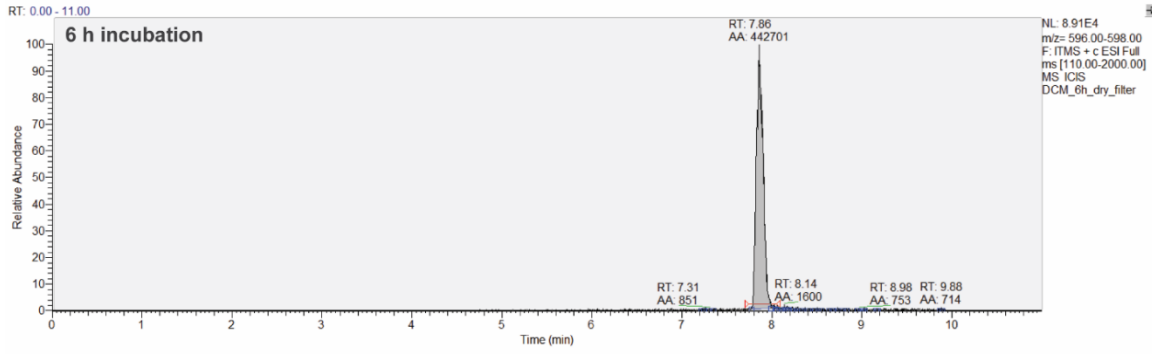


## B

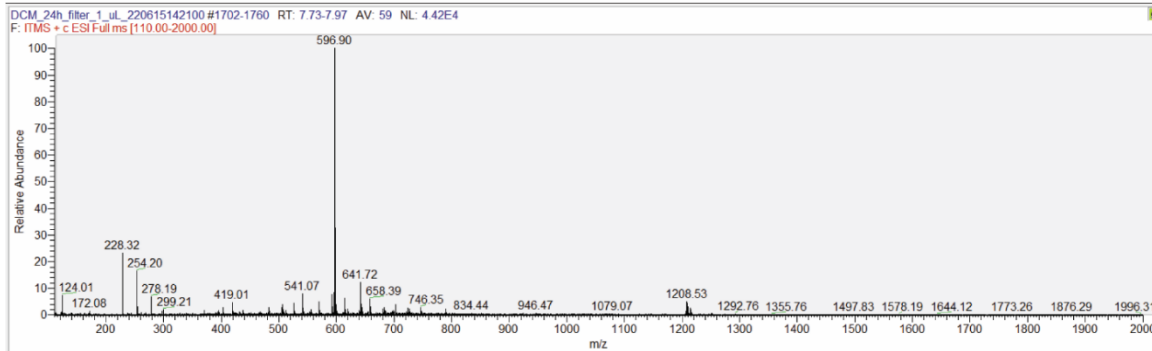
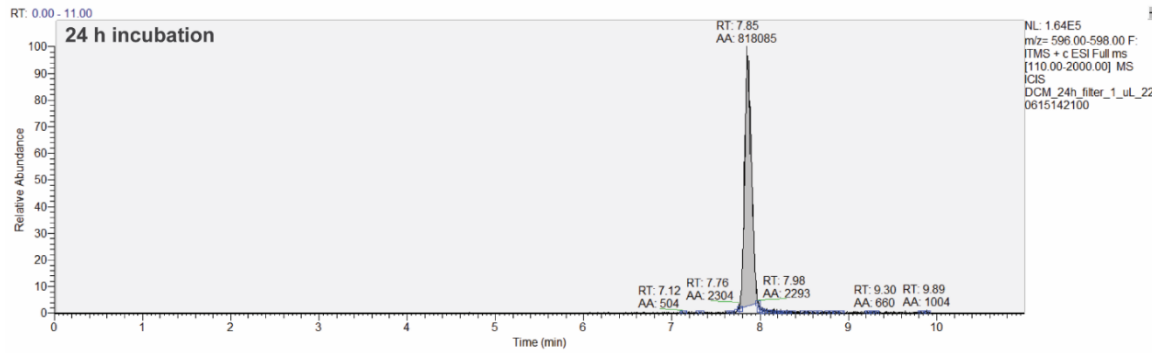


# Results

## C



## D



## Results

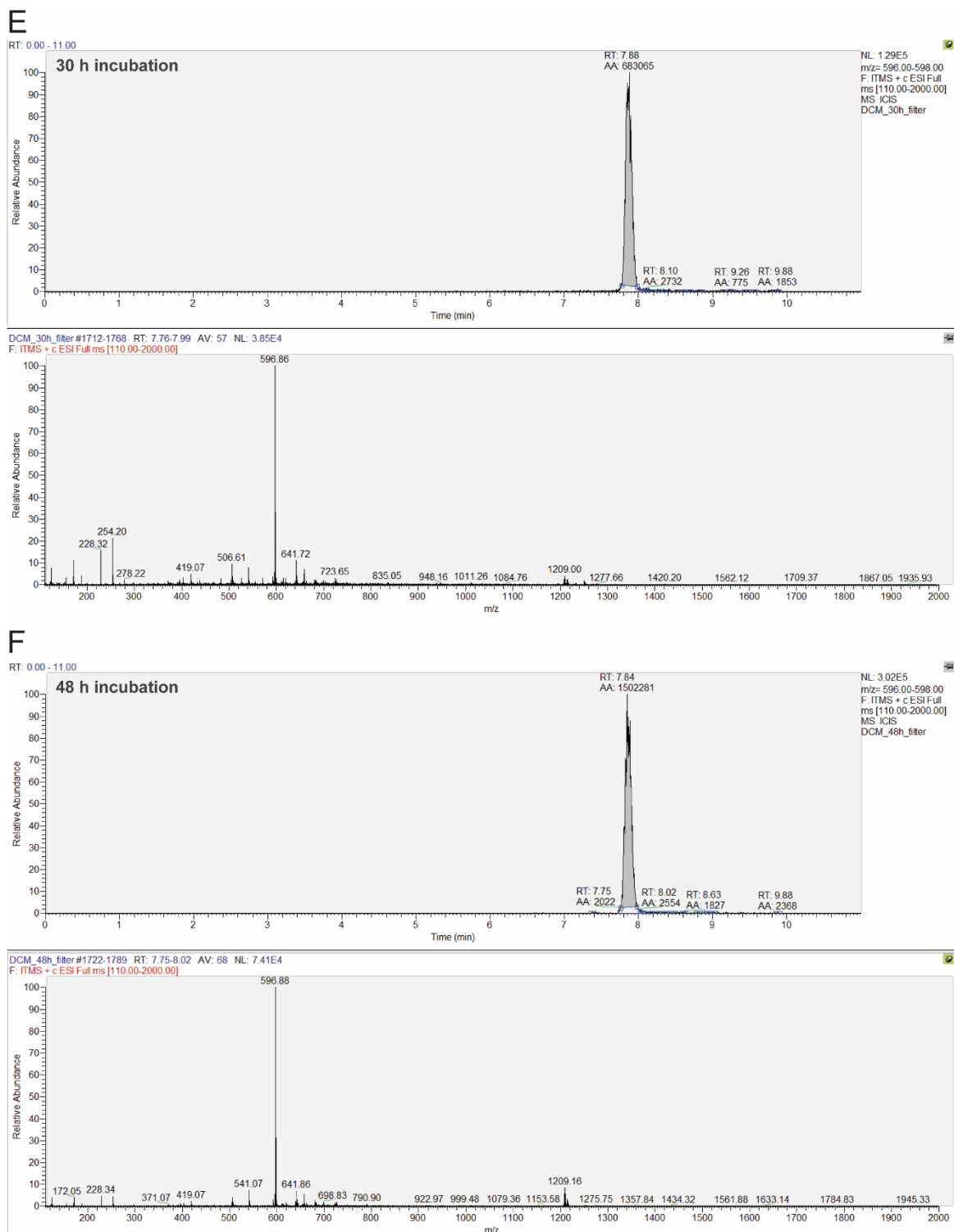


**Figure 15:** Stability of apoxidole-1 in serum. A) Reference HPLC-ESI-MS spectra of apoxidole-1 in DCM. B)-F) 400  $\mu$ M Apoxidole-1 was incubated in fetal bovine serum (FBS) for up to 48 h at 37°C prior to extraction of the compound with DCM. The organic phase was dried and filtered, then subjected to HPLC-ESI-MS analysis.

In the following, the initial hit compound (*S,R*)-**1b** and apoxidole-1 (*S,R*)-**1d** were characterized in various biochemical and cellular assays. The aim was to elucidate the molecular mechanism leading to reduced cellular Kyn levels. Therefore, it was analyzed if the compounds interfere

## Results

with the induction of IDO1 expression, directly engage and inhibit IDO1 and if the MMOA is selective for IDO1 over TDO and IDO2.

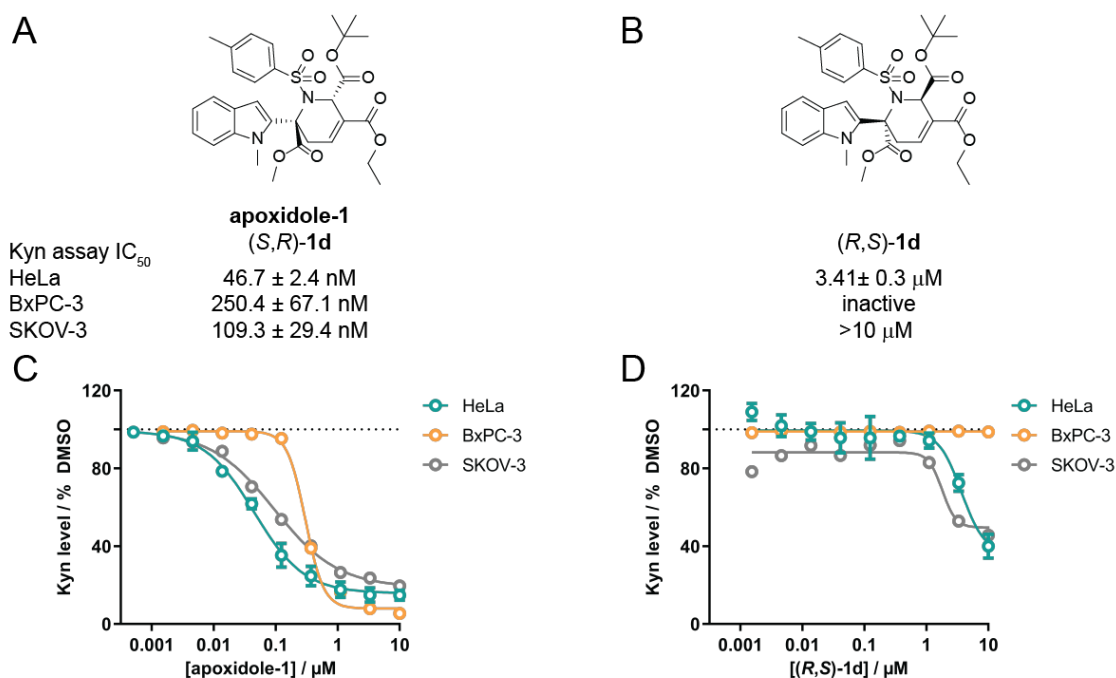


**Figure 16:** Influence of the PNPs apoxidole-1 and its (*R,S*) enantiomer on Kyn levels. A-B) Structures and IC<sub>50</sub> values in the Kyn assay in different cell lines for (*S,R*)-**1d** (apoxidole-1) and (*R,S*)-**1d** (mean ± SD, n = 3). C-D) Determination of Kyn levels in HeLa, BxPC-3 and SKOV-3 cells upon treatment with IFN-γ, Trp and C) (*S,R*)-**1d** or D) (*R,S*)-**1d** for 48 h and detection of Kyn using *p*-DMAB (mean ± SD, n ≥ 3).

### 5.1.2 Influence on IDO1 Expression

The Kyn pathway is initiated by binding of IFN-γ to its receptor, which provokes JAK/STAT signaling and leads to *IDO1* gene expression. By interfering with one of these processes, IDO1 expression is reduced, which in turn decreases cellular Kyn levels. Thus, the influence of apoxidoles on the IFN-γ stimulus and the *IDO1* promoter (Figure 17) as well as IDO1 protein expression (Figure 18) was investigated to analyze if the reduced Kyn production is based on decreased IDO1 levels.

## Results

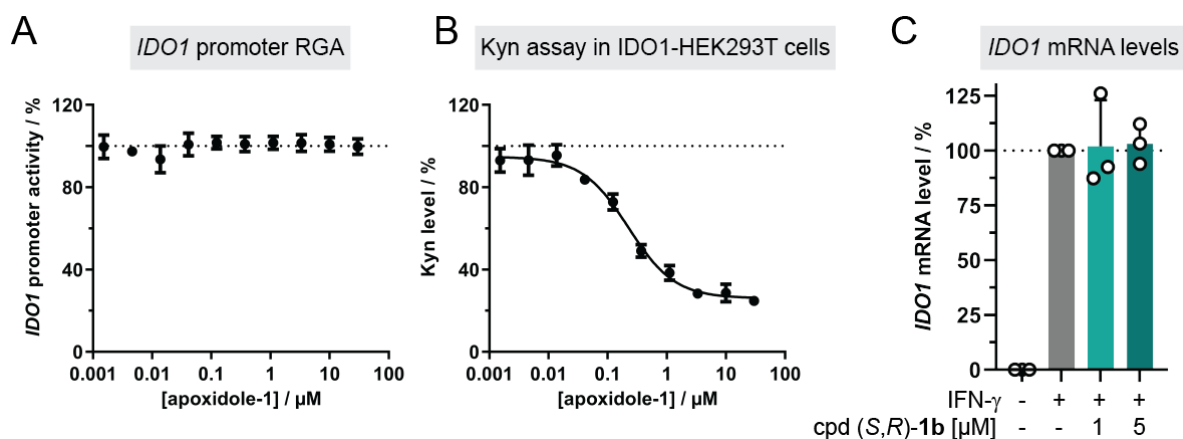


**Figure 17:** Influence of apoxidoles on *IDO1* expression. A) Reporter gene assay (RGA) in HEK293T cells expressing firefly luciferase (Fluc) under the control of the *IDO1* promoter and constitutive *Renilla* luciferase (Rluc) expression. Expression of Fluc was monitored by measuring luminescence upon addition of IFN- $\gamma$  with simultaneous treatment with apoxidole-1 for 48 h (mean  $\pm$  SD, n=3). B) Kyn assay in HEK293T cells transiently expressing human *IDO1* under the control of a CMV promoter. Cells were treated with Trp and apoxidole-1 for 24 h prior to measuring Kyn levels with *p*-DMAB (mean  $\pm$  SD, n=3). C) *IDO1* mRNA expression in HeLa cells upon treatment with IFN- $\gamma$  and the hit compound (*S,R*)-**1b** for 24 h (mean  $\pm$  SD, n=3). cpd: compound.

A reporter gene assay (RGA) was employed to analyze if apoxidole-1 alters *IDO1*-promoter driven gene expression. Therefore, HEK293T cells were transfected with a reporter plasmid encoding a Firefly luciferase (Fluc) under the control of the full-length *IDO1* promoter. 24 h post transfection, the cells were treated simultaneously with IFN- $\gamma$  and different concentrations of apoxidole-1 prior to incubation for 48 h (Figure 17A). While the addition of IFN- $\gamma$  strongly induces Fluc expression, treatment with apoxidole-1 did not alter the luminescence signal compared to the DMSO+IFN- $\gamma$  control. Complementary, it was tested if apoxidole-1 reduces cellular Kyn levels independent of IFN- $\gamma$ , JAK/STAT signaling and the *IDO1* promoter. Thus, HEK293T cells were transiently transfected with a construct for *IDO1* expression under the control of a cytomegalovirus (CMV) promoter in the absence of IFN- $\gamma$  (Figure 17B). 20 h after transfection, the cells were treated with the *IDO1* substrate Trp and apoxidole-1 for additional 24 h. Compared to the DMSO control, apoxidole-1 reduced the Kyn level by  $75.3 \pm 3.2\%$  at 20  $\mu\text{M}$  with an  $\text{IC}_{50}$  of  $209.3 \pm 59.4$  nM. Additionally, post-transcriptional gene regulation on the mRNA level, e.g. *via* miRNA and the RNA-induced silencing complex (RISC)<sup>168</sup>, can silence the *IDO1* gene. Hence, hit compound (*S,R*)-**1b** was tested for reduction of *IDO1* mRNA. (*S,R*)-**1b** did not decrease *IDO1* mRNA levels in HeLa cells quantified by means of RT-qPCR (Figure 17C). Taken together, these results indicate that Kyn level reduction by apoxidoles is independent of the IFN- $\gamma$  stimulus and not mediated by altered gene expression.



## Results

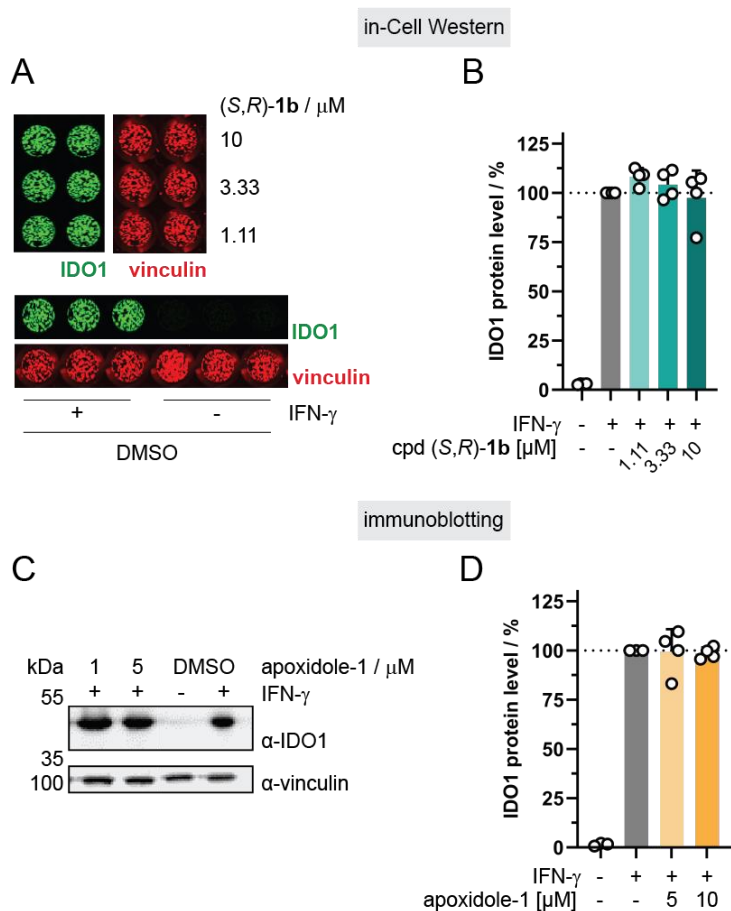


**Figure 18:** Influence of apoxidoles on IDO1 protein expression. A-B) In-cell Western of IDO1 protein levels in BxPC-3 cells upon treatment with IFN- $\gamma$  and the hit compound (S,R)-1b or DMSO for 24 h. Representative images are shown (A, mean  $\pm$  SD, n=4). IDO1 fluorescence intensities were normalized to the reference protein vinculin (B). C-D) IDO1 protein levels in HeLa cells that were treated with IFN- $\gamma$  and apoxidole-1 or DMSO for 24 h. Representative immunoblot is shown (C, mean  $\pm$  SD, n $\geq$ 2). IDO1 band intensities were normalized to the reference protein vinculin (D). cpd: compound.

Apoxidoles might alter IDO1 levels by inhibiting translation of *IDO1* mRNA or increasing protein turnover. Therefore, the influence of apoxidoles on the IDO1 protein levels was analyzed by in-cell Western (Figure 18A) and immunoblotting (Figure 18C). In the absence of IFN- $\gamma$ , no IDO1 was detected with both in-cell Western (Figure 18B) and immunoblotting (Figure 18D). On the other hand, stimulation with IFN- $\gamma$  strongly induced IDO1 protein expression. The IDO1 protein levels upon IFN- $\gamma$ -induced expression were not altered after treatment with both the initial hit compound (S,R)-1b or apoxidole-1 in BxPC-3 or HeLa cells. This demonstrates that apoxidoles do not reduce Kyn levels by decreased IDO1 protein levels.

### 5.1.3 Influence on Trp Uptake

Kyn is produced following the conversion of Trp to *N*-formyl-Kyn by IDO1. Since IDO1 is a cytosolic protein, sufficient amounts of Trp has to be taken up by the cells to be readily available for catalysis. Hence, inhibition of the Trp uptake can reduce Kyn production. A Trp uptake assay was employed to investigate whether compound treatment lowers the availability

## Results

of the IDO1 substrate Trp within cells. Trp cannot freely diffuse into cells, but has to be imported through specific transport mechanisms<sup>169</sup>. It can be taken up by cells *via* an IFN- $\gamma$ -independent and -dependent route. The transmembrane system L-type amino acid transporter (LAT) imports large neutrally charged amino acids into the cells such as Leu, Phe, Tyr or Trp<sup>170</sup>. Because LATs are responsible for the majority of Leu uptake, the IFN- $\gamma$ -independent Trp uptake by LATs can be inhibited by saturating concentrations of Leu<sup>171, 172</sup>. On the other hand, Trp can be taken up by the IFN- $\gamma$ -induced tryptophanyl-tRNA synthetases (TrpRS)<sup>169</sup>. The canonical function of TrpRS is the catalysis of the aminoacylation reaction of Tr with its cognate tRNA within the cell<sup>173</sup>. Nevertheless, TrpRS also has non-canonical functions connected to cell signaling, the immune system and angiogenesis and it represents the only IFN- $\gamma$ -inducible tRNA synthetase<sup>174</sup>. TrpRS can be secreted into the extracellular space<sup>175</sup>, where it can bind Trp with higher affinity compared to LATs<sup>174</sup> and selectively transports Trp into the cells<sup>174, 176</sup>. Trp uptake via TrpRS can be inhibited by the Trp derivative 1-methyl-L-tryptophan (1-MT)<sup>169</sup>.

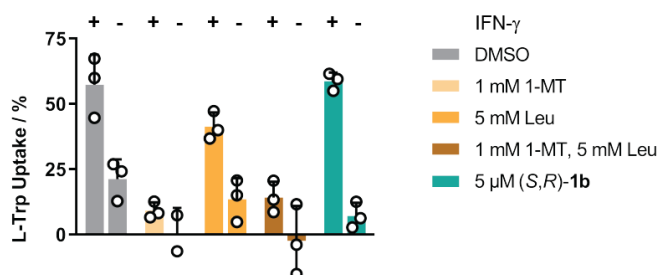


**Figure 19:** Influence of hit compound (*S,R*)-**1b** on the uptake of Trp. BxPC-3 cells were starved for Trp for 72 h and treated with IFN- $\gamma$  for 24 h prior to addition of control inhibitors (5 mM L-Leu, 1 mM 1-MT) or 5  $\mu$ M (*S,R*)-**1b** for 30 min. Afterwards, 50  $\mu$ M Trp was added and Trp uptake was quantified by HPLC-MS/MS (mean  $\pm$  SD,  $n \geq 3$ ). L-Leu: L-leucine. 1-MT: 1-methyl-L-tryptophan.

Treating the cells with IFN- $\gamma$  increased the Trp uptake almost threefold from  $21.3 \pm 6.1\%$  to  $57.3 \pm 9.5\%$  (Figure 19). Addition of the TrpRS inhibitor 1-MT reduced the Trp uptake in both IFN- $\gamma$ -treated and -untreated conditions drastically to  $9.2 \pm 2.6\%$  and  $0.52 \pm 6.9\%$ , respectively. Similarly, saturating the LATs with Leu decreased the Trp uptake to  $41.3 \pm 4.4\%$  in the presence and to  $13.5 \pm 6.6\%$  in the absence of IFN- $\gamma$ . Combination of both TrpRS and LAT inhibitors likewise abolished the Trp uptake to  $14.2 \pm 4.9\%$  and  $-2.5 \pm 10.9\%$  in the presence or absence of IFN- $\gamma$ , respectively. On the contrary, the initial hit compound (*S,R*)-**1b** did not significantly interfere with Trp uptake: Upon treatment with (*S,R*)-**1b**, the cells were able to import  $58.6 \pm 2.7\%$  and  $7.2 \pm 4.1\%$  of the supplemented Trp in the presence or absence of IFN- $\gamma$ , respectively. Therefore, (*S,R*)-**1b** does not reduce Kyn levels by impairing Trp uptake.

### 5.1.4 Identification and Validation of the Molecular Target of Apoxidole-1

Direct inhibition of the IDO1 protein reduces Kyn levels. Röhrig *et al.*<sup>98</sup> classified five types of IDO1 inhibitors, with three of them targeting the holo-enzyme, one of them binding to apo-

## Results

IDO1 and the last one acting by a redox mechanism. An *in vitro* Kyn assay with purified full-length human IDO1 was performed to investigate if apoxidole-1 inhibits the IDO1 protein directly (Figure 20).

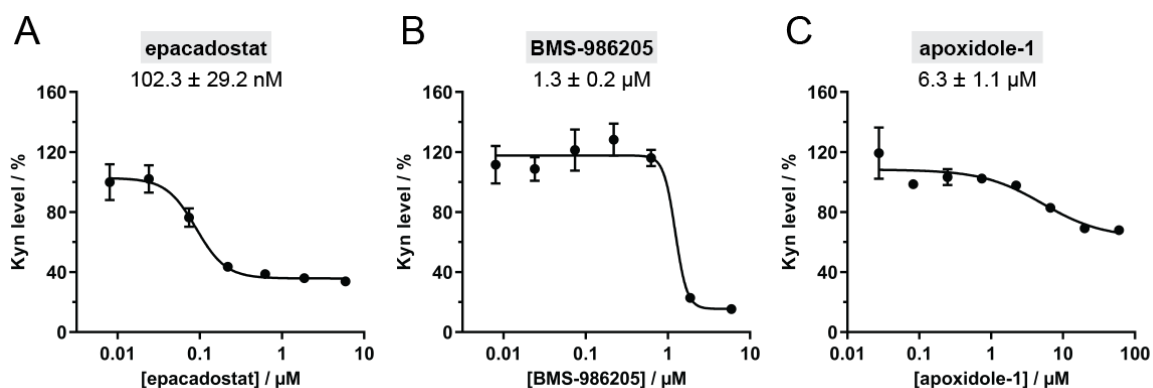


**Figure 20:** Influence on *in vitro* IDO1 activity. Purified human holo-IDO1 protein was treated with A) epacadostat, B) BMS-986205 and C) apoxidole-1 for 40 min at 37 °C prior to addition of the IDO1 substrate Trp for 60 min at 37°C. Kyn levels were detected using *p*-DMAB (mean  $\pm$  SD,  $n=2$ ).

Therefore, IDO1 was pre-treated with compounds for 40 min at 37°C prior to initiation of the reaction by addition of the IDO1 substrate Trp. The holo-IDO1 inhibitor epacadostat potently reduced Kyn levels with an  $IC_{50}$  value of  $102 \pm 29$  nM (Figure 20A), while the apo-IDO1 inhibitor BMS-986205 was approximately 13-fold less active with an  $IC_{50}$  of  $1.3 \pm 0.2$   $\mu$ M (Figure 20B). Apoxidole-1 partially decreased Kyn levels by  $32.0 \pm 2.8\%$  with an  $IC_{50}$  of  $6.3 \pm 1.1$   $\mu$ M (Figure 20C). Because the heme release is a slow process, apo-IDO1 inhibitors display only weak inhibition in the biochemical Kyn assay. Since apoxidole-1 only partially reduced Kyn levels (Figure 20C), this indicated that apoxidole-1 might be an apo-IDO1 inhibitor.

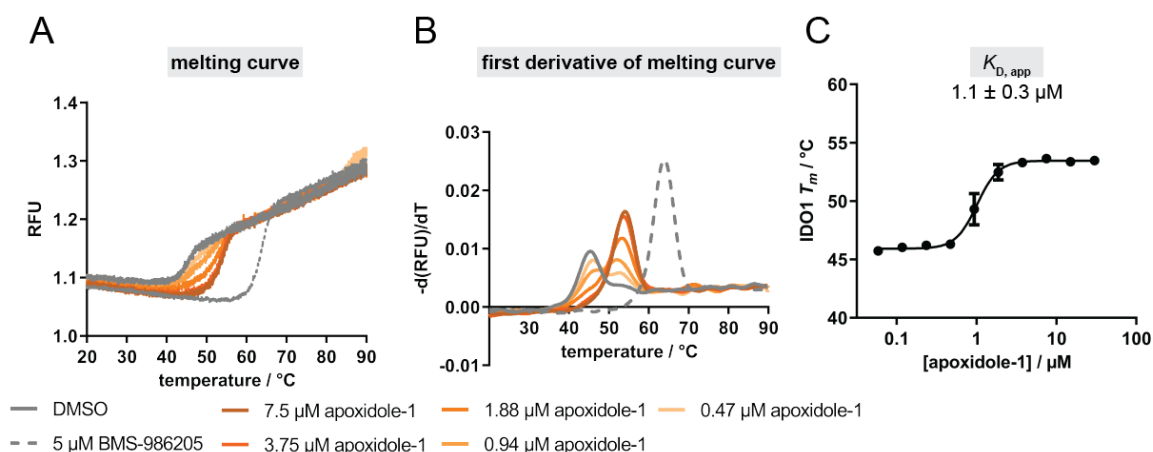


**Figure 21:** Influence of apoxidole-1 on the thermostability of IDO1. A-B) Purified holo-IDO1 was treated with apoxidole-1 or DMSO for 60 min at 37 °C prior to detection of the intrinsic Trp/Tyr fluorescence upon thermal denaturation. Representative melting curves (A) and first derivative of melting curves (B) are shown ( $n=3$ ). C) Apoxidole-1 binds to IDO1 with an apparent  $K_{D, app}$  value of  $1.1 \pm 0.3$   $\mu$ M, as determined using the data from A and B (mean  $\pm$  SD,  $n=3$ ).

## Results

Analyzing the thermal stability of a protein upon compound treatment can give hints about target engagement. By binding to its target, a compound can (de-)stabilize it, changing its thermal denaturation temperature  $T_m$ . Nano differential scanning fluorimetry (nanoDSF) uses the intrinsic fluorescence of tyrosines (Tyr) and Trps to detect denaturation of proteins in a thermal gradient. During unfolding of the protein, the environment of these fluorophores changes and, thus, alters their fluorescence intensity<sup>177</sup>. IDO1 contains six tryptophanes and twelve tyrosines, thereby being suitable for nanoDSF analysis. Treatment of purified IDO1 with BMS-986205 or different concentrations of apoxidole-1 dose-dependently shifted the melting curves of IDO1 to higher temperatures (Figure 21A). Using the first derivative of the melting curves, the corresponding melting temperatures  $T_m$  can be determined as the highest peak of the curve (Figure 21B). Binding of BMS-986205 increased the melting temperature of IDO1 by  $18.4 \pm 0.6^\circ\text{C}$  from  $45.7 \pm 0.2^\circ\text{C}$  to  $64.1 \pm 0.6^\circ\text{C}$ , while treatment with apoxidole-1 increased the  $T_m$  value by  $7.7 \pm 0.3^\circ\text{C}$  to  $53.5 \pm 0.2^\circ\text{C}$  (Figure 21B). With the  $T_m$  values of IDO1 at different doses of apoxidole-1 an apparent  $K_{D, \text{app}}$  value of  $1.1 \pm 0.3 \mu\text{M}$  was obtained (Figure 21C).

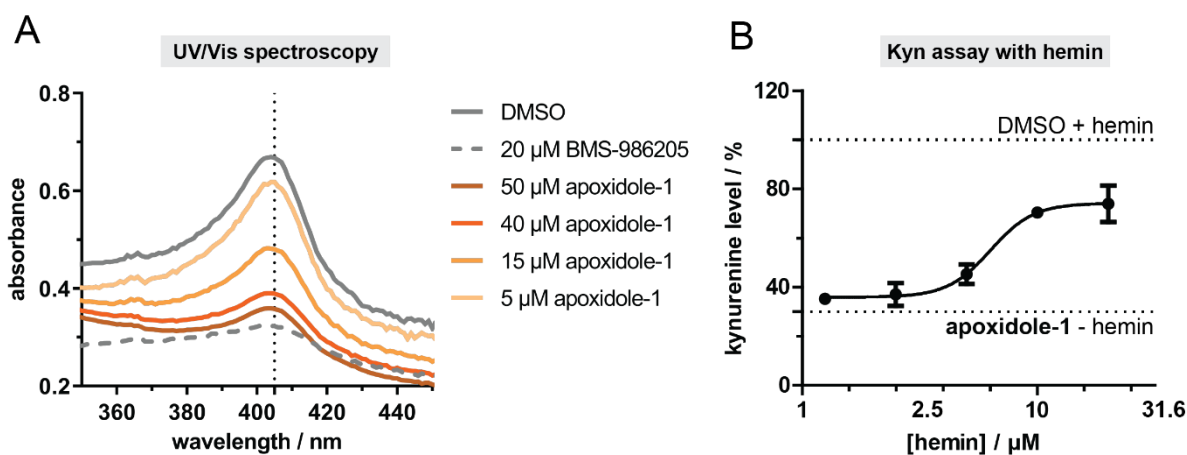


**Figure 22:** Binding of apoxidole-1 to holo-IDO1 releases heme. A) Purified holo-IDO1 was treated with apoxidole-1, BMS-986205 or DMSO for 2 h at  $37^\circ\text{C}$  prior to acquiring UV/Vis spectra. Representative spectra are shown ( $n=3$ ). The dotted line indicates the Soret peak at 404 nm. B) Determination of cellular Kyn levels in the presence of hemin. BxPC-3 cells were treated with IFN- $\gamma$ , Trp, hemin and 600 nM apoxidole-1 for 48 h prior to measuring Kyn levels with *p*-DMAB (mean  $\pm$  SD,  $n=3$ ).

As apo-IDO1 inhibitors show decreased potency in the biochemical Kyn assay compared to the cellular assay, it was investigated if binding of apoxidole-1 to IDO1 releases the heme cofactor. IDO1 was treated with apoxidole-1 or BMS-986205 and the Soret peak was monitored by means of UV/Vis spectroscopy (Figure 22A). The Soret peak is the characteristic absorbance maximum at 404 nm of the iron in heme-containing enzymes. A red-shift of the peak indicates ligand coordination to the heme iron, while a reduction of the peak demonstrates heme loss<sup>178</sup>. Treatment with both BMS-986205 and apoxidole-1 decreased the Soret peak compared to the DMSO control (Figure 22A). Furthermore, addition of free hemin

## Results

dose-dependently reduced the potency of apoxidole-1 in the cellular Kyn assay (Figure 22B). Taken together, these results demonstrate that apoxidole-1 binds to IDO1 and induces heme release, thereby inhibiting Kyn production.

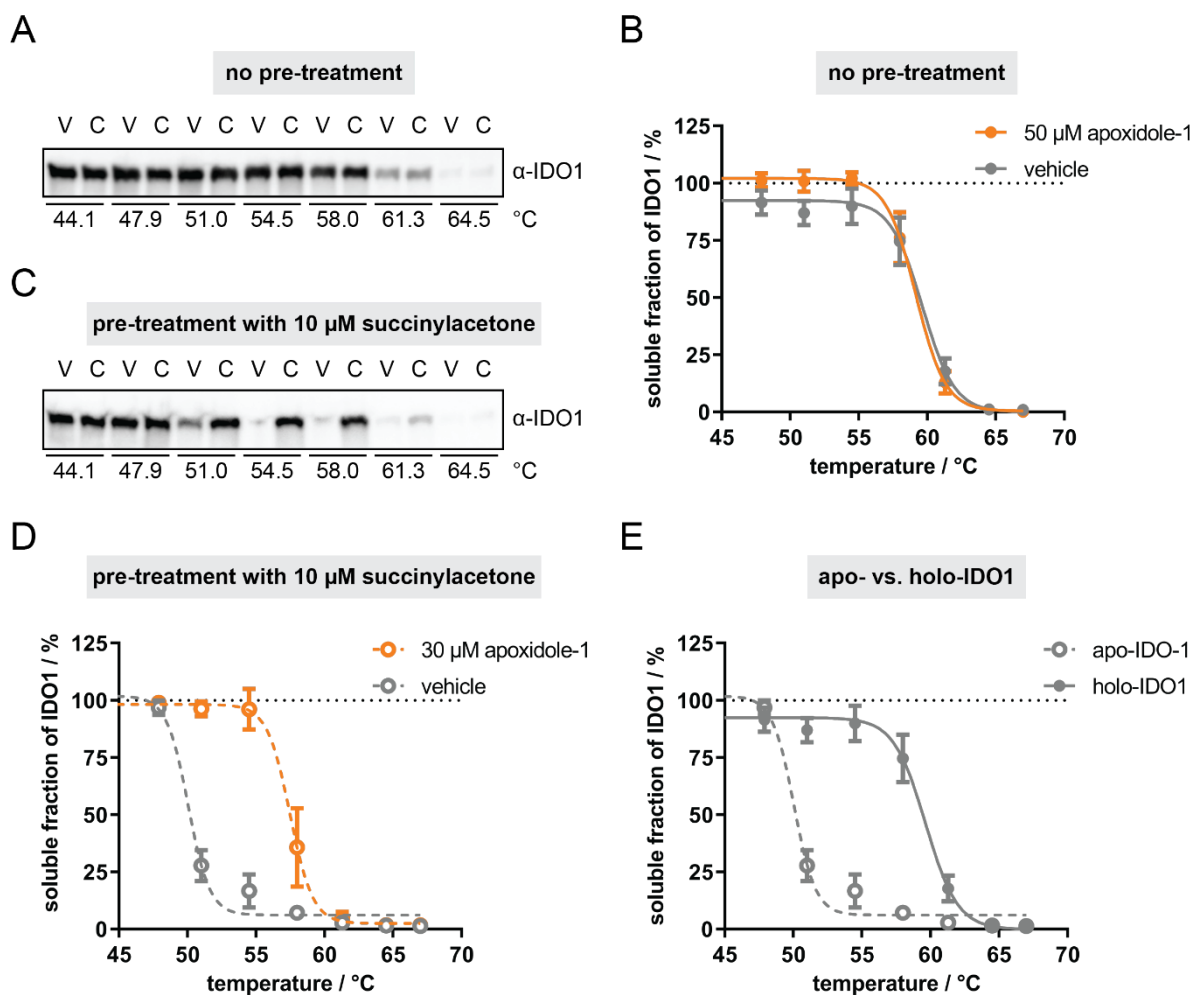


**Figure 23:** Apoxidole-1 binds to apo-IDO1 in cells. A) Cellular thermal shift assay (CETSA) for IDO1 in SKOV-3 cells. Cells were treated with IFN- $\gamma$  for 24 h prior to addition of 50  $\mu$ M apoxidole-1 (compound, C) or DMSO (vehicle, V) for 15 min. Representative immunoblot is shown. B) Thermal profiles of IDO1 upon compound treatment. Quantification of IDO1 band intensities from A shown in B (mean  $\pm$  SD, n=4). C) CETSA for apo-IDO1 in SKOV-3 cells. Cells were treated with IFN- $\gamma$  and 10  $\mu$ M succinylacetone (heme synthesis inhibitor, SA) for 24 h prior to addition of 30  $\mu$ M apoxidole-1 or DMSO for 15 min. Representative immunoblot is shown. D) Thermal profiles of IDO1 upon compound treatment. Quantification of IDO1 band intensities from C shown in D (mean  $\pm$  SD, n=3). E) Thermal profiles of holo- (in the absence of SA) and apo-IDO1 (in the presence of SA).

Subsequently, target engagement in cells using a cellular thermal shift assay (CETSA)<sup>136, 137</sup> was studied. Therefore, SKOV-3 cells were treated with apoxidole-1 or DMSO for 15 min prior to performing the thermal shift assay and analysis of the soluble protein fraction using immunoblotting. Treatment of apoxidole-1 did not alter the thermal stability of IDO1 (Figure 23A-B). However, pre-treatment of the cells with the heme synthesis inhibitor succinylacetone for 24 h, followed by the thermal shift assay, increased the melting temperature  $T_m$  of IDO1 by  $7.9 \pm 0.6^\circ\text{C}$  (Figure 23C-D). Upon treatment with succinylacetone, IDO1 was mainly present

## Results

as apo protein. The increased melting temperature  $T_m$  in the presence of succinylacetone thus strongly indicates that apoxidole-1 engages apo-IDO1. Additionally, holo-IDO1 displays a higher melting temperature  $T_m$  with  $59.9 \pm 0.2^\circ\text{C}$  compared to apo-IDO1 with a  $T_m$  of  $50.2 \pm 0.2^\circ\text{C}$  (Figure 23E).

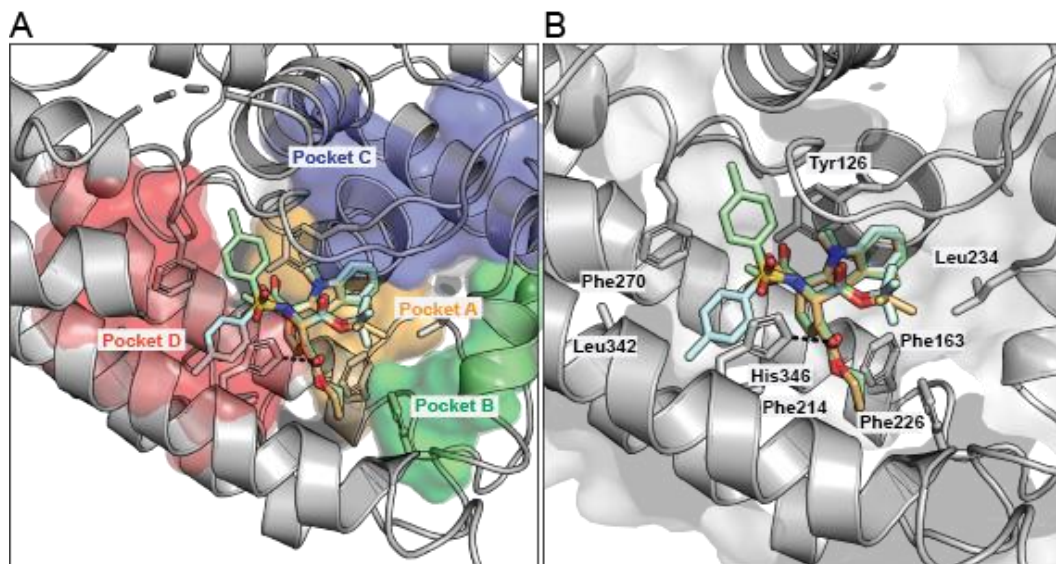


**Figure 24:** Co-crystal structure analysis of apoxidole-1 bound to apo-IDO1 (pdb 8abx). A) Apoxidole-1 displaces the heme cofactor and occupies pockets A and D of apo-IDO1. The IDO1 active site consists of four sub-pockets: Pockets A (orange), B (green), C (blue) and D (red). B) Secondary structure elements stabilizing apoxidole-1 in the IDO1 active site. Apoxidole-1 binds to the hydrophobic pocket of apo-IDO1 (gray cartoons) in two different conformations (green and cyan sticks, a third conformation lacking the tosyl residue on the THP of apoxidole-1 is shown in orange). The amino acids in the active site are labeled with the three-letter code. The dotted black line indicates a hydrogen bond between His346 and the carbonyl oxygen of the ethyl ester of apoxidole-1. Heteroatoms of the ligand are depicted in red (oxygen), blue (nitrogen) and yellow (sulfur). Amino acids 383–389 are omitted for clarity.

A co-crystal structure of apo-IDO1 in complex with apoxidole-1 was obtained in collaboration with Dr. Raphael Gasper (crystallography and biophysics department, Max Planck Institute of Molecular Physiology) and the Swiss Light Source (Paul Scherrer Institut, CH) to determine the binding mode of apoxidole-1 to IDO1 (Figure 24, pdb 8abx). The crystal structure revealed that apoxidole-1 binds to the active site of IDO1 in two different conformations, occupying the heme-binding site and sub-pockets A and D (Figure 24A). The compound is stabilized mainly by hydrophobic interactions with Tyr126, Phe163, Phe214, Phe226, Leu234, Phe270, and Leu342 (B). Additionally, a hydrogen bond is formed between His346 and the carbonyl oxygen of the ethyl ester of apoxidole-1.

### 5.1.5 Selectivity of Apoxidole-1 for IDO1 over TDO and IDO2

In addition to IDO1, IDO2 and TDO may also contribute to Trp catabolism in the TME. Even though all three heme-containing enzymes catalyze the same reaction, there are substantial differences between them. IDO1 and IDO2 are encoded by homologous genes and share 43% sequence identity<sup>179, 180</sup>. The active site of human IDO2 is composed of the residues required

## Results

for the conversion of Trp, but still IDO2 is substantially less active than IDO1 with a 325-fold increased  $K_m$  value for Trp<sup>180, 181</sup>. In contrast to that, TDO and IDO1 have similar catalytic properties, while they are encoded by distinct genes and share only 16% sequence identity<sup>179, 182</sup>. Moreover, TDO has a higher substrate specificity and is generally resistant to apo-inhibitors<sup>180, 182</sup>. Since TDO and IDO2 are not inducible by IFN- $\gamma$ , the inhibitors discovered in the screening assay most likely interfere with IDO1-related Kyn production. However, TDO and IDO2 still might be present in the TME. Thus, it is crucial to investigate the selectivity of apoxidole-1 towards IDO1. In contrast to the oxygen-competitive IDO1 inhibitor epacadostat, the apo-IDO1 inhibitors BMS-986205 and apoxidole-1 did not reduce TDO or IDO2 activity (Figure 25A-B). Hence, apo-IDO1 inhibitors are selective for IDO1, while the holo-IDO1 inhibitor epacadostat inhibits all three Trp-catabolizing enzymes to a certain extent.

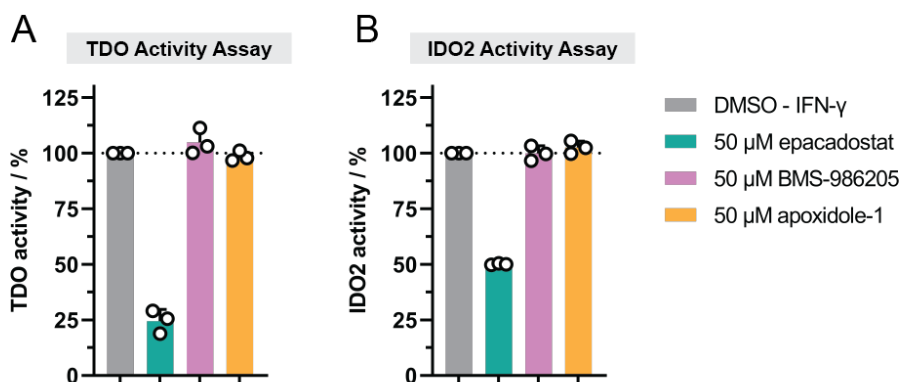


**Figure 25:** Influence on TDO and IDO2 activity. A) Purified TDO protein was treated with epacadostat, BMS-986205 or apoxidole-1 for 120 min at 37°C prior to detection of the reaction product using the Universal IDO1/IDO2/TDO Inhibitor Screening Assay Kit (mean  $\pm$  SD, n=3). B) Purified IDO2 protein was treated with epacadostat, BMS-986205 or apoxidole-1 for 90 min at 30°C prior to addition of the IDO2 substrate. Samples were incubated for another 120 min at 30°C prior to detection of the reaction product using the Universal IDO1/IDO2/TDO Inhibitor Screening Assay Kit (mean  $\pm$  SD, n=3).

In summary, apoxidole-1 binds to IDO1 and abolishes its catalytic activity by displacement of the heme cofactor. Apoxidole-1 selectively targets IDO1 over TDO and IDO2 and thus, reduces cellular Kyn levels upon stimulation with IFN- $\gamma$ .

## Results

### 5.2 Epoxykynin sEH Inhibitors as Potent Kyn Pathway Modulators

#### 5.2.1 Confirmation of Reduced Cellular Kyn Levels

Compound **2a** (Figure 11) decreased Kyn levels in BxPC-3 cells in the automated Kyn assay by  $95.5 \pm 3.0\%$  with an  $IC_{50}$  value of  $89.2 \pm 27.8$  nM. To exclude it as a false positive hit, its influence on Kyn levels was tested manually in HeLa cells (Figure 26A) and with HPLC-ESI-MS/MS as an orthogonal readout (Figure 26B).

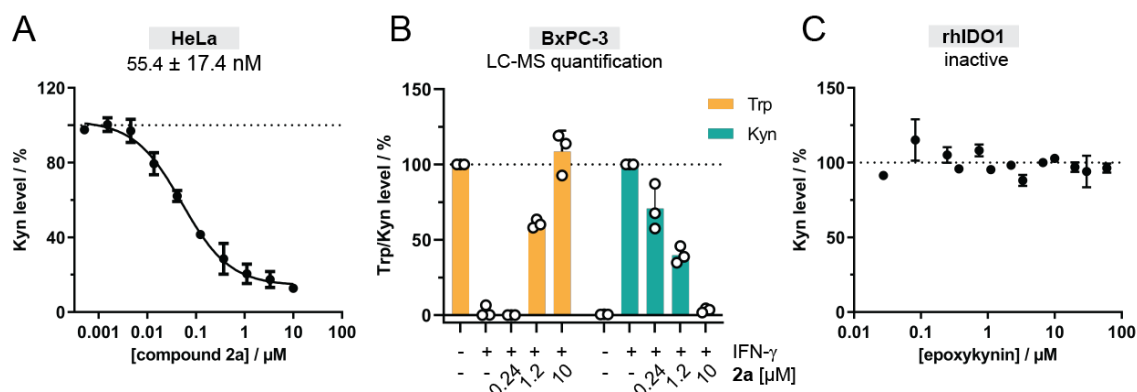


**Figure 26:** Influence of hit compound **2a** and epoxykynin on Kyn levels. A) Determination of Kyn levels in HeLa cells upon treatment with IFN- $\gamma$ , Trp and compound **2a** for 48 h and detection of Kyn levels using *p*-DMAB (mean  $\pm$  SD,  $n=3$ ). B) Determination of Trp and Kyn levels in BxPC-3 cells upon treatment with IFN- $\gamma$ , Trp and compound **2a** for 48 h and quantification of Trp and Kyn levels with HPLC-ESI-MS/MS (mean  $\pm$  SD,  $n \geq 2$ ). C) Purified human holo-IDO1 protein was treated with epoxykynin **2I** for 40 min at 37  $^{\circ}$ C prior to addition of the IDO1 substrate Trp for 60 min at 37 $^{\circ}$ C. Kyn levels were detected using *p*-DMAB (mean  $\pm$  SD,  $n=2$ ).

Hit compound **2a** dose-dependently decreased cellular Kyn levels also in HeLa cells with an  $IC_{50}$  of  $55.4 \pm 17.4$  nM (Figure 26A). Furthermore, HPLC-ESI-MS/MS was used as an orthogonal readout to quantify the levels of Kyn and Trp upon compound treatment. Compound **2a** reduced Kyn levels at a concentration of 0.24  $\mu$ M, while in parallel the level of Trp increased (Figure 26B). Furthermore, the most potent derivative epoxykynin **2I** was tested for direct inhibition of IDO1 in an enzymatic assay and did not impair the IDO1 catalytic activity (Figure 26C). These results confirmed that compound **2a** inhibited the conversion of Trp to Kyn and validated **2a** as true positive hit from the Kyn screen. Additionally, it became apparent that the Kyn level reduction was not mediated by direct inhibition of IDO1.

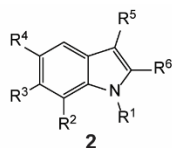
##### 5.2.1.1 Structure-Activity Relationship of N-substituted Indoles

Subsequently, the SAR for a total of 96 derivatives for Kyn reduction in the automated Kyn assay was explored (Table 2 and Table S1).



## Results

**Table 2:** Structures and structure-activity relationship (SAR) of selected N-substituted indoles for reduction of Kyn levels. IC<sub>50</sub> values were determined in BxPC-3 cells using the automated Kyn assay (mean ± SD, n≥3). See also **Table S1**.



entry	compound	R <sup>1</sup>	R <sup>2</sup>	R <sup>3</sup>	R <sup>4</sup>	R <sup>5</sup>	R <sup>6</sup>	Kyn assay IC <sub>50</sub> [μM]
1	<b>2a</b>		H	H	Br	COCF <sub>3</sub>	H	0.09 ± 0.03
2	<b>2b</b>		H	H	Br	COCF <sub>3</sub>	H	0.10 ± 0.02
3	<b>2c</b>		H	H	Br	COCF <sub>3</sub>	H	3.01 ± 0.8
4	<b>2d</b>		H	H	Br	COCF <sub>3</sub>	H	>10
5	<b>2e</b>		H	H	Br	COCF <sub>3</sub>	H	5.43 ± 0.6
6	<b>2f</b>		H	H	Br	COCF <sub>3</sub>	H	0.05 ± 0.02
7	<b>2g</b>		H	H	Br	COCF <sub>3</sub>	H	3.05 ± 0.25
8	<b>2h</b>		H	H	Br	COCF <sub>3</sub>	H	0.10 ± 0.03
9	<b>2i</b>	CH <sub>2</sub> CONH <sub>2</sub>	H	H	H	COCF <sub>3</sub>	H	0.05 ± 0.01
10	<b>2j</b>		H	H	Br	COCF <sub>3</sub>	H	0.40 ± 0.10
11	<b>2k</b>		H	H	H	COCF <sub>3</sub>	H	3.49 ± 0.3
12	<b>2l</b> (epoxykynin)		H	H	Br	COCF <sub>3</sub>	H	0.04 ± 0.02
13	<b>2m</b>		H	H	H	COCF <sub>3</sub>	H	1.73 ± 0.1
14	<b>2n</b>		H	H	H	COCF <sub>3</sub>	H	>10
15	<b>2o</b>		H	H	Br	COCF <sub>3</sub>	H	1.94 ± 0.2
16	<b>2p</b>		H	H	H	COCF <sub>3</sub>	H	7.24 ± 3.8
17	<b>2q</b>		H	H	H	COCF <sub>3</sub>	H	>10
18	<b>2r</b>	Bn	H	H	Br	COCF <sub>3</sub>	H	>10
19	<b>2s</b>	<i>o</i> -Cl-Bn	H	H	Br	COCF <sub>3</sub>	H	>10
20	<b>2t</b>	<i>p</i> -F-Bn	H	H	Br	COCF <sub>3</sub>	H	0.77 ± 0.41
21	<b>2u</b>	<i>p</i> -F-Bn	H	H	H	COCF <sub>3</sub>	H	>10
22	<b>2v</b>	CH <sub>2</sub> CONH <sub>2</sub>	Et	H	H	COCF <sub>3</sub>	H	>10
23	<b>2w</b>	CH <sub>2</sub> CONH <sub>2</sub>	H	H	H	COCF <sub>3</sub>	Me	>10
24	<b>2x</b>	CH <sub>2</sub> CONH <sub>2</sub>	H	H	Br	CHO	H	>10

## Results

The compound library contained derivatives with diverse modifications at the indole nitrogen in R<sup>1</sup> position. Generally, ether and amide N-substituents (Table 2, entries 1-16) were favorable compared to esters, benzyls, or ketones (Table 2, entries 17-21 and Table S1). For aromatic moieties connected *via* an ether linker, *ortho*-substitutions and small, electron-withdrawing groups were favorable (Table 2, entries 2-8). Comparison of amide-linked residues in R<sup>1</sup> position revealed that aliphatic and lipophilic moieties provide high activities (Table 2, entries 10-13), in contrast to tertiary amides or heterocycles (Table 2, entries 14-16, and Table S1). Compounds with substitutions in R<sup>2</sup>, R<sup>3</sup> and R<sup>6</sup> positions are less active (Table 2, entries 22-23, and Table S1), as well as derivatives where the trifluoro acetyl group in R<sup>5</sup> position was replaced (Table 2, entry 24, and Table S1). The bromine in R<sup>4</sup> position is crucial for activity, since it increased the potency of compound **2l** 50-fold compared to the bromine-lacking compound **2m** (Table 2, entries 12-13). Finally, derivative **2l** combined a hydrophobic N-cycloheptyl acetamide group in R<sup>1</sup> with bromo and trifluoro acetyl substituents in R<sup>4</sup> and R<sup>5</sup> positions, and was the most active derivative with an IC<sub>50</sub> value of 36.0 ± 15.0 nM in the automated Kyn assay (Table 2, entry 12). This analogue was termed epoxykynin and subsequently, its potency was validated manually in HeLa and BxPC-3 cells (Figure 27).

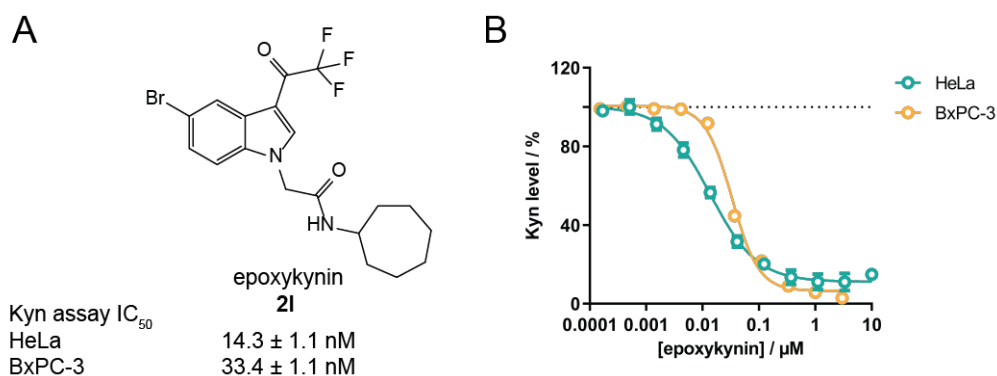


**Figure 27:** Epoxykynin decreases cellular Kyn levels in HeLa and BxPC-3 cells. A) Structure of epoxykynin and IC<sub>50</sub> values for Kyn level reduction. B) Determination of Kyn levels in HeLa and BxPC-3 cells upon treatment with IFN-γ, Trp and epoxykynin for 48 h and detection of Kyn levels using *p*-DMAB (mean ± SD, n=3).

## Results

### 5.2.2 Influence on IDO1 Expression

In the following, epoxykynin was characterized to elucidate the MMOA. First, the influence of epoxykynin on the expression of IDO1 and on Kyn levels without IFN- $\gamma$  was analyzed. Therefore, different cell-based assays were employed.

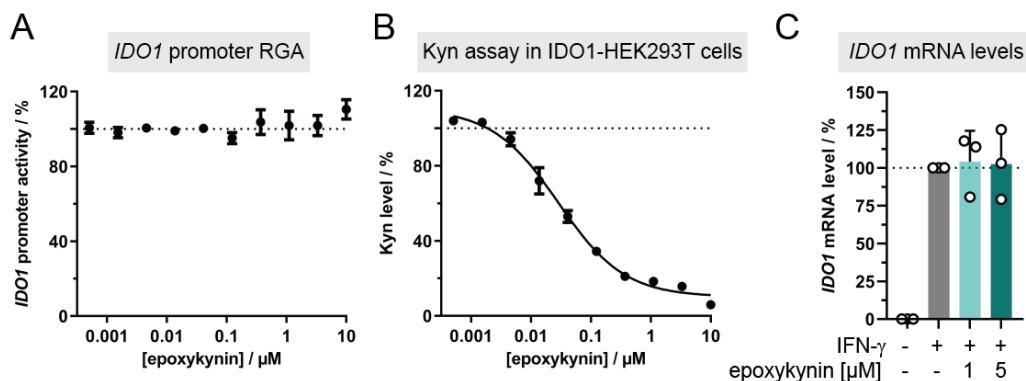


**Figure 28:** Influence of epoxykynin on *IDO1* expression. A) Reporter gene assay (RGA) in HEK293T cells expressing firefly luciferase (Fluc) under the control of the *IDO1* promoter and constitutive *Renilla* luciferase (Rluc) expression. Expression of Fluc was monitored by measuring luminescence upon addition of IFN- $\gamma$  with simultaneous treatment with apoxidole-1 for 48 h (mean  $\pm$  SD, n=3). B) Kyn assay in HEK293T cells transiently expressing human *IDO1* under the control of a *CMV* promoter. Cells were treated with Trp and epoxykynin for 24 h prior to measuring Kyn levels with *p*-DMAB (mean  $\pm$  SD, n=3). C) *IDO1* mRNA expression in HeLa cells upon treatment with IFN- $\gamma$  and epoxykynin for 24 h (mean  $\pm$  SD, n=3).

The influence of epoxykynin on the *IDO1* promoter was investigated by means of a reporter gene assay (RGA). Therefore, cells were transiently transfected with a reporter gene under control of the full-length *IDO1* promoter and subsequently treated with epoxykynin and IFN- $\gamma$  for 48 h (Figure 28A). While IFN- $\gamma$  strongly induced the reporter signal, epoxykynin did not alter the reporter's luminescence. Furthermore, epoxykynin dose-dependently reduced Kyn levels in HEK293T cells transiently expressing *IDO1* under control of a *CMV* promoter in the absence of IFN- $\gamma$  with an  $\text{IC}_{50}$  value of  $29.0 \pm 8.4$  nM (Figure 28B). This indicates that epoxykynin altered the Kyn levels independent of the IFN- $\gamma$  signaling cascade. Additionally, treatment with epoxykynin did not impair transcription of the *IDO1* gene as quantified by *IDO1* mRNA levels (Figure 28C). Thus, epoxykynin reduces Kyn levels without altering *IDO1* gene expression.

## Results

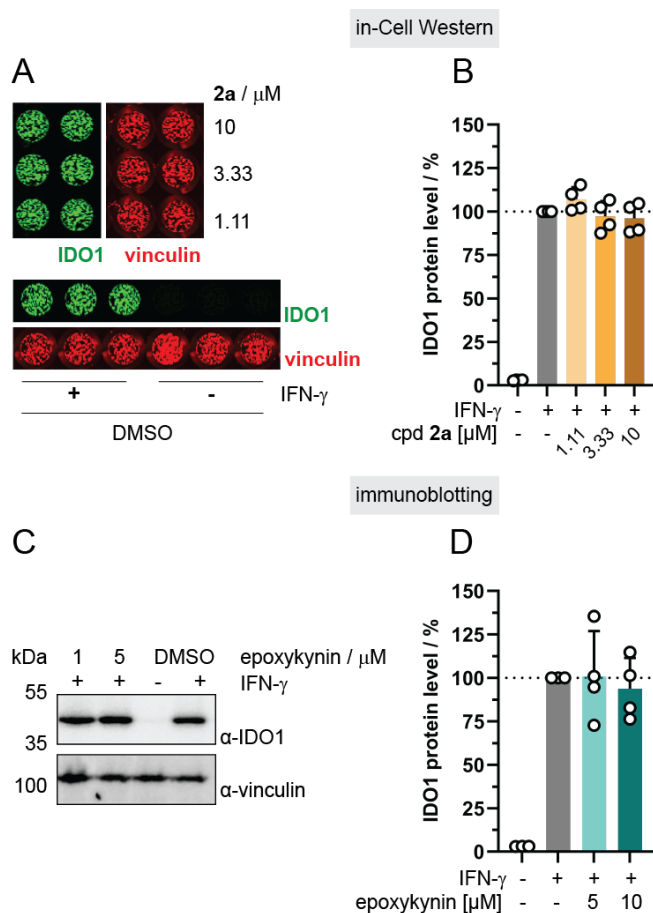


**Figure 29:** Influence of epoxykynin on IDO1 protein expression. A) In-cell Western of IDO1 protein levels in BxPC-3 cells upon treatment with IFN- $\gamma$  and the hit compound **2a** or DMSO for 24 h. Representative images are shown (mean  $\pm$  SD, n=4). IDO1 fluorescence intensities were normalized to the reference protein vinculin (B). C) IDO1 protein levels in HeLa cells that were treated with IFN- $\gamma$  and epoxykynin or DMSO for 24 h. Representative immunoblot is shown (mean  $\pm$  SD, n $\geq$ 2). IDO1 band intensities were normalized to the reference protein vinculin (D). cpd: compound.

Moreover, compound **2a** and epoxykynin's influence on the IDO1 protein level was investigated. Upon treatment with epoxykynin, the IDO1 protein level was not altered at concentrations up to 10  $\mu$ M as detected by means of in-cell western (Figure 29C) and immunoblotting (Figure 29B). Taken together, epoxykynin did impair Kyn production by diminishing IDO1 protein levels.

### 5.2.3 Influence on Trp Uptake

Subsequently, the IFN- $\gamma$ -independent Trp import *via* LATs and the IFN- $\gamma$ -dependent Trp uptake *via* TrpRS were analyzed to elucidate if epoxykynin lowers the availability of the IDO1 substrate Trp. 1-MT and Leu were used to inhibit the Trp-selective and IFN- $\gamma$ -dependent import by TrpRS and the IFN- $\gamma$ -independent uptake of large, neutral amino acids by LATs, respectively. In the presence of IFN- $\gamma$  only,  $57.3 \pm 9.5\%$  of supplemented Trp was taken up by the cells (Figure 30). Treatment with the control inhibitors 1-MT and Leu significantly reduced Trp import. However, upon treatment with epoxykynin the Trp uptake was not impaired (Figure 30). In the presence of IFN- $\gamma$ ,  $55.1 \pm 10.8\%$  of the supplemented Trp was

## Results

taken up by the cells after compound treatment. In the absence of IFN- $\gamma$ , the cells imported  $14.3 \pm 4.3\%$  of Trp upon compound treatment. This demonstrated, that epoxykynin did not reduce Kyn levels by lowering the availability of the IDO1 substrate in cells.

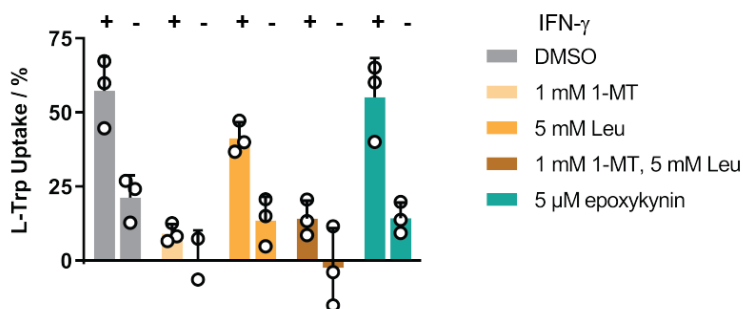


**Figure 30:** Epoxykynin does not inhibit the uptake of Trp. BxPC-3 cells were starved for Trp for 72 h and treated with IFN- $\gamma$  for 24 h prior to addition of control inhibitors (5 mM L-Leu, 1 mM 1-MT) or 1  $\mu$ M epoxykynin for 30 min. Afterwards, 50  $\mu$ M Trp was added and Trp uptake was quantified by HPLC-MS/MS (mean  $\pm$  SD,  $n \geq 3$ ). L-Leu: L-leucine. 1-MT: 1-methyl-L-tryptophan.

### 5.2.4 Identification of the Molecular Target of Epoxykynin

For target identification, different high-resolution mass spectrometry (HRMS)-based proteome analyses were employed, such as global proteome profiling, thermal proteome profiling (TPP) and affinity-based chemical proteomics. These less biased strategies enable target identification on a proteome-wide level.

#### 5.2.4.1 Target Identification *via* Global Proteome Profiling

Global proteome profiling quantifies the levels of proteins within the cells using tandem mass tags (TMT) as chemical labels<sup>183</sup> and allows for detection of up- or downregulated proteins after compound treatment. This strategy was employed to monitor protein levels upon treatment with epoxykynin on a proteome-wide scale. The results of the global proteome profiling might give hints abouts regulated pathways and thus, enable the prediction of potential targets.

In this experiment, BxPC-3 cells were treated for 24 h with DMSO or 3  $\mu$ M epoxykynin in the absence or presence of IFN- $\gamma$  which led to the identification of in total 4,992. These proteins included proteins that are directly connected to the Kyn pathway, such as JAK1, STAT1 and STAT2, IDO1, kynureninase (KYNU), SHP1 and SHP2 (PTPN6 and PTPN11), AhR and TrpRS (WARS). Subsequently, proteins that were regulated by the stimulus IFN- $\gamma$  (Figure 31A) and epoxykynin (Figure 31B) were evaluated.

The levels of 84 proteins were significantly altered in cells treated with DMSO and IFN- $\gamma$  compared to cells only treated with DMSO (Figure 31A), from which 50 proteins were up- (Table S2) and 34 proteins were downregulated (Table S3). These proteins included known IFN- $\gamma$ -regulated proteins, e.g. interferon-induced protein with tetratricopeptide repeats 2, 3 and 5 (IFIT2, IFIT3, IFIT5) and interferon-related developmental regulator 1 (IFRD1). Among the

## Results

upregulated proteins were some proteins connected to the Kyn pathway, such as STAT1, IDO1 and TrpRS (WARS). Additionally, the levels of four different isoforms of guanylate-binding proteins (GBPs) were found to be increased, namely GBP1, GBP2, GBP4 and GBP5.

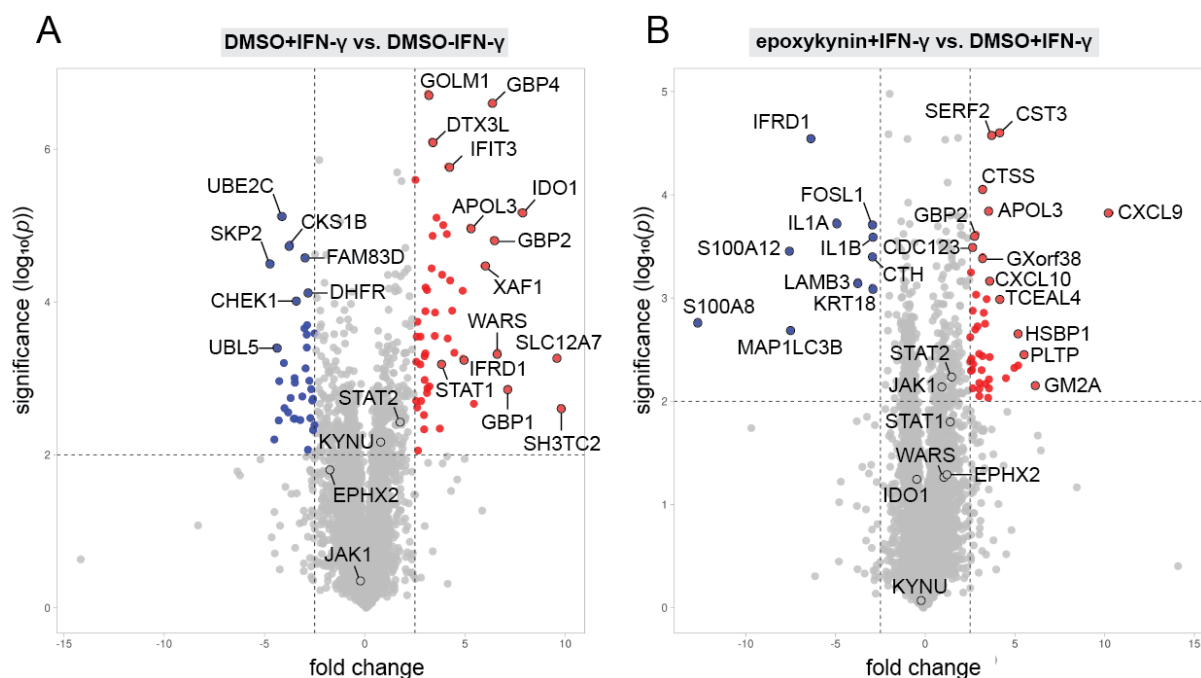


**Figure 31:** Global proteome profiling. A) BxPC-3 cells were treated with DMSO in the absence or presence of IFN- $\gamma$  for 24 h prior to cell lysis and subsequent HRMS quantification ( $n=3$ , FDR 0.01). B) BxPC-3 cells were treated with 3  $\mu$ M epoxykynin and IFN- $\gamma$  or DMSO and IFN- $\gamma$  for 24 h prior to cell lysis and subsequent HRMS quantification ( $n=3$ , FDR 0.01). The volcano plots for up- (red) and downregulated proteins (blue) were created with VolcaNoseR<sup>184, 185</sup>. See Table S2-S5 for a list of all regulated proteins.

Treatment with epoxykynin (Figure 31B) increased the levels of 42 proteins (Table S4) and decreased the levels of 10 proteins (Table S5) compared to the DMSO control. None of the regulated proteins include a protein directly associated with the Kyn pathway. However, some proteins that were upregulated upon stimulation with IFN- $\gamma$  were even more increased by epoxykynin (Figure 32). Interestingly, none of the proteins that were reduced by IFN- $\gamma$  showed even lower levels upon treatment with epoxykynin. On the other hand, multiple proteins that were downregulated by IFN- $\gamma$  were increased upon treatment with epoxykynin. Additionally, five proteins were upregulated by IFN- $\gamma$ , but inversely regulated by epoxykynin.

## Results

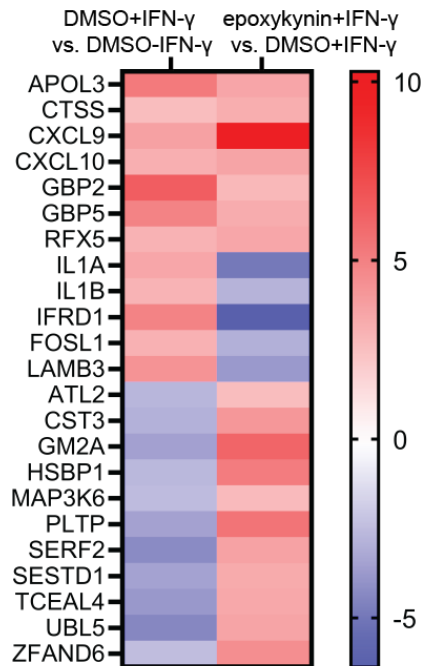


**Figure 32:** Heat map of fold changes of proteins that were regulated upon treatment with IFN- $\gamma$  and epoxykynin in the global proteome profiling.

Computational overrepresentation analyses provide information on an input omics data set by comparison to annotated data sets. Gene ontology (GO)<sup>186-189</sup> represents a common approach of overrepresentation analysis. GO uses a collection of associations between genes and biological terms to predict biological processes. A second strategy is pathway enrichment analysis<sup>188-191</sup> which uses associations between genes and pathways from pathway databases, such as Reactome<sup>190, 191</sup>. Both analyses revealed that the modulated proteins belong to acute inflammatory and immunological stimulus response pathways (Figure 33). Especially the upregulated biological processes and pathways are associated with IFN signaling. Since many of the proteins regulated by epoxykynin were also regulated by IFN- $\gamma$  (Figure 32), the overrepresentation analysis listed almost identical pathways for both DMSO+IFN- $\gamma$  vs. DMSO-IFN- $\gamma$  (Figure 33A and C) and epoxykynin+IFN- $\gamma$  vs. DMSO+ IFN- $\gamma$  (Figure 33B and D).

Taken together, the global proteome profiling discovered proteins that were regulated upon treatment with IFN- $\gamma$  and epoxykynin. However, it is challenging to build a target hypothesis from these results, because the enormous cellular response to the IFN stimulus hindered the identification of pathways altered by epoxykynin.

## Results

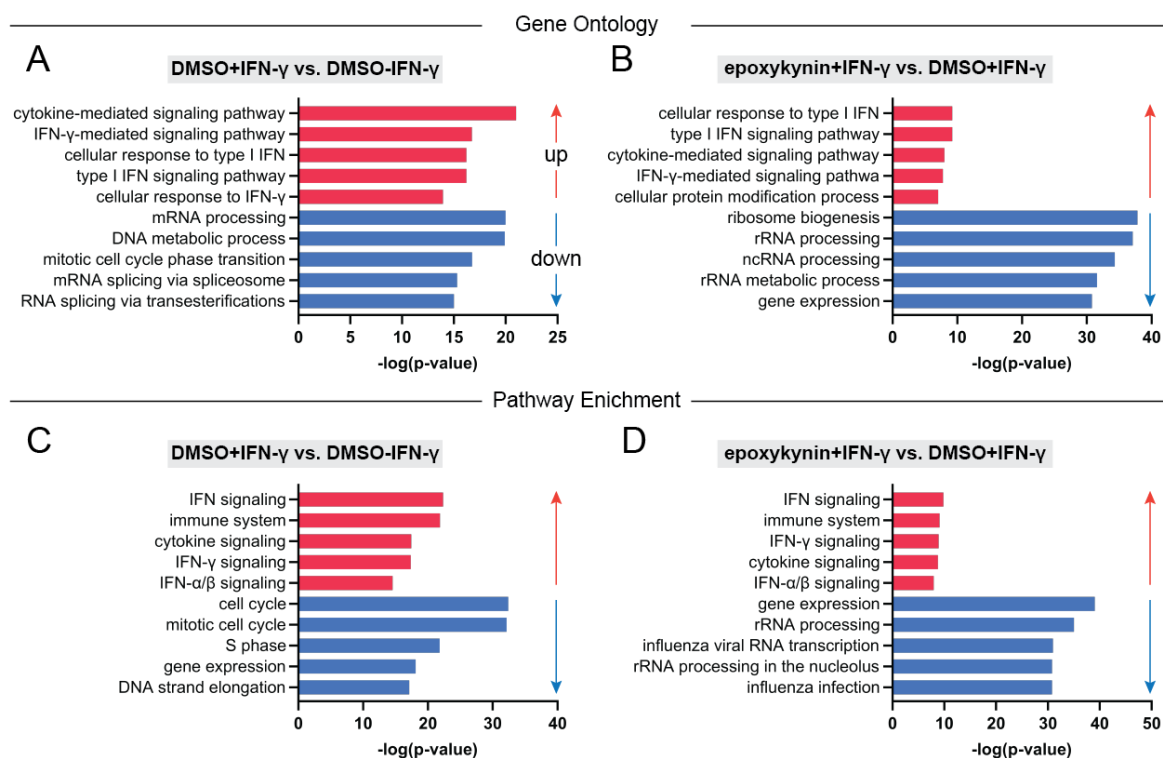


**Figure 33:** Gene ontology and pathway enrichment analyses. Gene ontology (A-B) and pathway enrichment (C-D) analyses results were obtained from Enrichr<sup>188, 192, 193</sup> using the proteome profiling data set. A comparison of DMSO+IFN- $\gamma$  vs. DMSO-IFN- $\gamma$  is shown in A and C, epoxykynin+IFN- $\gamma$  vs. DMSO+IFN- $\gamma$  is shown in B and D. The most significant processes by means of the  $p$ -value are depicted. Red bars indicate upregulation, blue bars indicate downregulation.

### 5.2.4.2 Target Identification *via* Thermal Proteome Profiling

In addition to the global proteome profiling, thermal proteome profiling (TPP) was employed. While proteome profiling can give hints about the pathway regulation of the target protein, TPP provides information about direct target engagement. TPP, as a proteome-wide version of CETSA<sup>137</sup>, profiles small molecule-induced alterations in the thermal stability of proteins<sup>136</sup>. Performing the TSA in IFN- $\gamma$ -stimulated HeLa cell lysate led to HRMS-based identification of in total 6,474 proteins, of which 38 proteins displayed a significant shift in the thermal melting temperature  $T_m$  upon treatment with 3  $\mu$ M epoxykynin (Table 3).

**Table 3:** Gene names of proteins with shifted melting temperature  $T_m$  upon compound treatment in the thermal proteome profiling (TPP). HeLa cells were treated with IFN- $\gamma$  for 24 h prior to cell lysis. The lysate was treated with 3  $\mu$ M epoxykynin or DMSO for 10 min at room temperature, followed by the thermal shift assay and subsequent HRMS analysis ( $n=3$ ,  $N=1$ ).

Gene name	$\Delta T_{m,1}$	$\Delta T_{m,2}$	$\Delta T_{m,3}$	$\Delta T_{m,mean}$	Gene name	$\Delta T_{m,1}$	$\Delta T_{m,2}$	$\Delta T_{m,3}$	$\Delta T_{m,mean}$
SURF1	-2.3	-1.2	-1.4	-1.6	UFD1L	1.9	3.0	2.4	2.4
SCARB2	1.7	2.6	-1.3	1.0	APPL2	1.7	3.4	2.3	2.5
PPP2R5C	1.1	1.4	1.2	1.2	DCTN5	2.6	2.7	2.9	2.7
ASCC2	1.9	1.9	0.9	1.6	OXR1	1.2	3.4	3.9	2.8
PLCH1	1.9	1.8	1.3	1.7	PTEN	4.4	2.3	1.9	2.9
MBNL1	1.9	1.5	1.9	1.8	CADM1	3.1	3.9	1.9	3.0
<b>HMOX1</b>	<b>2.4</b>	<b>1.3</b>	<b>1.7</b>	<b>1.8</b>	PTER	2.5	4.9	1.5	3.0
PRPSAP2	1.8	2.3	1.5	1.9	GARS	2.4	2.7	4.0	3.0



## Results

Gene name	$\Delta T_{m,1}$	$\Delta T_{m,2}$	$\Delta T_{m,3}$	$\Delta T_{m,\text{mean}}$	Gene name	$\Delta T_{m,1}$	$\Delta T_{m,2}$	$\Delta T_{m,3}$	$\Delta T_{m,\text{mean}}$
TPP1	1.5	1.4	2.9	1.9	CBWD2	1.5	2.0	5.6	3.0
ASPSCR1	1.6	1.7	2.6	2.0	DPH2	2.6	3.8	2.9	3.1
NDE1	1.8	2.9	1.3	2.0	MYDGF	2.9	3.9	2.8	3.2
PRDX3	2.2	2.2	1.6	2.0	RXRB	5.2	1.6	3.0	3.3
ARPC4	1.7	2.2	2.1	2.0	KCTD12	2.6	3.7	3.6	3.3
GSS	1.9	1.6	2.7	2.1	ROMO1	3.5	2.6	4.3	3.5
PANX1	2.1	2.4	1.9	2.1	MAU2	5.4	2.9	2.6	3.6
ENO2	2.4	1.7	2.4	2.1	EXOSC5	4.5	5.9	2.0	4.1
ERMP1	3.2	2.7	1.2	2.4	PLEKHO2	4.8	3.5	4.5	4.3
AKT2	1.9	2.6	2.8	2.4	KCTD2	6.4	4.6	2.7	4.6
MZT1	3.0	2.4	1.9	2.4	FABP3	8.5	5.1	6.1	6.6

With one exception, all identified proteins were stabilized by epoxykynin upon heat denaturation. The two proteins with the biggest epoxykynin-induced alterations in  $T_m$  were surfet locus protein 1 ((SURF1), Figure 34A) and fatty acid-binding protein 3 (FABP3, Figure 34B) with  $\Delta T_m$ s of  $-1.6 \pm 0.5^\circ\text{C}$  and  $6.6 \pm 1.4^\circ\text{C}$ , respectively. None of the identified proteins was either found to be regulated by epoxykynin in the global proteome profiling, nor is a member of the Kyn pathway. Nonetheless, the TPP gave rise to a first target hypothesis: Heme oxygenase 1 (HMOX1) catalyzes the oxidative cleavage of the porphyrin ring of heme *b* to produce biliverdin IX $\alpha$ , ferrous iron and carbon monoxide<sup>194</sup>. It was stabilized upon treatment with epoxykynin by  $1.8 \pm 0.5^\circ\text{C}$  (Figure 34C), thereby indicating direct target engagement.

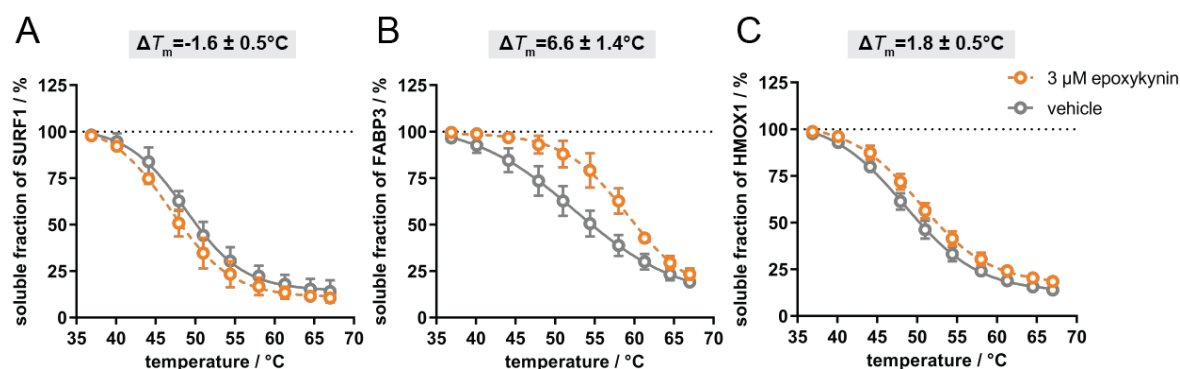


**Figure 34:** Thermal profiles of SURF1, FABP3 and HMOX1 upon treatment with 3  $\mu\text{M}$  epoxykynin or DMSO obtained in the TPP experiment (see Table 3,  $n=3$ ,  $N=1$ )

### 5.2.4.3 Target Identification *via* Affinity-based Chemical Proteomics (Pull-down)

Complementary to the TPP approach, affinity-based chemical proteomics was utilized for target identification. Therefore, an active and control affinity probe were generated based on the SAR of epoxykynin. Since the trifluoro acetyl group was required for biological activity and modifications on the indole nitrogen mainly drove changes in the compounds' potency, the amine-PEG4-alkyne linker was attached in 5-position of the indole ring. Hence, epoxykynin and the inactive derivative **2r** were used as scaffolds to yield the active and control affinity probes, respectively (Figure 35A).

## Results

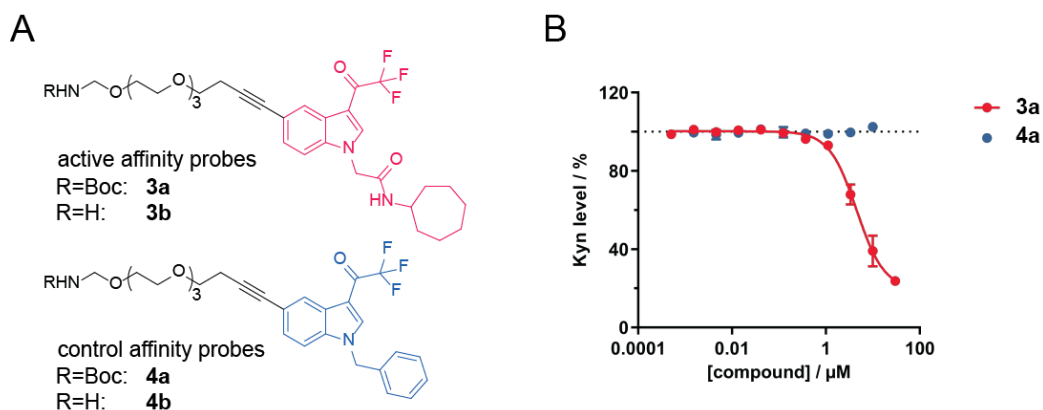


**Figure 35:** Probes for affinity-based chemical proteomics (pull-down). A) Structures of active affinity probes **3a** and **3b** and control affinity probes **4a** and **4b**. B) Influence of the pull-down probes **3a** and **4a** on Kyn levels. HeLa cells were treated with IFN- $\gamma$ , Trp and compounds for 48 h prior to measuring Kyn levels using *p*-DMAB (mean values  $\pm$  SD,  $n=3$ ).

The Boc-protected precursors **3a** and **4a** of probes **3b** and **4b** were initially tested for Kyn reduction (Figure 35B). The active probe **3a** decreased cellular Kyn levels by  $76.3 \pm 1.2\%$  at a concentration of  $20 \mu\text{M}$ , while control probe **4a** did not alter the Kyn levels. The free amine probes **3b** and **4b** were subsequently immobilized on NHS-activated magnetic beads and incubated with IFN- $\gamma$ -stimulated HeLa cell lysate. The enriched proteins were analyzed *via* HRMS (Figure 36).

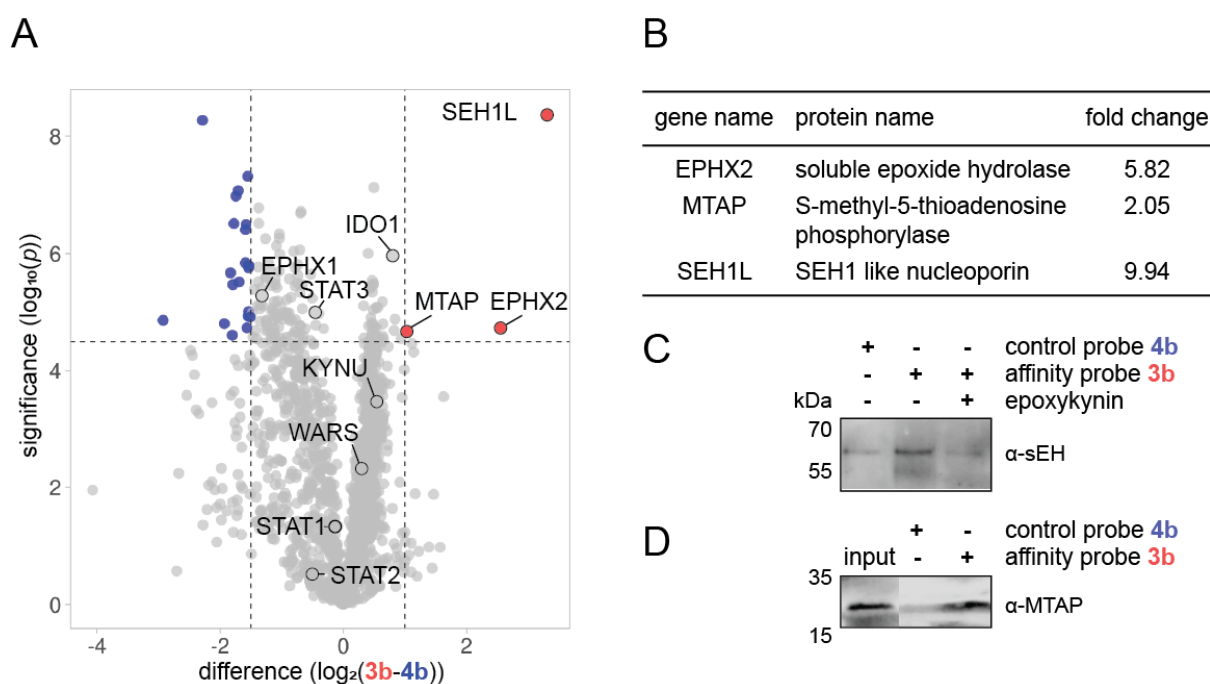


**Figure 36:** Affinity-based chemical proteomics (pull-down). The affinity probes **3b** and **4b** were immobilized on NHS-activated beads and incubated for 2 h at  $4^\circ\text{C}$  with lysate of HeLa cells that were treated with IFN- $\gamma$ . Enriched proteins were analyzed using HRMS ( $n=2$ ,  $N=4$ , FDR 0.01), representative replicate is shown. See Table S6 and Table S7 for lists of all enriched proteins. Volcano plot for proteins enriched by probe **3b** (red) or probe **4b** (blue) created with VolcanoSeR<sup>184, 185</sup>. B) Proteins from A) which were significantly enriched with the active pull-down probe **3b**. C-D) Selective enrichment of soluble epoxide hydrolase (C, EPHX2, sEH) and MTAP (D) using probe **3b** and competition with epoxykynin. For the competition experiment, HeLa cell lysate was pre-incubated with  $10 \mu\text{M}$  epoxykynin for 1 h at

## Results

4°C prior to incubation with the immobilized probes **3b** and **4b**. The enriched proteins were analyzed using immunoblot.

1579 proteins were identified in total. Among these proteins were members of the Kyn pathway, such as STAT proteins, kynureninase (KYNU) and TrpRS (WARS), but none of them were enriched on either of the affinity probes. Gratifyingly, only three proteins were selectively enriched by the active affinity probe **3b** (Figure 36A-B), namely SEH1-like nucleoporin (SEH1L), methylthioadenosine phosphorylase (MTAP) and the soluble epoxide hydrolase (sEH, EPHX2). The selective enrichment of sEH (Figure 36C) and MTAP (Figure 36D) using the active affinity probe **3b** was visualized by immunoblotting. Additionally, pre-incubation of the cell lysate with epoxykynin prevented binding to the affinity probe **3b** (Figure 36C).

SEH1L is a component of the Nup107-160 subcomplex as part of the nuclear pore complex (NPC). Proteins of the Nup107-160 subcomplex are essential for the assembly of NPCs<sup>195</sup> that are large multi-protein structures controlling the transport of macromolecules between the cytosol and the nucleus<sup>196</sup>. MTAP is important for the salvage of both methionine and adenosine triphosphate (ATP), by initiating the pathway through cleavage and phosphorylation of methylthioadenosine (MTA) to form 5-methylthioribose-1-phosphate (MTR-1-P) and adenine<sup>197</sup>. sEH is a bifunctional enzyme consisting of a C-terminal fatty acid epoxide hydrolase (sEH-H) and an N-terminal lipid phosphatase (sEH-P)<sup>198</sup>. While the role of sEH-P remains unknown, sEH-H is a member of the CYP epoxygenase branch of the arachidonic acid (AA) pathway and converts epoxy fatty acids into the respective dihydroxy fatty acids<sup>199</sup>.

SEH1L, MTAP and sEH emerged as potential targets of epoxykynin from the affinity-based chemical proteomics. Since nucleoporins are highly abundant proteins that are frequently identified in pulldown experiments<sup>200, 201</sup>, MTAP and sEH were considered more relevant and investigated further.

### 5.2.4.4 *In silico* Target Predictions for Epoxykynin

In addition to experimental targetID methods, the three web-based computational target prediction tools similarity ensemble approach (SEA)<sup>202, 203</sup>, Swiss Target Prediction<sup>204, 205</sup> and SuperPred Target Prediction<sup>206, 207</sup> were employed to search for potential targets of epoxykynin (Table 4). Except for one bacterial protein (Beta sliding clamp, dnaN), all predicted targets were mammalian proteins. Three target protein candidates emerged from all three tools, namely cannabinoid receptor 1 and 2 (CB1 and CB2 receptors, CNR1 and CNR2) and the microsomal epoxide hydrolase (mEH, EPHX1).

Additionally, the SEA tool listed plasminogen activator inhibitor 1 (SERPINE1), and membrane primary amine oxidase (AOC3) as potential targets. The Swiss Target prediction found Malonyl-CoA decarboxylase (MLYCD) and Cholesteryl ester transfer protein (CETP) as target

## Results

candidates. Lastly, SuperPred predicted NF- $\kappa$ B1 (NFKB1), 5-hydroxytryptamine receptor 2C (HTR2C) and DNA topoisomerase 2- $\alpha$  (TOP2A) to be targets of epoxykynin.

**Table 4:** Top 5 target predictions for epoxykynin according to web-based computational tools.

SEA Target Prediction <sup>202, 203</sup>	Swiss Target Prediction <sup>204, 205</sup>	SuperPred Target Prediction <sup>206, 207</sup>
dnaN	CNR1	CNR1
SERPINE1	CNR2	NFKB1
CNR2	MLYCD	HTR2C
AOC3	EPHX1	EPHX1
EPHX1	CETP	TOP2A

Some of the *in silico* predicted targets were also detected in the TPP, namely mEH, NF- $\kappa$ B1, MLYCD and TOP2A, but they did not show a compound-induced shift in the thermostability (Figure 37).

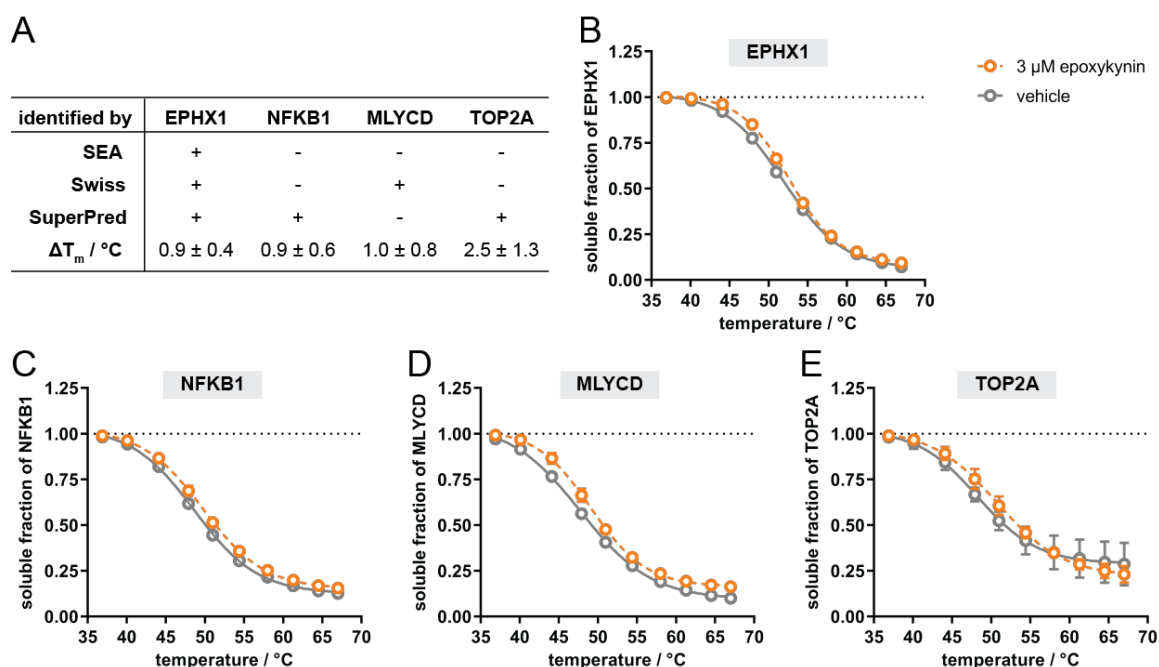


**Figure 37:** Thermal profiles for the predicted targets of epoxykynin as determined by TTP.  $\Delta T_m$  values (A) and thermal profiles for mEH (B, EPHX1), NF- $\kappa$ B1 (C, NFKB1), MLYCD (D) and TOP2A (E).

Based on chemical similarity, these tools relate a small molecule to potential protein targets according to known references<sup>203, 205, 207</sup>. Ligands for CB1 and CB2 receptors and mEH with high similarity to epoxykynin according to the target predictions are depicted in Figure 38.

## Results

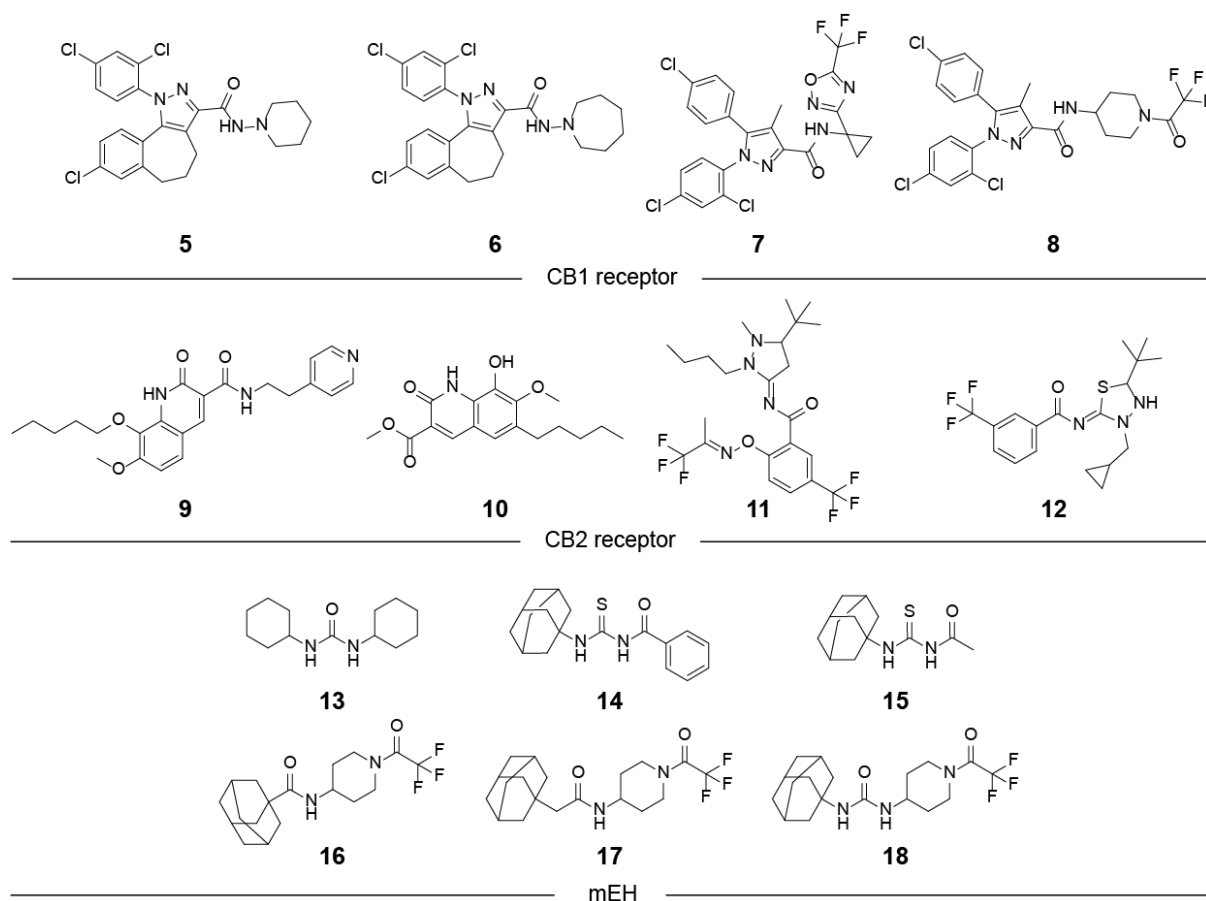


**Figure 38:** Ligands binding to CB1 and CB2 receptors and mEH that are chemically similar to epoxykynin according to SEA and Swiss Target Prediction<sup>204, 206</sup>.

The reference ligands **5** to **8** for the CB1 receptor all contain a pyrazole, chloro substituents on the aromatic groups and an amide or acyl hydrazide. Compounds **5**, **6** and **8** bear a piperidine or an azepane and compounds **7** and **8** possess an electron-withdrawing trifluoro methyl group. The CB2 receptor ligands **9** and **10** have a 2-quinolone scaffold with an amide, ester and ether functionalization. The other two CB2 ligands **11** and **12** contain pyrazolidine or thiadiazolodine heterocycles, trifluoro methyl and *t*-butyl groups. The mEH reference compounds **13** to **18** are ureas, thioureas or amides. They bear hydrophobic moieties, such as adamantyl and cycloheptyl groups, and two of them have trifluoroacetyl piperidines.

CB1 and CB2 receptors are GPCRs of the endocannabinoid system<sup>208</sup> that bind hydrophobic ligands with different ligand selectivity<sup>209, 210</sup>. The reverse agonists rimonabant and otenabant for CB1 and BML-190 and SR144528 for CB2 were tested in the Kyn assay (blue curves, Figure 39) to evaluate whether CB1 and CB2 receptor ligands affect Kyn levels. Additionally, it was investigated if epoxykynin and any of these compounds have synergistic or additive effects on Kyn level reduction (orange curves, Figure 39).

## Results

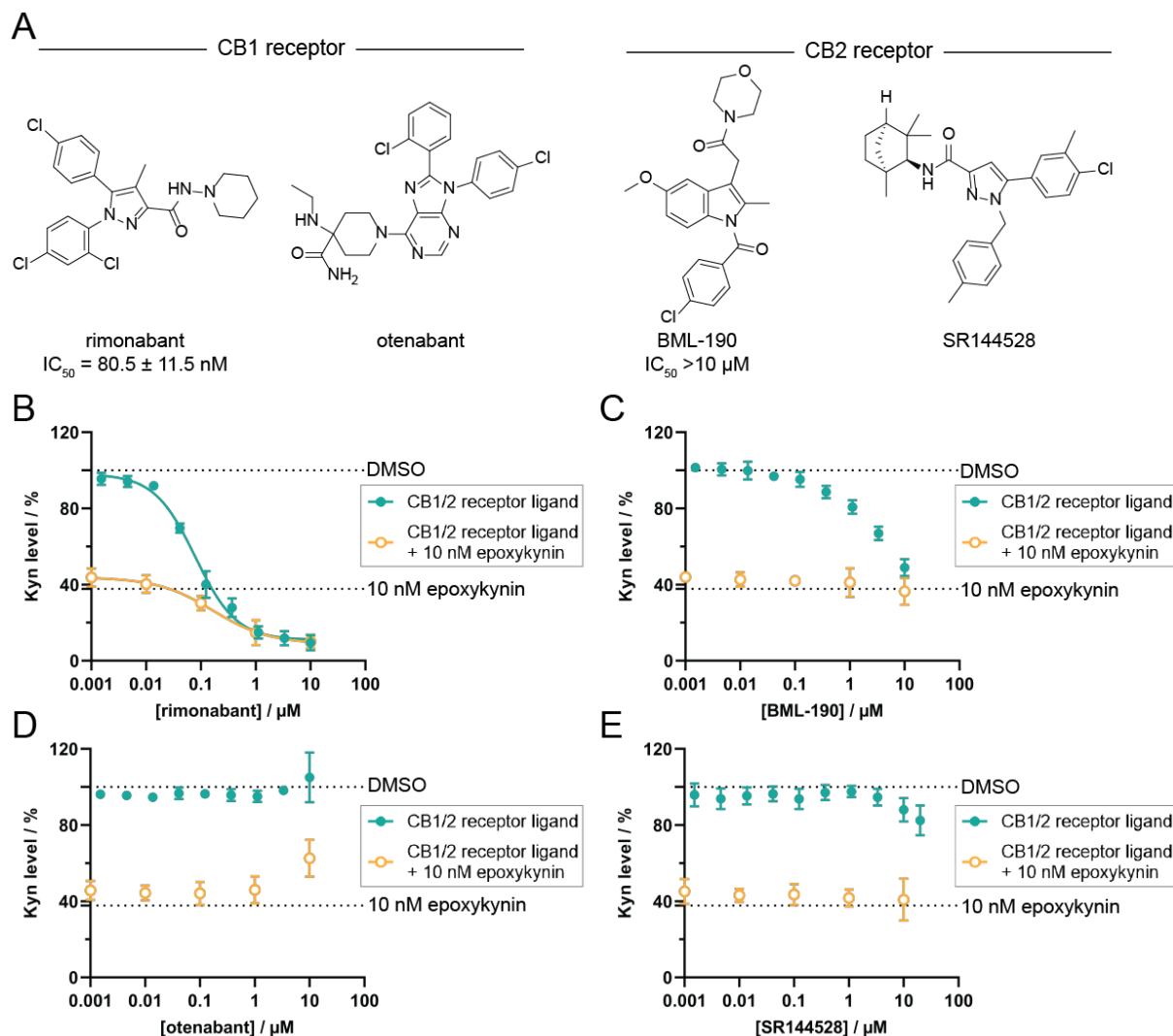


**Figure 39:** Influence of CB1 and CB2 receptor ligands on cellular Kyn levels. A) Structures and  $IC_{50}$  values for Kyn reduction of CB1 and CB2 receptor ligands. B-E) Determination of Kyn levels in HeLa cells upon treatment with IFN- $\gamma$ , Trp, epoxykynin and the CB1 receptor ligands rimonabant (B) and otenabant (D) or CB2 receptor ligands BML-190 (C) and SR144528 (E) quantified using *p*-DMAB (mean  $\pm$  SD,  $n=3$ ). The dotted lines indicate Kyn levels of the DMSO+IFN- $\gamma$  and epoxykynin+IFN- $\gamma$  controls.

Only two out of four compounds reduced cellular Kyn levels: rimonabant potently abolished cellular Kyn production with an  $IC_{50}$  value of  $80.5 \pm 11.5$  nM (Figure 39B), whereas BML-190 displayed weak inhibition with an  $IC_{50}$  greater than  $10$   $\mu$ M (Figure 39C). Treatment with  $10$  nM epoxykynin decreased cellular Kyn levels by approximately 60%. Co-treatment of  $10$  nM epoxykynin with the CB receptor ligands did not reduce Kyn levels below this threshold (Figure 39B-E). These results indicate that the co-treatment has no synergistic or additive effect on Kyn reduction. As only one ligand of each CB1 and CB2 receptors decreased Kyn levels, it is highly likely that the Kyn reduction is independent of CB receptor signaling. Despite that, Kyn levels might be abolished by direct inhibition of IDO1. Thus, the catalytic activity of purified human IDO1 was quantified upon treatment with rimonabant and BML-190 (Figure 40). Rimonabant reduced the IDO1 activity by  $42.7 \pm 10.7\%$  at  $50$   $\mu$ M (Figure 40A), whereas

## Results

BML-190 did not significantly alter Kyn levels (Figure 40B). Since rimonabant was a potent inhibitor of Kyn production in cells but only moderately reduced Kyn levels *in vitro*, rimonabant might be an apo-IDO1 inhibitor. BML-190 is structurally similar to epoxykynin. Thus, the reduction of cellular Kyn levels might be due to the same MMOA.

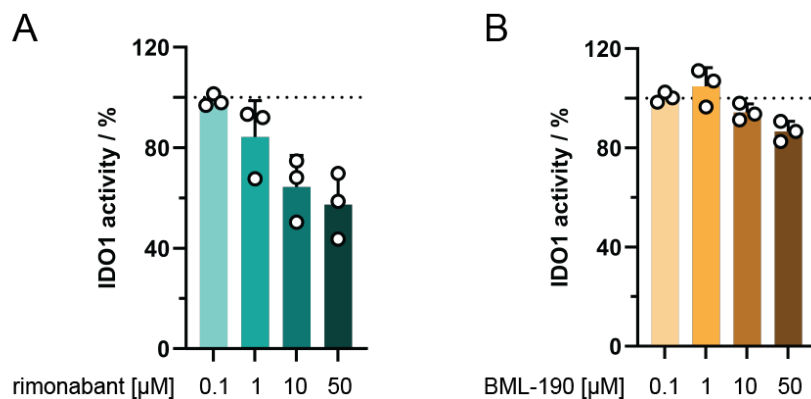


**Figure 40:** Influence on *in vitro* IDO1 activity. Purified human holo-IDO1 protein was treated with rimonabant (A) or BML-190 (B) for 40 min at 37 °C prior to addition of the IDO1 substrate Trp for 60 min at 37°C. Kyn levels were detected using *p*-DMAB (mean  $\pm$  SD,  $n=3$ ).

Similar to sEH, mEH contributes to the detoxification of xenobiotic epoxides. Because they differ in cellular localization, with mEH being an ER-resident protein, it was long thought that both enzymes have distinct functions. However, it has now become apparent that mEH also hydrolyzes CYP epoxygenase-generated epoxyeicosatrienoic acids (EETs) to dihydroxy-eicosatrienoic acids (DHETs)<sup>211</sup>. Because of the conserved catalytic triad and the overlapping substrate specificity of mEH and sEH<sup>211</sup>, it comes as no surprise that the compounds on which the target prediction is based on, are also known to bind to sEH<sup>212</sup>, such as the dicyclohexylurea **13** (Figure 38).

The *in silico* target predictions strengthen the hypothesis that sEH might be the target of epoxykynin. While the CB1 and CB2 receptors were also predicted to be target protein candidates, the experimental data suggest otherwise.

## Results

### 5.2.5 Target Validation Studies

Different target hypotheses arose from the application of various proteomics-based methods (5.2.4). In the following, the potential targets and their roles in Kyn reduction were investigated.

#### 5.2.5.1 HMOX1 as Potential Target of Epoxykynin

HMOX1 displayed an epoxykynin-induced shift in the thermal melting temperature  $T_m$  in the TPP experiment (5.2.4.2). HMOX1 catalyzes the oxidative cleavage of the porphyrin ring of heme *b* to produce biliverdin IX $\alpha$ , ferrous iron and carbon monoxide<sup>194</sup>. Hence, epoxykynin might modulate the activity of HMOX1 and thereby enhance the degradation of the IDO1 cofactor heme. Since IDO1 requires heme for catalysis, a deficiency of heme results in reduced Kyn levels. Thus, the cellular target engagement on immunoblot level *via* CETSA (Figure 42 and Figure 43), the enzymatic activity of HMOX1 upon treatment with epoxykynin (Figure 45, Figure 46 and Figure 47) and the role of HMOX1 for Kyn production were analyzed (Figure 48).

The last 23 C-terminal amino acids of HMOX1 form a transmembrane segment (TMS) that anchors HMOX1 in the endoplasmic reticulum (ER) and facilitates oligomerization<sup>213</sup>. Truncated forms of HMOX1 lacking the TMS can be found in the cytoplasm or nucleus<sup>213, 214</sup>. The expression of HMOX1 can be induced upon treatment with its substrate hemin<sup>215</sup> (Figure 41).

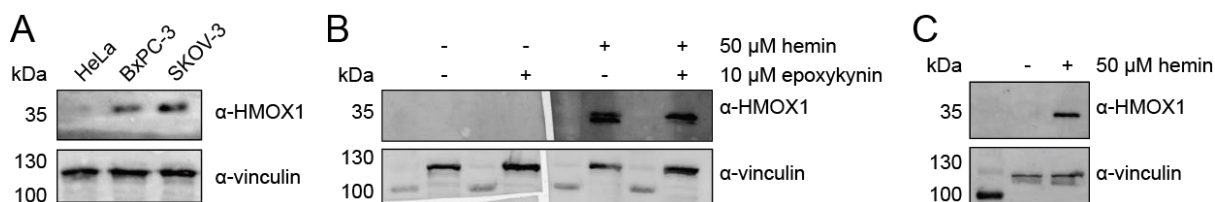


**Figure 41:** HMOX1 expression in different cell lines. A) HeLa, BxPC-3 and SKOV-3 cells were treated with 50  $\mu$ M hemin for 18 h prior to analysis of protein levels *via* immunoblotting. Representative immunoblots for the HMOX1 monomer are shown (n=2). B) SKOV-3 cells were treated with 50  $\mu$ M hemin and 10  $\mu$ M epoxykynin for 24 h prior to analysis of the HMOX1 monomer *via* immunoblotting. C) HAP1 cells were treated with 50  $\mu$ M hemin for 18 h prior to analysis of the HMOX1 monomer *via* immunoblotting. Representative immunoblots are shown (n=3).

Using immunoblotting, HMOX1 monomers and trimers could be detected (Figure 42A-B). Subsequently, the thermal stability of HMOX1 upon epoxykynin treatment was analyzed by means of in-lysate CETSA (Figure 42C-E) and in-cell CETSA (Figure 42F-H). For the lysate-based CETSA, only the monomer fraction of HMOX1 showed a thermal destabilization upon compound treatment of  $\Delta T_m$  of  $-3.2 \pm 1.4^\circ\text{C}$  (Figure 42E), but the  $T_m$ s of the HMOX1 total protein, i.e. monomer and trimer fractions, and the trimer did not shift (Figure 42C-D). Furthermore, epoxykynin did not alter the thermal stability of HMOX1 in the cell-based CETSA (Figure 42F-H).



## Results

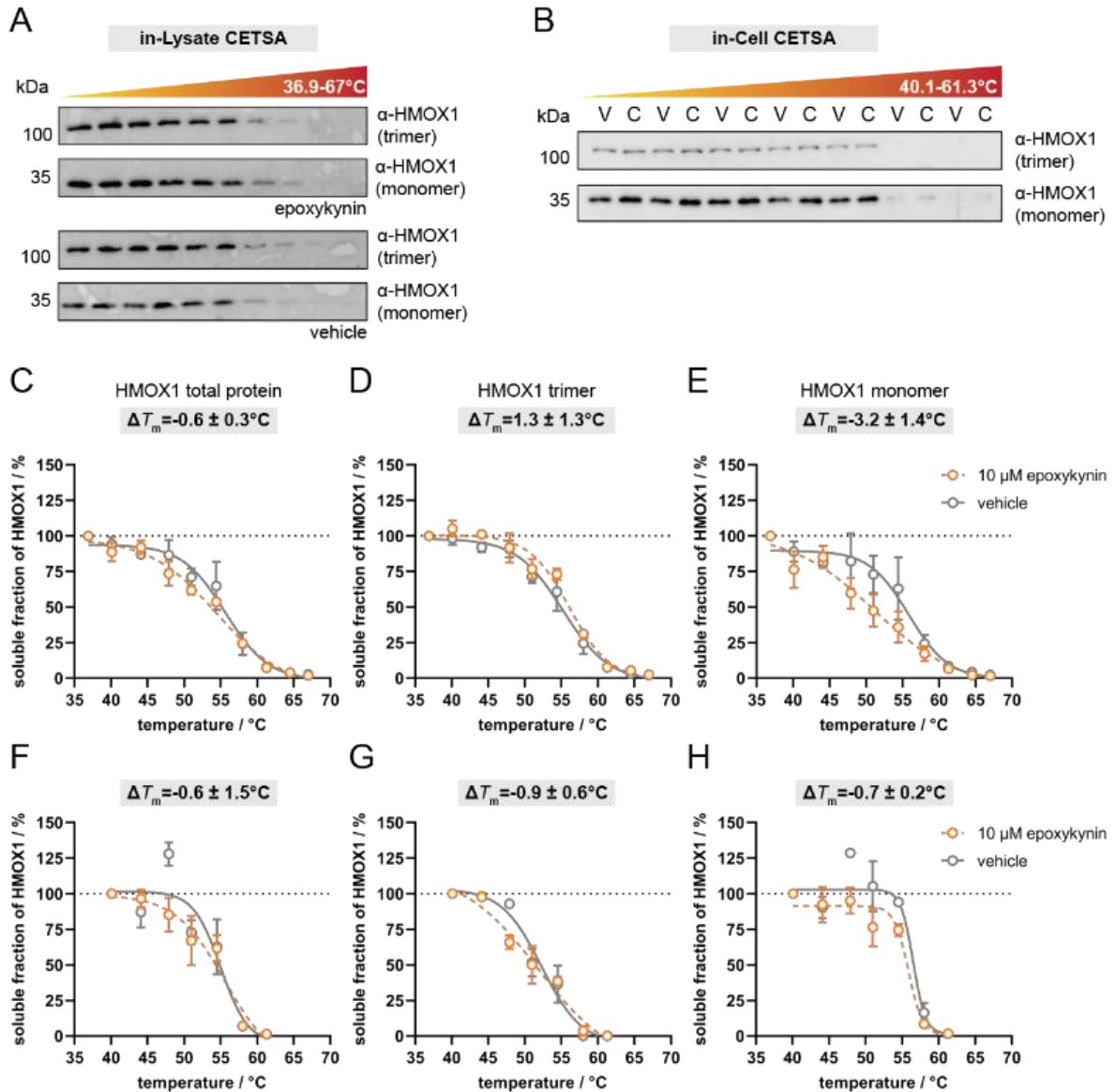


**Figure 42:** CETSA for HMOX1 in SKOV-3 cells. A) In-lysate CETSA for HMOX1. Cells were treated with 50 μM hemin for 18 h prior to cell lysis. The lysate was treated with 10 μM epoxykyinin or DMSO (vehicle) for 10 min at room temperature prior to performing the thermal shift assay with subsequent immunoblotting (mean values  $\pm$  SD,  $n \geq 3$ ). B) In-cell CETSA for HMOX1. Cells were treated with 50 μM hemin for 18 h prior to treatment with 10 μM epoxykyinin (C) or DMSO (V) for 10 min. The thermal shift assay was performed prior to cell lysis and subsequent immunoblotting (mean values  $\pm$  SD,  $n = 2$ ). C-E) Thermal profiles for in-lysate CETSAs for HMOX1 as depicted in A). Profiles of the total HMOX1 protein (C), the HMOX1 trimer (D) and HMOX1 monomer (E) are shown (mean values  $\pm$  SD,  $n \geq 3$ ). F-H) Thermal profiles for in-cell CETSAs for HMOX1 as depicted in B). Profiles of the total HMOX1 protein (F), the HMOX1 trimer (G) and HMOX1 monomer (H) are shown (mean values  $\pm$  SD,  $n = 2$ ).

Additionally, in-cell CETSA with HEK293T cells that transiently express HMOX1-eGFP was performed in the absence of hemin (Figure 43). Again, no target engagement could be detected for the fusion protein with a melting temperature shift  $\Delta T_m$  of  $0.2 \pm 0.1^\circ\text{C}$ .

## Results

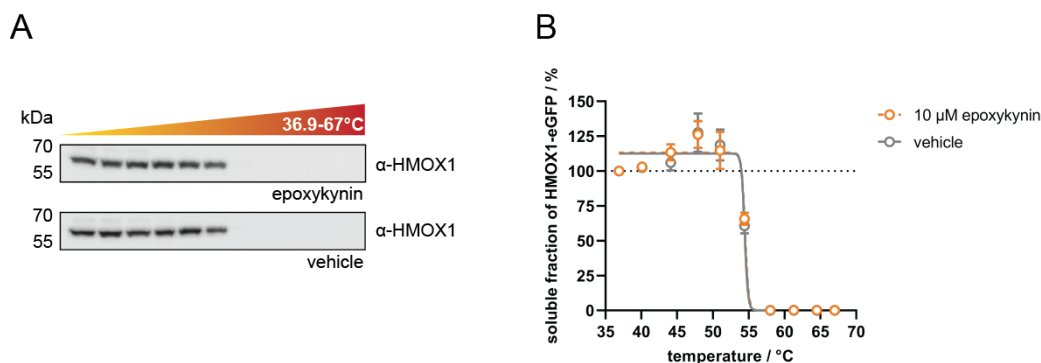


**Figure 43:** In-cell CETSA for HMOX1-eGFP in HEK293T cells. A) Cells were transfected with pCX-HO1-2A-EFGP for 48 h prior to treatment with 10  $\mu$ M epoxykynin or DMSO for 20 min. The thermal shift assay was performed prior to cell lysis and subsequent immunoblotting for HMOX1. Representative immunoblot is shown in A, thermal profiles are shown in B (mean values  $\pm$  SD,  $n=3$ ).  $\Delta T_m=0.2 \pm 0.1^\circ\text{C}$ .

The enzymatic reaction catalyzed by HMOX1 generates carbon monoxide (Figure 44A). Therefore, the influence of epoxykynin on the enzymatic activity of HMOX1 can be investigated directly by monitoring cellular carbon monoxide levels. A CO-sensitive fluorescein ether-based probe<sup>216</sup> was employed to detect CO in living cells (Figure 44B).

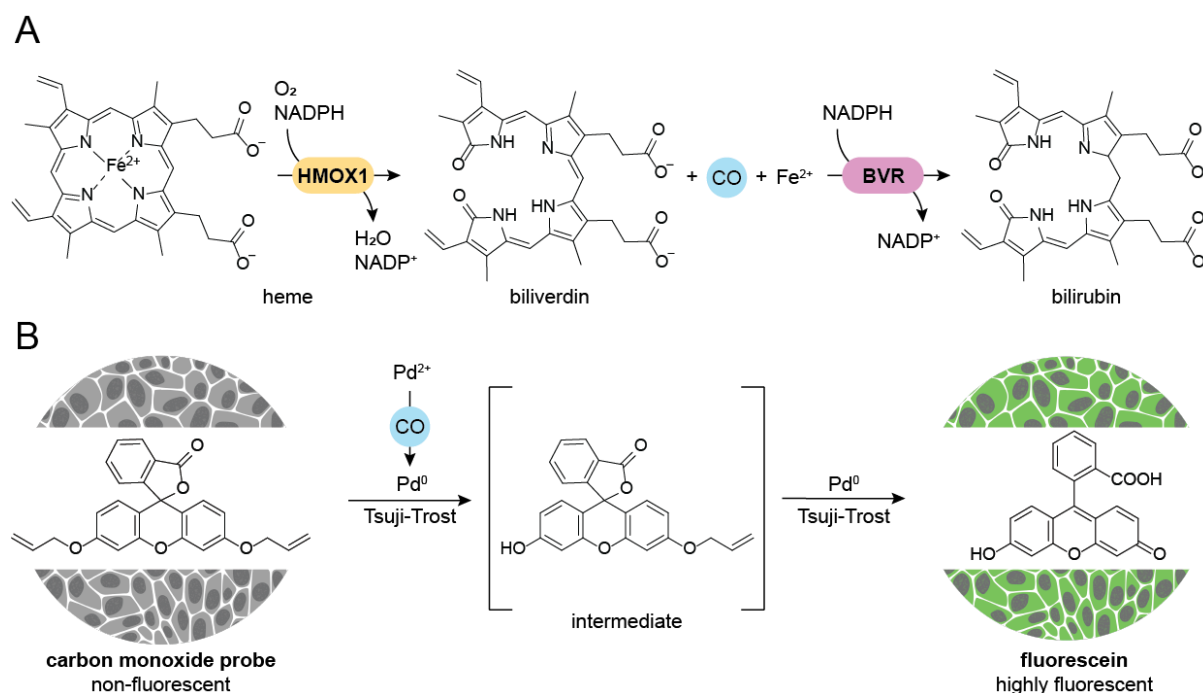


**Figure 44:** Carbon monoxide detection in cells. A) HMOX1 catalyzes the ring opening of heme to yield biliverdin, which is subsequently reduced to bilirubin by BVR. B) Sensing mechanism for CO in cells using a fluorescein ether-based probe<sup>216</sup>.

Hence, HeLa cells were treated with hemin, epoxykynin or a combination of both hemin and epoxykynin in the absence or presence of IFN- $\gamma$  (Figure 45A). As expected, stimulation with IFN- $\gamma$  did not alter CO levels (Figure 45A). Compared to the DMSO controls, treatment with 10  $\mu$ M epoxykynin slightly increased CO levels to  $163.3 \pm 37.5\%$  in the absence of IFN- $\gamma$  (Figure 45B), whereas it did not significantly modulate CO production in the presence of IFN-

## Results

$\gamma$  (Figure 45C). Upon addition of 100  $\mu$ M hemin, the generated CO doubled with and without IFN- $\gamma$  (Figure 45B-C), which might be due to induced expression of HMOX1. Co-treatment with both hemin and epoxykynin resulted in the highest CO levels. Without IFN- $\gamma$ , 2.5  $\pm$  0.5-fold the amount of CO was generated compared to the DMSO control (Figure 45B) and with IFN- $\gamma$ , CO levels were elevated to 395.9  $\pm$  76.4% (Figure 45C). The increase in HMOX1 catabolite levels is not due to enhanced protein expression of HMOX1 as detected by immunoblotting (Figure 41B).

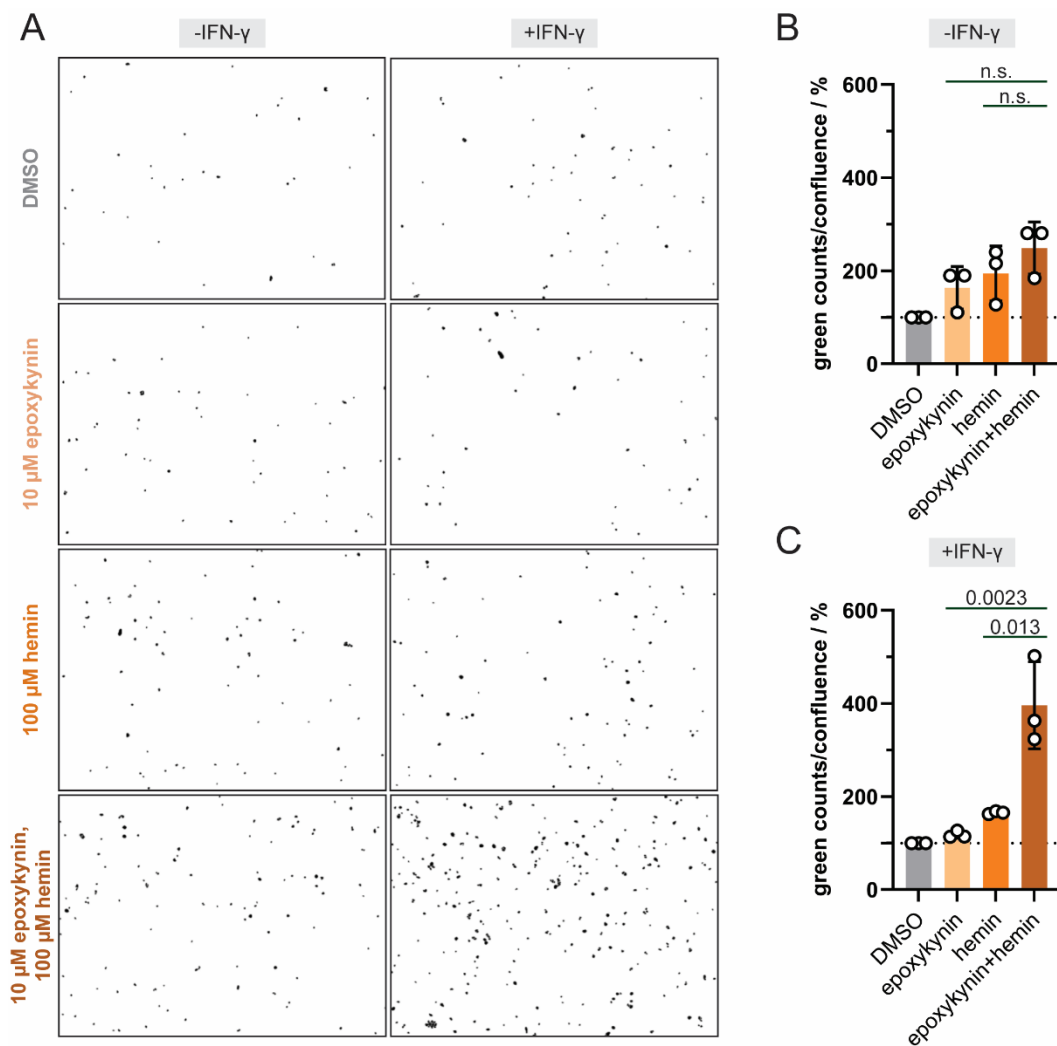


**Figure 45:** Carbon monoxide detection in HeLa cells. A) Cells were treated with IFN- $\gamma$ , 10  $\mu$ M epoxykynin and 100  $\mu$ M hemin for 24 h. 1  $\mu$ M BioTracker Carbon Monoxide Probe 1 Live Cell Dye<sup>216</sup> and 1  $\mu$ M Pd(II)Cl<sub>2</sub> were added for 30 min prior to imaging with the IncuCyte S3 Live-Cell Analysis System at 10x magnification. Images were inverted and depicted in grey scale for better visualization. B-C) Quantification of green counts from A) are shown in B) in the absence of IFN- $\gamma$  and in C) for cells stimulated with IFN- $\gamma$  (mean values  $\pm$  SD, n=3). *p* values derived by an unpaired Student's *t*-test are depicted above the bars. n.s.: non-significant.

In the following, two less active derivatives of epoxykynin, namely compounds **2m** and **2r** (IC<sub>50</sub> for Kyn reduction 1.73  $\pm$  0.1  $\mu$ M and >10  $\mu$ M, respectively), and the IDO1 inhibitors BMS-986205 and epacadostat were tested for carbon monoxide generation in combination with

## Results

100  $\mu\text{M}$  hemin in the presence of IFN- $\gamma$  (Figure 46). All of the aforementioned compounds did not increase CO levels compared to hemin-treated cells. These results indicate, that the increase of carbon monoxide upon treatment with epoxykynin and hemin is an epoxykynin-specific effect. The increase of CO is dependent on the potency of the epoxykynin derivative and is not a side effect of IDO1 inhibition.

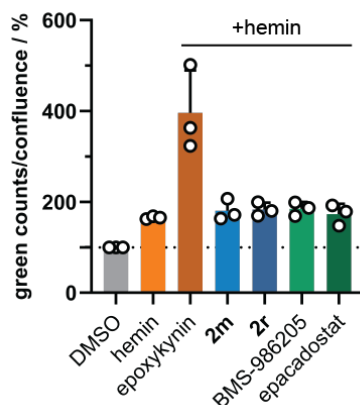


**Figure 46:** Comparison of carbon monoxide generation in HeLa cells upon treatment with different compounds. Cells were treated with IFN- $\gamma$ , 10  $\mu\text{M}$  compounds and 100  $\mu\text{M}$  hemin for 24 h. 1  $\mu\text{M}$  BioTracker Carbon Monoxide Probe 1 Live Cell Dye<sup>216</sup> and 1  $\mu\text{M}$  Pd(II)Cl<sub>2</sub> were added for 30 min prior to imaging with the IncuCyte S3 Live-Cell Analysis System under 10x magnification (mean values  $\pm$  SD, n=3).

The second product of the HMOX1 enzymatic reaction is the cleaved porphyrin ring biliverdin I $\alpha$  which is further converted to bilirubin by the biliverdin reductase (BVR). While bilirubin is poorly soluble in aqueous solutions, it can be extracted from the cell culture supernatant by organic solvents<sup>217</sup> and quantified as an indirect measure of the HMOX1 catalytic activity (Figure 47).

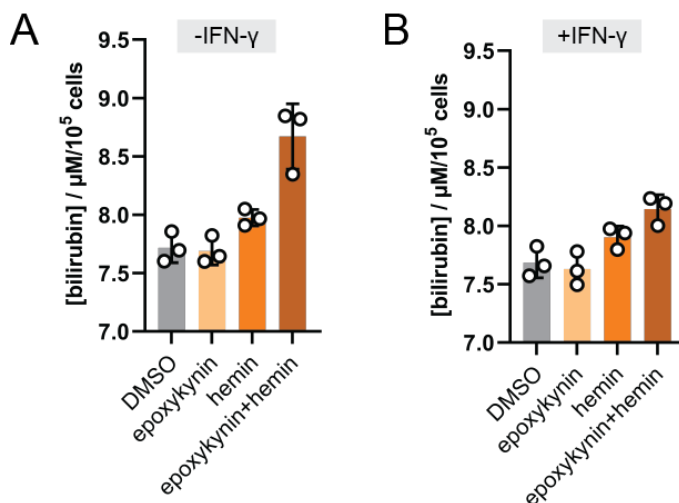


**Figure 47:** Bilirubin quantification in SKOV-3 cells. Cells were treated with 10  $\mu\text{M}$  epoxykynin and 100  $\mu\text{M}$  hemin in the absence (A) or presence of IFN- $\gamma$  (B) and incubated for 72 h. Bilirubin was

## Results

extracted from the cell culture supernatant with benzene and quantified by absorbance at 450 nM using the molar attenuation coefficient of bilirubin dissolved in benzene<sup>217</sup> (mean values  $\pm$  SD, n=3). For time-dependent treatments of 24-56 h see Figure S1.

The cells produced equal basal levels of bilirubin in the DMSO controls in the absence or presence of IFN- $\gamma$  with concentrations of  $7.7 \pm 0.1 \mu\text{M}/10^5$  cells (Figure 47A-B). Treatment with epoxykynin did not alter the bilirubin production, while treatment with hemin slightly increased bilirubin levels to  $8.0 \pm 0.1 \mu\text{M}/10^5$  cells (Figure 47A) and  $7.9 \pm 0.1 \mu\text{M}/10^5$  cells (Figure 47B) without and with IFN- $\gamma$ , respectively. However, co-treatment of hemin and epoxykynin elevates bilirubin concentrations to  $8.7 \pm 0.2 \mu\text{M}/10^5$  cells in the absence of IFN- $\gamma$  (Figure 47A) and to  $8.1 \pm 0.1 \mu\text{M}/10^5$  cells in the presence of IFN- $\gamma$  (Figure 47B). This effect could only be observed after treatment times of at least 48 h and the effect became stronger with extended incubation time (Figure S1). Taken together, the increase of both CO and bilirubin suggests that the activity of HMOX1 is modulated upon treatment with hemin and epoxykynin. However, the HMOX1 catabolite levels were not altered by treatment with epoxykynin in the absence of hemin.

In addition to target engagement studies and monitoring the enzymatic activity of HMOX1 in cells, the role of HMOX1 for Kyn production was studied using HAP1 HMOX1 knockout (KO) cells in comparison to HAP1 wildtype (wt) cells (Figure 48).

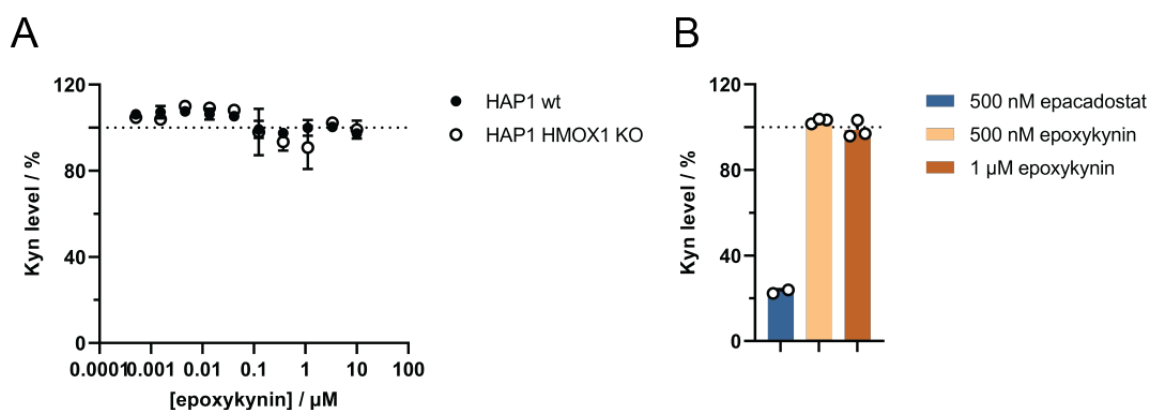


**Figure 48:** Genetic devalidation of HMOX1 as target of epoxykynin with HAP1 HMOX1 knockout (KO) cells. A) HAP1 wildtype (wt) and HAP1 HMOX1 KO cells were treated with IFN- $\gamma$ , Trp and epoxykynin for 48 h prior to quantification of Kyn levels using *p*-DMAB (mean values  $\pm$  SD, n=3). B) HAP1 wt cells were treated with IFN- $\gamma$ , Trp, epacadostat and epoxykynin for 48 h prior to quantification of Kyn levels using *p*-DMAB (mean values  $\pm$  SD, n $\geq$ 2).

Interestingly, epoxykynin did not impair Kyn production in both HAP1 wt and HAP1 HMOX1 KO cells (Figure 48A), while 500 nM of the IDO1 inhibitor epacadostat reduced Kyn levels by  $76.9 \pm 0.8\%$  in the HAP1 wt cells (Figure 48B). These findings demonstrate that although the Kyn pathway is inducible and active, the target protein of epoxykynin is not present in HAP1 cells. However, HMOX1 is expressed in HAP1 cells as curated in databases<sup>218</sup> and detected on immunoblots (Figure 41C).

## Results

### 5.2.5.2 MTAP as Potential Target of Epoxykynin

MTAP was one of the three proteins that was selectively enriched on affinity probe **3b** during the affinity pulldown. Thus, it was tested if epoxykynin directly binds to MTAP (Figure 49), if a published MTAP inhibitor reduces cellular Kyn levels (Figure 50) and if the knockout of MTAP phenocopies the Kyn production inhibition mediated by epoxykynin (Figure 51).

In the lysate-based CETSA, epoxykynin did not cause a significant shift in the melting temperature of MTAP with  $T_m$  values of  $72.7 \pm 1.5^\circ\text{C}$  for the vehicle control and  $73.2 \pm 0.1^\circ\text{C}$  for the epoxykynin treatment (Figure 49).

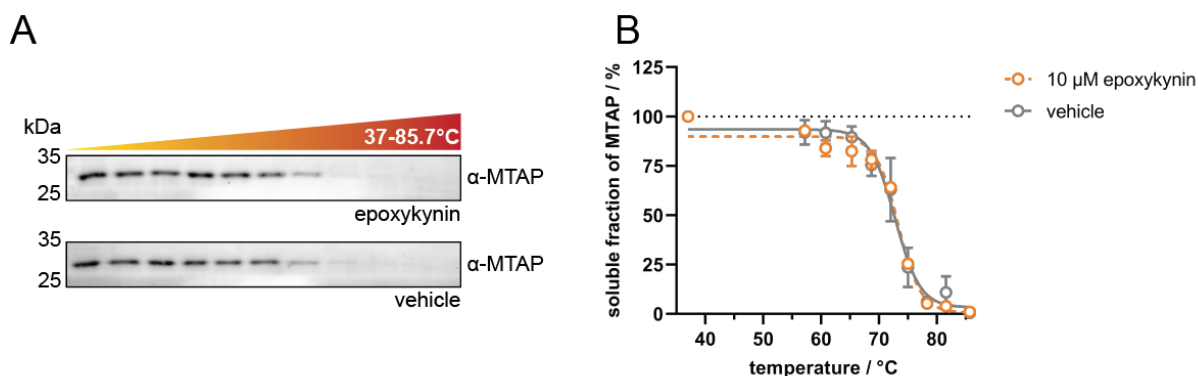


**Figure 49:** Cellular thermal shift assay (CETSA) for MTAP in HeLa cell lysate. The cell lysate was treated with 10  $\mu\text{M}$  epoxykynin or DMSO (vehicle) for 20 min at room temperature. The thermal shift assay was performed prior to immunoblotting. Representative immunoblots are shown in A, thermal profiles are shown in B (mean values  $\pm$  SD,  $n=3$ ).  $\Delta T_m=0.5 \pm 1.5^\circ\text{C}$ .

Subsequently, the MTAP inhibitor methylthio-DADMe-Immucillin A (MT-DADMe-ImmA, Figure 50A) was tested for Kyn reduction (Figure 50B). Upon compound treatment, Kyn levels were decreased by only  $16.5 \pm 1.7\%$  at a concentration of 20  $\mu\text{M}$ .

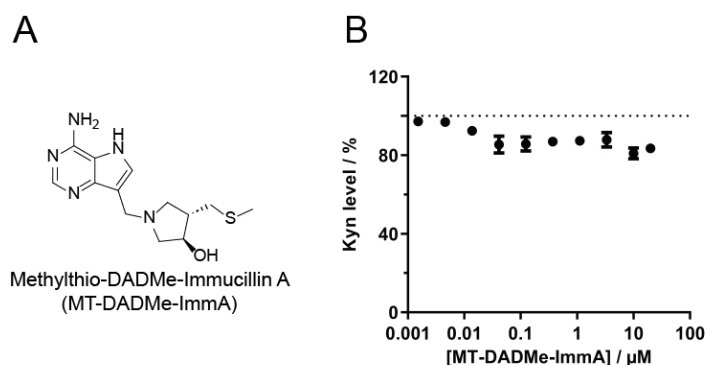


**Figure 50:** Chemical devaluation of MTAP as target of epoxykynin. A) Structure of the MTAP inhibitor methylthio-DADMe-immucillin A (MT-DADMe-ImmA). B) Influence of MT-DADMe-ImmA on Kyn levels. HeLa cells were treated with IFN- $\gamma$ , Trp and compounds for 48 h prior to measuring Kyn levels using *p*-DMAB (mean values  $\pm$  SD,  $n=3$ ).

Finally, HCT116 MTAP<sup>-/-</sup> cells that transiently express IDO1 were used to genetically investigate MTAP as a potential target of epoxykynin (Figure 51). Transfection of HCT116 wt cells with an IDO1 construct under the control of a CMV promoter and subsequent addition of

## Results

500  $\mu\text{M}$  Trp increased Kyn levels 9-fold compared to untransfected HCT116 wt cells (Figure 51A). Similarly, transfection with IDO1 elevated Kyn levels 11-fold in HCT116 MTAP<sup>-/-</sup> cells (Figure 51A) in comparison with the untransfected cells. Subsequently, epoxykynin was tested in IDO1-HCT116 and IDO1-HCT116 MTAP<sup>-/-</sup> cells for Kyn level reduction (Figure 51B). Epoxykynin potently decreased cellular Kyn levels in both wt and MTAP<sup>-/-</sup> cells with IC<sub>50</sub> values of  $20.7 \pm 11.5$  nM and  $20.5 \pm 15.9$  nM, respectively.

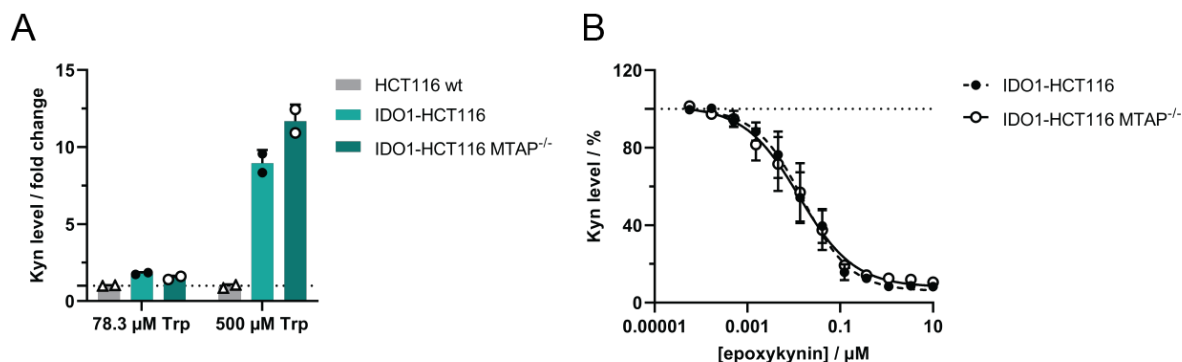


**Figure 51:** Genetic devalidation of MTAP as target of epoxykynin. A) HCT116 wildtype (wt) and HCT116 MTAP<sup>-/-</sup> cells were transiently transfected with IDO1 for 24 h prior to addition of medium with different concentrations of Trp (78.3 or 500  $\mu\text{M}$ ) for 36 h. Kyn levels were quantified using *p*-DMAB (mean values  $\pm$  SD,  $n=2$ ). B) Kyn assay in HCT116 and HCT116 MTAP<sup>-/-</sup> cells that transiently express IDO1. Cells were transfected with IDO1 for 24 h prior to addition of 500  $\mu\text{M}$  Trp and epoxykynin for 48 h. Kyn levels were quantified using *p*-DMAB (mean values  $\pm$  SD,  $n=3$ ).

In summary, no target engagement of epoxykynin to MTAP was proven and the published MTAP inhibitor as well as depletion of MTAP in cells failed to phenocopy inhibition of Kyn production by epoxykynin. Thus, MTAP was devalidated as target protein of epoxykynin.

### 5.2.5.3 sEH as Potential Target of Epoxykynin

sEH was selectively enriched by affinity probe **3b** in chemical proteomics. To investigate if epoxykynin directly binds to sEH, target engagement *in vitro* and *in cellulo* was studied.

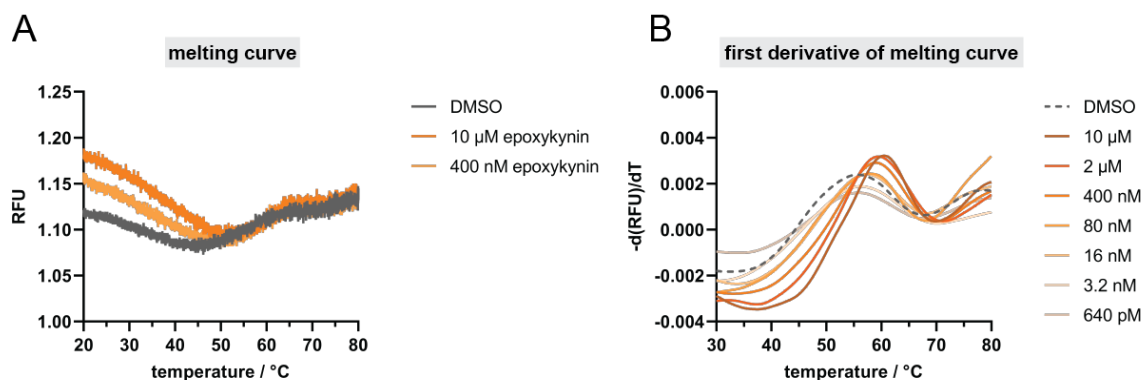


**Figure 52:** Influence of epoxykynin on the thermostability of sEH. A-B) Purified human sEH was treated with epoxykynin or DMSO for 10 min at 22 $^{\circ}\text{C}$  prior to detection of the intrinsic tryptophan/tyrosine fluorescence upon melting. Representative melting curves (A) and first derivate of melting curves (B) are shown ( $n=4$ ).

## Results

Treatment of purified human full-length sEH with epoxykynin altered the melting curve of sEH compared to the DMSO control (Figure 52A). The fluorescence at 20°C, which corresponds to the native protein state, was increased, whereas the minimum of the curve was shifted to higher temperatures, making the slope for determination of the melting temperature  $T_m$  shorter. Using the first derivative of the melting curves (Figure 52B), the thermal melting temperatures  $T_m$  can be obtained from the highest peak of the curve. Binding of epoxykynin to sEH dose-dependently increased the thermal melting temperature  $T_m$  by  $5.5 \pm 1.5^\circ\text{C}$  compared to the DMSO control.

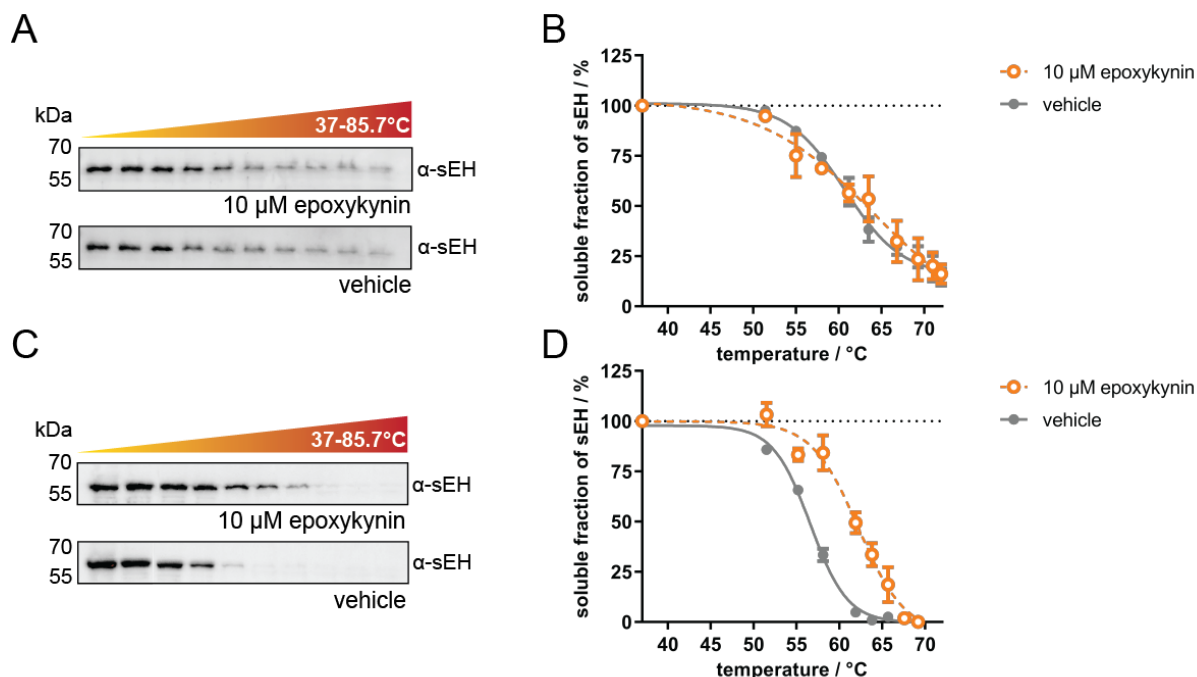


**Figure 53:** Cellular thermal shift assay (CETSA) for sEH in Jurkat cells. A-B) The cell lysate was treated with 10  $\mu\text{M}$  epoxykynin or DMSO (vehicle) for 20 min at room temperature. The thermal shift assay was performed prior to immunoblotting. Representative immunoblot is shown in A, thermal profiles are shown in B (mean values  $\pm$  SD,  $n=3$ ). C-D) Cells were treated with 10  $\mu\text{M}$  epoxykynin or DMSO (vehicle) for 15 min at 37°C. The thermal shift assay was performed prior to cell lysis and subsequent immunoblotting. Representative immunoblot is shown in C, thermal profiles are shown in D (mean values  $\pm$  SD,  $n=3$ ).

Subsequently, the thermostability of sEH was investigated in a cellular environment using CETSA. In a lysate-based setup, treatment with epoxykynin did not alter the thermal stability of sEH (Figure 53A-B), while for in-cell CETSA epoxykynin induced a stabilization upon heat treatment in Jurkat cells with a  $\Delta T_m$  of  $5.9 \pm 1.2^\circ\text{C}$  (Figure 53C-D). In conclusion, epoxykynin engages with sEH *in vitro* and in cells and, thereby, increases its thermostability.

After confirming that epoxykynin binds to sEH, its influence on the sEH catalytic activity was investigated. First, the inhibitory effect of epoxykynin on the fatty acid epoxide hydrolase domain (sEH-H) was tested. Therefore, the conversion of the fluorogenic epoxide PHOME by sEH-H was monitored (Figure 54A)<sup>219</sup>. Purified sEH was treated with epoxykynin and the



## Results

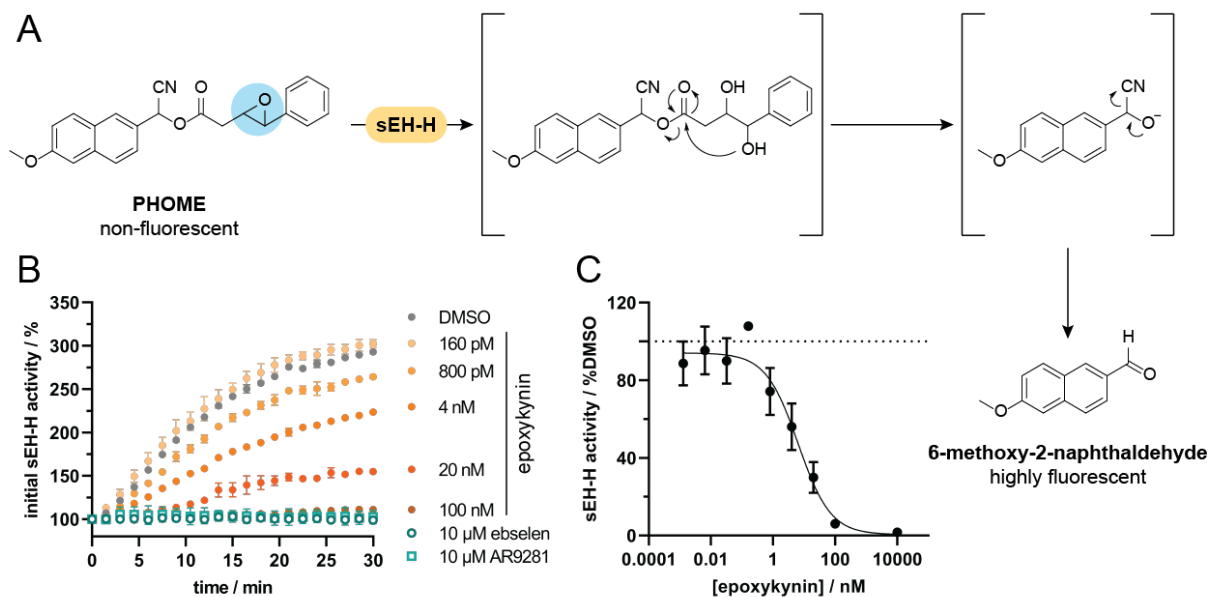


**Figure 54:** Inhibition of sEH-H by epoxykynin. A) The enzymatic sEH-H activity was measured by means of the conversion of the fluorogenic sEH-H substrate (3-phenyl-oxiranyl)-acetic acid cyano-(6-methoxy-naphthalen-2-yl)-methyl ester (PHOME) to the highly fluorescent 6-methoxy-2-naphthaldehyde<sup>219</sup>. B-C) Inhibition of sEH-H upon treatment with epoxykynin, ebselen or AR9281 for 30 min. Representative curves are shown in B, the dose-dependent inhibition curve is shown in C (mean values  $\pm$  SD, n=3).

control inhibitors ebselen<sup>220</sup> and AR9281<sup>221</sup> (Figure 54B). Compared to the DMSO control, treatment of sEH with both control inhibitors, as well as 100 nM of epoxykynin abolished the catalytic activity of sEH-H. Epoxykynin potently inhibited sEH-H in a dose-dependent manner with an  $IC_{50}$  value of  $6.7 \pm 3.2$  nM (Figure 54C).

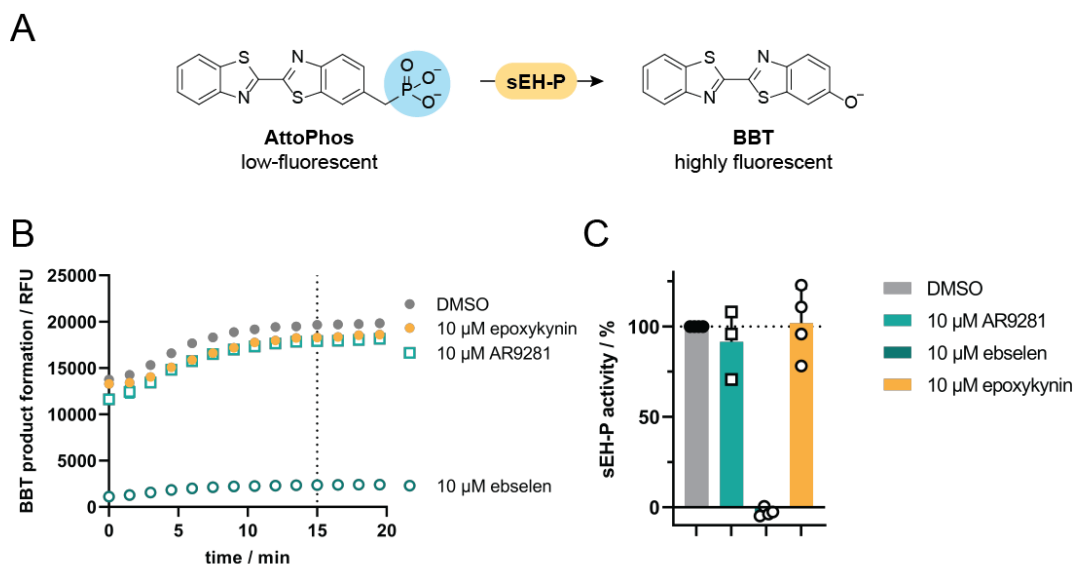


**Figure 55:** Epoxykynin does not inhibit sEH-P. A) The enzymatic sEH-P activity was measured by means of the conversion of the sEH-P substrate AttoPhos (2'-(2-benzothiazoyl)-6'-hydroxybenzothiazole phosphate (BBTP)) to the highly fluorescent 2'-(2-benzothiazoyl)-6'-hydroxybenzothiazole (BBT)<sup>220</sup>. B-C) The enzymatic sEH-P activity was measured upon treatment with epoxykynin, AR9281 or ebselen for 20 min. Representative curves are shown in B, the normalized inhibition after 15 min of treatment is shown in C (mean values  $\pm$  SD, n=3).

## Results

In addition to the hydrolase activity, sEH contains a lipid phosphatase domain (sEH-P). The enzymatic activity of sEH-P was evaluated by the conversion of the AttoPhos reagent to a fluorescent product (Figure 55A)<sup>220</sup>. The effect of epoxykynin on sEH-P was tested by treatment of purified sEH with epoxykynin and the control inhibitors ebselen and AR9281 (Figure 55B). While epoxykynin and AR9281 did not inhibit sEH-P, ebselen completely abolished the sEH-P catalytic activity compared to DMSO (Figure 55C). Concisely, epoxykynin impairs the catalytic activity of sEH-H, but does not inhibit sEH-P.

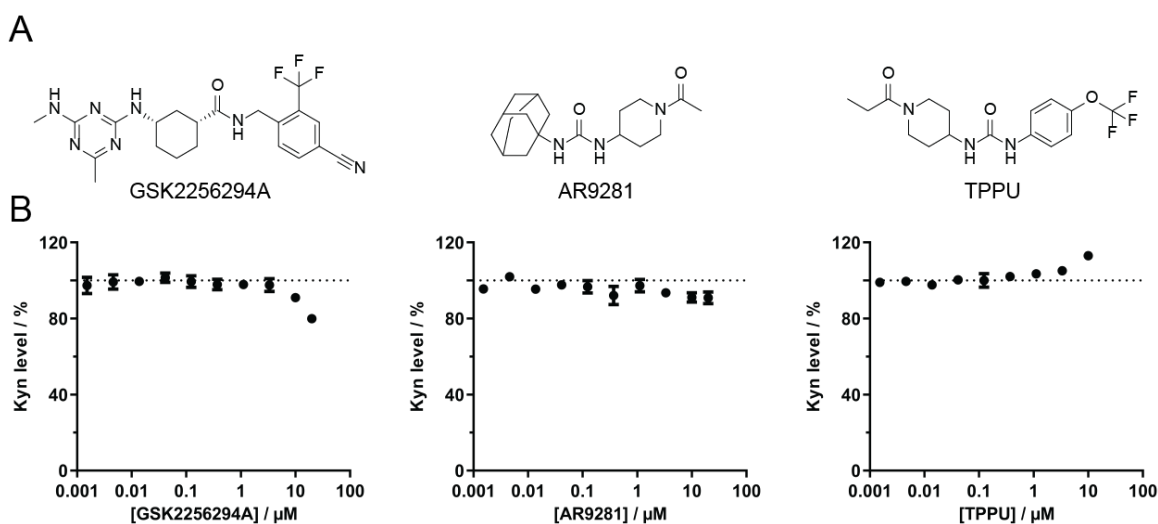


**Figure 56:** A) Structures and B) influence of sEH-H inhibitors on Kyn levels. HeLa cells were treated with IFN- $\gamma$ , Trp and compounds for 48 h prior to measuring Kyn levels using *p*-DMAB (mean values  $\pm$  SD,  $n=3$ ).

Furthermore, three sEH-H inhibitors GSK2256294A<sup>222</sup>, AR9281 and TPPU<sup>212</sup> were tested for cellular Kyn reduction (Figure 56). None of these compounds significantly altered Kyn levels in HeLa cells. The urea-based sEH-H inhibitors AR9281 and TPPU are known to have poor pharmacokinetics (PK)<sup>223</sup>. Thus, they may be very active in biochemical assays, though not as potent in a cellular setup.

Additionally, the sEH-P inhibitors SWE101<sup>224</sup>, ebselen and auranofin were investigated in the Kyn assay (Figure 57). The selective sEH-P inhibitor SWE101 did not reduce Kyn levels, while ebselen decreased cellular Kyn levels by  $43.8 \pm 3.6\%$  at  $10 \mu\text{M}$  with an  $\text{IC}_{50}$  value greater than  $10 \mu\text{M}$  and auranofin potently inhibited Kyn production with an  $\text{IC}_{50}$  of  $57.3 \pm 28.5 \text{ nM}$ .

## Results

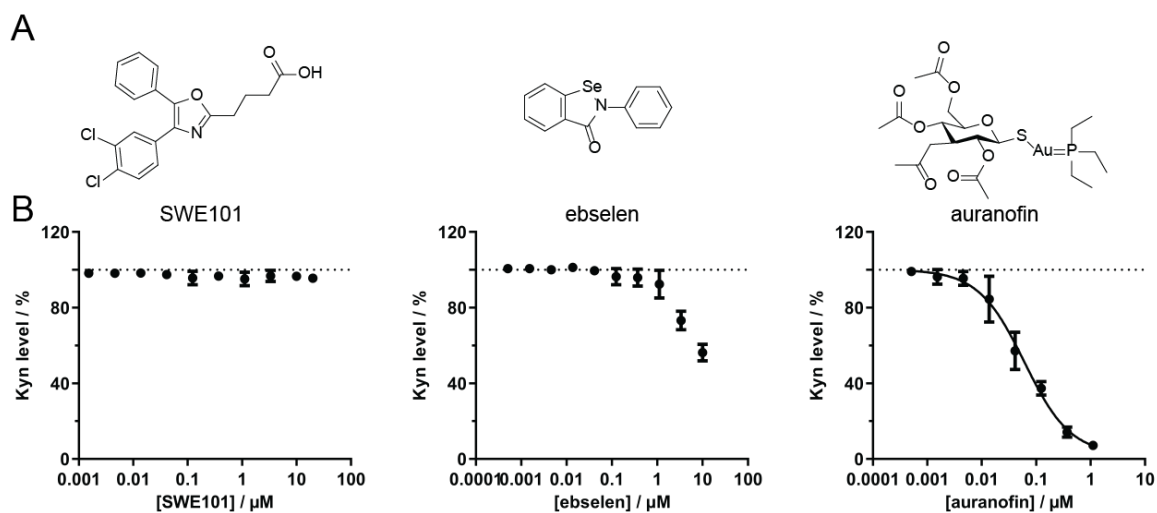


**Figure 57:** A) Structures and B) influence of sEH-P inhibitors on Kyn levels. HeLa cells were treated with IFN- $\gamma$ , Trp and compounds for 48 h prior to measuring Kyn levels using *p*-DMAB (mean values  $\pm$  SD, n=3).

Taken together, the published sEH-H and sEH-P inhibitors did not reduce cellular Kyn levels, except for ebselen and auranofin. Both of these small molecules are promiscuous compounds<sup>225-227</sup>, with the thioredoxin reductase (TrxR) being their common annotated target<sup>225, 227</sup>. Hence, epoxykynin was tested for direct inhibition of TrxR (Figure 58).

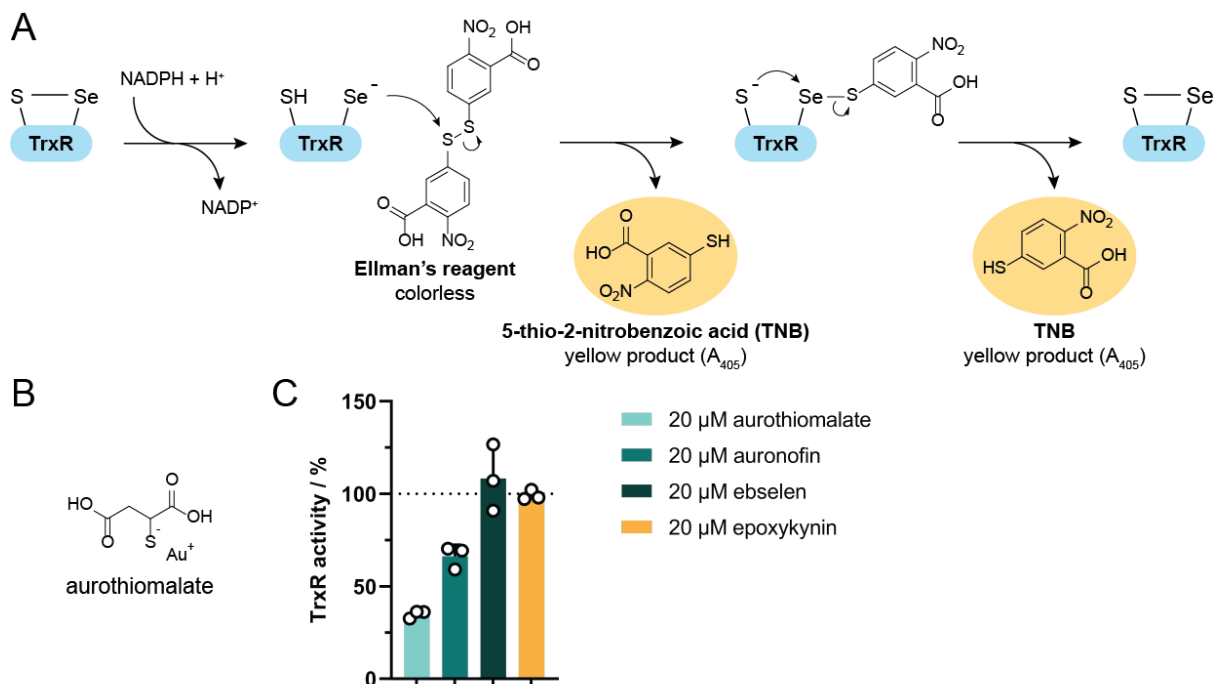


**Figure 58:** Thioredoxin reductase (TrxR) assay. A) TrxR activity was monitored by the reduction of the Ellman's reagent (5,5'-dithio-bis(2-dinitrobenzoic acid) (DTNB)) to 5-thio-nitrobenzoic acid (TNB) in the presence of NADPH. B) Structure of the TrxR inhibitor aurothiomalate. C) TrxR was extracted from HeLa cell lysate and the enzymatic TrxR activity was measured upon treatment with aurothiomalate, auranofin, ebselen or epoxykynin for 15 min (mean values  $\pm$  SD, n=3).

## Results

The thioredoxin system consists of thioredoxin (Trx), TrxR and NADPH. Upon reduction of a protein disulfide bridge by Trx, the pair of cysteines in the Trx active site oxidize and form a disulfide. Thereafter, TrxR reduces the Trx disulfide with NADPH as electron source<sup>228</sup>. Thus, together with the glutathione system, the Trx system regulates the redox state of cysteine residues in proteins. TrxR was derived from HeLa cell lysate and its catalytic activity was monitored by the reduction of the Ellman's reagent (5,5'-dithio-bis(2-dinitrobenzoic acid) (DTNB)) in the presence of NADPH (Figure 58A)<sup>229</sup>. The TrxR inhibitor aurothiomalate (Figure 58B)<sup>230</sup> reduced TrxR activity to  $35.0 \pm 1.7\%$  at  $20 \mu\text{M}$  (Figure 58C). Similarly,  $20 \mu\text{M}$  auranofin inhibited TrxR by  $33.8 \pm 5.0\%$ , while ebselen and epoxykynin did not impair the TrxR enzymatic activity (Figure 58C). Thus, epoxykynin does not reduce Kyn levels *via* modulation of the Trx system.

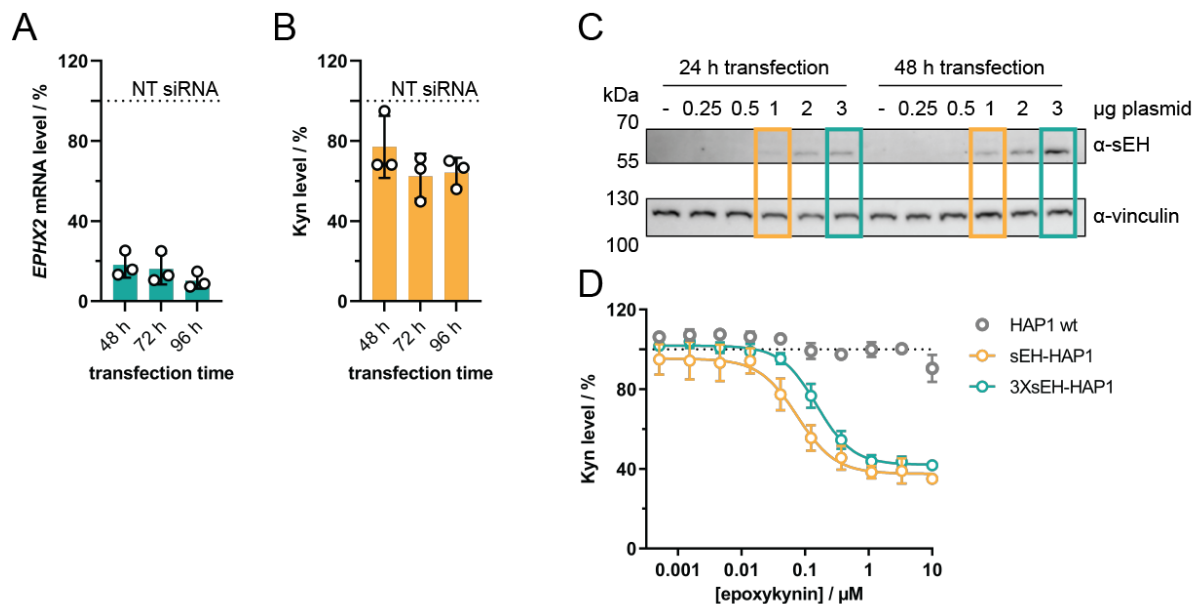


**Figure 59:** Genetic validation of sEH as a target of epoxykynin for Kyn reduction. A-B) Knockdown of sEH (*EPHX2*) decreased cellular Kyn levels. HeLa cells were transfected with 50 nM non-targeting (NT) or *EPHX2*-targeting siRNA for 48-96 h and treated with Trp and IFN- $\gamma$  for 48 h prior to detection of *EPHX2* mRNA (A, mean values  $\pm$  SD,  $n=3$ ) and Kyn levels with *p*-DMAB (B, mean values  $\pm$  SD,  $n=3$ ). The dotted lines indicate signal levels of the NT siRNA controls. C) Overexpression of sEH in HAP1 cells that do not endogenously express sEH. HAP1 cells were transfected with empty vector (mock) or pCMV3-*EPHX2* for 24-48 h prior to quantification of protein levels by immunoblotting. Representative immunoblots are shown (mean values  $\pm$  SD,  $n=3$ ). The plasmid amounts indicated refer to the amount per 96-well plate. The orange and blue boxes correspond to the transfection conditions used in D). D) HAP1 cells that transiently express sEH were treated with epoxykynin, Trp and IFN- $\gamma$  for 48 h prior to measuring Kyn levels *p*-DMAB (mean values  $\pm$  SD,  $n=3$ ). sEH-HAP1: 1  $\mu\text{g}$  plasmid/96-well plate, 3XsEH-HAP1: 3  $\mu\text{g}$  plasmid/96-well plate.

sEH was depleted in HeLa cells using siRNA to investigate the role of sEH in the Kyn pathway. A partial knockdown of  $82 \pm 5\%$ ,  $84 \pm 6\%$  and  $90 \pm 3\%$  was achieved after 48, 72 and 96 h, respectively (Figure 59A). Simultaneously, Kyn levels were reduced by  $23 \pm 13\%$ ,  $38 \pm 9\%$  and  $36 \pm 6\%$  after 48, 72 and 96 h, respectively (Figure 59B). Furthermore, sEH was overexpressed in HAP1 cells that hardly express any sEH according to the ProteinAtlas

## Results

database (Figure 59C)<sup>231, 232</sup>. In the wildtype (wt) cells, epoxykynin did not reduce cellular Kyn levels upon stimulation with IFN- $\gamma$ , whereas in sEH-HAP1 cells epoxykynin inhibited Kyn production with an IC<sub>50</sub> value of  $68.4 \pm 9.7$  nM (Figure 59D). Transfecting HAP1 cells with thrice the amount of plasmid DNA shifted the IC<sub>50</sub> to  $159.7 \pm 49.1$  nM (Figure 59D).

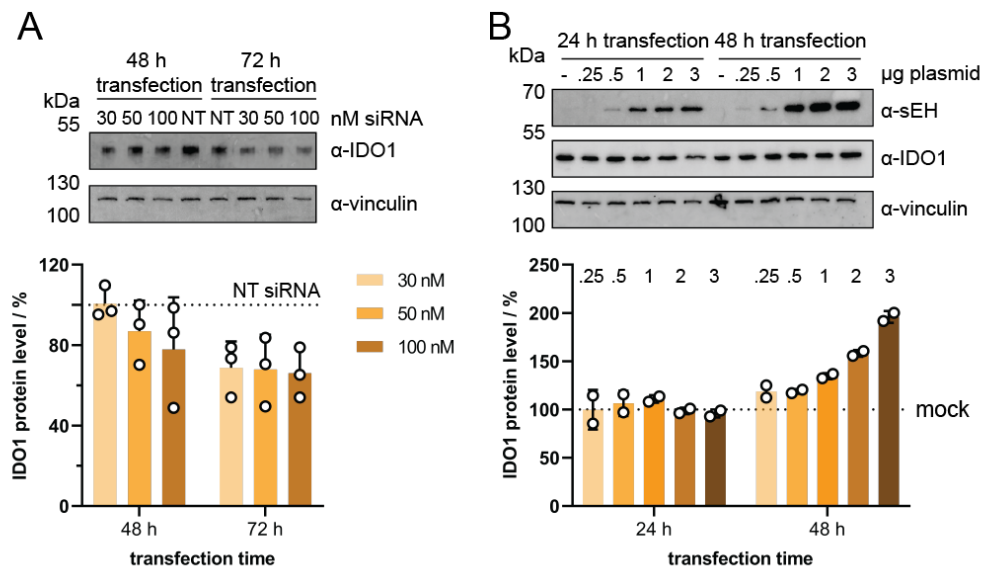


**Figure 60:** Influence of altered sEH levels on IDO1 levels. A) KD of sEH decreases IDO1 levels. HeLa cells were transfected with non-targeting (NT) or *EPHX2*-targeting siRNA for 48-72 h and treated with IFN- $\gamma$  for 48 h prior to quantification of protein levels by immunoblotting. Representative immunoblots are shown (mean values  $\pm$  SD, n=3). B) Overexpression of sEH resulted in increased IDO1 levels. HeLa cells were transfected with empty vector (mock) or pCMV3-EPHX2 for 24-48 h and treated with IFN- $\gamma$  for 48 h prior to quantification of protein levels by immunoblotting. Representative immunoblots are shown (mean values  $\pm$  SD, n=2). The plasmid amounts indicated refer to the amount per 96-well plate.

Subsequently, the influence of sEH knockdown or overexpression on the IDO1 protein levels was investigated in HeLa cells (Figure 60). Depletion of sEH reduced cellular IDO1 levels by up to  $35.0 \pm 10.1\%$  after 72 h (Figure 60A). On the other hand, overexpression of sEH doubled the IDO1 levels after 48 h, but did not modulate IDO1 levels after 24 h (Figure 60B). These results demonstrate that sEH expression controls IDO1 protein levels. Since the effect appears only after 48 h, this indicates cross-regulation of both signaling pathways.

Additionally, Kyn levels were quantified in IDO1-containing BxPC-3 cell lysate (Figure 61). In cell lysates, signal transduction within protein networks is no longer possible. Hence, these experiments elucidate if pathway activity is required for the inhibition by epoxykynin. Upon treatment of the lysate with  $10 \mu$ M epacadostat, Kyn levels were decreased by  $89.6 \pm 6.9\%$ , while  $10 \mu$ M epoxykynin did not alter Kyn levels (Figure 61A). However, pre-treatment of the cells with  $5 \mu$ M epoxykynin or *EPHX2*-targeting siRNA prior to quantification of Kyn levels in the cell lysate reduced Kyn levels to  $11.2 \pm 1.9\%$  and  $74.5 \pm 1.3\%$ , respectively (Figure 61B). These findings demonstrate that acute inhibition of sEH is not sufficient to reduce Kyn levels. Instead, a cross-talk between sEH and the Kyn pathway are necessary to decrease Kyn levels.

## Results

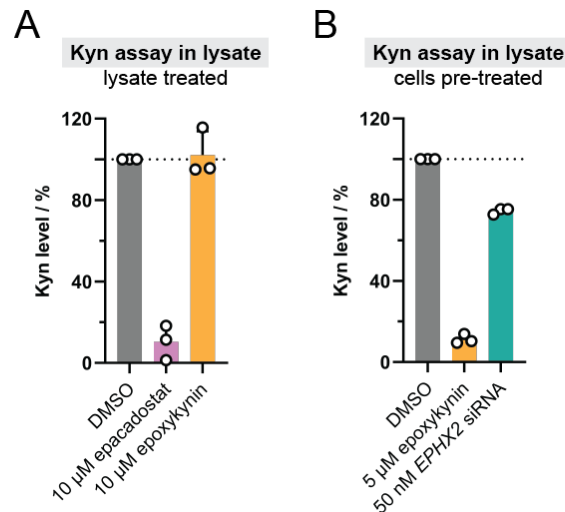


**Figure 61:** sEH inhibition modulates the Kyn pathway. A-B) Kyn assay in BxPC-3 cell lysate. A) BxPC-3 cells were treated with IFN- $\gamma$  for 24 h prior to cell lysis. The lysate was treated with 10  $\mu$ M epacadostat, 10  $\mu$ M epoxykynin or DMSO for 45 min prior to detection of Kyn levels (mean values $\pm$ SD, n=3). D) BxPC-3 cells were treated with 5  $\mu$ M epoxykynin, 50 nM *EPHX2*-targeting siRNA or DMSO and IFN- $\gamma$  for 48 h prior to cell lysis and detection of Kyn levels (mean values  $\pm$  SD, n=3).

sEH-H catalyzes the conversion of epoxyeicosatrienoic acids (EETs) to dihydroxyeicosatrienoic acids (DHETs, Figure 62A). In the cellular environment, EETs are unstable and are rapidly converted into the biologically less active DHETs<sup>233, 234</sup>. Inhibition of sEH results in accumulation of EETs, as well as deprivation of DHETs, which might contribute to the reduction of Kyn levels. The influence on Kyn levels of two of the four regioisomer EETs (Figure 62B) and DHETs (Figure 62C) was investigated. Upon treatment of BxPC-3 cells with 8,9-EET and 11,12-EET, Kyn levels were slightly increased up to  $130.7 \pm 3.2\%$  and  $137.8 \pm 4.4\%$  at 1  $\mu$ M EET, respectively (Figure 62B). These results contradict the expectations. Since EET substrates accumulate upon inhibition of sEH, the logical conclusion would be that treatment with the substrates would reduce Kyn levels. However, EETs can be incorporated into membranes and presumably have additional signaling functions unrelated to the AA pathway<sup>233-235</sup>. Therefore, it is challenging to draw a conclusion from this experiment. Moreover, treatment with 8,9- and 11,12-DHETs did not alter cellular Kyn production (Figure 62C). Since DHETs are less active than EETs, it is not surprising that they have no effect on Kyn levels.

## Results

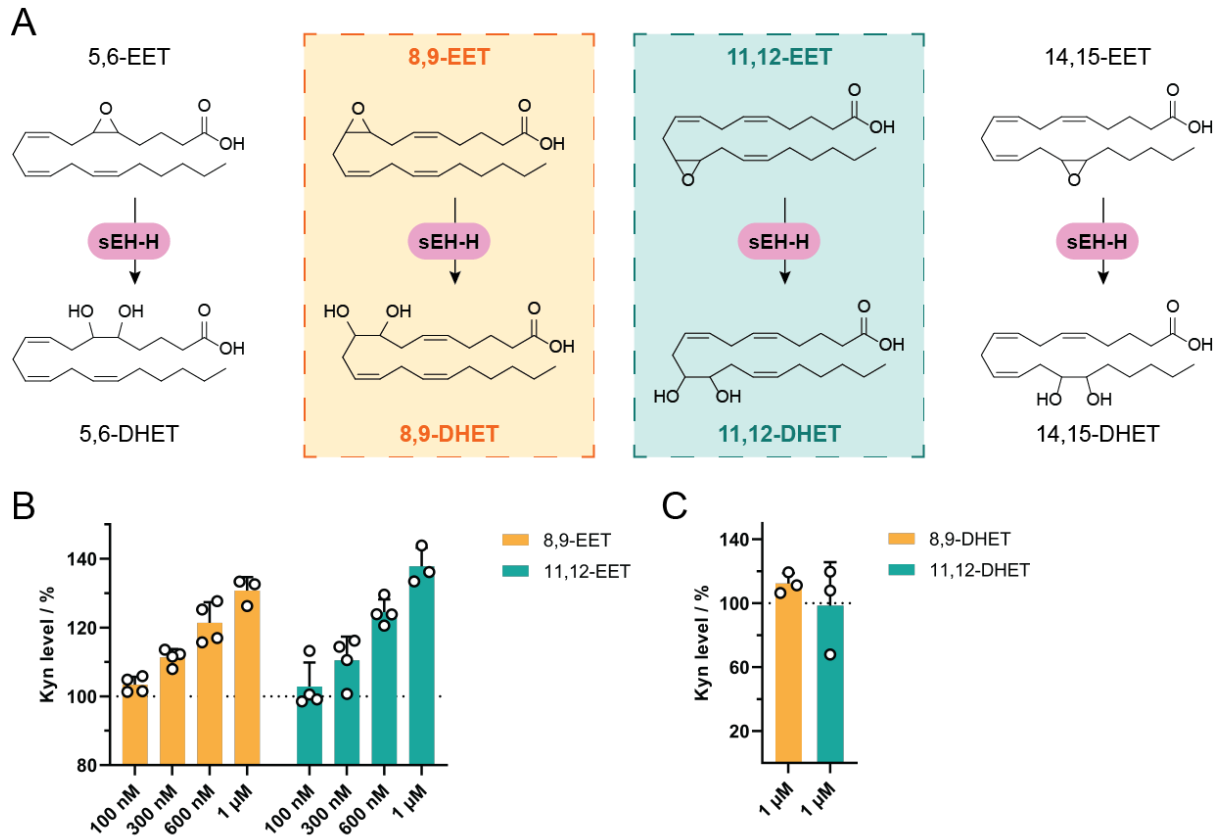


**Figure 62:** Kyn levels upon treatment with epoxyeicosatrienoic acids (EETs) and dihydroxyeicosatrienoic acids (DHETs). A) sEH-H catalyzes the conversion of CYP epoxygenase-derived 5,6-, 8,9-, 11,12- and 14,15-EETs to the corresponding DHETs. B-C) Influence of sEH-H substrates and products on Kyn levels. BxPC-3 cells were treated with BSA:EETs (B) or BSA:DHETs (C), Trp and IFN- $\gamma$  for 48 h under serum-reduced conditions prior to determination of cellular Kyn levels with *p*-DMAB (mean values  $\pm$  SD,  $n \geq 3$ ).

In conclusion, epoxykynin binds to sEH *in vitro* and in cells and thereby, inhibits the catalytic activity of sEH-H. Depletion of sEH in cells phenocopies inhibition of Kyn production by epoxykynin and altered expression of sEH modulates IDO1 protein levels. Thus, epoxykynin reduces cellular Kyn levels by inhibition of sEH-H.

### 6 Discussion

Cell-based screenings represent a powerful strategy to identify bioactive small molecules in disease-relevant systems. Compared to target-based assays that focus on single, validated protein targets, cell-based assays allow for a less biased discovery of new targets in cells. This approach not only facilitates the identification of bioactive compounds, but, moreover, enables better understanding of disease-related pathways and new conclusions on the link between a target and the disease<sup>236</sup>. To obtain reliable results, the screening has to be carefully designed and validated. For the design of robust screening assays, it is crucial to consider the phenotypic screening 'rule of 3': utilizing a disease-relevant system, employing a physiological stimulus and a downstream readout close to the clinical end point<sup>121</sup>. Since IDO1 expression and the Kyn pathway are associated with induced immune tolerance in the tumor microenvironment, the aim of this thesis was to discover inhibitors of this pathway. Therefore, a cell-based assay for the identification of modulators of cellular Kyn levels upon stimulation with IFN- $\gamma$ <sup>155</sup> was developed. The following paragraph discusses, why this assay is an excellent example for a predictive cell-based screening.

Since IDO1-induced immune suppression is associated with cancer progression, BxPC-3 cells<sup>237</sup> as a pancreatic cancer cell line represent a robust assay system. However, tumor-derived cell lines often display high genetic heterogeneity compared to normal tissue cells<sup>238</sup>. This might cause up- or downregulation of certain signaling pathways and aberrant metabolic processes. Accordingly, phenotypic assays can benefit from more native, patient- or tissue-originating cellular systems<sup>121</sup>. Nonetheless, primary patient-derived cells often show high donor-specific variations. Considering these factors, secondary validation of the screening results in other cancer cell lines, such as HeLa cells or SKOV-3 cells, was performed.

To induce Kyn production, the cytokine IFN- $\gamma$  was employed as stimulus. Induction with IFN- $\gamma$  leads to expression of IDO1, while the expression of two other Trp-catabolizing enzymes TDO and IDO2 cannot be induced by cytokines<sup>44, 180, 239</sup>. Thus, compounds identified by the screening most likely interfere with IDO1-related Kyn production. Additionally, IFN- $\gamma$  represents a disease-relevant stimulus, since suppressive lymphocytes within the TME secrete IFN- $\gamma$  to inhibit cytolytic immune cells<sup>240</sup> and it acts upstream of IDO1 expression. However, a system providing an intrinsic stimulus, such as a co-culture of cancer and cytotoxic T cells, would have higher physiological relevance<sup>121</sup>. Moreover, stimulation with IFN- $\gamma$  induces signaling events that involve different transcription factors and promoters, regulating a multitude of genes<sup>240</sup>. Therefore, it is important to investigate if the screening results are dependent on the stimulus or if the screening hits can also act on systems in the absence of the stimulus. This is also critical when considering that IDO1 expression can be regulated by diverse upstream factors, such as TGF- $\beta$  or PGE-2<sup>92, 241, 242</sup>. Hence, Kyn assays in HEK293T



## Discussion

cells that transiently express IDO1 under control of a promoter that is not inducible by IFN- $\gamma$  and SKOV-3 cells that endogenously express IDO1 without exogenous stimuli were employed.

Kyn levels were monitored as the assay readout of the screening. Since Kyn production is downstream of the signaling events, Kyn level modulation as the readout captures most of the mechanisms related to the Kyn pathway in this system. Thereby, the amount of built-in assumptions associated to adverse pathway events or deviant downstream signaling is minimized. Moreover, Kyn acts as a direct immunosuppressant responsible for T cell dysfunction<sup>243</sup>. Thus, it is closely associated with the clinical end point and has been used as biomarker to predict prognoses for cancer patients<sup>244, 245</sup>. This enables the potential translation of the screening results to *in vivo* models<sup>121</sup>.

Taken together, the cell-based screening employed in this thesis enabled the identification of Kyn pathway modulators that not only inhibit IDO1 directly, but also modulate targets within the Kyn pathway. With this assay in hand, apoxidole PNPs were discovered as type IV apo-IDO1 inhibitors and epoxykynins were found to reduce Kyn levels by inhibition of sEH.

### 6.1 Apoxidoles as Novel Type IV IDO1 Inhibitors

#### 6.1.1 Kyn Pathway Inhibition and Structure-Activity Relationship

To validate the screening results and exclude false positive hits, the inhibition of Kyn production by apoxidole PNPs was validated in different cell lines and using orthogonal readouts. For this purpose, manual Kyn assays were performed in HeLa, BxPC-3 and SKOV-3 cells employing the Ehrlich reagent or HPLC-ESI-MS/MS quantification as readout. The inhibition by apoxidole-1 was strongest in HeLa cells with an  $IC_{50}$  value of  $46.7 \pm 2.4$  nM, followed by SKOV-3 cells with an  $IC_{50}$  of  $109.3 \pm 25.5$  nM and BxPC-3 cells with an  $IC_{50}$  of  $250.4.3 \pm 67.1$  nM. The deviations in  $IC_{50}$ s might be due to different IDO1 expression levels in each cell line upon stimulation with IFN- $\gamma$  and different cell numbers. Nonetheless, these results are consistent with the  $IC_{50}$  value of  $36.7 \pm 9.4$  nM obtained from the automated Kyn screening in BxPC-3 cells by COMAS.

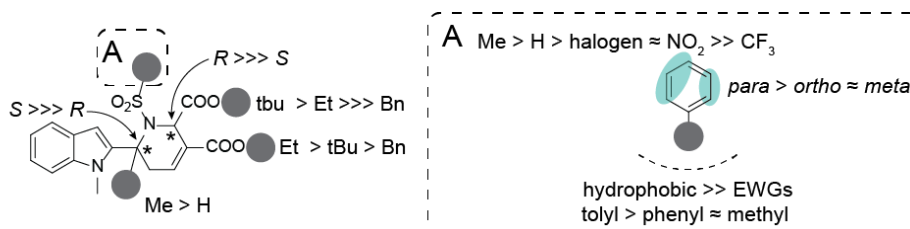


**Figure 63:** Condensed structure-activity relationship (SAR) for apoxidoles. Substituents of the sulfonyl group are shown in A. EWG: electron-withdrawing group.

Exploring the SAR (Figure 63) revealed that compounds derived from the (*R,R*) catalyst are significantly more potent than those originating from the (*S,S*) catalyst. Even if the majority of

## Discussion

the product corresponds to the (*S,R*) derivative, impurities with the (*R,S*) form reduce the compound activity. This is a well-known phenomenon commonly reported in literature<sup>246, 247</sup>. With a compound's protein target being a three-dimensional entity, it is not surprising that only the right enantiomer or diastereomer can bind with high affinity. Therefore, it is important to confirm the identity of each molecule, since different optical activity can result in unpredictable off-target events<sup>247</sup>. For instance, (*R*)-thalidomide cures morning sickness during pregnancy, while its (*S*)-enantiomer has severe teratogenic effects<sup>248</sup>. However, there are FDA-approved drugs marketed as both racemic mixtures and enantiopure agents (also due to interconversion *in vivo*), such as ibuprofen or warfarin<sup>249</sup>.

Most of the apoxidoles carry an ester group in the R<sup>1</sup>, R<sup>3</sup> and R<sup>4</sup> position. Esters are classical prodrugs of carboxylic acids, since they improve the poor bioavailability of their carboxylic acid precursors and can be hydrolyzed *in vivo* by ubiquitous esterases<sup>250</sup>. But not all esters are accessible for esterases, considering differences in the steric hindrance and electron density<sup>167</sup>. Serum-containing cell culture growth medium includes esterases<sup>166, 251</sup>, hence, it is a simple method to test the stability of ester-bearing compounds. The results indicate that all esters in apoxidole-1 are stable in serum for up to 48 h, which corresponds to the duration of the Kyn assay. Therefore, apoxidoles do not act as prodrugs, even though the cleavage of the esters inside the cell cannot be excluded completely.

Compounds without the methyl ester in R<sup>1</sup> position are generally less potent, indicating that the stereocenter is important for bioactivity. The combination of tBu and Et esters in R<sup>3</sup> and R<sup>4</sup> position, respectively, yielded the most active compound. Introducing bigger groups in both positions decreased the potency. Especially the R<sup>3</sup> position did not tolerate substitution of the tBu by the Bn group, suggesting that the increased size and hydrophobicity potentially diminish the activity.

The initial hit compound (*S,R*)-**1b** and nine further derivatives contain a nosyl group as sulfonyl moiety in R<sup>2</sup> position. Nitro groups are electron-withdrawing groups that can react with thiol nucleophiles, such as cysteines or glutathione, to form covalent adducts<sup>252, 253</sup>. Additionally, nitro groups can undergo enzymatic reduction to amines by nitroreductases within cells, involving the generation of potentially toxic nitroso derivatives, nitro radical anions, nitroxyl radicals, hydroxylamines and ROS<sup>254</sup>. However, no cytotoxicity has been observed for apoxidoles. Still the replacement of the nosyl group by other groups is desirable and, in this case, even led to more active derivatives. Substituents at R<sup>2</sup> position mostly include aromatic residues. Methyl, phenyl or *para*-substituted phenyl residues provided sub-micromolar activity. Especially introduction of lipophilic moieties, such as the tosyl group, increased the potency, whereas electron-withdrawing groups led to diminished activity.

## Discussion

In conclusion, apoxidole-1 combines the methyl ester in R<sup>1</sup> position with a *p*-Me-Ph group in R<sup>2</sup> and tBu and ethyl esters in R<sup>3</sup> and R<sup>4</sup> to be the most potent derivative with an IC<sub>50</sub> value of 46.7 ± 2.4 nM.

### 6.1.2 Identification of the Molecular Target of Apoxidole-1

Small molecules that reduce cellular Kyn levels in this screening assay can have miscellaneous targets. These compounds might impair the signal transduction of the IFN-γ stimulus, modulate gene levels or protein levels, lower the availability of the IDO1 substrate Trp, inhibit IDO1 directly or enhance the downstream degradation of Kyn. Thus, hit compound (*S,R*)-**1b** and apoxidole-1 were first characterized in different cell-based assays to narrow down the target of the apoxidoles. Apoxidoles did not alter *IDO1* promoter-driven expression, *IDO1* mRNA or IDO1 protein levels. Additionally, apoxidole-1 reduced cellular Kyn levels in the absence of the IFN-γ stimulus. These findings indicate that apoxidoles do not modulate the first part of the IDO1 pathway, including the binding of IFN-γ to its receptor and subsequent JAK/STAT signaling, as well as transcription and translation of the *IDO1* gene or mRNA, respectively. Furthermore, the unaltered IDO1 protein levels suggest that the turnover of the IDO1 protein is not enhanced by the compounds. Moreover, the target expression is not dependent on the IFN-γ stimulus and more specifically, on promoters containing a gamma interferon activation site (GAS). Additionally, apoxidoles do not interfere with the IFN-γ-independent or -dependent uptake of the IDO1 substrate Trp by LATs or TrpRS. Thus, the target of apoxidoles is not involved in the IFN-γ-induced expression of IDO1, nor in the import of Trp.

Upon treatment with 60 μM apoxidole-1, the activity of purified human full-length IDO1 was reduced by 32 ± 2.8%. This led to the hypothesis that apoxidole-1 might be an apo-IDO1 inhibitor. In contrast to holo-IDO1 inhibitors, such as epacadostat<sup>87, 255</sup>, apo-IDO1 inhibitors provide only weak inhibition in *in vitro* assays<sup>155, 256-258</sup>. The reason for this is that the displacement of the heme group is a slow and reversible process, since the affinity of heme to the apo-protein is usually high with *K<sub>D</sub>* values in the pico- to femto-molar range<sup>259</sup>. Hence, pre-incubation of holo-IDO1 in the presence of the compound at 37°C is required to observe inhibition by apo-IDO1 inhibitors. Nonetheless, once the inhibitor-apo-IDO1 complex is formed, it is thermodynamically stable and mimics the kinetics of irreversible inhibition<sup>260</sup>. This results in prolonged target engagement, leading to high potencies in cellular experiments. Additionally, heme-displacing inhibitors seem to be selective for IDO1<sup>260, 261</sup>, whereas some holo-IDO1 inhibitors act as dual inhibitors for TDO and IDO1<sup>89, 92</sup>.

### 6.1.3 Target Validation Studies

Validation of a small molecule's protein target can include genetic, chemical, *in vivo* and target engagement strategies. To confirm the binding of apoxidole-1 to IDO1, nano differential

## Discussion

scanning fluorimetry was employed. Treatment of holo-IDO1 with apoxidole-1 increased the thermal denaturation temperature by  $7.7 \pm 0.3^\circ\text{C}$  with an apparent  $K_{D, \text{app}}$  value of  $1.1 \pm 0.3 \mu\text{M}$ <sup>262, 263</sup>. Since binding constants described by the  $K_D$  value are temperature-

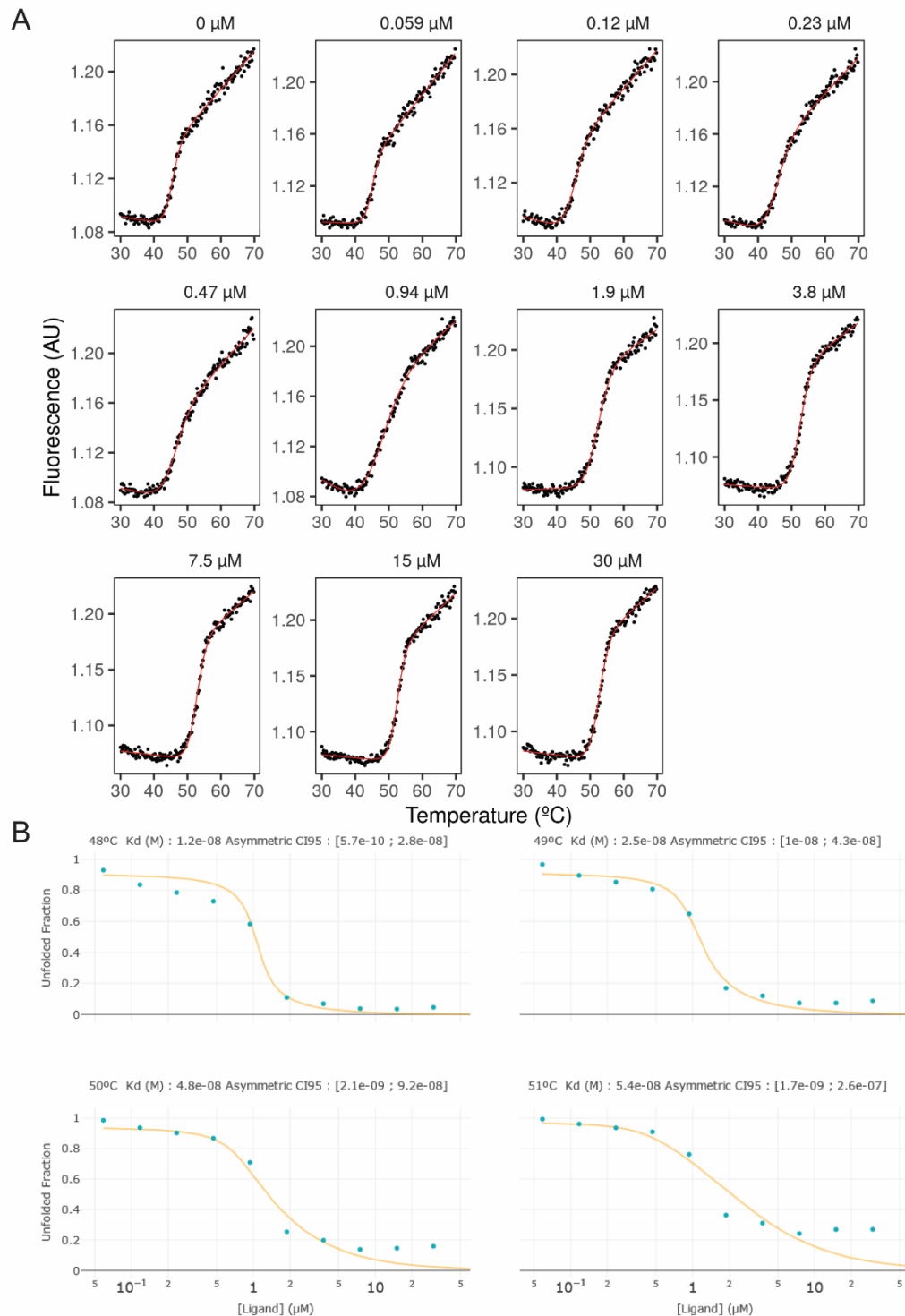


**Figure 64:** Isothermal analysis of the nanoDSF data. A) Fitting of the fluorescence-based thermal denaturation curves of IDO1 at different concentrations of apoxidole-1. B) Isothermal analysis of the nanoDSF data from A) at 48–51 $^\circ\text{C}$  (2.3 $^\circ\text{C}$  above the protein  $T_m$ ). A representative replicate is shown ( $n=3$ ). Plots were created by FoldAffinity<sup>263</sup> (spc.embl-hamburg.de).  $K_D$ , 48 $^\circ\text{C}$  = 11.6 nM;  $K_D$ , 49 $^\circ\text{C}$  = 24.7 nM;  $K_D$ , 50 $^\circ\text{C}$  = 48.4 nM;  $K_D$ , 51 $^\circ\text{C}$  = 54.4 nM.

## Discussion

dependent, isothermal methods are generally more suitable to determine binding affinities as TSA methods. Thus, only apparent  $K_{D, app}$  values can be obtained from nanoDSF experiments which can be converted into  $K_D$ s by isothermal analysis<sup>263</sup>. However, the isothermal fit uses the heat capacity change  $\Delta C_p$  upon unfolding of the protein. If the  $\Delta C_p$  is not known for the target protein, it can be assumed to have a value of zero<sup>263</sup>. Using the temperature-dependent nanoDSF data, a  $K_D$  value of  $20.7 \pm 0.01$  nM at 49 °C was calculated for apoxidole-1 binding to IDO1 (Figure 64).

Furthermore, observation of the Soret peak at 404 nm suggested that binding of apoxidole-1 induces heme release. The Soret peak not only provides information on whether the heme cofactor is displaced, but also about the oxidation state of the iron. While the absorbance maximum at 404 nm corresponds to ferric iron, a red-shifted peak is characteristic for ferrous IDO1<sup>178</sup>. Therefore, this method can also be used to characterize holo-IDO1 inhibitors, since there are inhibitors targeting either ferric or ferrous IDO1<sup>98</sup>. Taken together, these findings strongly indicate that apoxidole-1 binds and stabilizes apo-IDO1 upon thermal denaturation. Additionally, free hemin dose-dependently reduced the potency of apoxidole-1 in the cellular Kyn assay, indicating that hemin and apoxidole-1 compete for the same binding site.

Target engagement in cells was demonstrated using CETSA. Pre-treatment of the cells with the heme synthesis inhibitor succinylacetone was crucial to observe a thermal shift  $\Delta T_m$  of  $7.9 \pm 0.6^\circ\text{C}$  upon compound treatment. Since the affinity of heme to its apo-protein is generally very high with  $K_D$  values in the pico- to femto-molar range<sup>259</sup>, hemoproteins normally only exist in their holo-form within the cell. *In vitro* experiments showed that apoxidole-1 indeed induces heme loss, but high concentrations and long incubation times were required. Therefore, by inhibiting the heme biosynthesis, it was assured that apo-IDO1 was the pre-dominant protein form in the cells. This enabled the detection of the thermal shift after only 15 min of compound treatment. Certainly, longer incubation times could have led to the observed thermal shift, but then the advantage of the CETSA technology, namely the detection of rapid target engagement within the cellular context, would have been lost. Interestingly, holo-IDO1 displays higher thermal stability compared to apo-IDO1, demonstrating that both heme cofactor and ligand binding stabilize the protein.

Ultimately, the binding pose of apoxidole-1 to IDO1 was determined by means of a co-crystal structure (pdb 8abx). Similar to the well-characterized apo-IDO1 inhibitor BMS-986205 (Figure 65A), apoxidole-1 binds into the heme-binding pocket in the catalytic site of IDO1, ranging to sub-pockets A and D. The compound is stabilized mainly by hydrophobic interactions and an additional polar interaction between His346 and the carbonyl oxygen of the ethyl ester of apoxidole-1 (Figure 65B). This His residue coordinates to the proximal site of the heme in

## Discussion

holo-IDO1 (Figure 65C) and is an important hydrogen bond donor for most of the apo-IDO1 inhibitors (pdb 6dpr, 8abx, 6e43, 6azv, 6wjy, 6v52, 6wpe).

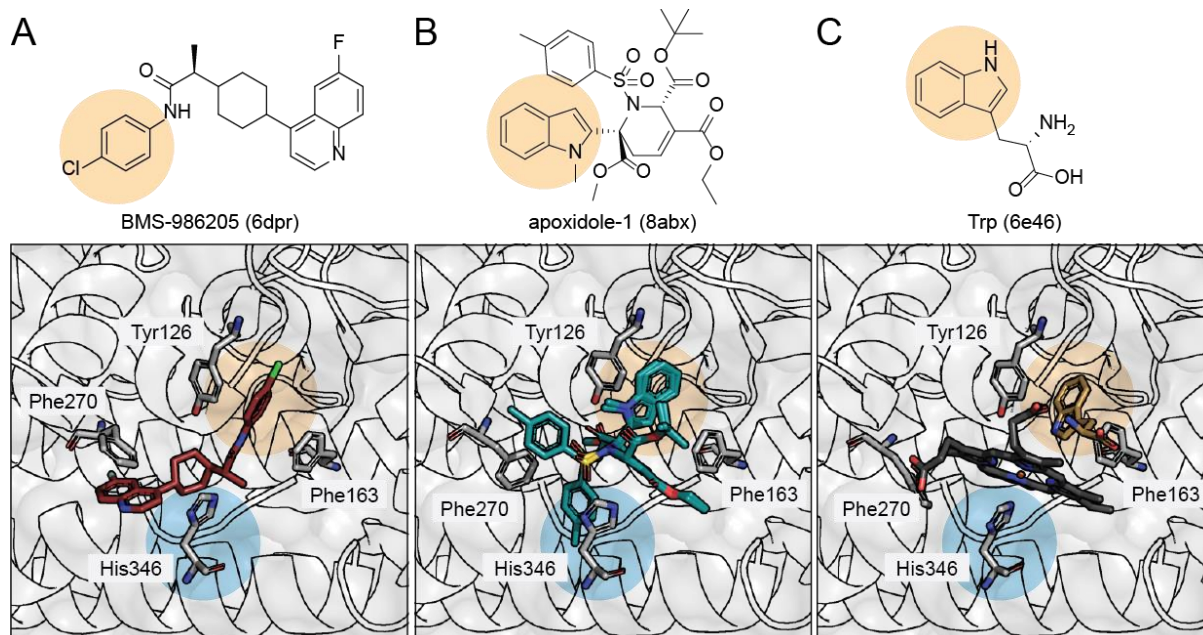


**Figure 65:** Structures of apo-IDO1 inhibitors bound to IDO1. A-C) Upon binding to apo-IDO1, BMS-986205 (A, pdb 6dpr, red sticks) and apoxidole-1 (B, pdb 8abx, teal sticks) are stabilized like heme (C, black sticks) and Trp (C, brown sticks) in Trp-bound ferrous IDO1 (C, 6e46). The hydrogen bond donor His346 is highlighted in blue, the  $\pi$ -stacking interactions with residues Tyr126 and Phe163 are highlighted in orange.

With the crystal structure, some of the observed trends from the SAR are elucidated. The combination of the stereogenic centers at  $R^1$  and  $R^3$  determine the three-dimensional structure of apoxidole-1, leading to a favorable orientation of the aromatics within the binding pocket so that they can interact with the surrounding hydrophobic amino acids. The stereocenters guide the indole of apoxidole-1 into pocket A, where it is stabilized through  $\pi$ -stacking interactions with residues Tyr126 and Phe163 (Figure 65B). The indole occupies the same position as the indole of the IDO1 substrate Trp when it is bound to the distal site of the heme (Figure 65C)<sup>264</sup>. In the ligand-free state, Phe163 closes pocket A, but in both Trp- and apoxidole-1-bound states, it moves apart to enable ligand binding. The catalytic center is closed by Arg231, Ile354 and Leu384 upon compound binding (Figure 66C). This explains why no larger substituents instead of the ethyl and tert-butyl ester in  $R^3$  and  $R^4$  position were tolerated: Bigger groups would clash with the aforementioned amino acids or other residues of the J helix.

Compared to other type IV apo-IDO1 inhibitors, apoxidoles stand out with a unique chemotype. Most of the co-crystallized type IV inhibitors are phenylureas (pdb 6azv, 6e43) or structurally similar to BMS-986205 (pdb 6dpq, 6dpr, 6mpq6, 6wpe, 6azw, 6wjy, 6v52). Apoxidoles instead combine indole and THP fragments, with the indole binding to pocket A and the THP covering the heme-binding site. Interestingly, some holo-IDO1 inhibitors contain

## Discussion

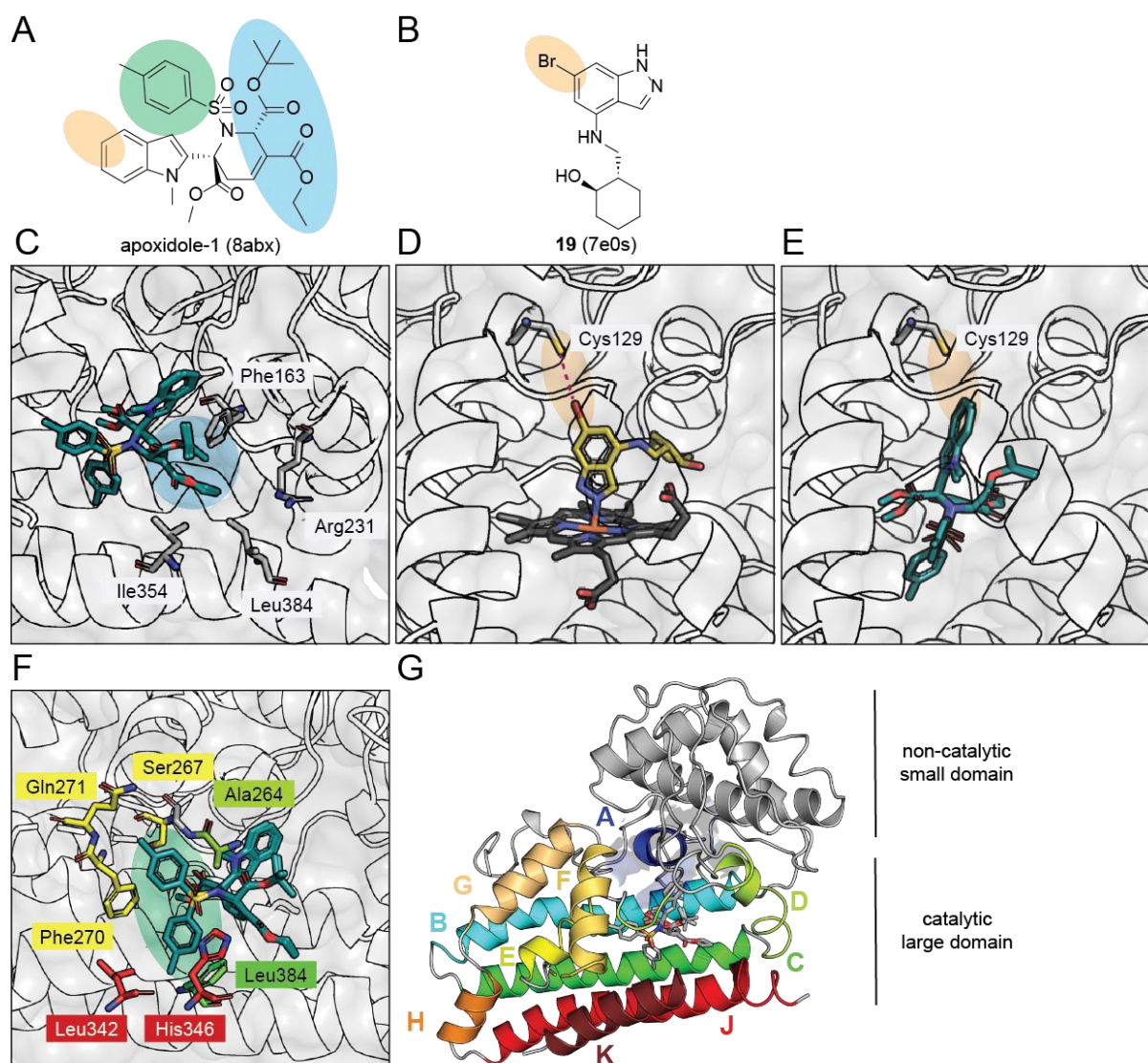


**Figure 66:** Structures of IDO1 inhibitors bound to IDO1. A-B) Structures of the apo-IDO1 inhibitor apoxidole-1 (A) and the indazole-based holo-IDO1 inhibitor **19** (B). Structure elements shown in C, D-E and F are highlighted in blue, orange and green, respectively. C) The ester groups of apoxidole-1 (teal sticks, pdb 8abx) are surrounded by residues Phe163, Arg231, Ile354 and Leu384 that close the IDO1 active site. D) Hydrogen bond between the bromine of indazole **19** (yellow sticks, pdb 7e0s) and Cys129. E) Orientation of the indole of apoxidole-1 (teal sticks) towards Cys129. F) Amino acids surrounding the tosyl group of apoxidole-1 (teal sticks, both conformations are shown). The residues are color-coded according to structure elements of IDO1 as depicted in G. G) Secondary structure elements of apoxidole-1-bound IDO1. The small domain of IDO1 is shown in grey. The eleven helices A to K of IDO1's large domain are highlighted in rainbow colors.

indoles (pdb 5whr, 6pz1) or indazoles (pdb 7e0s, 7e0t, 7e0u) that compete with the IDO1 substrate Trp for coordination to the distal heme site. All of these inhibitors have a halogen substituent in 5- or 6-position and in some structures, it has been shown to form a polar interaction with Cys129 (Figure 66D)<sup>264</sup>. Considering this, the affinity of apoxidole-1 for IDO1 could even be improved by adding a halogen in the 5-position of the indole to introduce an H bond (Figure 66E).

## Discussion

The *para*-toluene substituent on the sulfonyl group in R<sup>2</sup> can occupy two different conformations (Figure 66F), with one of them ranging into pocket D proximal of the heme-binding site. The tosyl group has the optimal size to fit into this hydrophobic area and points into the direction of the solvent and gas channel between helices E and F. Substituents in *ortho* or *meta* position would clash with helices DE2 and E (Figure 66F-G, Ala264, Ser267, Gln271, Phe270) or C and J (Figure 66F-G, Leu342, His346, Leu384). Smaller groups at this position, such as a methyl group, are too small to interact with the hydrophobic residues of the catalytic site.

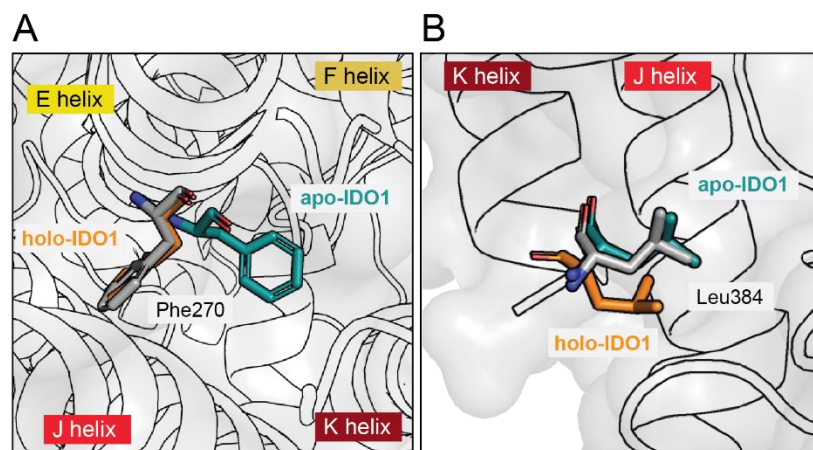


**Figure 67:** Comparison of holo- and apo-IDO1 structures. A) Conformation of Phe270. In apo-IDO1 (teal sticks, pdb 6e43), Phe270 covers pocket D; whereas Phe270 is in an open conformation in holo-IDO1 (orange sticks, pdb 7e0s) and the here described co-crystal structure (grey sticks, pdb 8abx). Helix H is omitted for clarity. B) Conformation of Leu384. In the here described crystal structure and apo-IDO1 (gray and teal sticks, pdb 8abx and 6e43), Leu384 moves into the free heme-binding pocket. In holo-IDO1 (orange sticks, pdb 7e0s), Leu384 points out of the pocket. The helices are color-coded according to structure elements of IDO1 as depicted in Figure 66G.

In contrast to previously published structures of apo-IDO1 inhibitors (pdb 6dpq, 6azv, 6azw, 6e43, 6v52, 6wpe, 6wjy, 6x5y, 7m63), Phe270 of apoxidole-1-bound IDO1 adopts a conformation where the solvent and gas channel between helices E and F is open (Figure 67A). The space occupied by Phe270 in other IDO1 structures is normally occupied by the heme cofactor for holo-IDO1 (pdb 2d0t, 6e42, 6f0a, 6kw7, 7ah6, 7e0s) or in case of apoxidole-1, by the tosyl group. Leu384 on the other hand has the same conformation as in published structures of apo-IDO1 (Figure 67B). Due to the missing heme, the K helix slightly moves towards the catalytic site, with Leu384 pointing towards the heme-binding site instead of helix J. As in most structures of apo-IDO1 inhibitors, the JK loop is not resolved, indicating high flexibility. Depending on the presence and type of the ligand, it can adopt an open or closed confirmation. For instance, with the IDO1 substrate Trp bound, the loop closes the active site and stabilizes Trp by formation of a hydrogen bond<sup>264</sup>. However, none of the apo-inhibitors seem to interact with this loop.



## Discussion

### 6.1.4 Selectivity for IDO1 over TDO and IDO2

The apo-IDO1 inhibitors apoxidole-1 and BMS-986205 did not impair the catalytic activity of TDO or IDO2, whereas the type II holo-IDO1 inhibitor epacadostat also inhibits the two other Trp-catabolizing enzymes. Despite all of these enzymes catalyze the same reaction, IDO1 only shares 16% and 43% sequence identity with TDO and IDO2, respectively<sup>179, 180</sup>. IDO1 and IDO2 are encoded by homologous genes, but they seem to have distinct functions, expression patterns and kinetics<sup>36</sup>. Even though the active site of human IDO2 is composed of the residues required for catalysis, IDO2 is substantially less active than IDO1 with a 325-fold increased  $K_m$  value for Trp<sup>180, 181</sup>. Its expression is mainly restricted to some tissues, such as the kidney, liver or APCs, but it has also been found to be expressed at low levels in some cancer types<sup>181</sup>. While TDO and IDO1 are well studied, the role of IDO2 is yet not completely understood, but it might be involved in the regulation of proinflammatory B cell response<sup>36</sup>. Similar to IDO1, TDO is expressed in human tumors<sup>180</sup>. Compared to IDO1, TDO has a higher substrate specificity and similar catalytic properties<sup>182</sup>. TDO has been shown to be resistant to apo-inhibitors<sup>180</sup>, which the results of this work also demonstrate. Models of published inhibitors of IDO2 suggest that they target the holo-protein<sup>265</sup>, thus the basis from the literature on apo-IDO2 inhibition is missing. However, the results for apoxidole-1 suggest that type IV inhibitors are also selective for IDO1 over IDO2.

The type II inhibitor epacadostat reduced the activity of both TDO and IDO2. Epacadostat binds to the distal heme site of ferrous IDO1, with its hydroxyamidine group competing with oxygen for the coordination to the iron atom and thereby, preventing both oxygen and Trp binding<sup>87, 264</sup>. Since the recruitment of oxygen and Trp to the heme cofactor is crucial for the catalysis of all three Trp-catabolizing enzymes, it is plausible that epacadostat inhibits to a certain extent all three proteins by this mechanism.

In summary, apoxidoles represent a novel type IV IDO1 inhibitor chemotype. Unlike other apo-IDO1 inhibitors, it combines features of holo-IDO1 inhibitors with heme displacement, leading to unique features in the protein structure. Once apo-IDO1 inhibitors have bound to their target, they mimic irreversible inhibition with slow off-rates and higher target occupancy compared to holo-inhibitors<sup>260</sup>. Additionally, they are selective for IDO1 over TDO and IDO2. However, the administration of dual- and pan-inhibitors might be necessary to oppose the compensatory expression of TDO and IDO2 in the TME upon inhibition of IDO1<sup>266</sup>. Furthermore, it is unclear whether apoxidoles or other apo-IDO1 inhibitors activate the AhR. This has been reported for epacadostat, which in turn induced DC-mediated long-term tolerance in the TME and resistance to IDO1 inhibition<sup>102</sup>.

## 6.2 Epoxykynin sEH Inhibitors as Potent Kyn Pathway Modulators

### 6.2.1 Kyn Pathway Inhibition and Structure-Activity Relationship

Similar as for the apoxidoles, epoxykynin's ability to decrease cellular Kyn levels was validated manually and with an orthogonal readout. Epoxykynin inhibited Kyn production in both HeLa and BxPC-3 cells with  $IC_{50}$  values of  $13.0 \pm 1.2$  nM and  $33.4 \pm 1.1$  nM, respectively. The  $IC_{50}$ s are consistent with the value obtained from the automated Kyn assay with  $36.0 \pm 15.0$  nM. Furthermore, epoxykynin has no influence on the IDO1 enzymatic activity as demonstrated by the *in vitro* Kyn assay. Thus, IDO1 is not the target responsible for Kyn reduction.

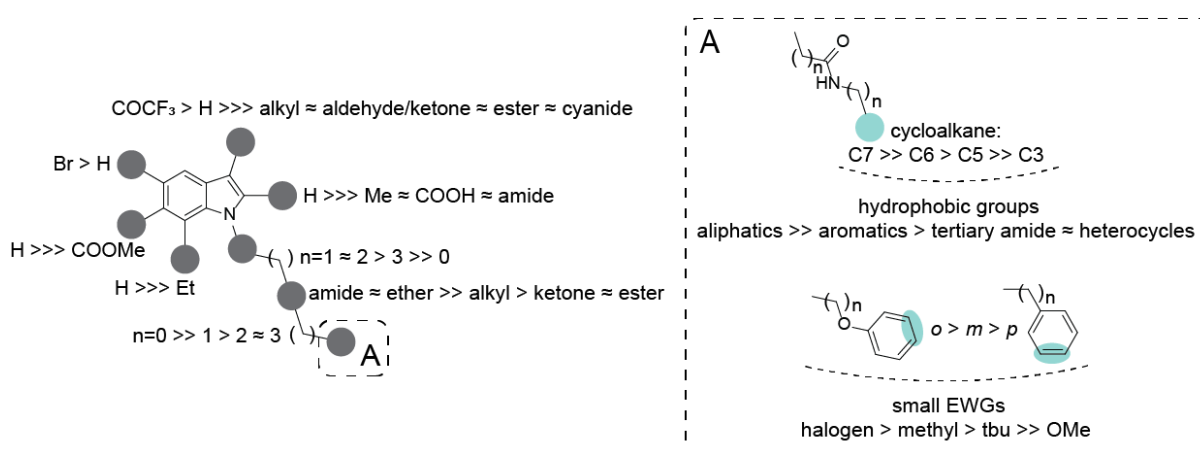


**Figure 68:** Condensed structure-activity relationship (SAR) for the N-substituted indole compound class. N-substituents are shown in A. EWG: electron-withdrawing group, o: ortho, m: meta, p: para.

96 epoxykynin derivatives were tested in the automated Kyn assay to explore the SAR (Figure 68). 22 compounds potently inhibited Kyn production with  $IC_{50}$ s below 2  $\mu$ M and 59 derivatives were poor inhibitors with  $IC_{50}$ s greater than 10  $\mu$ M. While there are multiple different substituents on the indole nitrogen, there is no derivative with modifications at the 4-position. The R<sup>2</sup> and R<sup>3</sup> positions only include an ethyl group and a methyl ester as modifications, which diminish the activity. A bromine in R<sup>4</sup> generally improves the compound's potency compared to the hydrogen. For the R<sup>5</sup> position, the presence of the trifluoro acetyl group is crucial for the compound's activity. There are several modifications in this position, for instance various ketones, alkyls or esters, that lead to increased  $IC_{50}$ s of 2  $\mu$ M or higher. The trifluoro ketone might act as a covalent warhead for cysteine residues close to the compound's binding site, as demonstrated for covalent inhibitors of the FGFR4 kinase<sup>267</sup>. The differences in activities of epoxykynins is mainly driven by the different N-substituents at R<sup>1</sup> position. Ether and amide groups with lipophilic moieties provided the most potent compounds, indicating that the binding site of the compound on the protein might be inside a hydrophobic pocket.

### 6.2.2 Identification of the Molecular Target of Epoxykynin

Epoxykynin was further characterized to evaluate IDO1 expression and protein levels, the IFN- $\gamma$  stimulus and Trp uptake. It became apparent that upon treatment with epoxykynin, none of

## Discussion

these cellular processes involved in the Kyn pathway were modulated. Therefore, the target of epoxykynin might mediate Kyn level reduction by a novel, maybe unprecedented mechanism. Hence, proteome-wide target identification strategies were employed to unravel epoxykynin's MMOA.

The first method used was global proteome profiling which gives a general overview of proteins and pathways that might be regulated upon compound treatment. In this experiment, three conditions were compared: i) DMSO in the absence of the stimulus IFN- $\gamma$ , ii) DMSO in the presence of IFN- $\gamma$  and iii) epoxykynin in the presence of IFN- $\gamma$ . In all samples, 4992 proteins were identified which covers a quarter of the predicted proteins encoded by the human genome<sup>268</sup>. This represents a good coverage of the proteome for quantitative proteomics, since not all proteins can be discovered upon tryptic digestion. To identify a protein, it must have at least two unique peptides after digestion, each optimally 7-30 amino acids in length<sup>269</sup>. This leaves particularly small proteins or proteins that have few trypsin cleavage sites undetected. Alternatively, samples can be treated with a second protease for double digestion to improve the coverage of the proteome<sup>269</sup>. Furthermore, only soluble proteins can be detected in proteomics, which facilitates the identification of cytosolic proteins. Membrane proteins, proteins that get secreted into the extracellular space or low-abundant proteins often remain undetected<sup>270</sup>.

Using the Interferome database<sup>271</sup>, the identified proteins were analyzed for regulation by different IFNs. With 4,617 proteins, almost all detected proteins are expressed under so-called IFN-regulated genes (IRGs, Figure 69). Since IFNs are a large pleiotropic class of cytokines mediating cell signaling especially in response to viral infections<sup>272</sup>, it comes as no surprise that many genes are under transcriptional control of IFNs. Generally, IFNs can be classified by the type of receptors which they bind to and, hence, sub-divided into type I IFNs, including IFN- $\alpha$  and - $\beta$  (and the poorly defined IFNs  $\epsilon$ ,  $\kappa$ ,  $\tau$ ,  $\delta$ ,  $\omega$  and  $\zeta$ ), type II IFN- $\gamma$  and type III IFN- $\lambda$ <sup>273</sup>. While IFN types I and III can be expressed in almost all cell types, IFN- $\gamma$  expression is mainly restricted to T cells and NK cells upon stimulation with macrophage-derived IL-12<sup>274</sup>. For the proteome profiling, IFN- $\gamma$  was used to induce the Kyn pathway. As expected, all of the 4,617 detected IRGs can be regulated by IFN- $\gamma$ , with 970 genes responding to IFN- $\gamma$  only (Figure 69). The expression of 3,256 genes can be modulated by both type I and II IFNs, whereas only eight IRGs are regulated by type II and type III IFNs. 113 IRGs are under the control of all three IFN types.

## Discussion

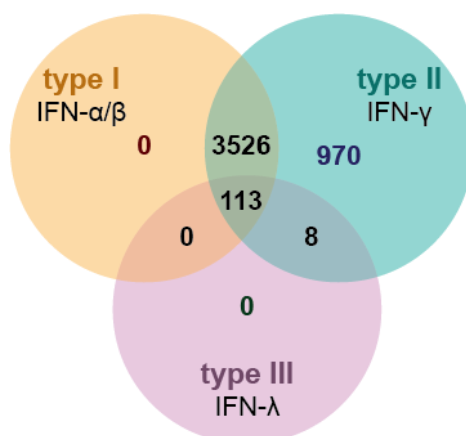


**Figure 69:** Venn diagram for IFN-regulated genes<sup>271</sup> identified in the global proteome profiling.

The expression of 84 proteins was significantly altered upon treatment with IFN- $\gamma$ . Among the upregulated proteins were proteins connected to the Kyn pathway. For instance, stimulation of the cells for 24 h was sufficient to increase IDO1 and TrpRS levels by 7.8- and 6.6-fold, respectively, whereas KYNU was not significantly upregulated. These findings are in line with data from the literature, in which expression of the IDO1 protein in BxPC-3 cells can be detected on immunoblots already 8 h after induction<sup>155</sup>, but KYNU expression is regulated by IFN- $\gamma$  to a much lesser extent<sup>275</sup>. Additionally, several other proteins which are known to be responsive to IFN- $\gamma$  were either upregulated, e.g. multiple isoforms of GBPs<sup>276</sup>, or downregulated, such as ZNF706 and UBE2C<sup>277</sup>. Enrichment analyses revealed that the modulated proteins belong to acute inflammatory and immunological stimulus response pathways, hence proving that IFN- $\gamma$  is suitable to induce the Kyn pathway.

In cells treated with IFN- $\gamma$  and epoxykynin the levels of the proinflammatory cytokines CXCL9, CXCL10, IL1A and IL1B were altered in comparison to cells treated with IFN- $\gamma$  and DMSO. While the CXC family chemokines were even more upregulated than for IFN- $\gamma$  only, the levels of the two interleukins were decreased instead. Interestingly, epoxykynin not only opposes the effect of IFN- $\gamma$  on the IL1A and IL1B expression, but also for 14 other proteins. However, most of the regulated proteins are as well connected to inflammatory response pathways by means of the overrepresentation analyses. One exception is the LC3B protein (MAP1LC3B) which was 3.8-fold downregulated upon treatment with epoxykynin. LC3B is a key player of autophagy, where it mediates the generation of autophagosomes<sup>278</sup>. However, decreased LC3B levels have been shown to be compensated by relocation of other members of the LC3 family, especially LC3C<sup>279</sup>. Epoxykynin was tested for autophagy inhibition by COMAS and reduced autophagy by 36% at 10  $\mu$ M. Thus, the moderate autophagy inhibition might be correlated to lower levels of LC3B and the subsequent partial rescue by other LC3 proteins.

Taken together, 92.5% of all identified proteins are IRGs responsive to IFN- $\gamma$ . Therefore, the analysis of pathways modulated by epoxykynin is hindered by the dominating effect of the

## Discussion

stimulus. For that reason, no target hypothesis could emerge from the global proteome profiling. Alternatively, cells endogenously expressing IDO1, such as the SKOV-3 cells, could be employed to reduce the high background of the IFN- $\gamma$  response. Nonetheless, proteome profiling might provide information about the pathways being regulated upon compound treatment. Thereby, it can be challenging to pinpoint the compound's direct target from this setup. Consequently, TPP in HeLa cell lysate pre-treated with IFN- $\gamma$  was applied to determine potential binding partners of epoxykynin.

In total, 6,474 proteins were detected in the TPP, of which 38 proteins displayed a difference in the thermostability upon treatment with. Except for SURF1, all proteins were stabilized by epoxykynin. Because small molecule binding introduces hydrophobic or polar interactions that can influence the flexibility of the binding region, most proteins become rigidified upon compound binding. This causes a decrease in entropy and the higher ordered protein-small molecule complex requires more energy, i.e. higher temperatures, for thermal denaturation compared to the protein alone<sup>280</sup>. Hence, most proteins have a positive shift in the melting temperature upon small molecule binding as observed in the TPP. Accordingly, proteins that do not show a ligand-induced shift in the melting temperature, such as intrinsically disordered proteins, cannot be identified as targets in TPP.

Among the proteins that were stabilized upon epoxykynin treatment was HMOX1. While the second isoform HMOX2 is constitutively expressed in certain tissues, the expression of HMOX1 as an important cellular antioxidant is under the control of antioxidant or stress response elements (*ARE* and *StRE*) and can be induced by stress stimuli, such as oxidants, pro-inflammatory molecules and the HMOX1 substrate heme (Figure 70). By catalyzing the first, rate-limiting step of heme degradation, HMOX1 regulates iron and redox homeostasis in macrophages, DCs and T cells during inflammation<sup>281</sup>. Most of the full-length protein with the C-terminal TMS is tethered to the ER, where it oligomerizes and faces into the cytosol<sup>213, 282, 283</sup>. It also has been found to be anchored in membranes of the mitochondria, Golgi apparatus and caveolae to a lesser extent<sup>213, 283</sup>. After proteasomal cleavage of the TMS, truncated HMOX1 is re-located into the nucleus and cytosol<sup>213</sup>. Both full-length and truncated forms are catalytically active, but oligomerization within the ER seems to increase the enzymatic activity<sup>213</sup>. Since IDO1 is a heme-containing enzyme, small molecule-induced degradation of heme by HMOX1 might be the MMOA of epoxykynin.

## Discussion

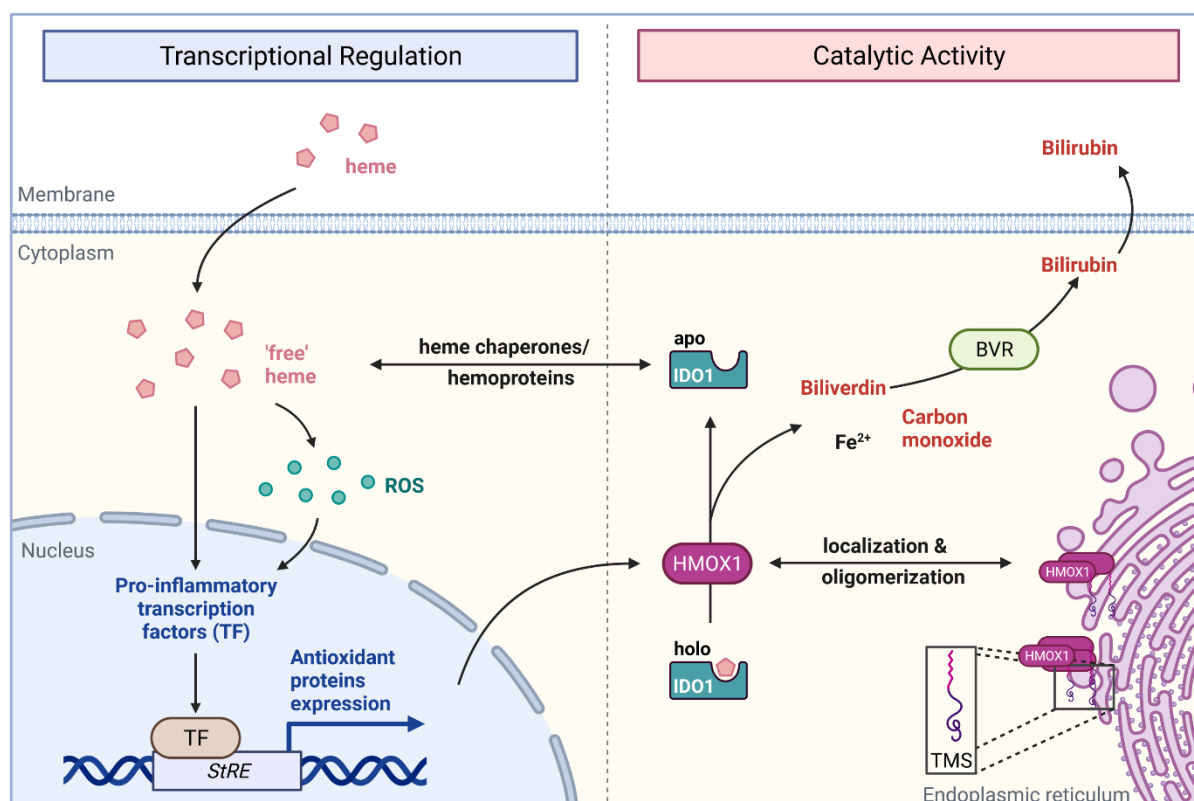


**Figure 70:** Regulation of HMOX1. The expression of HMOX1 can be upregulated by oxidative cellular stress stimuli, such as free heme, by induction of pro-inflammatory transcription factors (TF) that activate *ARE*- or *StRE*-mediated gene expression. Full-length HMOX1 is anchored to membranes by a C-terminal transmembrane segment (TMS) and can oligomerize. Truncated HMOX1 lacking the TMS can be located in the nucleus or cytoplasm. HMOX1 catalyzes the ring opening of heme *b* to form ferrous iron, biliverdin IX $\alpha$  and carbon monoxide. Biliverdin can be further metabolized by biliverdin reductases (BVRs) to yield bilirubin IX $\alpha$ . Figure was created with BioRender.com. ROS: reactive oxygen species, *ARE*: antioxidant response element; *StRE*: stress response element.

A second method that was employed to determine direct binding partners of epoxykynin was affinity-based chemical proteomics. For this approach, affinity and control chemical probes were designed based on epoxykynin and the inactive derivative **2r**, with a PEG-amine linker instead of the bromine at R<sup>4</sup> position. To reduce the hydrophobicity of the linker, PEGs are commonly applied instead of aliphatic linkers. As expected, the control probe did not reduce cellular Kyn levels, while the positive probe decreased Kyn levels by  $76.3 \pm 1.2\%$  at 20  $\mu\text{M}$ . The affinity probe is significantly less potent than epoxykynin regarding Kyn reduction. However, reduced potency was expected, since the SAR showed that the bromine is required for compound activity. Furthermore, attachment of the linker drastically increases the molecular weight of the small molecule which can affect the diffusion across the cell membrane. As the pull-down is performed in cell lysates, the limited cell permeability does not have a negative impact on the assay setup. During the pull-down, only MTAP, SEH1L and sEH were selectively enriched by the active affinity probe **3b**, while nine proteins were enriched by the control probe **4b**. The low number of identified proteins indicates that the washing steps

## Discussion

were stringent and removed low-affinity interactors. Since the control probe did not reduce Kyn levels, these proteins also are less likely to mediate the Kyn pathway inhibition by epoxykynin.

Altered methylthioadenosine metabolism due to MTAP deficiency can be found in various malignancies and the lack of MTAP creates sensitivity to inhibitors of protein arginine N-methyltransferase 5 (PRMT5) and its adaptor proteins<sup>284</sup>. MTAP cleaves methylthioadenosine (MTA) into 5-methylthioribose-1-phosphate (MTR-1-P) and adenine, which can be used to salvage methionine and adenosine triphosphate (ATP), respectively (Figure 71)<sup>197</sup>. MTAP also seems to have immunological functions, since T cells are strongly inhibited by MTA which accumulates in the TME of MTAP-deficient cancer cells<sup>285</sup>.

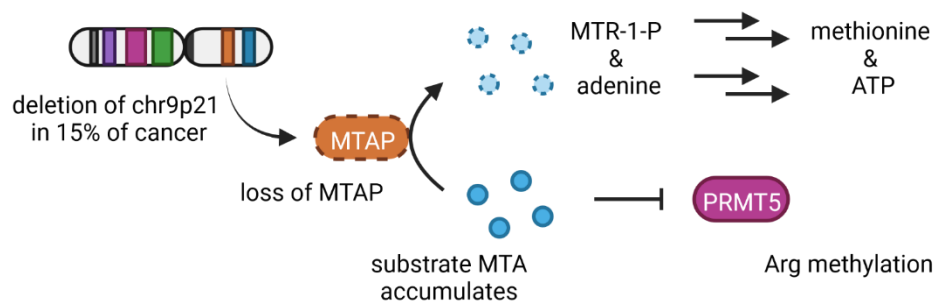


**Figure 71:** MTAP deficiency in cancer cells leads to accumulation of its substrate MTA, which creates vulnerability against PRMT5 targeting. Furthermore, the salvaging of adenine, methionine and ATP is impaired. Figure was created with BioRender.com. MTAP: S-methyl-5'-thioadenosine phosphorylase; MTA: methylthioadenosine; PRMT5: protein arginine N-methyltransferase 5; MTR-1-P: 5-methylthioribose-1-phosphate; ATP: adenosine triphosphate.

SEH1L is one out of nine components of the Nup107-160 subcomplex which is also known as Y complex due to its characteristic shape<sup>286</sup>. The Nup107-160 complex is essential for the assembly of nuclear pore complexes (NPCs)<sup>195</sup> that are large multi-protein structures consisting of approximately 30 different nucleoporins and NPC-associated proteins. NPCs control the transport of macromolecules between the cytosol and the nucleus across the nuclear envelope<sup>196</sup>. The Nup107-160 complex in particular plays a major role during mitosis by targeting kinetochores and spindles in a highly dynamic manner<sup>287</sup>.

sEH is a bifunctional enzyme consisting of a C-terminal fatty acid epoxide hydrolase (sEH-H) and an N-terminal lipid phosphatase (sEH-P), connected by a proline-rich linker<sup>198</sup>. While the role of the phosphatase domain is still elusive to date, the hydrolase domain has been intensively studied since its discovery in 1972<sup>288, 289</sup>. Epoxides, derived from endogenous metabolism and exogenous sources, are ubiquitous molecules containing a highly polarized oxygen-carbon bond<sup>290</sup>. sEH-H is a member of the CYP epoxygenase branch of the arachidonic acid (AA) pathway and converts epoxy fatty acids into the respective dihydroxy fatty acids (Figure 72)<sup>199</sup>.

## Discussion

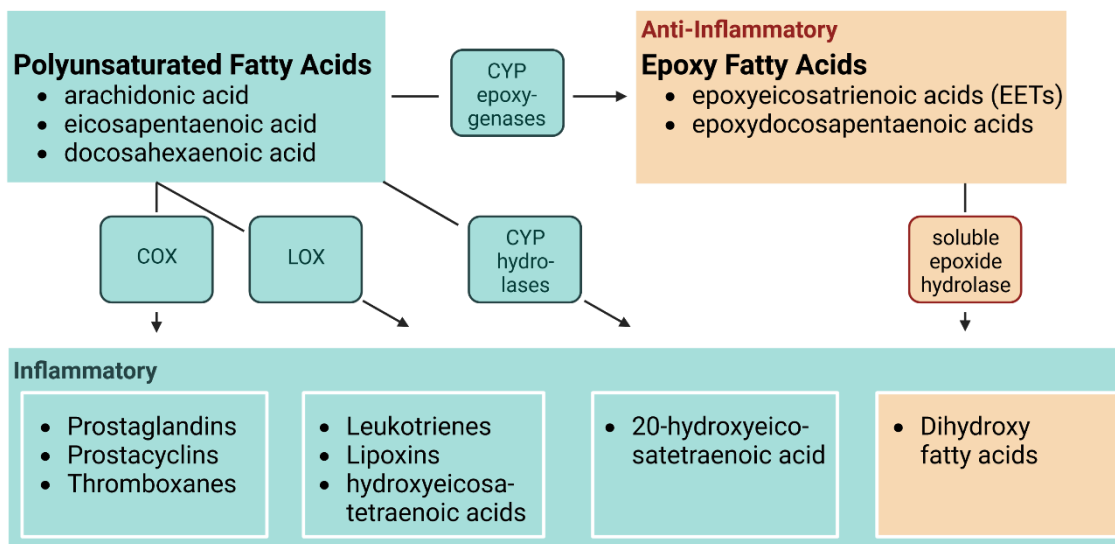


**Figure 72:** Metabolism of polyunsaturated fatty acids (PUFAs). The soluble epoxide hydrolase (sEH) catalyzes the hydrolysis of epoxyeicosatrienoic acids (EETs) and epoxydocosapentaenoic acids into the respective vicinal diols. Figure was created with BioRender.com. CYP: cytochrome P450; COX: cyclooxygenase; LOX: lipoxygenase.

Since the metabolism of polyunsaturated fatty acids (PUFAs) is associated with different diseases<sup>291-294</sup>, several classes of sEH inhibitors<sup>291-294</sup> have been developed that mimic the epoxide substrates. Especially ureas, carbamates and amides are used to target sEH-H directly<sup>295, 296</sup> and also to inhibit synergistic proteins of the other two major AA cascade branches by means of dual inhibitors<sup>297, 298</sup>.

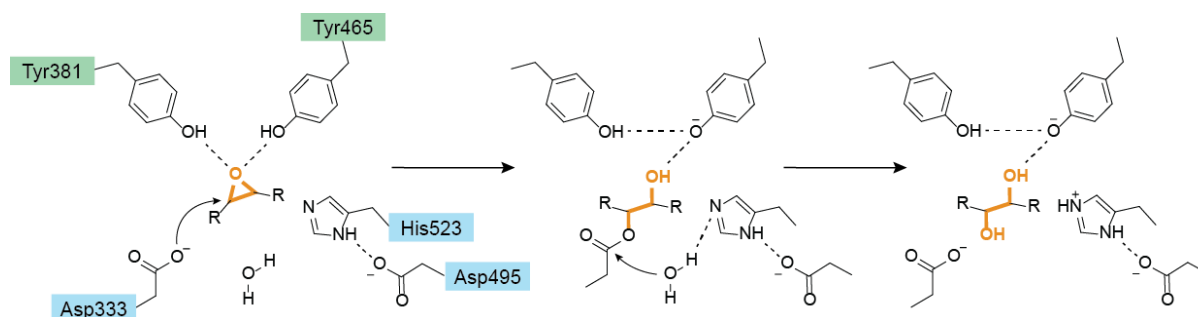


**Figure 73:** The two-step enzymatic hydrolysis of epoxides as catalyzed by sEH. In the first step, activated Asp333 forms a covalent bond with the epoxide. In the second step, the ester is hydrolyzed. The epoxide, the catalytic triad and the stabilizing residues are depicted in orange, blue and green, respectively.

The hydrolysis of epoxides by sEH-H is catalyzed by the catalytic triad Asp333-Asp495-His523 and supported by the two stabilizing residues Tyr381 and Tyr465 (Figure 73). The Tyr residues are located on the opposite site of the catalytic triad and form H-bonds to the oxygen of the epoxide, thereby serving as an oxyanion hole. The nucleophile Asp333 is activated by His523 and Asp495 and attacks the least sterically hindered carbon of the oxirane ring, leading to a ring opening and formation of a covalent enzyme-substrate  $\alpha$ -hydroxyester. In a second step, a conserved water molecule inside the catalytic site gets activated by His523 and Asp495 and



## Discussion

attacks the carbonyl carbon of the ester intermediate. Thus, the ester is hydrolyzed and the diol is released from the active site<sup>299, 300</sup>.

The CRAPome database<sup>201</sup> provides information on if the three potential target proteins represent *bona fide* interactors or if they are prone to appear as non-specific interactors. Even though a control probe was used to exclude proteins binding to the solid support, i.e. the surface of the magnetic beads, the identified proteins still might non-specifically bind to the affinity probe. Gratifyingly, sEH (EPHX2) was not found in any of the 716 affinity control experiments listed in CRAPome, whereas MTAP and SEH1L were found in 50 and 76 of 716 control experiments, respectively. Generally, nucleoporins and NPC proteins are frequent hitters in affinity pulldowns. Some of these proteins can be identified in 30% of all 716 control experiments, such as Nup214 or nucleoprotein TPR<sup>200, 201</sup>. When looking at the LFQ intensity values (Table S8 and Table S9), MTAP and SEH1L were also found to bind to the control probe with high prevalence. In contrast, sEH did not bind to the negative control in all experimental replicates. Therefore, sEH can be ranked as most significant hit among the three identified proteins for the affinity pulldown. Nevertheless, MTAP was also investigated as potential target of epoxykynin.

Additionally, three target prediction tools were applied to computationally investigate epoxykynin. Based on chemical similarity, these tools relate a small-molecule structure to potential protein targets according to their known ligands<sup>203, 205, 207</sup>. Some predicted targets were also detected in the TPP, namely mEH (EPHX1), NF- $\kappa$ B, malonyl-CoA decarboxylase and DNA topoisomerase 2- $\alpha$ , but they did not show a compound-induced shift in the thermostability. Additionally, mEH was identified in the affinity pulldown, yet it was not selectively enriched by either of the probes. All three tools predicted CB1 and CB2 receptors (CNR1 and CNR2) as well as mEH (EPHX1) to be possible targets of epoxykynin. As expected, the reference ligands differ for the three proteins. However, they have some common features, as they contain hydrophobic groups, such as adamantanes, basic nitrogens, e.g. piperidines, and trifluoro methyl or acetyl groups as electron-withdrawing groups. In contrast to the mEH ligands, all CB1 and CB2 receptor binders are composed of heterocycles.

CB1 and CB2 receptors are GPCRs of the endocannabinoid system that have 68% sequence identity in their transmembrane residues<sup>208</sup>. While the CB1 receptor is mainly expressed in the central nervous system, the CB2 receptor is prevalent on immune cells<sup>210</sup>. Both receptors bind hydrophobic ligands, such as endo- and plant cannabinoids, although they display different ligand selectivity<sup>209, 210</sup>. To test whether CB1 and CB2 receptor ligands affect Kyn levels, the reverse agonists rimonabant and otenabant for CB1 and BML-190 and SR144528 for CB2

## Discussion

were tested in the Kyn assay. Additionally, it was investigated if epoxykynin and any of these compounds have additive or synergistic effects on Kyn level reduction. Only two out of four compounds reduced cellular Kyn levels: rimonabant potently abolished cellular Kyn production with an  $IC_{50}$  value of  $80.5 \pm 11.5$  nM, whereas BML-190 displayed weak inhibition with an  $IC_{50}$  greater than 10  $\mu$ M. Since BML-190 is structurally similar to epoxykynin, Kyn level reduction may be mediated by the same MMOA. Furthermore, there was no additive effect on Kyn reduction when cells were co-treated with the CB receptor ligands and 10 nM epoxykynin. As only one ligand of each CB1 and CB2 receptors decreased Kyn levels, it is highly likely that the Kyn reduction is independent of CB receptor signaling. Although there is evidence that the CB and Kyn pathways are related<sup>301</sup>, the psychoactive CB receptor agonists  $\Delta^9$ -tetrahydrocannabinol (THC) and cannabidiol (CBD) have been shown to abolish IDO1 activity without CB receptor activation<sup>302</sup>. In line with these findings, rimonabant inhibited IDO1 in the enzymatic Kyn assay. The weak inhibition of the IDO1 enzymatic activity compared to the potent cellular inhibition suggests that rimonabant is an apo-IDO1 inhibitor.

Similar to sEH, mEH contributes to the detoxification of xenobiotic epoxides. Because they differ in cellular localization, with mEH being an ER-resident protein, it was long thought that both enzymes have distinct functions. However, it has now become apparent that mEH also hydrolyzes CYP epoxygenase-generated EETs to dihydroxyeicosatrienoic acids (DHETs)<sup>211</sup>. Because of the conserved catalytic triad and the overlapping substrate specificity of mEH and sEH<sup>211</sup>, it comes as no surprise that the compounds on which the target prediction is based on, are also known to bind to sEH<sup>212</sup>, such as the urea-based small molecules.

Taken together, the target predictions suggested CB receptors or epoxide hydrolases as potential targets of epoxykynin. Kyn inhibition by CB receptor ligands is highly likely to be independent of receptor signaling, thus, it can be concluded that CNR1 and CNR2 are not the targets of epoxykynin mediating Kyn level reduction. mEH did not show an epoxykynin-induced shift in its thermostability as well as no significant enrichment on either of the affinity pulldown probes. In contrast, sEH was identified as potential target by the affinity pulldown and is known to bind the same substrates and compounds as mEH. Thus, there is a high probability that sEH is a target of epoxykynin.

### 6.2.3 Target Validation Studies

To investigate potential target proteins of epoxykynin, functional assays, direct target engagement studies and chemical and genetic strategies were employed. In the following, the de-validation of HMOX1 and MTAP, as well as the validation of sEH as responsible target for Kyn level reduction are discussed.

## Discussion

### 6.2.3.1 HMOX1 as Potential Target of Epoxykynin

HMOX1 as highly inducible enzyme responsible for redox homeostasis can be located in different cellular compartments depending on whether the full-length protein is present or the TMS is cleaved. Related to its localization, HMOX1 has diverse functions regarding cellular signaling and also different sources for its substrate heme. In the TPP experiment, the different forms of HMOX1 could not be distinguished, but instead the total protein fraction was used to determine the epoxykynin-induced change in the thermostability. With CETSA, HMOX1 monomers and trimers could be detected. Because the presence of the TMS is associated with anchoring of HMOX1 to the ER membrane and subsequent oligomerization, the trimer most likely corresponds to membrane-bound HMOX1. However, it cannot be excluded that the monomer is also tethered to membranes. The TMS is formed by only 23 amino acids which corresponds to a small difference in molecular weight of only 2.5 kDa. Thus, the two species cannot be clearly distinguished with immunoblotting. Therefore, the  $T_m$  shifts for both HMOX1 monomer and trimer, as well as the total protein (to match the TPP experiment) were analyzed in lysate- and cell-based CETSA. Only the monomer fraction of HMOX1 showed a thermal destabilization upon compound treatment of  $\Delta T_m$  of  $-3.2 \pm 1.4^\circ\text{C}$  in the in-lysate CETSA. Considering the high standard deviation and that the TPP detected a positive  $\Delta T_m$ , this result does not significantly indicate target engagement. Also, in contrast to the TPP, heme was used to induce HMOX1 expression to a sufficient level for immunoblotting in the CETSA experiments. Because epoxykynin might bind to the same site as heme, in-cell CETSA with HEK293T cells that transiently express HMOX1-eGFP in the absence of hemin was performed. Nevertheless, also for this experimental setup, no target engagement could be detected. Protein expression using a plasmid generally leads to overexpression. Additionally, not the native protein, but a GFP-fusion protein was expressed. These two factors could lead to the fact that no target engagement could be detected in HEK293T cells.

The enzymatic activity of HMOX1 upon treatment with epoxykynin and hemin was evaluated in cells using a CO-labile dye in the presence of palladium. Carbon monoxide is a so-called gasotransmitter that almost exclusively originates from heme degradation and avidly coordinates to the iron of heme-containing enzymes<sup>303</sup>. Upon treatment with hemin, twice the amount of CO is generated by the cells. HMOX1 expression is mainly limited to macrophages, but can be induced in other cell types by stress stimuli<sup>281</sup>. Hence, the increase in CO levels corresponds to the expression of HMOX1 in the presence of hemin. The basal levels of CO can be attributed to HMOX2 which, in contrast to HMOX1, is constitutively expressed in all tissues at low levels<sup>281, 303</sup>. Treatment with epoxykynin slightly increased CO levels to  $163.3 \pm 37.5\%$  and  $118.1 \pm 6.1\%$  in the absence or presence of IFN- $\gamma$ , respectively. Compound treatment might generate cellular stress or ROS which in turn causes elevated

## Discussion

levels of CO. Even though epoxykynin did not show ROS induction after 90 min in the COMAS screening (6% ROS induction), it cannot be excluded that ROS are produced over a longer period. Co-treatment of hemin and epoxykynin increased CO levels  $2.5 \pm 0.5$ - and  $4.0 \pm 0.8$ -fold in the absence or presence of IFN- $\gamma$ , respectively. This demonstrates that co-treatment of epoxykynin and hemin generally has an additive effect on generated CO. This might be due to enhanced catalytic activity of HMOX1 or higher expression of HMOX1 due to increased stress stimuli. However, increased HMOX1 expression upon compound treatment was not detected in the global proteome profiling or on immunoblots, indicating that epoxykynin does not induce HMOX1 expression. A difference in produced CO regarding the IFN- $\gamma$  stimulus is detectable only upon co-treatment with hemin and epoxykynin. Because many proteins are regulated by IFN- $\gamma$ , it is challenging to explain the observed effect. A possible reason could be the increased expression of hemoproteins, such as IDO1, and therefore enhanced biogenesis of heme. Furthermore, according to the Interferome database<sup>271, 272</sup>, the *HMOX1* gene itself is an IRG responsive to IFN- $\alpha$  and IFN- $\gamma$ . However, the respective datasets show a downregulation of HMOX1 upon IFN stimulation in macrophages<sup>304, 305</sup> which contradicts to the observed trend in this experiment. Furthermore, if the IFN- $\gamma$  stimulus significantly altered the HMOX1 expression, different CO levels compared to unstimulated cells should have been detectable for all conditions. Furthermore, the less active and inactive derivatives **2m** and **2r**, as well as the IDO1 inhibitors BMS-986205 and epacadostat did not increase CO levels compared to hemin-treated cells. These results demonstrate that the modulation of HMOX1 is a compound-specific effect and not a side effect of IDO1 inhibition.

The bilirubin levels generated by cells were quantified as a second measure for HMOX1 catalytic activity. Because bilirubin is not a direct metabolite of HMOX1, but a product of the biliverdin reductase (BVR), this method monitors the HMOX1 activity indirectly. Similar to the CO detection, bilirubin levels were upregulated upon treatment with hemin, but not by epoxykynin. The combination of both hemin and epoxykynin increased the bilirubin concentration per  $10^5$  cells by  $1.0 \pm 0.2$   $\mu$ M and  $0.4 \pm 0.2$   $\mu$ M in the absence and presence of IFN- $\gamma$ , respectively. Even though the effect is small compared to the CO detection, it still suggests modulation of the HMOX1 enzymatic activity. In contrast to HMOX1, BVR expression is not inducible by hemin<sup>306</sup>. Therefore, BVR present in the cells may simply not be able to convert all the generated biliverdin in a timely manner. This is supported by the fact that elevated bilirubin levels were only observed after at least 48 h and that the effect becomes stronger over longer incubation periods.

To genetically validate HMOX1 as target of epoxykynin mediating Kyn level reduction, the Kyn assay was performed in HAP1 HMOX1 wt and KO cells. Surprisingly, epoxykynin did not decrease Kyn levels in both wt and KO cells, whereas the IDO1 inhibitor epacadostat potently

## Discussion

abolished Kyn production. This indicates that the protein responsible for the inhibition by epoxykynin is not expressed in HAP1 cells. However, HMOX1 is expressed in HAP1 cells as curated in databases<sup>218</sup> and detected on immunoblots.

Taken together, the increase of HMOX1 enzymatic activity suggested that HMOX1 is a target of epoxykynin. Nonetheless, the fact that epoxykynin is inactive in HAP1 cells expressing HMOX1 demonstrates that this protein is not the functional target for Kyn reduction. Still, it is possible that epoxykynin modulates HMOX1 in an off-target manner.

### 6.2.3.2 MTAP as Potential Target of Epoxykynin

Since MTAP emerged as a potential target protein from the affinity pulldown using a modified chemical probe, it is pivotal to also evaluate binding of the unmodified compound to the potential target protein. Therefore, target engagement of epoxykynin and MTAP was studied *via* CETSA. Treatment of HeLa cell lysate with epoxykynin did not induce a significant shift in the thermostability with  $\Delta T_m$  of MTAP of only  $0.5 \pm 1.5^\circ\text{C}$ . This value is consistent with the  $\Delta T_m$  for MTAP derived from the TPP which is at  $0.3 \pm 1.2^\circ\text{C}$ . Both experiments did not indicate direct binding of epoxykynin to MTAP. Even though MTAP was identified as potential target of epoxykynins by chemical proteomics, it might only engage with affinity probe **3b**, but not with epoxykynin.

The MTAP inhibitor MT-DADMe-ImmA was used to chemically investigate whether MTAP inhibition reduces Kyn levels. MT-DADMe-ImmA is a transition state analogue that mimics the ribooxacarbenium ion of MTA generated during the phosphorylation reaction<sup>307</sup> with an inhibitory constant  $k_i$  of  $86 \pm 10 \text{ nM}$ <sup>308</sup>. In cancer cells, MTAP activity is decreased by 96% upon treatment with  $1 \mu\text{M}$  MT-DADMe-ImmA for 24 h<sup>309</sup>. Thus, MT-DADMe-ImmA is suitable to study the role of MTAP inhibition in Kyn production. However, MT-DADMe-ImmA did not significantly alter cellular Kyn levels even at concentrations of  $20 \mu\text{M}$ . Therefore, MTAP enzymatic activity seems not to be involved in the regulation of the Kyn pathway.

Ultimately, MTAP was de-validated as target protein by comparing Kyn levels in IDO1-HCT116 and IDO1-HCT116 MTAP<sup>-/-</sup> cells upon treatment with epoxykynin. Because HCT116 cells did not produce Kyn upon stimulation with IFN- $\gamma$ , the cells were transfected with an IDO1-encoding plasmid. After transfection, both HCT116 wt and HCT116 MTAP<sup>-/-</sup> cells generated similar levels of Kyn. Hence, the assay conditions were suitable to test and compare epoxykynin in both cell lines. Epoxykynin decreased Kyn levels in both wt and MTAP<sup>-/-</sup> cells with  $\text{IC}_{50}$  values of  $20.7 \pm 11.5 \text{ nM}$  and  $20.5 \pm 15.9 \text{ nM}$ , respectively. If MTAP was the target of epoxykynin, one would expect epoxykynin to be completely inactive in the MTAP-deficient cells.

## Discussion

In conclusion, MTAP was de-validated as a target protein of epoxykynin for Kyn reduction. The CETSA and TPP did not show target engagement and beyond that, it was chemically and genetically de-validated by employing a known inhibitor of MTAP and an MTAP-deficient cell line.

### 6.2.3.3 sEH as Potential Target of Epoxykynin

As sEH arose as possible target protein of epoxykynin from the affinity-based chemical proteomics and the *in silico* target predictions, the target engagement of unmodified epoxykynin and sEH was investigated *in vitro* and *in cellulo*. Interestingly, binding of epoxykynin to purified human sEH already altered the native protein state, as can be seen by an increase of fluorescence values at 20°C. The relative fluorescence units (RFU) depict the ratio of fluorescence signals at 350 nm and 330 nm. For most proteins, the intrinsic protein fluorescence mainly originates from Trp residues, with smaller contributions of Tyr side chains. Upon unfolding, Trps which are often buried within the protein become solvent exposed, resulting in quenching and a red-shift of the fluorescence. Overall, this usually increases the 350 nm/330 nm fluorescence ratio upon denaturation. The higher 350 nm/330 nm ratio for epoxykynin-treated sEH at 20°C compared to the DMSO control might indicate a change in the environment of one or more Trp residues upon compound binding. sEH contains twelve Trp residues, with ten of them being located in the hydrolase domain. Comparing crystal structures of ligand-free sEH (pdb 1S8O) and *t*-AUCB-bound sEH-H (pdb 3WKE, Figure 74), Trp510 moves into the protein upon compound binding (Figure 74). In the ligand-free state, Pro362 and Ile363 are oriented towards Trp510 and push it towards the protein surface. In the ligand-bound state, Ile363 is flipped into the long branch sub-pocket of sEH and pointing towards the adamantane ring of *t*-AUCB (Figure 74C). This results in a conformational change of NC-loop Tyr348-Ser370 framing the long branch and connecting the core and cap domain of sEH<sup>310</sup>. Residues Pro361-Asn366 move closer towards the catalytic triad, making more room for Trp510. Since amide sEH inhibitors are known to bind to the catalytic triad in a similar manner as urea inhibitors, such as *t*-AUCB (Figure 75), binding of epoxykynin to sEH might induce a conformational change of Trp510. This modulation of the native protein state can then be observed by an increased 350 nm/330 nm fluorescence ratio at 20°C in the nanoDSF.

## Discussion

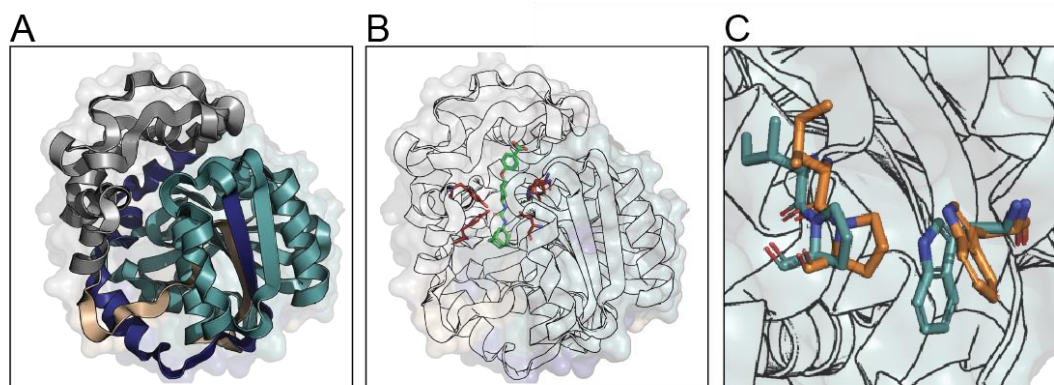


**Figure 74:** Crystal structure of sEH-H. A) SEH-H consists of a main (teal) and the cap domain (grey) that are connected by the NC (wheat) and back loops (deep blue, pdb 3wke) B) Structure of the sEH-H inhibitor *t*-AUCB bound to sEH-H. The urea oxygen of *t*-AUCB (green sticks) forms polar interactions with two stabilizing residues Tyr381 and Tyr465 (red) on the opposite site of the catalytic triad Asp333-Asp495-His523 (red, pdb 3WKE). C) Upon binding of *t*-AUCB, Pro362, Ile363 and Trp510 adopt a different confirmation (teal, pdb 3WKE) compared to ligand-free sEH-H (orange, pdb 1s8o).

Both the nanoDSF and in-cell CETSA showed target engagement with comparable shifts in the  $T_m$  of  $5.5 \pm 1.5^\circ\text{C}$  and  $5.9 \pm 1.2^\circ\text{C}$ , respectively. Yet the lysate-based CETSA did not show a compound-induced shift in the melting temperature. Differences between lysate- and cell-based CETSA approaches are commonly observed, since in-cell CETSA requires the applied compound to be membrane permeable, unless the target is not present on the cell surface. Furthermore, proteins in lysates are not in their native environment, i.e. protein complexes, interactions with physiological ligands and cellular compartments being disrupted<sup>311</sup>. Thus, some drug-target interactions can only be observed in one of the approaches.

Because sEH is a bifunctional molecule, the catalytic activity of both domains was studied separately. For this purpose, the control inhibitors ebselen and AR9281 were employed. While the urea-based AR9281 mimics the sEH epoxide substrates and coordinates to the catalytic triad of sEH-H<sup>221</sup>, ebselen targets sEH-P and cooperatively inhibits sEH-H by conformational changes<sup>220</sup>. Ebselen is a selenium-containing Cys-reactive small molecule known to have many protein targets, such as the thioredoxin reductases (TrxR) and even IDO<sup>225, 226</sup>. Thus, the application of ebselen as control inhibitor in cellular environments ought to be obviated. Yet it can be employed as control in enzymatic assays, where only one protein is present and the observed effect can be distinctly attributed to the respective enzyme. Both control inhibitors AR9281 and ebselen acted on the two proteins domains as expected, with AR9281 only abolishing the activity of sEH-H and ebselen impeding both sEH-H and sEH-P. Subsequently, epoxykynin was analyzed in analogy. Similar to AR9281, epoxykynin only inhibited the enzymatic activity of sEH-H with an  $\text{IC}_{50}$  of  $6.7 \pm 3.2$  nM. While knowledge about sEH-P and its biological role is lacking, sEH-H is well characterized. Understanding of the catalytic mechanism and crystal structure analysis (Figure 73 and Figure 74A-B) facilitated the development of potent inhibitors. The first published selective sEH-H inhibitors were chalcone

## Discussion

oxides<sup>312</sup>. However, they are unstable and can be hydrolyzed by sEH. From there, urea and carbamate inhibitors have been developed<sup>296</sup> and especially the urea scaffold displayed excellent binding kinetics and high affinity to the catalytic triad Asp333-Asp495-His523 of sEH-H<sup>212</sup>. The urea oxygen forms polar interactions with the two stabilizing residues Tyr381 and Tyr465 opposite of the catalytic triad (Figure 74B), whereas the urea nitrogens act as hydrogen bond donors to Asp333 of the catalytic triad<sup>296</sup>.

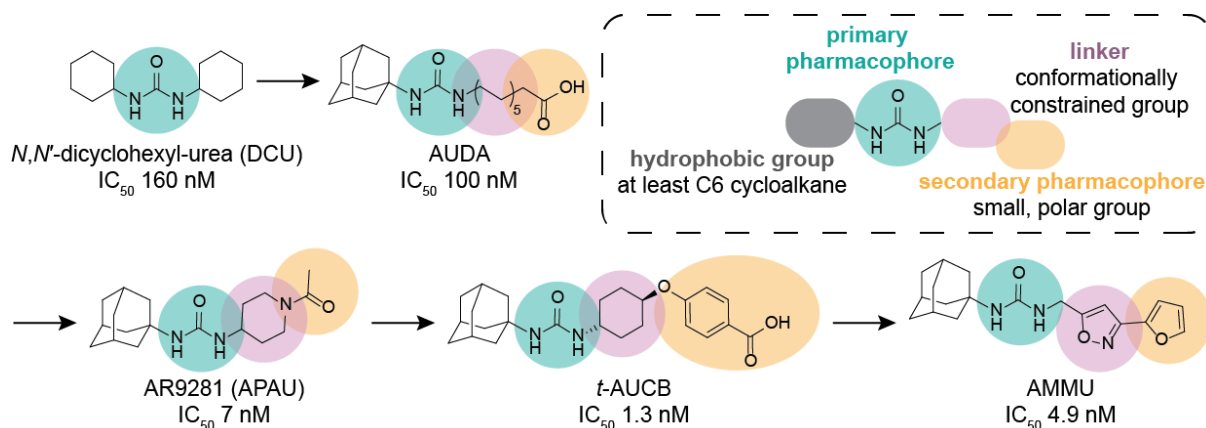


**Figure 75:** Development of early sEH-H inhibitors and SAR of urea inhibitors<sup>212, 313</sup>.  $IC_{50}$  values for purified human sEH reprinted from Sun *et al.* 'Discovery of Soluble Epoxide Hydrolase Inhibitors from Chemical Synthesis and Natural Products'<sup>212</sup>.

*N,N'*-dicyclohexylurea (DCU) was the first sEH-H inhibitor applied *in vivo* and was shown to decrease EET hydrolysis rates in rats<sup>314</sup>. Hence, the urea scaffold served as primary pharmacophore to further develop sEH-H inhibitors of the first generation (Figure 75). To improve the poor water solubility and low bioavailability of DCU, more flexible substituents were introduced on one side of the urea, such as in 12-(3-adamantan-1-ylureido)dodecanoic acid (AUDA). Even though AUDA and its *n*-butyl ester prodrug proved to be better soluble and could be administered to animals *via* drinking water<sup>315</sup>, they are prone to  $\beta$ -oxidation and subsequent catabolism<sup>212</sup>. To reduce metabolism and simultaneously improve pharmacokinetic (PK) properties, a second pharmacophore and conformationally constrained linkers between the primary and secondary pharmacophores were introduced. Installing a small, polar group in at least five atoms distance (approximately 7.5 Å) from the urea moiety improved solubility and PKs, which can be even further enhanced by an additional polar group in 13 atoms distance (approximately 17 Å) from the primary pharmacophore<sup>316</sup>. Conformationally restricted linkers replaced the flexible alkyl chain to separate primary and secondary pharmacophores, which led to significant improvement of the metabolic stability<sup>317</sup>. The first linkers comprised saturated rings, such as piperidine or cyclohexyl, but soon also unsaturated rings and aromatics were implemented<sup>318, 319</sup>. With this, the early generation urea-based sEH-H inhibitors, such as AR9281 (*N*-(1-acetylpiperidin-4-yl)-*N*-(adamant-1-yl)urea, APAU), *trans*-4-[4-(3-adamantan-1-ylureido)-cyclohexyloxy]benzoic acid (*t*-AUCB) and 1-



## Discussion

(adamant-1-ylmethyl)-3-[(3-methylisoxazol-5-yl)methyl]urea (AMMU) were developed (Figure 75). Although adamantyl-urea inhibitors potently inhibit sEH-H, they are rapidly metabolized and have short half-lives *in vivo*. Replacement of the adamantane ring and the urea moiety and additionally, introduction of aromatics drastically improves PK properties, without abolishing the inhibitory effect<sup>212</sup>.

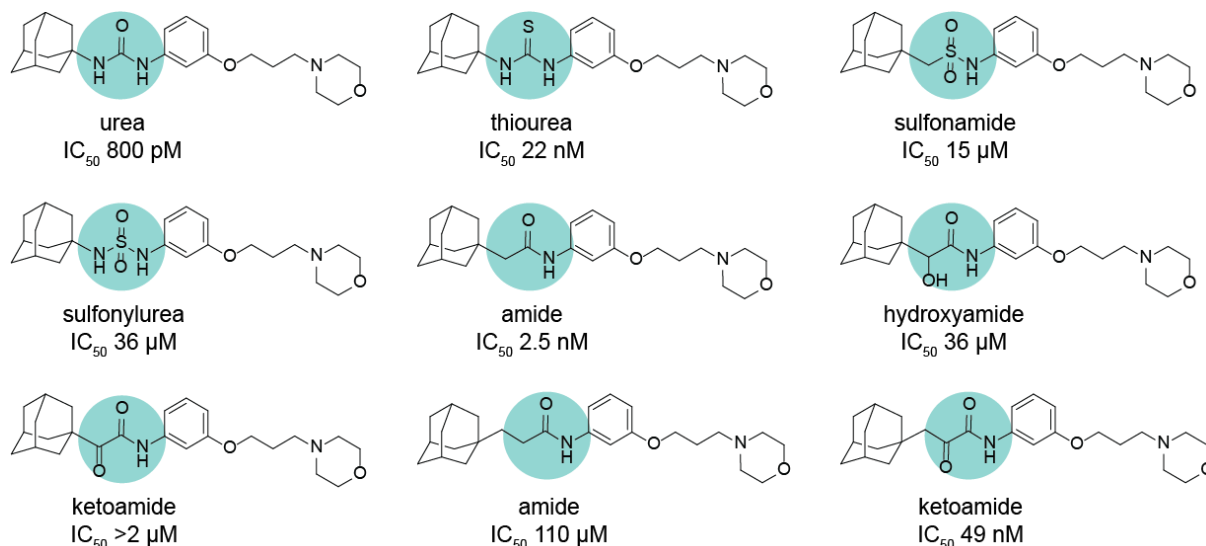


**Figure 76:** Modifications of the primary pharmacophore and the influence on sEH-H inhibition<sup>212</sup>. IC<sub>50</sub> values for purified human sEH reprinted from Sun *et al.* 'Discovery of Soluble Epoxide Hydrolase Inhibitors from Chemical Synthesis and Natural Products'<sup>212</sup>.

In order to enhance the solubility of sEH-H inhibitors, the urea moiety was replaced by different groups (Figure 76). Among the sulfur-containing derivatives, thioureas provided nanomolar IC<sub>50</sub> values, while sulfonamide or sulfonylurea pharmacophores abolished the inhibitory effect. An amide substitution did not significantly decrease the inhibitory potency, whereas for hydroxyamides or ketoamides a loss of activity can be observed. However, installing of an additional methylene group between the adamantane and the ketoamide restored the inhibitory properties<sup>212, 320</sup>. Ketoamides can be both hydrogen bond acceptors for non-covalent interactions as well as covalent inhibitors targeting serine or cysteine residues<sup>321, 322</sup>. Thus, many natural products, antibiotics or virus protease inhibitors contain α-ketoamides, such as rapamycin or telaprevir<sup>322, 323</sup>. Even though there are no serines or cysteines present in the active site of sEH-H, the activated nucleophile Asp333 of the catalytic triad may attack one of the carbonyl carbons of the ketoamide.

Figure 76 demonstrates that amide-bearing compounds can achieve similar inhibition of sEH-H compared to urea-based inhibitors while having improved PK properties. To further increase metabolic stability, the adamantyl group can be replaced by other cyclic hydrophobic moieties with at least six carbons, such as cyclohexyl or tetralyl groups<sup>313</sup>. Considering all these factors, epoxykynin represents an sEH-H inhibitor *par excellence*: The primary amide pharmacophore is on the one side substituted with a hydrophobic cycloheptane, while on the other side, the

## Discussion

constraint indole ring creates sufficient distance to the two polar secondary pharmacophores bromine and trifluoro acetyl (Figure 77).

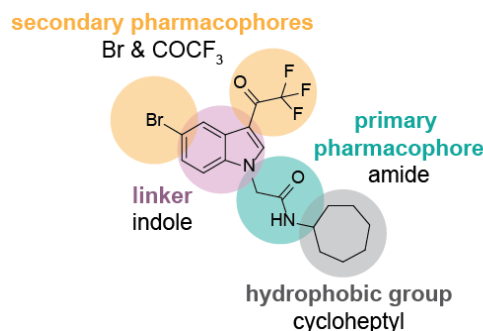


**Figure 77:** Pharmacophores of epoxykynin for sEH-H inhibition.

Surprisingly, the two sEH-H inhibitors GSK2256294A and AR9281, that are currently undergoing clinical trials, did not reduce cellular Kyn levels as well as the urea sEH inhibitor TPPU. The poor PK properties of AR9281 and TPPU and short drug-target residence times of only  $8.7 \pm 0.3$  min and  $15.9 \pm 0.3$  min, respectively<sup>223</sup>, might contribute to the poor cellular activity regarding Kyn reduction. However, GSK2256294A demonstrated improved PKs and sustained inhibition of sEH-H activity *in vivo*<sup>324</sup>. Hence, epoxykynin might act as a dual inhibitor targeting a yet unknown secondary protein. Alternatively, epoxykynin might covalently bind to a non-catalytic cysteine residue of sEH-H *via* the trifluoro acetyl group<sup>267, 297</sup>. With their reactive thiol group, cysteines are frequently involved in protein function. However, catalytic cysteines are often conserved among protein families, making selective targeting of specific proteins by modifying catalytic cysteines challenging<sup>325</sup>. Hence, trifluoromethyl ketones have been employed to reversibly target non-catalytic cysteine residues of kinases which are generally less conserved than catalytic cysteines<sup>267</sup>. This approach not only improves selectivity, but also extends target occupancy by the slow off-reaction. In contrast to irreversible covalent warheads, trifluoromethyl ketones can reversibly dissociate from the target and, thus, may minimize undesired side effects, such as reduced protein half-life due to the permanent modification<sup>267</sup>.

Furthermore, the sEH-P inhibitor SWE101 did not alter Kyn levels, while ebselen and auranofin decreased Kyn production. Since sEH-P is not as well characterized as sEH-H, there are only a few selective inhibitors available. SWE101 is the first selective *in vivo* active sEH-P inhibitor<sup>224</sup>, while ebselen and auranofin have multiple targets<sup>220, 225</sup>. Multi-target compounds are generally unsuitable as controls for cellular assays. However, as these two compounds were the only sEH inhibitors that reduced Kyn levels, their common target protein thioredoxin reductase (TrxR) was investigated<sup>225</sup>. Yet, epoxykynin did not inhibit the TrxR enzymatic activity.

## Discussion

After confirming that epoxykynin is a potent inhibitor of sEH-H enzymatic activity, the role of sEH in the epoxykynin-mediated Kyn reduction was analyzed. First, sEH was depleted to genetically validate its influence on Kyn production. In comparison to a knockout, a knockdown of the target protein is only partial, as can be observed here with 10-18% residual *EPHX2* mRNA levels. Even if the majority of a protein is depleted, the remainder might still be sufficient to carry out the regular cellular function. This holds true e.g. for phosphodiesterase 6 $\delta$  (PDE $\delta$ ): upon PROTAC-mediated degradation, only 15% of residual PDE $\delta$  is sufficient to translocate its interactors and thereby, maintain the spatial organization of prenylated proteins<sup>326</sup>. Thus, a knockdown might only lead to an ambiguous outcome, whereas a knockout provides a definite result. Especially the near-haploid HAP1 cell line is widely used for knockouts, since it has only one copy of each gene and is therefore amenable for gene editing<sup>327</sup>. However, a knockout in HAP1 cells cannot be achieved for all genes, since some proteins are essential for cell homeostasis and metabolism<sup>328</sup> and not all proteins are expressed in every cell line. According to the ProteinAtlas database<sup>231, 232</sup>, HAP1 cells hardly express any sEH, which renders them unsuitable for a knockout. Therefore, sEH was depleted in HeLa cells using siRNA. The partial knockdown decreased cellular Kyn levels and thereby phenocopies sEH inhibition by epoxykynin. The effect of the knockdown on Kyn reduction was weaker than the epoxykynin-mediated inhibition. This might be due to the residual amount of sEH protein which was sufficient to partly counterbalance the effect of the depletion on the Kyn level. Nevertheless, the knockdown demonstrated that sEH is involved in the Kyn pathway. As HAP1 cells do not express sEH, epoxykynin did not inhibit Kyn production in this cell line. Hence, it served as a model for a 'knockin'. Transient transfection of HAP1 cells with an sEH expression construct and subsequent treatment with epoxykynin reduced Kyn levels. Additionally, increasing the amount of transfected plasmid dampened the inhibition, confirming that sEH is the target of epoxykynin that mediates Kyn reduction.

Furthermore, it was investigated if there is a functional link between sEH and the Kyn pathway. sEH expression regulates IDO1 protein levels in the absence of small molecules. Upon knockdown of sEH, IDO1 protein levels decreased and vice versa, overexpression of sEH increased IDO1 expression. In line with these findings, Zhou *et al.*<sup>329</sup> recently reported increased *IDO1* mRNA levels upon sEH overexpression in HCT116 cells. Interestingly, these effects were only observed with treatment times of at least 48 h. This indicates a cross-regulation of gene expression rather than modulation of the canonical degradation pathway of IDO1, since alterations of proteasomal degradation by proteasome inhibitors or PROTACs can already be detected after 1-2 h<sup>330, 331</sup>. Moreover, epoxykynin treatment did not reduce Kyn levels in lysates. This result indicates that acute inhibition of sEH is not sufficient for Kyn

## Discussion

reduction. Yet, pre-treatment of cells prior to the lysate-based Kyn assay decreased Kyn levels, demonstrating that a cross-talk of the two pathways is necessary for decreased Kyn levels.

The functional link between fatty acid metabolism and Kyn production has yet to be elucidated. However, there are several hints towards cross-regulation between the two pathways. For instance, Kreiß *et al.*<sup>332</sup> demonstrated that human 5-lipoxygenase – as part of the second branch of the AA cascade – controls the expression of kynureninase. Furthermore, Kyn<sup>333</sup> and fatty acid metabolites, such as 12(R)-hydroxy-5(Z),8(Z),10(E),14(Z)-eicosatetraenoic acid (12(R)-HETE)<sup>334</sup>, act as endogenous agonists for the AhR. Since the AhR is an important transcriptional regulator for immune response by enhancing IDO1 expression in DCs, increased IDO1 levels upon sEH overexpression might be mediated by an AhR-mediated feedback loop. This hypothesis is supported by previous studies<sup>335</sup>, showing that an AhR antagonist in the diet of mice lowered the plasma levels of AA, whereas vice versa, Kyn administration increased AA levels. Thus, the sEH substrate and product eicosanoids might activate the AhR. The necessity of transcriptional regulation might explain why effects on the IDO1 protein levels upon altered sEH levels can only be observed after at least 48 h and, moreover, acute inhibition of sEH in lysates is not sufficient to reduce Kyn levels.

The sEH substrate EETs have anti-inflammatory effects, probably by acting as autocrine and paracrine lipid mediators *via* binding to GPCRs<sup>233</sup>. The identity of EET-specific GPCRs is still elusive and only low-affinity receptors for EETs have been identified<sup>235</sup>. Additionally, EETs are incorporated into membrane phospholipids and also bind to cytosolic proteins, indicating that some functions might be independent of GPCR binding<sup>233</sup>. However, studying the roles of EETs has proven to be difficult, since they are unstable and rapidly converted into the biologically less active DHET diols<sup>233, 234</sup>. Treatment of BxPC-3 cells with EETs did slightly increase Kyn levels, but it is challenging to conclude from these results. If substrate accumulation due to sEH inhibition is a mediator for Kyn reduction, it is difficult to mimic this condition by treatment with exogenous EETs. Even though the EETs were administered under serum-reduced conditions with BSA as a carrier, it might be that they still remained outside the cell or became incorporated into the cell membrane. Therefore, the EETs might not have reached their intracellular targets. More importantly, Kyn levels were increased upon EET treatment. If Kyn reduction is a result of EET accumulation, EET treatment should decrease Kyn levels. Thus, the results of the EET treatment should be interpreted with caution. As expected, the less active sEH product DHETs did not affect Kyn levels.

Beyond that, there are published correlations between EETs and HMOX1. According to literature reports, HMOX1 and other antioxidant enzymes are upregulated by the expression of CYP2J2 and EETs produced by CYP2J2<sup>336</sup>. Additionally, depletion of sEH induces *HMOX1*

## Discussion

gene expression<sup>337</sup>. On the contrary, HMOX1-derived carbon monoxide and bilirubin diminish EET formation<sup>338</sup>. Hence, the interplay between PUFA metabolism and antioxidants contributes to the oxidative homeostasis within the cell. In essence, epoxykynin-mediated inhibition of sEH and thus, accumulation of EETs might contribute to the observed increase in HMOX1 activity.

By weight, around 50% of pharmaceuticals sold per year target the AA cascade<sup>223</sup>, demonstrating the relevance of this pathway for medicinal chemistry programs. Especially the COX and LOX pathways have been extensively leveraged in the past for the treatment of pain and inflammatory diseases. Even today, they are still relevant targets for drug development with the constant discovery of new pathway members and metabolites<sup>339</sup>. Since chronic inflammation represents a hallmark of cancer<sup>10</sup>, blocking pro-inflammatory signals by COX inhibition proved to be effective in the prevention of some cancer types<sup>340, 341</sup>. As part of the third branch of the AA pathway, sEH inhibition is heavily underrepresented with no approved drug targeting sEH to date<sup>342-346</sup>. However, the importance of sEH-H, fatty acid epoxides and their corresponding diols for inflammation, vasodilation, angiogenesis, neuropsychiatrics and pain is widely acknowledged<sup>339</sup>, even to an extent that there is a debate whether there were any pathologies with which sEH is not associated<sup>223</sup>. Furthermore, the potential to target sEH-P and its role in the aforementioned biological processes has yet to be deciphered. Clinical trials for two structurally distinct sEH-H inhibitors have been launched for various indications, including hypertension, diabetes mellitus, chronic pulmonary obstructive disease, and subarachnoid haemorrhage<sup>347</sup>. The first clinically investigated sEH-H inhibitor is the piperidine carboxamide-based GSK2256294A and the second one is the urea-based AR9281 small molecule. Additionally, a second urea sEH-inhibitor EC5026 has entered clinical safety trials<sup>223</sup>. To date, no amide-based sEH-H inhibitors have advanced to clinical investigations, even though they proved to have beneficial properties compared to urea inhibitors.

Taken together, epoxykynin represents a classical example of an amide-based sEH-H inhibitor. By abolishing the hydrolase activity of sEH, it reduces Kyn levels in cancer cells. Furthermore, a cross-talk between sEH and the Kyn pathway was uncovered. However, the direct functional link has yet to be elucidated.

### 7 Conclusion and Future Perspective

The immune system is an important regulator of tumorigenesis, with both pro- and anti-tumor properties. The survival of cancer patients is extended by enhancing the ability of the patient's immune system to find and eliminate malignant cells. Additionally, immunotherapy is widely applicable for various cancer types and is generally better tolerated than traditional chemotherapies. Besides targeting immune checkpoints, modulation of the immunosuppressive enzyme IDO1 and its Trp catabolites kynurenines has proven to be an appealing target to revert cancer-induced immune tolerance. To identify inhibitors of the Kyn pathway, a phenotypic screening assay for cellular Kyn reduction was developed at the Max Planck Institute of Molecular Physiology.

Among the hit compounds of the screening, the pseudo-natural products apoxidoles were discovered. Apoxidoles combine THP and indole fragments in a monopodal connection not prevalent in nature. Biological characterization revealed that apoxidole-1 is a potent type IV apo-IDO1 inhibitor. By binding to the catalytic site, apoxidole-1 induces release of the heme cofactor and thus, catalytically inactivates IDO1. In comparison to the other three direct IDO1 inhibitor types, type IV inhibitors are the only class that targets apo-IDO1, which has several advantages. Once bound, apo-IDO1 inhibitors mimic irreversible inhibition with slow off-rates and high target occupancy. Furthermore, they display high selectivity for IDO1 over the two other Trp-catabolizing enzymes TDO and IDO2. In comparison to other apo-IDO1 inhibitors, apoxidole-1 has a unique chemotype, since all well characterized type IV inhibitors are phenylureas or structurally similar to BMS-986205. Thus, apoxidole-1 might not only serve as a tool to study IDO1 inhibition, but also as an inspiration to expand the structural scope of apo-IDO1 inhibitors in the future.

However, it has yet to be elucidated whether type IV inhibitors prove to be effective in clinical trials. Similar to the advanced holo-IDO1 inhibitor epacadostat, apo-IDO1 inhibitors might activate the AhR and thereby induce long-term tolerance by constitutive expression of IDO1. Additionally, IDO1 inhibition might be compensated by increased expression of TDO and IDO2 in the TME, which cannot be addressed by the selective apo-IDO1 inhibitors.

Hence, modulation of the Kyn pathway by not directly targeting IDO1 represents an alternative, attractive approach to revert immune suppression. The small molecule epoxykynin was identified to reduce cellular Kyn levels without inhibiting IDO1. Instead, epoxykynin abolishes the catalytic activity of the C-terminal fatty acid hydrolase domain of sEH. sEH-H is part of the third branch of the AA acid cascade and plays a crucial role in the metabolism of polyunsaturated fatty acids. While the COX and LOX branches are targets for multiple pharmaceuticals, the CYP epoxygenase branch is significantly less exploited for the treatment of diseases. sEH-H is a highly active enzyme that regulates inflammation, vasodilation,

## Conclusion and Future Perspective

angiogenesis, neuropsychiatries and pain by conversion of epoxy fatty acids to the corresponding vicinal diols. Several types of sEH-H inhibitor have been discovered to date, from urea-containing small molecules as first-generation inhibitors to more advanced compounds comprising different chemical modalities, such as amides like epoxykynin. Moreover, the herein described results demonstrate a cross-talk between sEH and the Kyn pathway. However, the functional link still remains elusive.

In future perspectives, epoxykynin might be used to further investigate the interplay of sEH and Kyn production, since it was highly potent *in vitro* and in cells. For instance, it can be applied to study the effect of sEH inhibition on AhR activation and the resulting impact on gene expression. Additionally, epoxykynin's high affinity for sEH makes it an excellent compound for co-crystallization to unravel the exact binding mode. At large, inhibition of sEH may represent an appealing therapeutic approach in immuno-oncology. Indirect inhibition of the Kyn pathway could circumvent the difficulties resulting from direct inhibition of IDO1, e.g. the compensatory effects of TDO and IDO2.

Taken together, the employed automated cell-based assay proved to be a powerful tool for the detection of Kyn pathway modulators. The screening enabled the identification of two structurally unrelated compound classes that represent two distinct strategies to interfere with Kyn production. Especially the discovery of epoxykynin demonstrates the high relevance of cell-based screenings, as a target-centered approach would not have been able to uncover the functional link between sEH and Kyn.

## 8 Experimental Part

### 8.1 Materials and Instruments

#### 8.1.1 Chemicals and Reagents

name	supplier	catalog number
680C91	Tocris Biosciences, UK	4392
acetic acid, glacial	Fisher Scientific, UK	10171460
acetonitrile	VWR International, US	83640.290
30% acrylamide solution	AppliChem GmbH, DE	A4983
ammonium persulfate	SERVA Electrophoresis GmbH, DE	13375
ascorbic acid	Sigma-Aldrich, US	A92902
AttoPhos reagent	Promega Corp., US	S1011
barium chloride	Alfa Aesar, US	A12905
BioTracker Carbon Monoxide Probe 1 Live Cell Dye	Sigma-Aldrich, US	SCT051
BIS-TRIS	SERVA Electrophoresis GmbH, DE	15107.13
BMS-986205/Linrodostat	Cayman Chemicals, US	25025
bovine serum albumin (BSA)	AppliChem GmbH, DE	A2244
bromophenol blue	Carl Roth GmbH + Co. KG, DE	A512
calcium chloride	Riedel-de Haën AG, DE	31307
catalase from bovine liver	Sigma-Aldrich, US	C9322
2-chloroacetamide	Sigma-Aldrich, US	C0267
4',6-Diamidine-2'-phenylindole dihydrochloride (DAPI)	Sigma-Aldrich, US	10236276001
DC Protein Assay	Bio-Rad Laboratories, Inc., US	500-0116
(±)8,9-dihydroxy-5Z,11Z,14Z-icosatrienoic acid	Cayman Chemicals, US	51351
(±)11,12-dihydroxy-5Z,8Z,14Z-icosatrienoic acid	Cayman Chemicals, US	51511
dimethyl sulfoxide (DMSO)	Sigma-Aldrich, US	41639
dithioerythritol (DTE)	Sigma-Aldrich, US	D8255
dithiotreitol (DTT)	Thermo Fisher Scientific Inc., US	D9779
epacadostat	Selleckchem	S7910
(±)8,9-epoxyeicosa-5Z, 11Z, 14Z-trienoic acid (8,9)-EET	Santa Cruz Biotechnology Inc., US	sc-221157
(±)11,12-epoxyeicosa-5Z, 8Z, 14Z-trienoic acid (11,12)-EET	Santa Cruz Biotechnology Inc., US	sc-471310
ethanol (EtOH)	Sigma-Aldrich, US	153386F
fetal bovine serum	Gibco, US	10099-141
formic acid	VWR International, US	84865.180
glycerol	Gerbu Biotechnik GmbH, DE	2006.5000
glycine	Carl Roth GmbH & Co. KG, DE	3790.2
hemin	Sigma-Aldrich, US	51280
hydrochloric acid	VWR International, US	30024.29
IFN- $\gamma$	PeproTech, Inc., DE	300-02



## Experimental Part

<b>name</b>	<b>supplier</b>	<b>catalog number</b>
Intercept® (PBS) Blocking Buffer	LI-COR Biosciences, US	927-70001
iodoacetamide	AppliChem GmbH, DE	A1666
Lipofectamine™ 2000 Transfection Reagent	Invitrogen Life Technologies GmbH, DE	11668-027
Lysyl Endopeptidase® (Lys-C)	Wako Pure Chemical Industries, Ltd., JP	125-05061
MEM non-essential amino acids	PAN Biotech GmbH, DE	P08-32100
methanol (MeOH)	VWR International, US	20846.361
methylene blue	Sigma-Aldrich, US	MB1
milk powder, non-fat dry	AppliChem GmbH, DE	A0830
NHS Mag Sepharose	Cytiva, US	28-9440-09
NP40 alternative	Merck KGaA, DE	492016
Opti-MEM serum-reduced medium	Gibco, US	31985-062
PageRuler™ Plus Prestained Protein Ladder	Thermo Fisher Scientific Inc., US	26619
PBS tablets	Jena Bioscience	AK-102P
PhosphoStop	Roche Holding AG; CH	4906845001
Plasmid DNA Purification Kit	QIAGEN, NL	
potassium chloride	J.T.Baker, US	0509
potassium phosphate, dibasic	Merck KGaA, DE	1.04873.1000
potassium phosphate, monobasic	Sigma-Aldrich, US	30407
propan-2-ol	Riedel-de Haën AG, DE	33539
Protease inhibitor cocktail	Roche Holding AG, CH	11836170001
sodium chloride	VWR International, US	28.810.295
sodium dodecylsulfate (SDS)	Carl Roth GmbH & Co. KG, DE	CN30.3
sodium pyruvate	PAN Biotech GmbH, DE	P04-43100
SsoAdvanced™ Universal SYBR® Green Supermix	Bio-Rad Laboratories, Inc., US	1725274
succinylacetone (SA)	TCI Chemicals, DE	U0127
SuperSignal™ West Pico PLUS Chemiluminescent Substrate	Thermo Fisher Scientific Inc., USA	34580
SuperSignal™ West Femto Maximum Sensitivity Substrate	Thermo Fisher Scientific Inc., USA	34095
trichloroacetic acid (TCA)	Sigma-Aldrich, US	T0699
trifluoroacetic acid (TFA)	Thermo Fisher Scientific Inc., US	85183
triethylammonium bicarbonate (TEAB)	Sigma-Aldrich, US	T7408
TRIS	Carl Roth GmbH & Co. KG, DE	4855.2
TRIS-HCl	Sigma-Aldrich, US	B2261
tris(2-carboxyethyl)phosphine	Thermo Fisher Scientific Inc., USA	20491
triton X-100	SERVA Electrophoresis GmbH, DE	37240.01
trypan blue	Invitrogen Life Technologies GmbH, DE	T10282
trypsin, recombinant	Roche Holding AG, CH	03708969001
trypsin/EDTA	PAN-Biotech GmbH, DE	P10-023100
Tween™ 20	Fisher Scientific, UK	BP337-100

## Experimental Part

<b>name</b>	<b>supplier</b>	<b>catalog number</b>
Universal IDO1/IDO2/TDO Inhibitor Screening Assay Kit	BPS Bioscience Inc., US	72035
urea	AppliChem GmbH, DE	A1049

### 8.1.2 Buffers

<b>buffer</b>	<b>composition</b>
alkylation buffer 1	375 mM iodoacetamide in 200 mM TEAB
alkylation buffer 2	50 mM chloroacetamide in denaturing/reducing buffer 2
AttoPhos assay buffer	25 mM BIS-TRIS, 1 mM MgCl <sub>2</sub> x 6 H <sub>2</sub> O, 0.1 mg/mL bovine serum albumin pH 7
AttoPhos solution	166.7 μM AttoPhos reagent in AttoPhos assay buffer
AttoPhos stop solution	100 mM NaOH in AttoPhos assay buffer
blocking buffer 1	500 mM ethanolamine, 500 mM sodium chloride, pH 8.3
blocking buffer 2	100 mM sodium acetate, 500 mM sodium chloride, pH 4
coupling buffer	150 mM triethanolamine, 500 mM sodium chloride, pH 8.3
denaturing/reducing buffer 1	200 mM TCEP, in 200 mM TEAB
denaturing/reducing buffer 2	8 M urea, 50 mM TRIS, pH 7.5, 1 mM DTT
digestion buffer 1	27.9 mg/L trypsin in 100 mM TEAB
digestion buffer 2	6.06 mg/L trypsin in 50 mM TRIS, pH 7.5

## Experimental Part

buffer	composition
equilibration buffer	1 mM HCl
Kyn sensor buffer	50 mM H <sub>3</sub> PO <sub>4</sub> , 120 mM NaCl, pH 1
1X Laemmli buffer	8% (v/v) glycerol, 22 mM TRIS-HCl, pH 6.8 3.1 mM SDS, 4.44 mM DTT, 33.2 mM bromophenol blue
NP40-based lysis buffer	150 mM NaCl, 1% (v/v) NP40 alternative, 50 mM TRIS-HCl, pH 8.0
PBS	140 mM NaCl, 7.36 mM K <sub>2</sub> HPO <sub>4</sub> , 2.64 mM KH <sub>2</sub> PO <sub>4</sub> , 3 mM KCl, pH 7.45
PBS-T	0.1% (v/v) Tween® 20 in PBS
potassium phosphate buffer (K-PO <sub>4</sub> buffer)	16.9 mM K <sub>2</sub> HPO <sub>4</sub> , 33.1 mM KH <sub>2</sub> PO <sub>4</sub> , pH 6.5
PreScission protease buffer	50 mM TRIS-HCl, pH 7.0, 150 mM NaCl, 1 mM DTE, 200 µM hemin
protein expression buffer 1	50 mM TRIS-HCl, 500 mM NaCl, 10 mM MgCl <sub>2</sub> , pH 8
protein expression buffer 2	50 mM TRIS-HCl, 500 mM NaCl, 10 mM MgCl <sub>2</sub> , 20 mM imidazole, 3 mM DTT, pH 8
protein expression buffer 3	50 mM TRIS-HCl, pH 7.4, 100 mM NaCl
protein expression buffer 4	50 mM TRIS-HCl, pH 7.4,

## Experimental Part

buffer	composition
	100 mM KCl
protein expression buffer 5	25 mM TRIS-HCl, pH 8.0, 100 $\mu$ M TCEP
1X SDS-PAGE running buffer	25 mM glycine, 2.5 mM TRIS, 350 $\mu$ M SDS
SDS-PAGE separating gel buffer	33.3% (v/v) 30% acrylamide mix, 25% (v/v) 1.5 M TRIS, pH 8.8, 1% (v/v) 10% SDS, 0.04% (v/v) TEMED
SDS-PAGE stacking gel buffer	16.7% (v/v) 30% acrylamide mix, 12.5%(v/v) 1 M TRIS, pH 6.8, 1% (v/v) 10% SDS, 0.01% (v/v) TEMED
Stage-Tip buffer 1	0.1% formic acid
Stage-Tip buffer 2	0.1% formic acid, 80% (v/v) acetonitrile
transfer buffer	192 mM glycine, 25 mM TRIS, 10% (v/v) methanol
TrxR extraction buffer	50 mM K-PO <sub>4</sub> buffer, 1 mM EDTA, pH 7.4
washing buffer	50 mM PIPES (pH 7.4), 50 mM sodium chloride, 75 mM MgCl <sub>2</sub> , 5 mM EGTA, 0.1% (v/v) NP40 alternative, 0.1% (v/v) Triton X-100, 0.1% (v/v) Tween® 20

### 8.1.3 Consumables

name	supplier
3MTM Empore™ C18 Extraction Disk	Thermo Fisher Scientific, US
96-well sitting drop iQ drop plate	SPT Labtech, UK
Breathe-Easy® sealing membrane	Sigma-Aldrich, US
DC Protein Assay	Bio-Rad, US
DNase I recombinant, RNase-free	QIAGEN, DE

## Experimental Part

<b>name</b>	<b>supplier</b>
Dual-Glo® Luciferase Assay System	Promega, US
Empore™ High Performance Extraction Disks, C18	3M Bioanalytical Technologies, IN
Glass coverslips	Thermo Fisher, US
Indoleamine 2,3-Dioxygenase 1 (IDO1) Activity Assay Kit	BioVision, US
Mounting medium	Polysciences Europe, DE
MycoAlert™ Mycoplasma Detection Kit	Roche, CH
NHS Mag Sepharose®	Cytiva, US
PVDF Transfer Membranes, 0.45 µm	Thermo Fisher Scientific, US
QIAGEN Plasmid Kits	QIAGEN, DE
QuantiTect Reverse Transcription Kit	QIAGEN, DE
RNeasy Plus Kits	QIAGEN, DE
Soluble Epoxide Hydrolase Inhibitor Screening Assay Kit	Cayman, US
SsoAdvanced Universal SYBR Green Supermix	Bio-Rad, US
Mini-PROTEAN TGX Stain-Free Precast Gels	Bio-Rad, US
TMT10plex labels	Thermo Fisher Scientific, US
Thioredoxin Reductase Colorimetric Assay Kit	Cayman, US
Universal IDO1/IDO2/TDO Inhibitor Screening Assay Kit	BPS Bioscience, US
Whatman® gel blotting paper	Sigma-Aldrich, US

### 8.1.4 Instruments and Softwares

<b>name</b>	<b>specification</b>	<b>supplier</b>
Adobe Creative Cloud	illustration softwares	Adobe, US
BioRender	illustration software	BioRender, US
Cell Countess II	cell counter	Thermo Fisher Scientific, US
CFX Maestro	qPCR data analysis software	Bio-Rad, US
CFX96 Touch Real-Time PCR Detection System	qPCR cyclers	Bio-Rad, US
ChemiDoc™ MP Imaging System	immunoblot imager	Bio-Rad, US
ChemDraw 18.2	Chemical analysis software	PerkinElmer, US
FoldAffinity	nanoDSF data analysis	EMBL-Hamburg, DE
GraphPad Prism 9.0	data analysis software	GraphPad Software
ImageJ	Gel/blot analysis software	open source
ImageLab	Gel/blot analysis software	Bio-Rad, US
Image Studio 5.2	in-cell Western analysis software	LI-COR Biosciences, US
ImageXpress Micro XL	high-throughput widefield imager	Molecular Devices, US
IncuCyte 2019B Rev2	live cell imaging analysis software	Sartorius, DE
IncuCyte S3	live cell imaging	Sartorius, DE
Ingenuity Pathway Analysis	pathway enrichment analysis	QIAGEN, DE
LTQ Orbitrap Velos Pro	mass spectrometer	Thermo Fisher Scientific, US
MasterCycler EpGradient S	PCR cyclers	Eppendorf, DE
Mastercycler® X50	PCR cyclers	Eppendorf, DE
MaxQuant	proteomics data analysis software	Max Planck Society, DE

## Experimental Part

<b>name</b>	<b>specification</b>	<b>supplier</b>
MetaXpress	widefield imager analysis software	Molecular Devices, US
Mini PROTEAN Tetra Vertical Electrophoresis Cell	electrophoresis chamber	Bio-Rad, US
Mini Trans-Blot® Cell	wet tank immunoblotting	Bio-Rad, US
mosquito® crystal	crystallization drop setting robot	SPT Labtech, UK
Nanodrop 2000	spectrophotometer	Thermo Fisher Scientific, US
Odyssey CLx Imaging System	in-cell Western imager	LI-COR Biosciences, US
Orbitrap Fusion Lumos Tribrid Mass Spectrometer	mass spectrometer	Thermo Fisher Scientific, US
Perseus	proteomics data analysis software	Max Planck Society, DE
Q Exactive HF	mass spectrometer	Thermo Fisher Scientific, US
Q Exactive Plus	mass spectrometer	Thermo Fisher Scientific, US
Sonoplus HD2070	ultrasound sonicator	BANDELIN electronic, DE
TECAN Infinite M200	plate reader	Tecan, CH
TECAN Spark®	plate reader	Tecan, CH
ROCK IMAGER®	crystallization imager	Formulatrix, AE
ROCK MAKER®	crystallization software	Formulatrix, AE
UltiMate 3000 RSLC HPLC	nano-HPLC system	
VolcaNoseR	proteomics data analysis software	van Leeuwenhoek Centre for Advanced Microscopy, NL
Zeiss APOCHROMAT	microscope objective	Carl Zeiss Microscopy, DE
Zeiss AxioCam MRm	microscope camera	Carl Zeiss Microscopy, DE
Zeiss Observer Z1	microscope	Carl Zeiss Microscopy, DE
Zeiss ZEN	microscopy software	Carl Zeiss Microscopy, DE

### 8.1.5 Cell Culture Media

<b>name</b>	<b>supplements</b>	<b>cell lines</b>	<b>supplier</b>	<b>catalog number</b>
DMEM	10% (v/v) FBS, 1 mM sodium pyruvate, 1X MEM non-essential amino acids (NEAA)	HCT116, HeLa, HEK293T	PAN Biotech GmbH, DE	P04-03550
DMEM	10% (v/v) FBS, 1 mM sodium pyruvate, 1X MEM NEAA	HCT116, HeLa, HEK293T, SKOV-3	PAN Biotech GmbH, DE	P04-01161
IMDM	10% (v/v) FBS	HAP1	PAN Biotech GmbH, DE	P04-20150
McCoy's 5A	10% (v/v) FBS	SKOV-3	PAN Biotech GmbH, DE	P04-05500
RPMI	10% (v/v) FBS	BxPC-3, Jurkat	PAN Biotech GmbH, DE	P04-18047
RPMI	10% (v/v) FBS	BxPC-3	PAN Biotech GmbH, DE	P04-16515

## Experimental Part

### 8.1.6 Cell Lines

name	culture conditions	supplier	accession number
BxPC-3	RPMI-based growth medium, 5% CO <sub>2</sub> , 37°C	DSMZ GmbH, DE	DSMZ#760
HAP1	IMDM-based growth medium, 5% CO <sub>2</sub> , 37°C	Horizon Discovery Group plc, UK	c631
HAP1 HMOX1 KO	IMDM-based growth medium, 5% CO <sub>2</sub> , 37°C	Horizon Discovery Group plc, UK	HZGHC005983c001
HCT116	DMEM-based growth medium, 5% CO <sub>2</sub> , 37°C	DSMZ GmbH, DE	DSMZ#581
HCT116 MTAP -/-	DMEM-based growth medium, 0.3 mg/mL G418, 5% CO <sub>2</sub> , 37°C	Horizon Discovery Group plc, UK	HD R02-033
HEK293T	DMEM-based growth medium, 5% CO <sub>2</sub> , 37°C	ATCC, US	ATCC#11268
HeLa	DMEM-based growth medium, 5% CO <sub>2</sub> , 37°C	DSMZ GmbH, DE	DSMZ#57
Jurkat	RPMI-based growth medium, 5% CO <sub>2</sub> , 37°C	DSMZ GmbH, DE	DSMZ#282
SKOV-3	McCoy's 5A- based growth medium, 5% CO <sub>2</sub> , 37°C	DKFZ, DE	ATCC#HTB-77

### 8.1.7 Antibodies

antibody	origin	dilution	blocking buffer	supplier	catalog number
EPHX2	rabbit, polyclonal	1:1,000	50% Intercept Blocking Buffer (v/v) in PBS-T	ABclonal, DE	A1885
HMOX1	rabbit, monoclonal	1:250	5% milk (w/v) in PBS-T	Abcam, UK	ab68477
IDO1	rabbit, monoclonal	1:5,000	5% milk (w/v) in PBS-T	Abcam, UK	ab211017
MTAP	mouse, monoclonal	1:1,000	50% Intercept Blocking Buffer (v/v) in PBS-T	Santa Cruz, US	sc-100782
α-tubulin (FITC conjugate)	mouse, monoclonal	1:1,000	5% BSA in PBS	Sigma-Aldrich, US	F2168
vinculin	mouse, monoclonal	1:5,000	50% Intercept Blocking Buffer (v/v) in PBS-T	Merck, DE	V9131

## Experimental Part

antibody	origin	dilution	blocking buffer	supplier	catalog number
mouse 680RD	donkey	1:5,000	50% Intercept Blocking Buffer (v/v) in PBS-T	LI-COR Biosciences, DE	926-68074
mouse 800CW	goat	1:5,000	50% Intercept Blocking Buffer (v/v) in PBS-T	LI-COR Biosciences, DE	926-32210
rabbit 680RD	donkey	1:5,000	50% Intercept Blocking Buffer (v/v) in PBS-T	LI-COR Biosciences, DE	926-68071
rabbit 800CW	donkey	1:5,000	50% Intercept Blocking Buffer (v/v) in PBS-T	LI-COR Biosciences, DE	926-32213
rabbit HRP	goat	1:10,000	5% milk (w/v) in PBS-T	Pierce Biotechnology, US	31460

### 8.1.8 Plasmids

name	vector	insert	supplier
pCMV3-IDO1	pCMV3-untagged	IDO1	Sino Biological US Inc., US
pXPG-IDO1	pXPG	IDO1 promoter	kindly provided by G. M. Doody <sup>348</sup>
pRL-TK	pRL	HSV-thymidine kinase promoter	Promega Corporation, US
pCX-HO1-2A-EGFP	pCX-2A-2A	HMOX1	Addgene (#74672), US
pRSF-EPHX2	pRSF	sEH	kindly provided by E. Proschak <sup>349</sup>
pCMV3-EPHX2	pCMV3-untagged	sEH	Sino Biological US Inc., US
pGEX6p-GST-IDO1	pGEX6p-2rbs	IDO1	kindly provided by A. De Antoni <sup>350</sup>

### 8.1.9 Primers

target gene	forward primer 5' to 3'	reverse primer 5' to 3'	supplier
<i>IDO1</i>	GCCTGATCTCATAGAGTCTGGC	TGCATCCCAGAACTAGACGTGC	Eurofins Scientific SE, LU
<i>EPHX2</i>	CCTTCATACCAGCAAATCCCAACA	TTCAGCCTCAGCCACTCCT	
<i>GAPDH</i>	GTCTCCTCTGACTTCAACAGCG	ACCACCCTGTTGCTGTAGCCAA	



### 8.2 Cell Biology Methods

All cell culture experiments were performed under sterile conditions using a laminar flow cabinet and appropriate sterile equipment.

#### 8.2.1 Sub-cultivation of Adherent Cells

Mammalian cell lines were grown at 37°C and 5% CO<sub>2</sub> under humidified atmosphere until a confluence of about 80-90% was reached. For passaging, medium was removed, cells were washed with pre-warmed PBS and cells were detached by addition of trypsin/EDTA solution for 2 to 10 min. To stop trypsinization, an appropriate volume of cell culture medium was added and cells were separated with a serological pipette to achieve a single cell suspension. Different volumes of cell suspension depending on growth rates were seeded into new cell culture flasks.

All cell lines were sub-cultivated at least twice a week.

#### 8.2.2 Sub-cultivation of Suspension Cells

Jurkat cells were grown to a maximum cell density of  $2 \times 10^6$  cells/mL at 37°C and 5% CO<sub>2</sub> under humidified atmosphere. For passaging, cells were centrifuged at 300 x g for 5 min and the cell pellet was resuspended, diluted to a concentration of  $1-1.5 \times 10^5$  cells/mL and seeded into new culture flasks.

#### 8.2.3 Cryo-conservation and Thawing of Cells

To cryo-preserve cells, cells grown to confluence in a T-75 culture flask were detached following the procedure described in 8.2.1. The cell suspension was centrifuged at 300 x g for 5 min and the medium was exchanged for 10 mL complete medium supplemented with 10% DMSO. 1 mL of the resulting cell suspension was transferred into one cryo-conservation vial. To allow cells to freeze at an even temperature reduction rate, conservation vials were stored in a Mr. Frosty™ freezing container at -80°C overnight. On the next day, cells were transferred to the liquid nitrogen tank for long-term storage.

Frozen cells were thawed at 37°C and rapidly transferred to a tube containing 9 mL of pre-warmed complete growth medium. After centrifugation at 300 x g for 5 min, the pellet was resuspended in 10 mL warm complete growth medium and transferred to a cell culture flask. The cells were maintained in culture as described in 8.2.1 and 8.2.2.

#### 8.2.4 Mycoplasma Detection

To ensure contaminant-free cell culture conditions, cell lines were tested monthly and additionally prior to cryo-preservation for *Mycoplasma* bacteria contamination using Lonza's MycoAlert™ Mycoplasma Detection Kit. The assay was performed following the manufacturer's protocol.

## Experimental Part

### 8.2.5 Cell Counting and Seeding

Cells were detached and resuspended in growth medium as described in 8.2.1. To remove trypsin and floating dead cells as well as optionally exchanging the medium to assay medium, cells were centrifuged at 300 x g for 5 min. After discarding the supernatant, the pellet was resuspended in an appropriate volume of assay medium.

For cell counting, 10  $\mu$ L of cell suspension was added to 10  $\mu$ L of trypan blue stain and mixed rigorously by pipetting. 10  $\mu$ L of the resulting solution was pipetted into each of the two sides of a disposable counting chamber. Using an automated cell counter, the total cell number, the number of viable cells and the viability (%) were determined. Only the number of viable cells was considered for calculations of a suitable cell titer for seeding. After dilution of the cell suspension with assay medium, appropriate volumes of cell suspension were seeded into tissue culture dishes or tissue culture well plates using serological, single-channel or eight-channel pipettes. Rows *A* and *H* of 96-well tissue culture plates were not used for generating experimental data due to heavy edge effects. To avoid excessive medium evaporation, these outer wells were filled with sterile PBS or pure medium and the plates were sealed with a gas-permeable membrane.

### 8.2.6 Compound Treatment

To evaluate the influence of various compounds on cells, dose-dependent response curves were measured in different assays. The compounds were dissolved in DMSO at concentrations of 2 or 10 mM and stored in aliquots at -20°C to avoid multiple freeze-thaw cycles. Serial dilutions of the compound stocks were prepared in DMSO and the DMSO-diluted compounds were further diluted in assay medium or buffer. Cells treated with DMSO only were used as control for compound-treated cells. For each experiment, the DMSO concentration remained the same in all experimental conditions and was between 0.2 and 0.5% (v/v).

### 8.2.7 Kynurenine (Kyn) Assays

*Compound screening was performed in collaboration with the Compound Management and Screening Center (COMAS), Dortmund. The kynurenine production assay described below was established and scaled up for high-throughput implementation by Dr. Elisabeth Hennes. The COMAS compound library was screened to identify modulators of the Kyn pathway by means of altered L-kynurenine production.*

#### 8.2.7.1 Automated Kyn Assay by COMAS

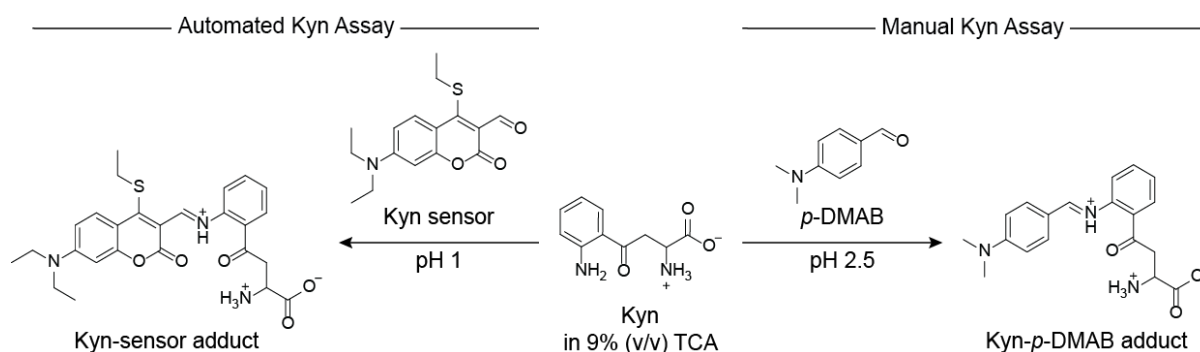
BxPC-3 cells (6,000 cells/well) were seeded in black, clear bottom 384-well tissue culture plates in total a volume of 25  $\mu$ L/well. After 24 h incubation at 37°C and 5% CO<sub>2</sub> in humidified atmosphere, cells were treated with the respective compound. At the same time, Trp (380  $\mu$ M final concentration) was supplemented and the Kyn pathway was induced by addition of IFN- $\gamma$  (50 ng/mL final concentration). The cells were incubated for 48 h. The cell viability was

## Experimental Part

assessed by addition of 5 ng/mL Hoechst-3334, followed by incubation for 30 min at 37°C and subsequent imaging with the ImageXpress Micro XL (excitation: 377/50 nm, emission: 447/60 nm, Molecular Devices, US). Image analysis was performed by means of cell count with the Cell Proliferation HT Application Module of the MetaXpress software (Molecular Devices, US). Afterwards, 30  $\mu$ L (46.15% (v/v), 65  $\mu$ L final volume) of 30% (v/v) trichloroacetic acid solution in water was added and cells were incubated for 10 min at 37°C. Plates were centrifuged at 1550 x g for 10 min. The Kyn sensor in Kyn sensor buffer was added to a final concentration of 14  $\mu$ M and the emerging fluorescence was measured immediately at an excitation wavelength of 555 nm and emission wavelengths of 586-600 nm.

### 8.2.7.2 Manual Kyn Assay

HeLa (5,000 cells/well), BxPC-3 (20,000 cells/well) or SKOV-3 cells (6,250 cells/well) were seeded in transparent 96-well (HeLa, BxPC-3) or 384-well (SKOV-3) tissue culture plates in medium without phenol red prior to incubation for 24 h at 37°C and 5% CO<sub>2</sub> in humidified atmosphere. Subsequently, medium was removed and replaced by medium containing 50 ng/mL (HeLa, BxPC-3) or 17.6 ng/mL IFN- $\gamma$  (SKOV-3) and 164.15  $\mu$ M (HeLa), 380  $\mu$ M (BxPC-3) or 450  $\mu$ M (SKOV-3) Trp. At the same time, the cells were treated with compounds and incubated for another 48 h at 37°C and 5% CO<sub>2</sub> in humidified atmosphere. For the hemin competition assay, hemin was added together with IFN- $\gamma$ , Trp and the compounds. Subsequently, trichloroacetic acid was added to a final concentration of 7% (v/v), the plates were incubated for 15 min at room temperature and centrifuged at 1800 x g for 10 min. Afterwards, an equal volume of freshly prepared 2% (w/v) *p*-DMAB in glacial acetic acid (Ehrlich reagent) was added prior to measuring the absorbance at 492 nm and 650 nm on the Spark® Multimode Microplate Reader (Tecan, AT). To negate well-dependent chromogenic scattering differences, the absorbance at 650 nm was measured as reference wavelength and subtracted from the L-kynurenine-derived absorbance A<sub>492</sub>, prior to normalization to the DMSO control. Data analysis was performed using a non-linear regression curve fit and GraphPad Prism 9.0 (GraphPad Software, Inc, US) to generate dose-response curves and obtain IC<sub>50</sub> values.



## Experimental Part

### 8.2.7.3 Kyn Assay in IDO1-HEK293T Cells

HEK293T cells were transiently reverse-transfected with the pCMV3-IDO1 vector (1 µg/96-well plate, Sino Biological, CN) using Lipofectamine™ 2000 (Invitrogen, US) following a modified protocol of the manufacturer's guidelines. Briefly, 1 µg of plasmid DNA in serum-free Opti-MEM was mixed in a 1:3 ratio with Lipofectamine™ 2000 and added to 9 mL cell suspension ( $2.78 \times 10^5$  cells/mL) in medium without phenol red. Immediately afterwards, cells were seeded in transparent 96-well tissue culture plates at a density of 25,000 cells/well prior to incubation for 20 h. Subsequently, cells were treated with 500 µM Trp and the compounds for 24 h. Thereafter, trichloroacetic acid was added to a final concentration of 7% (v/v), the plates were incubated for 15 min at room temperature and centrifuged for 10 min at 1800 x g. Afterwards, an equal volume of freshly prepared 2% (w/v) *p*-DMAB in glacial acetic acid (Ehrlich reagent) was added prior to measuring the absorbance at 492 nm and 650 nm on the Spark® Multimode Microplate Reader (Tecan, AT). To determine the Kyn levels, the absorbance of the Kyn-*p*-DMAB adduct  $A_{492}$  was subtracted by the background absorbance  $A_{650}$  and normalized to the DMSO control. Data analysis was performed using a non-linear regression curve fit and GraphPad Prism 9.0 (GraphPad Software, Inc, US) to generate dose-response curves and obtain  $IC_{50}$  values.

### 8.2.7.4 Kyn Assay in Lysates

The Kyn assay in lysate was performed using the commercial Indoleamine 2,3-Dioxygenase 1 (IDO1) Activity Assay Kit (cat# K972-100, BioVision Inc, US). Therefore, BxPC-3 cells ( $2 \times 10^6$  cells for 24 h treatment,  $1 \times 10^6$  cells for 48 h treatment) or HeLa cells ( $6.5 \times 10^5$  cells for 48 h treatment) were seeded in 60 mm-dishes and incubated for 24-48 h. On the next day, the medium was replaced by medium containing 50 ng/mL IFN- $\gamma$  and the cells were incubated for 24 to 48 h. If the cells were pre-treated, compounds or siRNA were simultaneously added with IFN- $\gamma$ . The plates were washed twice with warm PBS prior to detaching the cells with 750 µL trypsin/EDTA solution. The cell suspension was transferred to a tube and diluted with 5 mL ice-cold PBS. The cells were collected by centrifugation at 4°C and 300 x g for 5 min. The supernatant was removed and the pellet was resuspended in 300 µL of IDO1 assay buffer containing protease inhibitors. The cells were lysed by three consecutive freeze/thaw cycles as described in 8.2.13.3. The protein concentration was determined with the DC assay as in 8.3.2 and the cell lysates were aliquoted, snap-frozen in liquid nitrogen and stored at -80°C if necessary.

For Kyn detection, the 2X reaction premix was prepared by diluting the antioxidant mix 50-fold in IDO1 assay buffer. A 10X working solution of the IDO1 substrate Trp was prepared by 10-fold dilution of the stock in IDO1 assay buffer (final Trp concentration in the assay: 100 µM). The compounds were pre-diluted in DMSO, followed by a dilution in IDO1 assay buffer. The

## Experimental Part

assay was set up in black, low-volume 384-well plates with a total volume of 11  $\mu\text{L}$ . 5.5  $\mu\text{L}$  of the 2X reaction premix was mixed with inhibitor or DMSO (final DMSO concentration: 1% (v/v)) and 7  $\mu\text{g}$  lysate. The reaction was initiated by addition of 1.1  $\mu\text{L}$  of the IDO1 substrate Trp. The plate was sealed with a sticky silver sealer and incubated for 45 min at 37°C and 300 rpm in the dark prior to addition of 5  $\mu\text{L}$  of the fluorogenic developer solution. The plate was incubated for another 3 h at 45°C and 300 rpm in the dark. After cooling down for at least 1 h, the fluorescence was measured at an excitation wavelength of 402 nm and an emission wavelength of 488 nm on the Spark® Multimode Microplate Reader (Tecan, AT).

### 8.2.7.5 Influence of EETs on Kyn Levels

BxPC-3 cells (20,000 cells/well) were seeded in transparent 96-well tissue culture plates in medium without phenol red prior to incubation for 24 h. Subsequently, medium was removed and replaced by medium with reduced serum (1% (v/v) FBS) containing 50 ng/mL IFN- $\gamma$  and 380  $\mu\text{M}$  Trp. At the same time, the cells were treated with ( $\pm$ )8,9-epoxyeicosa-5Z,11Z,14Z-trienoic acid (8,9-EET) and ( $\pm$ )11,12-epoxyeicosa-5Z,8Z,14Z-trienoic acid (11,12-EET) dissolved in ethanol at a stock concentration of 50  $\mu\text{g}/\text{mL}$  ( $\approx$  156.02  $\mu\text{M}$ ). For better delivery of the EETs into the cells, BSA was added as a carrier protein (1:2 BSA to EET molar ratio). Due to the instability of the EETs at 37°C, cells were re-treated every 4-6 h for a total incubation time of 48 h. Subsequently, an equal volume of freshly prepared 2% (w/v) *p*-DMAB in glacial acetic acid (Ehrlich reagent) was added prior to measuring the absorbance at 492 nm and 650 nm on the Spark® Multimode Microplate Reader (Tecan, AT). To determine the Kyn levels, the absorbance of the Kyn-*p*-DMAB adduct  $A_{492}$  was subtracted by the background absorbance  $A_{650}$  and normalized to the EtOH control. Data analysis and representation as bar graphs was performed using GraphPad Prism 9.0 (GraphPad Software, Inc, US).

### 8.2.8 IDO1 Promoter Reporter Gene Assay

A reporter gene assay was performed to detect any interference with expression of the *IDO1* gene by compound treatment. The pXPG-IDO1 plasmid<sup>348</sup> (kindly provided by Gina M. Doody, Leeds, UK) containing the full-length *IDO1* promoter controlling the expression of a firefly luciferase (Fluc) was used as a reporter, whereas *Renilla* (Rluc) luciferase expression driven by the TK promoter *via* the pRL-TK vector (Promega Corporation, US) was used as a viability control.

HEK293T cells were transiently reverse-transfected with the aforementioned plasmids using Lipofectamine™ 2000 (Invitrogen, US) following a modified protocol of the manufacturer's guidelines. Briefly, a mixture of 4  $\mu\text{g}$  of the Fluc plasmid and 300 ng of the Rluc plasmid in serum-free Opti-MEM were mixed in a 1:3 ratio with Lipofectamine™ 2000 and added to 9 mL cell suspension at a cell density of  $2.78 \times 10^5$  cells/mL. Immediately afterwards, cells were seeded in transparent 96-well tissue culture plates at a density of 25,000 cells/well prior to

## Experimental Part

incubation for 24 h. On the next day, *IDO1* promoter-driven expression of Fluc was induced by addition of IFN- $\gamma$  (final concentration 50 ng/mL) with simultaneous compound treatment. After incubation for additional 48 h, luciferase activity was measured with the Dual-Glo<sup>®</sup> Luciferase Assay System with the Spark<sup>®</sup> Multimode Microplate Reader (Tecan, AT) following a modified version of the manufacturer's protocol. To determine the *IDO1* promoter activity, Fluc signals were divided by RLuc signals and normalized to the values of the DMSO control which was set to 100%. Data analysis was performed using a non-linear regression curve fit and GraphPad Prism 9.0 (GraphPad Software, Inc, US) to generate dose-response curves and obtain IC<sub>50</sub> values.

### 8.2.9 Luciferase Activity Assay

Luciferase activity assays were performed to exclude direct inhibition of the luciferases by the tested compounds in the reporter gene assay. Therefore, a suspension of  $1.65 \times 10^6$  HEK293T cells was reverse-transfected with 3.72  $\mu$ g of pXPG-*IDO1* plasmid and 280 ng of pRL-TK plasmid using 12  $\mu$ L of Lipofectamine 2000 (1:3 DNA to transfection reagent ratio). Cells were seeded in a 60-mm tissue culture dish and incubated for 24 h. Thereafter, IFN- $\gamma$  at a final concentration of 50 ng/mL was added to induce *IDO1* promoter-driven expression of Fluc prior to incubation for 24 h. Afterwards, cell culture medium was aspirated and cells were carefully washed with pre-warmed sterile PBS. 2.2 mL 1X Passive Lysis Buffer (PLB) was added and the plate was shaken on a microplate shaker for 25 min. For further usage, the lysate was aliquoted, snap-frozen in liquid nitrogen and stored at -80°C.

9  $\mu$ L of cell lysate was added to each well of a white half-area 96-well plate. 1  $\mu$ L of pre-diluted compound in 1X PLB was added to the lysate and the plate was incubated for 60 min at room temperature. Luciferase activities were determined using the Dual-Glo<sup>®</sup> Luciferase Assay System with the Spark<sup>®</sup> Multimode Microplate Reader (Tecan, AT) following a modified version of the manufacturer's protocol. To determine inhibition of the luciferases, signals were normalized to the values of the respective DMSO controls and analyzed using a non-linear regression curve fit in GraphPad Prism 9.0 (GraphPad Software, Inc, US) to generate dose-response curves and obtain IC<sub>50</sub> values.

### 8.2.10 Trp Uptake Assay

BxPC-3 cells (30,000 cells/well) were seeded in 96-well plates in Trp-free RPMI 1640 medium and incubated for 48 h prior addition of 50 ng/mL IFN- $\gamma$ . Trp starvation was continued for another 24 h. Afterwards, medium was exchanged for Trp-free medium containing the control inhibitors 5 mM L-Leu (inhibitor of system-L amino acid transporters (LAT)), 1 mM 1-methyl-L-tryptophan (inhibitor of tryptophanyl-tRNA synthetase (TrpRS)) and compounds and cells were incubated for 30 min. Subsequently, 50  $\mu$ M Trp was added and samples were incubated for another 30 min. The supernatant was transferred to a new plate, trichloroacetic acid was

## Experimental Part

added to a final concentration of 7% (v/v) and plates were incubated for 15 min at room temperature. Samples were centrifuged for 10 min at 1800 x g and Trp was quantified by HPLC-MS/MS using the LTQ Velos Pro and Dionex HPLC (Thermo Fisher Scientific, US). Data analysis was performed with Xcalibur™ (Thermo Fisher Scientific, US) and represented using GraphPad Prism 9.0 (GraphPad Software, Inc, US).

### 8.2.11 RNA Purification and reverse transcription-qPCR

HeLa cells (250,000 cells/well) were seeded in 6-well plates and incubated for 24 h prior to addition of 50 ng/mL IFN- $\gamma$  and compounds. After 24-48 h, RNA was extracted using the RNeasy Plus Mini Kit (QIAGEN, DE) following the manufacturer's procedure. DNA was removed on column by DNase digestion with RNase-free DNase Set (QIAGEN, DE) according to the manufacturer's instructions. Following the manufacturer's protocol, cDNA templates were synthesized from 800 ng total RNA using the QuantiTect Reverse Transcription Kit (QIAGEN, DE).

The expression levels of the *IDO1* and *EPHX2* genes and the reference *GAPDH* were assessed by real-time quantitative PCR (qPCR). Therefore, 100-120 ng cDNA was amplified using 500 nM of gene-specific primers and SsoAdvanced Universal SYBR Green Supermix (Bio-Rad Laboratories, DE) in a total volume of 10  $\mu$ L for 50 cycles using the CFX96 Touch™ Real-Time PCR Detection System (Bio-Rad Laboratories, DE). Relative *IDO1* and *EPHX2* expression levels were calculated using the  $\Delta\Delta C_t$  method with *GAPDH* as reference gene<sup>351</sup> and represented using GraphPad Prism 9.0 (GraphPad Software, Inc, US).

### 8.2.12 Immunofluorescence

HeLa cells (50,000 cells/well) were seeded onto glass coverslips in 24-well plates and incubated for 24 h. Subsequently, cells were treated with compounds and incubated for additional 24 h. Cells were washed with PBS prior to fixation with 4% paraformaldehyde in PBS for 15 min. Afterwards, cells were washed thrice with PBS and permeabilized by addition of 0.5% Triton X-100 for 15 min. Again, cells were washed thrice with PBS, followed by blocking with 5% BSA in PBS. The nuclei were stained with DAPI (1:1,000) and microtubules with a FITC-conjugated  $\alpha$ -tubulin antibody (1:1,000) in 5% BSA in PBS at 4°C overnight. On the next day, the coverslips were fixed onto microscopy slides with mounting medium and visualized using the Zeiss Observer Z1 microscope, equipped with the Zeiss APOCHROMAT objective (63X magnification) and the Zeiss AxioCam MRm camera. The images were analyzed with the Zeiss ZEN software.

### Cell Lysis

#### 8.2.13.1 Cell Lysis with Laemmli Buffer

Cells were washed with PBS prior to addition of ice-cold 1X Laemmli Buffer without DTT and bromophenol blue. Using a rubber policeman, cells were detached from the bottom of the well and transferred to a fresh tube on ice. Afterwards, samples were homogenized by sonication

## Experimental Part

(twice for 15-30 s, 3 cycles at a power of 10-15%) and protein concentration was determined using the *DC* protein assay according to 8.3.2, followed by addition of 4.44 mM DTT and 33.2 mM bromophenol blue and boiling of the samples at 95°C for 5 min.

### 8.2.13.2 Cell Lysis with NP40-based Lysis Buffer

Cells were washed with PBS prior to addition of ice-cold NP40-based lysis buffer. Using a cell scraper, cells were detached from the bottom of the well and transferred to a fresh tube on ice. Afterwards, samples were incubated on ice for 30 min and centrifuged at 13,000 x g and 4°C for 10 min. The supernatant was transferred to a new tube and the protein concentration was determined using the *DC* protein assay according to 8.3.2. For gel electrophoresis, the samples were mixed in a 5:1 ratio with 5X Laemmli buffer prior to boiling of the samples at 95°C for 5 min.

### 8.2.13.3 Cell Lysis by Freeze/Thaw Cycles

Cells were washed with PBS prior to addition of trypsin/EDTA and incubation at 37°C for approximately 5 min. The detached cells were collected in ice-cold PBS and washed thrice with PBS by centrifugation and resuspension (twice at 300 x g at 4°C for 5 min and once at 1000 x g at 4°C for 5 min). The pellet was resuspended in PBS and lysed by five consecutive freeze/thaw cycles as described in the following: The samples were frozen in liquid nitrogen and thawed at room temperature until about 60-80% of the cells are thawed. The cells were kept on ice until the samples were thawed completely. Afterwards, the samples were snap-frozen in liquid nitrogen again. After completing the five cycles, the samples were centrifuged at 13,000 x g and 4°C for 10 min and the supernatant was transferred to a new tube. Afterwards, protein concentration was determined according to 8.3.2. For gel electrophoresis, the samples were mixed in a 5:1 ratio with 5X Laemmli buffer prior to boiling of the samples at 95°C for 5 min.

## 8.2.14 Cellular Thermal Shift Assay (CETSA)

### 8.2.14.1 In-lysate CETSA

HeLa (1.65 x 10<sup>6</sup> cells/flask), SKOV-3 (2.5 x 10<sup>6</sup> cells/flask) or Jurkat cells (7.5 x 10<sup>6</sup> cells/flask) were seeded in T175 tissue culture flasks and incubated 24 (HeLa and SKOV-3) to 48 h (Jurkat). For the induction of IDO1 expression, 50 (HeLa) or 17.6 ng/mL IFN- $\gamma$  (SKOV-3) were added prior to incubation for 24 h. Afterwards, cells were harvested and lysed in NP40-based lysis buffer according to 8.2.13.2. Soluble protein fractions were separated from the pellet by centrifugation at 100,000 x g and 4°C for 20 min. The protein concentration was determined using the *DC* protein assay according to 8.3.2 and lysates were diluted to final concentrations of 1.5-6.5 g/L prior to treatment with the compound or DMSO as vehicle for 10 to 60 min at room temperature or 37°C. C- and V-treated samples were distributed equally into ten tubes each and subjected to heating at different temperatures (see



## Experimental Part

Table 5) in the MasterCycler EpGradient S or MasterCycler X50s (Eppendorf SE, DE). Soluble fractions were separated from denatured proteins by centrifugation at 100,000 x g and 4°C for 20 min. Supernatants were transferred to new tubes and subjected to immunoblot analysis according to 8.3.3. For quantification of the soluble protein fraction, the intensity of compound- and vehicle-treated protein bands were normalized to the intensity at the lowest temperature of each condition (36.9°C or 37°C) and thermal denaturation temperatures  $T_m$  were determined using non-linear regression curve fit from GraphPad Prism 9.0 (GraphPad Software, Inc, US).

### 8.2.14.2 In-cell CETSA

SKOV-3 cells ( $1.25 \times 10^6$  cells/flask) were seeded in two T75 tissue culture flasks and incubated for 24 h prior to addition of 17.6 ng/mL IFN- $\gamma$  and 10  $\mu$ M succinylacetone (SA, heme synthesis inhibitor). Jurkat ( $1 \times 10^7$  cells/flask) were seeded in 4 mL medium in two T75 tissue culture flasks and treated immediately after seeding. The cells were treated with the compound or DMSO as a vehicle for 15 min at 37°C. Cells were harvested and washed thrice in ice-cold PBS after resuspension in ice-cold PBS. C- and V-treated samples were distributed equally into ten tubes each and subjected to heating at different temperatures (see Table 5) in the MasterCycler EpGradient S or MasterCycler X50s (Eppendorf SE, DE). Afterwards, NP40 alternative was added to a final concentration of 0.4% (v/v) and cells were lysed by five consecutive freeze/thaw cycles according to 8.2.13.3. Soluble fractions were separated from denatured proteins by centrifugation at 100,000 x g and 4°C for 20 min. Supernatants were transferred to new tubes and subjected to immunoblot analysis according to 8.3.3. For quantification of the soluble protein fraction, the intensity of compound- and vehicle-treated protein bands were normalized to the intensity at the lowest temperature of each condition (36.9°C or 37°C) and thermal denaturation temperatures  $T_m$  were determined using a non-linear regression curve fit from GraphPad Prism 9.0 (GraphPad Software, Inc, US).

**Table 5:** Temperature gradients for CETSA.

IDO1 and HMOX1:

<b>cycler 1/°C</b>	36.9	40.1	44.1	47.9	51
<b>cycler 2/°C</b>	54.4	58	61.3	64.5	67

MTAP:

<b>cycler 1/°C</b>	37	57.2						
<b>cycler 2/°C</b>	60.8	65.3	68.7	72	75	78.3	81.6	85.7

sEH:

<b>cycler 1/°C</b>	37	51.5	55.2				
<b>cycler 2/°C</b>	58.1	61.9	63.8	65.7	67.6	69.2	72.1

## Experimental Part

### 8.2.15 In-cell Western

BxPC-3 cells (10,000 cells/well) were seeded in 96-well plates and incubated for 24 h prior to the addition of 50 ng/mL IFN- $\gamma$  and the compounds at the indicated concentrations for 48 h. Cells were fixed with 4% paraformaldehyde for 20 min at room temperature followed by permeabilization with 0.5% Triton X-100 for 15 min at room temperature. Afterwards, unspecific binding sites were blocked with 5% non-fat dry milk in PBS with 0.1% (v/v) Tween-20 (PBS-T) for 60 min at room temperature followed by overnight incubation at 4°C with the primary antibodies. For detection of IDO1 and the reference protein vinculin, the primary antibodies anti-IDO1 (1:3,000, ab211017, Abcam, GBR) and anti-vinculin (1:5,000, V9131, Merck KGaA, DE) were used in 5% milk in PBS-T. For visualization, secondary antibodies conjugated to IRDye® Infrared Fluorescent Dyes (1:500, LI-COR Biosciences, US) were used (Bio-Rad Laboratories, DE). Images were acquired with the Odyssey® CLx Infrared Imaging System (LI-COR Biosciences, US) and processed using Image Studio 5.2 (LI-COR Biosciences, US). IDO1 protein levels were normalized to the levels of the reference protein vinculin.

### 8.2.16 Carbon Monoxide Detection

HeLa cells ( $1 \times 10^4$  cells/well) were seeded in black 96-well plates with transparent bottom in medium without phenol red and incubated for 24 h prior to treatment with 50 ng/mL IFN- $\gamma$ , hemin and compound. Cells were incubated for additional 24 to 72 h and afterwards, 10  $\mu$ L of a stock solution consisting of 10  $\mu$ M BioTracker Carbon Monoxide Probe 1 Live Cell Dye<sup>216</sup> and 10  $\mu$ M of Pd(II)Cl<sub>2</sub> in 0.5% (v/v) DMSO in medium was added to reach final concentration of 1  $\mu$ M for both BioTracker Carbon Monoxide Probe 1 Live Cell Dye and Pd(II)Cl<sub>2</sub>. The cells were incubated for 30 min and subsequently washed thrice with PBS prior to imaging for brightfield and green fluorescence in the IncuCyte S3 Live-Cell Analysis System (Sartorius AG, DE) at 10X magnification. The amount of green counts/well and the confluence were determined using the IncuCyte 2019B Rev2 software (Sartorius AG, DE). For data analysis, the green counts/well were normalized to the confluence, followed by normalization to the DMSO control. The quantified data was represented using GraphPad Prism 9.0 (GraphPad Software, Inc, US).

### 8.2.17 Bilirubin Quantification

SKOV-3 cells ( $1 \times 10^5$  cells/well) were seeded in transparent 24-well plates and incubated for 24 h. Afterwards, cells were treated with 50 ng/mL IFN- $\gamma$ , hemin and compound prior to incubation for 24 to 72 h. 500  $\mu$ L of the supernatant was transferred to a new tube and mixed with 250 mg of BaCl<sub>2</sub> by vortexing for 10-15 s. Then, 750  $\mu$ L of benzene was added and the samples were vortexed for 50-60 s, resulting in a white emulsion. The benzene layer was collected by centrifugation at 13,000 x g and room temperature for 30 min and the absorbance

## Experimental Part

at 450 nm and 620 nm as reference wavelength were determined on the Spark® Multimode Microplate Reader (Tecan, AT). The quantity of bilirubin was calculated with the Lambert–Beer law and the molar attenuation coefficient of bilirubin dissolved in benzene ( $\epsilon_{450} = 27.3 \text{ mM}^{-1} \text{ cm}^{-1}$ )<sup>217</sup> and represented using GraphPad Prism 9.0 (GraphPad Software, Inc, US).

### 8.2.18 TrxR Assay

HeLa cells ( $1 \times 10^6$  cells/dish) were seeded in 15-cm dishes and incubated for 48 h. Subsequently, the medium was removed and the cells were washed with 10 mL warm PBS prior to harvesting in 5 mL cold PBS using a rubber policeman. The cell suspension was centrifuged for 5 min at  $300 \times g$  and  $4^\circ\text{C}$  and resuspended in TrxR extraction buffer ( $150 \mu\text{L}/5 \text{ mL}$  cells suspension) prior to cell lysis with seven consecutive freeze/thaw cycles as described in 8.2.13.3. The lysates were centrifuged for 15 min at  $10,000 \times g$  and  $4^\circ\text{C}$  and the supernatant was transferred to a new LoBind tube. The protein concentration was determined with the DC protein assay as in 8.3.2. If necessary, the lysates were snap-frozen in liquid nitrogen and stored at  $-80^\circ\text{C}$ .

The activity of thioredoxin reductase (TrxR) was measured with the Thioredoxin Reductase Colorimetric Assay Kit (cat# 10007892, Cayman, US) following the manufacturer's protocol. Briefly,  $400 \mu\text{g}$  of cell lysate was treated with  $20 \mu\text{M}$  compounds and the reaction was initiated by addition of NADPH and Ellman's reagent (DTNB, 5,5'-dithiobis-(2-nitrobenzoic acid)). After 10 s, the absorbance at 405 nm was recorded once every minute over 15 min on the Spark® Multimode Microplate Reader (Tecan, AT), the background was subtracted from all values and normalized to the DMSO control.

### 8.2.19 RNA Interference

For genetic target validation, cells were transfected with on-target or non-targeting siRNA using the DharmaFECT 1 transfection reagent (cat# T-2001-03, Horizon Discovery, UK). The ON-TARGETplus Human EPHX2 siRNA SMARTPool (cat# L-010006-00-0005, Horizon Discovery, UK) and ON-TARGETplus Non-targeting Control siRNAs (cat# D-001810-01-05, Horizon Discovery, UK) were reconstituted in RNase-free water to concentrations of 10 and  $20 \mu\text{M}$ , respectively. HeLa cells ( $150,000$  cells/well) were seeded in 6-well plates in a total volume of 2 mL and incubated for 24 h. On the next day, the siRNA was diluted to  $2 \mu\text{M}$  in Opti-MEM in a total volume of  $50 \mu\text{L}$  (final siRNA concentration: 50 nM).  $6 \mu\text{L}$  of the DharmaFECT 1 reagent was mixed with  $44 \mu\text{L}$  of Opti-MEM ( $6 \mu\text{L}$  DharmaFECT 1/well) and both siRNA and transfection reagent were incubated for 5 min at room temperature prior to addition of the DharmaFECT solution to the siRNA solution. The transfection mixture was incubated for another 20 min at room temperature to allow formation of the siRNA:lipid complex. Subsequently, 1.9 mL of culture medium was added to the transfection mixture and

## Experimental Part

the culture medium on the cells was replaced by the transfection mixture. The cells were incubated for up to 96 h. To quantify Kyn levels, 100  $\mu$ L of the supernatant was transferred to a transparent 96-well plate and the Kyn assay was performed as described in 8.2.7.2. The remaining supernatant was aspirated and the cells were prepared for immunoblotting (see 8.2.13.2 and 8.3.3) or qPCR analysis (see 8.2.11).

### 8.3 Molecular Biology, Biochemical and Biophysical Methods

#### 8.3.1 Isolation of Plasmids

Plasmids were isolated from pelleted chemically competent *E. coli* strain One Shot OmniMAX™ 2 T1<sup>R</sup> (Thermo Fisher Scientific Inc, US) using the QIAGEN® Plasmid Purification Maxi Kit (QIAGEN, DE) following the manufacturer's protocol. Briefly, cells were lysed under alkaline conditions, followed by isolation of the plasmid DNA on a resin under low-salt and low-pH conditions. Impurities were removed by medium-salt wash steps prior to the elution of the plasmid in high-salt buffer and desalting by isopropanol precipitation. The isolated plasmids were resuspended in sterile water and the DNA concentration was determined by measuring the absorbance at 260 nm with the NanoDrop™ 2000 Spectrophotometer (Thermo Fisher Scientific Inc, US).

#### 8.3.2 Determination of Protein Concentrations

Protein concentrations were determined using the colorimetric DC Protein Assay (Bio-Rad Laboratories, Inc., US) following the manufacturer's protocol. Briefly, the peptide bonds of the proteins react with copper(II) ions in the alkaline reaction solution, leading to reduction of Cu(II) to Cu(I) and to oxidation of the peptide bond, followed by reduction of the Folin reagent and oxidation of aromatic amino acids. The protein concentration can be determined by measuring the absorbance at 750 nm on the Spark® Multimode Microplate Reader (Tecan, AT) and comparing to a standard protein of known concentration.

#### 8.3.3 Immunoblotting

15 to 100  $\mu$ g total protein was separated by molecular weight using discontinuous 10% polyacrylamide gels or Any kD™ Mini-PROTEAN® TGX Stain-Free™ Protein Gels (Bio-Rad Laboratories, DE) under reducing/denaturing conditions in a TRIS/glycine-based system (30 min at 80 V, 45 to 60 min at 150 V). PVDF membranes were activated in methanol for 5 s, washed with ddH<sub>2</sub>O for 10 min and equilibrated in transfer buffer. Afterwards, proteins from the polyacrylamide gels were transferred to the PVDF membranes for 60 min at 100 V (Thermo Fisher Scientific, USA) using wet tank transfer in a Mini Trans-Blot® Cell (Bio-Rad Laboratories, DE). Subsequently, the membranes were blocked with primary antibody-specific blocking conditions (see 8.1.7) for 60 min at room temperature, followed by overnight

## Experimental Part

incubation at 4°C with the primary antibodies. On the next day, membranes were washed thrice with PBS-T for 5 min each and incubated with the secondary antibodies for 60 min. Subsequently, the membranes were washed twice with PBS-T and twice with PBS for 5 min each prior to visualization of the protein bands using the ChemiDoc MP Imaging System (Bio-Rad Laboratories, DE). Protein band intensities were quantified using ImageLab (Bio-Rad, US) or ImageJ (open source). Protein levels of the protein of interest were normalized to the reference protein.

### 8.3.4 Purification of Recombinant IDO1

*Expression and purification of human recombinant IDO1 were performed by Dr. Elisabeth Hennes and Christine Nowak.*

#### 8.3.4.1 Full-length Recombinant Human IDO1

Full-length recombinant human GST-IDO1 protein was expressed in *E. coli* BL21 DE3 cells using a pGEX6p-2rbs-GST-IDO1-FL vector as described previously<sup>350, 352</sup>. Bacteria were transformed with the vector by a heat shock at 42°C for 60 s and cells derived from a single colony were used to inoculate LB medium containing 100 µg/mL ampicillin and 30 µg/mL chloramphenicol prior to incubation overnight at 37°C with rotation. On the next day, 2,500 mL LB medium was inoculated with 50 mL of the bacteria suspension and IDO1 protein expression was induced by addition of 200 µM isopropyl β-d-1-thiogalactopyranoside (IPTG) prior to incubation at 18°C overnight.

Afterwards, the cells were pelleted by centrifugation at 3600 x g and 4°C for 20 min and resuspended in protein expression buffer 3 and homogenized by sonication, followed by mechanical cell lysis. The soluble fraction was separated from the cell debris by centrifugation at 13,000 x g and 10°C for 35 min and transferred to a GSTrap™ HP column (Cytiva, US). GST-IDO1 was washed on column with buffer 4, followed by on-column cleavage overnight with 3.2 mg/mL PreScission protease (Cytiva, US) in PreScission protease buffer. The eluted protein was purified by size exclusion chromatography with a HiLoad™ 16/600 Superdex™ 200 pg column (Cytiva, US) and purity of the protein was confirmed by SDS-PAGE.

#### 8.3.4.2 Truncated Recombinant Human IDO1

For crystallization experiments, a truncated version of recombinant human IDO1<sup>5-400</sup> of the 403 amino acid-long full-length human IDO1 was expressed in *E. coli* BL21 DE3 cells using a pGEX6p-2rbs-GST-IDO1-short vector and purified as described in 8.3.4.1.

After purification of the protein, the heme cofactor in the active site of IDO1 was removed to obtain recombinant human apo-IDO1 as described previously.<sup>256</sup> Therefore, the purified IDO1 protein was incubated with 166 mM 2-mercaptoethanesulfonate (MESNA) overnight to release the heme cofactor. On the next day, the protein was diafiltered and concentrated

## Experimental Part

against buffer 5 using an Amicon® Ultra-4 10K Centrifugal Filter (Merck Millipore Ltd., US). Heme occupancy was determined by UV/Vis spectrophotometry as described in 8.3.8.

### 8.3.5 Enzymatic Kyn Assay

To detect direct inhibition, 1  $\mu$ M rhIDO1 was incubated with compounds for 40 min at 37°C in 50 mM potassium phosphate buffer. Subsequently, 10 mM ascorbic acid, 10  $\mu$ M methylene blue, 2 mM Trp and 100  $\mu$ g/mL catalase were added and samples were incubated for 60 min at room temperature or 37°C. Trichloroacetic acid was added to a final concentration of 7% (v/v) and samples were incubated for 30 min at 70°C. Afterwards, an equal volume of freshly prepared 2% (w/v) p-DMAB in glacial acetic acid (Ehrlich reagent) was added prior to measuring absorbance at 492 nm and 650 nm on the Spark® Multimode Microplate Reader (Tecan, AT). To determine the Kyn levels, the absorbance of the Kyn-p-DMAB adduct  $A_{492}$  was subtracted by the background absorbance  $A_{650}$  and normalized to the DMSO control. Data analysis was performed using a non-linear regression curve fit and GraphPad Prism 9.0 (GraphPad Software, Inc, US) to generate dose-response curves and obtain  $IC_{50}$  values.

### 8.3.6 Crystallization of apo-IDO1

#### Crystallization of apo-IDO1

A truncated version of the 403 amino acid-long full-length recombinant human GST-IDO1 (rhIDO1<sup>5-400</sup>) was expressed in *E. coli* and purified as published previously (see 8.3.4.2)<sup>352</sup>. The heme cofactor was released from IDO1 by overnight incubation with MESNA as described previously (see 8.3.4.2)<sup>348</sup> and heme occupancy was determined by UV/Vis spectrophotometry (see 8.3.8).

450  $\mu$ M of IDO1 protein was mixed with 750  $\mu$ M apoxidole-1 (2.5% (v/v) DMSO) in 25 mM TRIS-HCl, pH 8.0, 100  $\mu$ M tris(2-carboxyethyl)phosphine (TCEP) and incubated for 2 h at 42°C. The soluble protein fraction was separated from the precipitate by centrifugation at 20,000 x g and 18°C for 10 min. Protein crystals were obtained from a sitting drop setup (iQ plates, SPT Labtech, UK) by addition of 100 nL of the reservoir solution (40% (v/v) PEG200 in 100 mM MES, pH 6.5) to 100 nL of protein solution and incubation at 20°C. Crystals were harvested after 7 days by the addition of reservoir solution as cryoprotectant to the drop prior to plunging of the crystals in liquid nitrogen. Synchrotron X-ray diffraction data was acquired to 1.6 Å from the X10SA beamline at the Swiss Light Source at the Paul Scherrer Institute, CH. The data was processed with XDS<sup>353</sup> and scaled using XSCALE. The structure was solved using a model of IDO1 from pdb 6dpq with Phaser<sup>354</sup> from the Phenix suite<sup>355</sup>, followed by repetitive cycles of refinement with phenix.refine and Coot<sup>356, 357</sup>. Figures were created with PyMOL Molecular Graphics System (Version 2.5.2 Schrödinger, LLC).

The integrity of apoxidole-1 in the protein solution was assessed 63 days after the crystallization setup by mixing the crystallization drop with 100  $\mu$ L of DCM and recording of

## Experimental Part

HPLC-ESI-MS spectra using the LTQ Fleet (Thermo Fisher Scientific, US), Ultimate 3000 HPLC (Thermo Fisher Scientific, US) and Xcalibur™ software (Thermo Fisher Scientific, US).

**Table 6:** HPLC method.

time [min]	%A	%B
0	90	10
0.5	90	10
7.5	5	95
9.0	5	95
11	90	10

A: ddH<sub>2</sub>O + 0.1% (v/v) formic acid; B: acetonitrile + 0.1% (v/v) formic acid; flow rate:0.4 mL/min.

### 8.3.7 Stability of Apoxidole-1 in Serum

400 µM of apoxidole-1 was incubated in Gibco® Qualified FBS (Thermo Fisher Scientific, Inc, US) at 37°C for up to 48 h. Samples of 50 µL were taken after 0, 6, 10, 24, 30 and 48 h, 200 µL of DCM was added and the compound was extracted by thorough vortexing for 1 min. Subsequently, the samples were centrifuged at 16,000 x g and 22°C for 15 min. The organic phase was dried with magnesium sulfate and filtered through a HPLC filter prior to HPLC-ESI-MS analysis using the LTQ Fleet (Thermo Fisher Scientific, US), Ultimate 3000 HPLC (Thermo Fisher Scientific, US) and Xcalibur™ software (Thermo Fisher Scientific, US) as described in 8.3.6 and Table 6.

### 8.3.8 UV/Vis Spectrophotometry

10 µM rhIDO1 was incubated with the compounds at the indicated concentrations for 120 min at 37°C in 50 mM potassium phosphate buffer using UV-transparent microplates (UV-STAR®, Greiner AG, AT). Subsequently, absorbance spectra from 250 nm to 550 nm were recorded on the Spark® Multimode Microplate Reader (Tecan, AT).

### 8.3.9 Nano Differential Scanning Fluorimetry (nanoDSF)

#### 8.3.9.1 IDO1

11 µM rhIDO1 was incubated with the compounds at the indicated concentrations for 60 min at 37°C in 50 mM potassium phosphate buffer. The thermal protein stability from 20°C to 90°C (1°C/min) was measured by means of the intrinsic tryptophan/tyrosine fluorescence using standard capillaries in the Prometheus™ NT.48 (NanoTemper® Technologies, DE). Melting scans, first derivatives of melting scans and melting temperatures were analyzed using the PR.ThermControl software (NanoTemper® Technologies, DE). Binding affinities were determined by plotting the melting temperature against the ligand concentration and fitting with a single site ligand binding function using GraphPad Prism 9.0 (GraphPad Software, Inc, US).

#### 8.3.9.2 sEH

rhsEH (cat# 600037, Cayman, US, from the Soluble Epoxide Hydrolase Inhibitor Screening Assay Kit, see 8.3.12) was diluted 18-fold in AttoPhos assay buffer and incubated with the

## Experimental Part

compounds at the indicated concentrations for 10 min at 22°C. The thermal protein stability from 20°C to 90°C (1°C/min) was measured by means of the intrinsic tryptophan/tyrosine fluorescence using high sensitivity capillaries in the Prometheus™ NT.48 (NanoTemper® Technologies, DE). Melting scans, first derivatives of melting scans and melting temperatures were analyzed using the PR.ThermControl software (NanoTemper® Technologies, DE).

### 8.3.10 TDO Activity Assay

Inhibition of tryptophan 2,3-dioxygenase (TDO) was tested using the Universal IDO1/IDO2/TDO Inhibitor Screening Assay Kit (cat# 72035, BPS Bioscience, US). 500 ng His-tagged TDO in TDO Assay Buffer was incubated with Reaction Solution and 50 µM compounds (0.5% (v/v) DMSO) for 120 min at 37°C with slow shaking in the dark. Afterwards, absorbance at 321 nm was recorded on the Spark® Multimode Microplate Reader (Tecan, AT), the background was subtracted from all values and normalized to the DMSO control.

### 8.3.11 IDO2 Activity Assay

Inhibition of indoleamine 2,3-dioxygenase 2 (IDO2) was tested using the Universal IDO1/IDO2/TDO Inhibitor Screening Assay Kit (cat# 72035, BPS Bioscience, US). 10 µg His-tagged IDO2 in IDO2 Assay Buffer was incubated with Complete IDO2 Reaction Solution (1% (v/v) component 2 in component 1) and 50 µM compounds (0.5% (v/v) DMSO) for 90 min at 30°C with slow shaking in the dark prior to initiation of the reaction by addition of 20% (v/v) IDO2 Substrate. Samples were incubated for 120 min at 30°C with slow shaking in the dark. Afterwards, absorbance at 321 nm was recorded on the Spark® Multimode Microplate Reader (Tecan, AT), the background was subtracted from all values and normalized to the DMSO control.

### 8.3.12 sEH-H Activity Assay

Inhibition of the C-terminal lipid epoxide hydrolase domain of the soluble epoxide hydrolase (sEH-H) was tested using the Soluble Epoxide Hydrolase Inhibitor Screening Assay Kit (cat# 10011671, Cayman, US). Briefly, 2.5 µL of 50-fold diluted sEH protein was treated with the compounds at the indicated concentrations and the reaction was initiated by addition of 250 nM fluorogenic sEH-H substrate PHOME ((3-phenyl-oxiranyl)-acetic acid cyano-(6-methoxy-naphthalen-2-yl)-methyl ester). The final volume for the assay was 100 µL in all wells. After 10 s, the fluorescence was recorded using an excitation wavelength at 330 nm and an emission wavelength at 465 nm at 25°C on the Spark® Multimode Microplate Reader (Tecan, AT) for up to 30 min in a kinetic loop with intervals of 90 s between measurements. The background was subtracted from all values and all values were normalized to the initial activity of each condition.



## Experimental Part

### 8.3.13 sEH-P Activity Assay

Inhibition of the N-terminal lipid phosphatase domain of the soluble epoxide hydrolase (sEH-P) was tested using an AttoPhos-based assay as described previously<sup>220</sup>. 5  $\mu\text{L}$  of 50-fold diluted sEH protein (cat# 600037, Cayman, US, from the Soluble Epoxide Hydrolase Inhibitor Screening Assay Kit, see 8.3.12) was incubated with compounds at indicated concentrations in AttoPhos assay buffer for 5 min at 23°C prior to addition of 7.5  $\mu\text{L}$  AttoPhos solution (final concentration 25  $\mu\text{M}$ ). The samples were incubated for 60 min at 23°C in the dark under mild shaking. Afterwards, 25  $\mu\text{L}$  of AttoPhos stop solution was added and the fluorescence was recorded using an excitation wavelength at 435 nm and an emission wavelength at 555 nm on the Spark® Multimode Microplate Reader (Tecan, AT) for up to 30 min in a kinetic loop with intervals of 90 s between measurements. The final volume for the assay was 75  $\mu\text{L}$  in all wells. The background was subtracted from all values and normalized to the DMSO control.

## 8.4 Proteomics Methods

*The preparation, measurement and analysis of HRMS samples were performed by Jens Warmers, Andreas Brockmeyer, Malte Metz and Dr. Petra Janning.*

### 8.4.1 Global Proteome Profiling

BxPC-3 cells ( $5 \times 10^6$  cells/flask) were seeded per T75 flask and incubated for 24 h at 37°C and 5%  $\text{CO}_2$  in humidified atmosphere. On the following day, the medium was exchanged for 6 mL fresh culture medium containing either i) 0.3% (v/v) DMSO, ii) 0.3% (v/v) DMSO and 50 ng/mL IFN- $\gamma$  or iii) 3  $\mu\text{M}$  compound and 50 ng/mL IFN- $\gamma$  prior to incubation for 24 h. The cells were harvested by trypsinization and resuspended in ice-cold PBS before washing thrice in 10, 5 and 1 mL cold PBS, respectively. The cell pellets were resuspended in 100  $\mu\text{L}$  PBS containing protease and phosphatase inhibitors and lysed by seven consecutive freeze/thaw cycles as described in 8.2.13.3. The protein concentration was determined as described in 8.3.2 and the lysates were snap-frozen in liquid nitrogen and stored at -80°C until further usage. 75  $\mu\text{L}$  of lysate containing 150  $\mu\text{g}$  total protein were subjected to in-solution tryptic digestion as described in 8.4.4.

### 8.4.2 Thermal Proteome Profiling

HeLa cells ( $5.54 \times 10^5$  cells/flask) were seeded per T175 flask and incubated for 72 h at 37°C and 5%  $\text{CO}_2$  in humidified atmosphere. The medium was exchanged for fresh culture medium containing 50 ng/mL IFN- $\gamma$  prior to incubation for 24 h. The cells were harvested by trypsinization and resuspended in ice-cold PBS before washing thrice in 10, 8 and 1 mL ice-cold PBS, respectively. The cell pellets were resuspended in 500  $\mu\text{L}$  PBS containing 0.4% (v/v) NP40 alternative, lysed by five consecutive freeze/thaw cycles as described in 8.2.13.3 and ultra-centrifuged for 20 min at 100,000  $\times g$  and 4°C. The protein concentration of the

## Experimental Part

supernatant was determined using the *DC* protein assay as described in 8.3.2 and the lysates were snap-frozen in liquid nitrogen and stored at -80°C until further usage.

1.4 mL of lysate with a protein concentration of 4 g/L was added to two LoBind tubes and incubated with either DMSO (V, vehicle, 0.3% (v/v)) or 3  $\mu$ M compound (C, compound) for 10 min at room temperature. 120  $\mu$ L of V- or C-treated lysate were added to PCR tubes and subjected to heating at different temperatures (Table 7) in the MasterCycler EpGradient S (Eppendorf SE, DE). Soluble fractions were separated from denatured proteins by ultra-centrifugation at 100,000 x g and 4°C for 20 min. 100  $\mu$ L of the supernatants were transferred to new tubes and subjected to in-solution tryptic digestion as described in 8.4.4. For quantification of the soluble protein fraction, protein band intensities for C- and V-treated samples were normalized to the lowest temperature of each condition (36.9°C) and thermal denaturation temperatures  $T_m$  were determined using non-linear regression curve fit.

**Table 7:** Temperature gradient for thermal proteome profiling experiments.

<b>cycler 1/°C</b>	36.9	40.1	44.1	47.9	51
<b>cycler 2/°C</b>	54.4	58	61.3	64.5	67

### 8.4.3 Affinity-based Chemical Proteomics

HeLa cells ( $5.54 \times 10^5$  cells/flask) were seeded per T175 flask and incubated for 72 h at 37°C and 5% CO<sub>2</sub> in humidified atmosphere. The medium was exchanged for fresh culture medium containing 50 ng/mL IFN- $\gamma$  prior to incubation for 24 h. The cells were harvested by trypsinization and resuspended in ice-cold PBS before washing thrice in 10, 8 and 1 mL cold PBS, respectively. The cell pellets were resuspended in 500  $\mu$ L NP40-based lysis buffer, lysed according to 8.2.13.2 and ultra-centrifuged for 20 min at 100,000 x g and 4°C. The protein concentration of the supernatant was determined as described in 8.3.2 and the lysates were snap-frozen in liquid nitrogen and stored at -80°C until further usage.

25  $\mu$ L of NHS Mag Sepharose beads (Cytiva 28-9440-09) were resuspended in 500  $\mu$ L ice-cold equilibration buffer by inversion and the equilibration buffer was removed prior to addition of 500  $\mu$ L of 10  $\mu$ M free-amine pulldown probe in coupling buffer (0.1% (v/v) DMSO). The beads were coated with the probes by overhead rotation for 1 h at room temperature. Subsequently, the residual active groups were quenched by i) addition of 500  $\mu$ L blocking buffer 1, inversion of the tubes and removal of buffer, ii) addition of 500  $\mu$ L blocking buffer 2, inversion of the tubes and removal of buffer, iii) addition of 500  $\mu$ L blocking buffer 1, overhead rotation for 15 min and removal of buffer, iv) addition of 500  $\mu$ L blocking buffer 2, inversion of the tubes and removal of buffer, v) addition of 500  $\mu$ L blocking buffer 1, inversion of the tubes and removal of buffer, vi) addition of 500  $\mu$ L blocking buffer 2, inversion of the tubes and removal of buffer.

## Experimental Part

After the compound immobilization, the beads were washed with 500  $\mu\text{L}$  NP40-based lysis buffer and 500  $\mu\text{L}$  of lysate with a protein concentration of 3 g/L was added to the beads prior to incubation with overhead rotation for 2 h at 4°C or 1 h at room temperature, respectively. For competition experiments, the cell lysate was pre-incubated with 10  $\mu\text{M}$  unmodified compound for 1 h at room temperature prior to addition to the beads. Subsequently, the supernatant was removed and the beads were washed twice with washing buffer and twice with PBS for 10 min under overhead rotation. The supernatant was removed and the samples were subjected to on-bead tryptic digestion according to 8.4.5.

### 8.4.4 In-Solution Tryptic Digestion

Cell lysates were diluted in 75  $\mu\text{L}$  of 100 mM TEAB prior to addition of 7.5  $\mu\text{L}$  denaturing/reducing buffer 1 and incubation for 1 h at 55°C. Afterwards, 7.5  $\mu\text{L}$  of alkylation buffer 1 was added and the samples were incubated at room temperature for 30 min in the dark. Six volumes (990  $\mu\text{L}$ ) of ice-cold acetone was added and proteins were precipitated at -20°C overnight.

On the following day, the samples were centrifuged for 10 min at 4°C and 8,000  $\times$  g. The supernatant was discarded and the pellets were air-dried for 30 to 45 min. The proteins were resuspended in 107.5  $\mu\text{L}$  digestion buffer 1 ( $\cong$  3  $\mu\text{g}$  trypsin) and digested for 2 to 3 h at 37°C prior to thorough mixing and continued incubation overnight. Subsequently, the samples were labeled with isobaric TMT10plex labels (ThermoFisher Scientific 90110). One vial of 0.8 mg TMT labels was dissolved in 82  $\mu\text{L}$  of anhydrous acetonitrile by occasional vortexing over 5 min. Using a gas-tight Hamilton syringe, 41  $\mu\text{L}$  of the respective label solution was transferred to 100  $\mu\text{L}$  of the C- or V-treated peptide sample and mixed thoroughly. After each pipetting step, the syringe was washed with acetonitrile. The samples were incubated for 2 h at room temperature prior to quenching of the reaction by addition of 8  $\mu\text{L}$  of 5% (v/v) hydroxylamine. 120  $\mu\text{L}$  of all C- or V-treated samples were combined, yielding two samples from which the solution was evaporated using a vacuum concentrator at 30°C. The pellets were dissolved in 120  $\mu\text{L}$  20 mM  $\text{NH}_4\text{COO}$  (pH 11) by ultrasonication for 2 min and subsequent vortexing for 1 min, followed by short centrifugation. 110  $\mu\text{L}$  of each sample were fractionated by HPLC at high pH value into ten fractions and evaporated using a vacuum concentrator at 30°C. The fractions were dissolved in 0.1% TFA and enriched and separated by nanoHPLC-MS/MS using two consecutive PepMap™ 100 C18 columns (ThermoFisher Scientific, US). The mass spectra were acquired using a hybrid-orbitrap mass spectrometer (ThermoFisher Scientific, US) Signals in the mass range of  $m/z$  300 to 1650 were measured for full scan (MS1), followed by 10 to 15 high-energy collision dissociation (HCD) scans (MS2) of the most intense at least doubly charged ions. Data and statistical data analysis were performed using MaxQuant<sup>358, 359</sup> and Perseus<sup>360, 361</sup>. Briefly, the data was analyzed using the

## Experimental Part

Andromeda search algorithm, the Homo sapiens reference proteome of the UniProt database and a MaxQuant contaminant database. Therefore, an MS/MS ion search was performed for enzymatic trypsin cleavage, allowing two missed cleavages. Carbamidomethylation was set as a fixed protein modification and oxidation of methionine and acetylation of the N-terminus were set as variable modifications. Only proteins for which at least two peptides were quantified were chosen for further validation.

For the TPP experiment, an in-house Excel macro<sup>136</sup> was used to generate TPP curves. Briefly, the soluble protein fraction was quantified according to the intensities of the lowest temperature (36.9°C) of each compound- and vehicle-treated condition. The thermal denaturation temperatures  $T_m$  were determined as the inflection point of a non-linear regression curve fit.

For the global proteome profiling, statistical data analysis was performed using Perseus<sup>360, 361</sup> including proteins which were identified in at least two out of three technical replicates in at least two of the three compared conditions. Relative quantification of proteins was performed by using the label-free quantification (LFQ) algorithm implemented in MaxQuant. LFQ intensities were log-transformed (log2); replicate samples were grouped together. Missing values were imputed using small normally distributed values, and a two-tailed *t*-test was performed. Volcano plots were generated using the VolcanoR<sup>184, 185</sup> web app.

### 8.4.5 On-Bead Tryptic Digestion

The beads were resuspended in 50  $\mu$ L denaturing/reducing buffer 2 and incubated for 30 min at room temperature. Afterwards, 5.55  $\mu$ L of alkylation buffer 2 was added and the samples were incubated for 30 min at room temperature prior to addition of 1  $\mu$ g Lys-C (0.5  $\mu$ g/ $\mu$ L in ddH<sub>2</sub>O) and incubation for 1 h at 37°C. The supernatant was transferred to new LoBind tubes. 165  $\mu$ L digestion buffer 2 ( $\cong$  1  $\mu$ g trypsin) was added to the beads and incubated for 1 h at 37°C. The supernatants from both the Lys-C and trypsin digestion were combined and another 1-2  $\mu$ g trypsin was added. The digestion was proceeded overnight at 37°C and the reaction was stopped on the next day by addition of 10% (v/v) TFA. The peptides were desalted by StageTip Purification as described in 8.4.6.

### 8.4.6 StageTip Purification of Peptides

Two layers of Empore<sup>TM</sup> High Performance Extraction C18 Disks (3M Bioanalytical Technologies, US) were stacked on top of each other in a 200  $\mu$ L pipette tip using a syringe. The filters were activated by addition of 100  $\mu$ L methanol and centrifugation until all liquid has passed through the disks. The filters were washed and equilibrated once with 100  $\mu$ L of StageTip Buffer 1 and twice with 100  $\mu$ L of StageTip Buffer 2 prior to loading of the samples from 8.4.5 and incubation for 1 min. The solution was removed by centrifugation and the filters were washed with 100  $\mu$ L of StageTip Buffer 1. 20  $\mu$ L of StageTip Buffer 2 were added and

## Experimental Part

samples were incubated for 1 min prior to elution of the sample into a new LoBind tube by centrifugation at 1,500 x g for 5 min. The previous step was repeated once and the supernatants were combined prior to evaporating using a vacuum concentrator at 30°C. The dried peptides were dissolved in 0.1% TFA and enriched and separated by nanoHPLC-MS/MS using two consecutive PepMap™ 100 C18 columns (ThermoFisher Scientific, US). The mass spectra were acquired using a hybrid-orbitrap mass spectrometer (ThermoFisher Scientific, US) Signals in the mass range of m/z 300 to 1650 were measured for full scan (MS1), followed by 10 to 15 high-energy collision dissociation (HCD) scans (MS2) of the most intense at least doubly charged ions. Data analysis was performed using MaxQuant<sup>358, 359</sup>. Briefly, the data was analyzed using the Andromeda search algorithm, the Homo sapiens reference proteome of the UniProt database and a MaxQuant contaminant database. Therefore, an MS/MS ion search was performed for enzymatic trypsin cleavage, allowing two missed cleavages. Carbamidomethylation was set as a fixed protein modification and oxidation of methionine and acetylation of the N-terminus were set as variable modifications. The false discovery rates (FDR) for peptide and protein identification were set to 0.01. Only proteins for which at least two peptides were quantified were chosen for further validation. Relative quantification of proteins was performed by using the label-free quantification (LFQ) algorithm implemented in MaxQuant.

Statistical data analysis of pulldown samples was performed separately for biological replicates (four technical replicates each) using Perseus<sup>360, 361</sup> including proteins which were identified in at least three out of four technical replicates in at least one of the two compared conditions. LFQ intensities were log-transformed (log<sub>2</sub>); replicate samples were grouped together. Missing values were imputed using small normally distributed values, and a two-sided t-test was performed. Volcano plots were generated using the VolcanoR<sup>184, 185</sup> web app.

## 9 References

1. International Agency for Research on Cancer (World Health Organization), Global Cancer Observatory. <https://gco.iarc.fr/> (accessed 23.03.2023).
2. Chhikara, B. S.; Parang, K., Global Cancer Statistics 2022: the trends projection analysis. *Chem Biol Lett* **2022**, *10* (1), 451.
3. National Cancer Institute (National Institute of Health). <https://www.cancer.gov/> (accessed 23.03.2023).
4. Wang, S.; Xie, K.; Liu, T., Cancer Immunotherapies: From Efficacy to Resistance Mechanisms - Not Only Checkpoint Matters. *Front Immunol* **2021**, *12*, 690112.
5. Ehrlich, P., *Ueber den jetzigen Stand der Karzinomforschung*. Ned. Tijdschr. Geneeskd.: 1908; Vol. 5.
6. Burnet, F., Cancer: a biological approach. III. Viruses associated with neoplastic conditions. IV. Practical applications. *British medical journal* **1957**, *1* (5023), 841-7.
7. Thomas, L.; Lawrence, H., Cellular and humoral aspects of the hypersensitive states. *New York: Hoeber-Harper* **1959**, 529-32.
8. Burnet, F., The concept of immunological surveillance. *Prog Exp Tumor Res* **1970**, *13*, 1-27.
9. Burnet, F., Immunological factors in the process of carcinogenesis. *Br Med Bull* **1964**, *20* (2), 154-158.
10. Hanahan, D.; Weinberg, R. A., Hallmarks of cancer: the next generation. *Cell* **2011**, *144* (5), 646-74.
11. Swann, J. B.; Smyth, M. J., Immune surveillance of tumors. *J Clin Invest* **2007**, *117* (5), 1137-46.
12. Chang, R. B.; Beatty, G. L., The interplay between innate and adaptive immunity in cancer shapes the productivity of cancer immunosurveillance. *Journal of leukocyte biology* **2020**, *108* (1), 363-376.
13. Chen, D. S.; Mellman, I., Oncology meets immunology: the cancer-immunity cycle. *Immunity* **2013**, *39* (1), 1-10.
14. Dunn, G. P.; Old, L. J.; Schreiber, R. D., The Three Es of Cancer Immunoediting. *Ann Rev Immunol* **2004**, *22* (1), 329-360.
15. Dunn, G. P.; Bruce, A. T.; Ikeda, H.; Old, L. J.; Schreiber, R. D., Cancer immunoediting: from immunosurveillance to tumor escape. *Nat Immunol* **2002**, *3* (11), 991-998.
16. Mountford, A. P.; Coulson, P. S.; Cheever, A. W.; Sher, A.; Wilson, R. A.; Wynn, T. A., Interleukin-12 can directly induce T-helper 1 responses in interferon-gamma (IFN-gamma) receptor-deficient mice, but requires IFN-gamma signalling to downregulate T-helper 2 responses. *Immunology* **1999**, *97* (4), 588-94.
17. Jacobson, N. G.; Szabo, S. J.; Weber-Nordt, R. M.; Zhong, Z.; Schreiber, R. D.; Darnell, J. E., Jr.; Murphy, K. M., Interleukin 12 signaling in T helper type 1 (Th1) cells involves tyrosine phosphorylation of signal transducer and activator of transcription (Stat)3 and Stat4. *J Exp Med* **1995**, *181* (5), 1755-62.
18. Ostrand-Rosenberg, S., Immune surveillance: a balance between protumor and antitumor immunity. *Curr Opin Genet Dev* **2008**, *18* (1), 11-18.
19. Castro, F.; Cardoso, A. P.; Gonçalves, R. M.; Serre, K.; Oliveira, M. J., Interferon-Gamma at the Crossroads of Tumor Immune Surveillance or Evasion. *Front Immunol* **2018**, *9*.
20. Gabrilovich, D. I.; Nagaraj, S., Myeloid-derived suppressor cells as regulators of the immune system. *Nat Rev Immunol* **2009**, *9* (3), 162-174.
21. Prendergast, G. C., Immune escape as a fundamental trait of cancer: focus on IDO. *Oncogene* **2008**, *27* (28), 3889-3900.
22. Anderson, N. M.; Simon, M. C., The tumor microenvironment. *Current biology : CB* **2020**, *30* (16), R921-r925.

## References

23. Piñeiro Fernández, J.; Luddy, K. A.; Harmon, C.; O'Farrelly, C., Hepatic Tumor Microenvironments and Effects on NK Cell Phenotype and Function. *Int J Mol Sci* **2019**, *20* (17).
24. Mijatović, S.; Savić-Radojević, A.; Plješa-Ercegovac, M.; Simić, T.; Nicoletti, F.; Maksimović-Ivanić, D., The Double-Faced Role of Nitric Oxide and Reactive Oxygen Species in Solid Tumors. *Antioxidants (Basel, Switzerland)* **2020**, *9* (5).
25. Bussard, K. M.; Mutkus, L.; Stumpf, K.; Gomez-Manzano, C.; Marini, F. C., Tumor-associated stromal cells as key contributors to the tumor microenvironment. *Breast Cancer Res* **2016**, *18* (1), 84.
26. Hanahan, D.; Coussens, Lisa M., Accessories to the Crime: Functions of Cells Recruited to the Tumor Microenvironment. *Cancer Cell* **2012**, *21* (3), 309-322.
27. Gleave, M.; Hsieh, J. T.; Gao, C. A.; von Eschenbach, A. C.; Chung, L. W., Acceleration of human prostate cancer growth in vivo by factors produced by prostate and bone fibroblasts. *Cancer Res* **1991**, *51* (14), 3753-61.
28. Park, J. H.; Richards, C. H.; McMillan, D. C.; Horgan, P. G.; Roxburgh, C. S. D., The relationship between tumour stroma percentage, the tumour microenvironment and survival in patients with primary operable colorectal cancer. *Annals of oncology : official journal of the European Society for Medical Oncology* **2014**, *25* (3), 644-651.
29. Curiel, T. J., Tregs and rethinking cancer immunotherapy. *J Clin Invest* **2007**, *117* (5), 1167-1174.
30. Battle, E.; Massagué, J., Transforming Growth Factor- $\beta$  Signaling in Immunity and Cancer. *Immunity* **2019**, *50* (4), 924-940.
31. Rubtsov, Y. P.; Rasmussen, J. P.; Chi, E. Y.; Fontenot, J.; Castelli, L.; Ye, X.; Treuting, P.; Siewe, L.; Roers, A.; Henderson, W. R., Jr.; Muller, W.; Rudensky, A. Y., Regulatory T cell-derived interleukin-10 limits inflammation at environmental interfaces. *Immunity* **2008**, *28* (4), 546-58.
32. Gondek, D. C.; Lu, L.-F.; Quezada, S. A.; Sakaguchi, S.; Noelle, R. J., Cutting Edge: Contact-Mediated Suppression by CD4+CD25+ Regulatory Cells Involves a Granzyme B-Dependent, Perforin-Independent Mechanism1. *J Immunol* **2005**, *174* (4), 1783-1786.
33. Puccetti, P.; Grohmann, U., IDO and regulatory T cells: a role for reverse signalling and non-canonical NF- $\kappa$ B activation. *Nat Rev Immunol* **2007**, *7* (10), 817-823.
34. Slominski, A.; Semak, I.; Pisarchik, A.; Sweatman, T.; Szczesniowski, A.; Wortsman, J., Conversion of L-tryptophan to serotonin and melatonin in human melanoma cells. *FEBS Letters* **2002**, *511* (1-3), 102-106.
35. Roberts, K. M.; Fitzpatrick, P. F., Mechanisms of tryptophan and tyrosine hydroxylase. *IUBMB life* **2013**, *65* (4), 350-7.
36. Merlo, L. M. F.; DuHadaway, J. B.; Montgomery, J. D.; Peng, W. D.; Murray, P. J.; Prendergast, G. C.; Caton, A. J.; Muller, A. J.; Mandik-Nayak, L., Differential Roles of IDO1 and IDO2 in T and B Cell Inflammatory Immune Responses. *Front Immunol* **2020**, *11*, 1861.
37. Zulfiqar, B.; Mahroo, A.; Nasir, K.; Farooq, R. K.; Jalal, N.; Rashid, M. U.; Asghar, K., Nanomedicine and cancer immunotherapy: focus on indoleamine 2,3-dioxygenase inhibitors. *Onco Targets Ther* **2017**, *10*, 463-476.
38. Albini, E.; Rosini, V.; Gargaro, M.; Mondanelli, G.; Belladonna, M. L.; Pallotta, M. T.; Volpi, C.; Fallarino, F.; Macchiarulo, A.; Antognelli, C.; Bianchi, R.; Vacca, C.; Puccetti, P.; Grohmann, U.; Orabona, C., Distinct roles of immunoreceptor tyrosine-based motifs in immunosuppressive indoleamine 2,3-dioxygenase 1. *J Cell Mol Med* **2017**, *21* (1), 165-176.
39. Orabona, C.; Pallotta, M. T.; Volpi, C.; Fallarino, F.; Vacca, C.; Bianchi, R.; Belladonna, M. L.; Fioretti, M. C.; Grohmann, U.; Puccetti, P., SOCS3 drives proteasomal degradation of indoleamine 2,3-dioxygenase (IDO) and antagonizes IDO-dependent tolerogenesis. *Proc Natl Acad Sci U S A* **2008**, *105* (52), 20828-33.
40. Pallotta, M. T.; Orabona, C.; Volpi, C.; Grohmann, U.; Puccetti, P.; Fallarino, F., Proteasomal Degradation of Indoleamine 2,3-Dioxygenase in CD8 Dendritic Cells is

## References

- Mediated by Suppressor of Cytokine Signaling 3 (SOCS3). *International journal of tryptophan research : IJTR* **2010**, *3*, 91-7.
41. Grohmann, U.; Mondanelli, G.; Belladonna, M. L.; Orabona, C.; Pallotta, M. T.; Iacono, A.; Puccetti, P.; Volpi, C., Amino-acid sensing and degrading pathways in immune regulation. *Cytokine Growth Factor Rev* **2017**, *35*, 37-45.
  42. Lovelace, M. D.; Varney, B.; Sundaram, G.; Lennon, M. J.; Lim, C. K.; Jacobs, K.; Guillemin, G. J.; Brew, B. J., Recent evidence for an expanded role of the kynurenine pathway of tryptophan metabolism in neurological diseases. *Neuropharmacology* **2017**, *112*, 373-388.
  43. Nguyen, N. T.; Nakahama, T.; Le, D. H.; Van Son, L.; Chu, H. H.; Kishimoto, T., Aryl Hydrocarbon Receptor and Kynurenine: Recent Advances in Autoimmune Disease Research. *Front Immunol* **2014**, *5*.
  44. Prendergast, G. C.; Metz, R.; Muller, A. J.; Merlo, L. M.; Mandik-Nayak, L., IDO2 in Immunomodulation and Autoimmune Disease. *Front Immunol* **2014**, *5*, 585.
  45. Ye, Z.; Yue, L.; Shi, J.; Shao, M.; Wu, T., Role of IDO and TDO in Cancers and Related Diseases and the Therapeutic Implications. *J Cancer* **2019**, *10* (12), 2771-2782.
  46. Munn, D. H.; Zhou, M.; Attwood, J. T.; Bondarev, I.; Conway, S. J.; Marshall, B.; Brown, C.; Mellor, A. L., Prevention of allogeneic fetal rejection by tryptophan catabolism. *Science* **1998**, *281* (5380), 1191-3.
  47. Munn, D. H.; Sharma, M. D.; Baban, B.; Harding, H. P.; Zhang, Y.; Ron, D.; Mellor, A. L., GCN2 kinase in T cells mediates proliferative arrest and anergy induction in response to indoleamine 2,3-dioxygenase. *Immunity* **2005**, *22* (5), 633-42.
  48. Munn, D. H.; Mellor, A. L., Indoleamine 2,3-dioxygenase and tumor-induced tolerance. *J Clin Invest* **2007**, *117* (5), 1147-54.
  49. Della Chiesa, M.; Carlomagno, S.; Frumento, G.; Balsamo, M.; Cantoni, C.; Conte, R.; Moretta, L.; Moretta, A.; Vitale, M., The tryptophan catabolite L-kynurenine inhibits the surface expression of NKp46- and NKG2D-activating receptors and regulates NK-cell function. *Blood* **2006**, *108* (13), 4118-25.
  50. Smith, C.; Chang, M. Y.; Parker, K. H.; Beury, D. W.; DuHadaway, J. B.; Flick, H. E.; Boulden, J.; Sutanto-Ward, E.; Soler, A. P.; Laury-Kleintop, L. D.; Mandik-Nayak, L.; Metz, R.; Ostrand-Rosenberg, S.; Prendergast, G. C.; Muller, A. J., IDO is a nodal pathogenic driver of lung cancer and metastasis development. *Cancer Discov* **2012**, *2* (8), 722-35.
  51. Mezrich, J. D.; Fechner, J. H.; Zhang, X.; Johnson, B. P.; Burlingham, W. J.; Bradfield, C. A., An interaction between kynurenine and the aryl hydrocarbon receptor can generate regulatory T cells. *J Immunol* **2010**, *185* (6), 3190-8.
  52. Quintana, F. J.; Murugaiyan, G.; Farez, M. F.; Mitsdoerffer, M.; Tukpah, A. M.; Burns, E. J.; Weiner, H. L., An endogenous aryl hydrocarbon receptor ligand acts on dendritic cells and T cells to suppress experimental autoimmune encephalomyelitis. *Proc Natl Acad Sci U S A* **2010**, *107* (48), 20768-73.
  53. Jeffery, C. J., Moonlighting proteins: old proteins learning new tricks. *Trends Genet* **2003**, *19* (8), 415-417.
  54. Jeffery, C. J., Moonlighting proteins. *Trends Biochem Sci* **1999**, *24* (1), 8-11.
  55. Adamo, A.; Frusteri, C.; Pallotta, M. T.; Pirali, T.; Sartoris, S.; Ugel, S., Moonlighting Proteins Are Important Players in Cancer Immunology. *Front Immunol* **2020**, *11*, 613069.
  56. Pallotta, M. T.; Orabona, C.; Volpi, C.; Vacca, C.; Belladonna, M. L.; Bianchi, R.; Servillo, G.; Brunacci, C.; Calvitti, M.; Bicciato, S.; Mazza, E. M. C.; Boon, L.; Grassi, F.; Fioretti, M. C.; Fallarino, F.; Puccetti, P.; Grohmann, U., Indoleamine 2,3-dioxygenase is a signaling protein in long-term tolerance by dendritic cells. *Nat Immunol* **2011**, *12* (9), 870-878.
  57. Fujigaki, H.; Seishima, M.; Saito, K., Posttranslational modification of indoleamine 2,3-dioxygenase. *Anal Bioanal Chem* **2012**, *403* (7), 1777-82.



## References

58. Polevoda, B.; Sherman, F., N-terminal Acetyltransferases and Sequence Requirements for N-terminal Acetylation of Eukaryotic Proteins. *J Mol Biol* **2003**, *325* (4), 595-622.
59. Ree, R.; Varland, S.; Arnesen, T., Spotlight on protein N-terminal acetylation. *Exp Mol Med* **2018**, *50* (7), 1-13.
60. Kang-Eun, L.; Ji-Eun, H.; Jeong-Mok, K.; and Cheol-Sang, H., N-Terminal Acetylation-Targeted N-End Rule Proteolytic System: The Ac/N-End Rule Pathway. *Mol Cells* **2016**, *39* (3), 169-178.
61. Brito, C.; Naviliat, M.; Tiscornia, A. C.; Vuillier, F.; Gualco, G.; Dighiero, G.; Radi, R.; Cayota, A. M., Peroxynitrite Inhibits T Lymphocyte Activation and Proliferation by Promoting Impairment of Tyrosine Phosphorylation and Peroxynitrite-Driven Apoptotic Death1. *J Immunol* **1999**, *162* (6), 3356-3366.
62. Denicola, A.; Rubbo, H.; Rodriguez, D.; Radi, R., Peroxynitrite-Mediated Cytotoxicity to *Trypanosoma cruzi*. *Arch Biochem Biophys* **1993**, *304* (1), 279-286.
63. Radi, R., Protein Tyrosine Nitration: Biochemical Mechanisms and Structural Basis of Functional Effects. *Acc Chem Res* **2013**, *46* (2), 550-559.
64. Greenacre, S. A. B.; Ischiropoulos, H., Tyrosine nitration: Localisation, quantification, consequences for protein function and signal transduction. *Free Radic Res* **2001**, *34* (6), 541-581.
65. Busch, W., Aus der Sitzung der medicinischen Section vom 13 November 1867. *Berl Klin Wochenschr* **1868**, *5* (5), 137.
66. Coley, W. B., The treatment of malignant tumors by repeated inoculations of erysipelas: With a report of ten original cases. 1. *AJMS (1827-1924)* **1893**, *105* (6), 487.
67. Coley, W. B., The treatment of sarcoma with the mixed toxins of erysipelas and bacillus prodigiosus. *BM&SJ* **1908**, *158* (6), 175-182.
68. Jerne, N. K., The natural-selection theory of antibody formation. *PNAS* **1955**, *41* (11), 849-857.
69. Fleischman, J. B.; Porter, R. R.; Press, E. M., THE ARRANGEMENT OF THE PEPTIDE CHAINS IN GAMMA-GLOBULIN. *The Biochemical journal* **1963**, *88* (2), 220-8.
70. Edelman, G. M.; Poulik, M. D., STUDIES ON STRUCTURAL UNITS OF THE  $\gamma$ -GLOBULINS. *JEM* **1961**, *113* (5), 861-884.
71. Porter, R. R., The hydrolysis of rabbit  $\gamma$ -globulin and antibodies with crystalline papain. *The Biochemical journal* **1959**, *73* (1), 119-26.
72. Köhler, G.; Milstein, C., Continuous cultures of fused cells secreting antibody of predefined specificity. *Nature* **1975**, *256* (5517), 495-497.
73. Oiseth, S. J.; Aziz, M. S., Cancer immunotherapy: a brief review of the history, possibilities, and challenges ahead. *J Canc Metastasis Treat* **2017**, *3*, 250-261.
74. Golomb, H. M.; Jacobs, A.; Fefer, A.; Ozer, H.; Thompson, J.; Portlock, C.; Ratain, M.; Golde, D.; Vardiman, J.; Burke, J., Alpha-2 interferon therapy of hairy-cell leukemia: a multicenter study of 64 patients. *J Clin Onc* **1986**, *4* (6), 900-905.
75. Galluzzi, L.; Vacchelli, E.; Bravo-San Pedro, J. M.; Buqué, A.; Senovilla, L.; Baracco, E. E.; Bloy, N.; Castoldi, F.; Abastado, J. P.; Agostinis, P.; Apte, R. N.; Aranda, F.; Ayyoub, M.; Beckhove, P.; Blay, J. Y.; Bracci, L.; Caignard, A.; Castelli, C.; Cavallo, F.; Celis, E.; Cerundolo, V.; Clayton, A.; Colombo, M. P.; Coussens, L.; Dhodapkar, M. V.; Eggermont, A. M.; Fearon, D. T.; Fridman, W. H.; Fučíková, J.; Gabilovich, D. I.; Galon, J.; Garg, A.; Ghiringhelli, F.; Giaccone, G.; Gilboa, E.; Gnjatic, S.; Hoos, A.; Hosmalin, A.; Jäger, D.; Kalinski, P.; Kärre, K.; Kepp, O.; Kiessling, R.; Kirkwood, J. M.; Klein, E.; Knuth, A.; Lewis, C. E.; Liblau, R.; Lotze, M. T.; Lugli, E.; Mach, J. P.; Mattei, F.; Mavilio, D.; Melero, I.; Melief, C. J.; Mittendorf, E. A.; Moretta, L.; Odunsi, A.; Okada, H.; Palucka, A. K.; Peter, M. E.; Pienta, K. J.; Porgador, A.; Prendergast, G. C.; Rabinovich, G. A.; Restifo, N. P.; Rizvi, N.; Sautès-Fridman, C.; Schreiber, H.; Seliger, B.; Shiku, H.; Silva-Santos, B.; Smyth, M. J.; Speiser, D. E.; Spisek, R.; Srivastava, P. K.; Talmadge, J. E.; Tartour, E.; Van Der Burg, S. H.; Van Den Eynde, B. J.; Vile, R.; Wagner, H.; Weber, J. S.; Whiteside, T. L.; Wolchok, J. D.; Zitvogel, L.; Zou, W.;

## References

- Kroemer, G., Classification of current anticancer immunotherapies. *Oncotarget* **2014**, *5* (24), 12472-508.
76. Maurer, S.; Zhong, X.; Prada, B. D.; Mascarenhas, J.; de Andrade, L. F., The Latest Breakthroughs in Immunotherapy for Acute Myeloid Leukemia, with a Special Focus on NKG2D Ligands. *Int J Mol Sci* **2022**, *23* (24).
77. Yang, L.; Ning, Q.; Tang, S. S., Recent Advances and Next Breakthrough in Immunotherapy for Cancer Treatment. *Journal of immunology research* **2022**, *2022*, 8052212.
78. Newick, K.; O'Brien, S.; Moon, E.; Albelda, S. M., CAR T Cell Therapy for Solid Tumors. *Ann Rev Med* **2017**, *68* (1), 139-152.
79. Frey, N.; Porter, D., Cytokine Release Syndrome with Chimeric Antigen Receptor T Cell Therapy. *Biol Blood Marrow Transplant* **2019**, *25* (4), e123-e127.
80. He, X.; Xu, C., Immune checkpoint signaling and cancer immunotherapy. *Cell Res* **2020**, *30* (8), 660-669.
81. Sharma, P.; Siddiqui, B. A.; Anandhan, S.; Yadav, S. S.; Subudhi, S. K.; Gao, J.; Goswami, S.; Allison, J. P., The Next Decade of Immune Checkpoint Therapy. *Cancer Discov* **2021**, *11* (4), 838-857.
82. Hodi, F. S.; O'Day, S. J.; McDermott, D. F.; Weber, R. W.; Sosman, J. A.; Haanen, J. B.; Gonzalez, R.; Robert, C.; Schadendorf, D.; Hassel, J. C.; Akerley, W.; van den Eertwegh, A. J. M.; Lutzky, J.; Lorigan, P.; Vaubel, J. M.; Linette, G. P.; Hogg, D.; Ottensmeier, C. H.; Lebbé, C.; Peschel, C.; Quirt, I.; Clark, J. I.; Wolchok, J. D.; Weber, J. S.; Tian, J.; Yellin, M. J.; Nichol, G. M.; Hoos, A.; Urba, W. J., Improved Survival with Ipilimumab in Patients with Metastatic Melanoma. *N Engl J Med* **2010**, *363* (8), 711-723.
83. Ribas, A., Tumor Immunotherapy Directed at PD-1. *N Engl J Med* **2012**, *366* (26), 2517-2519.
84. Dobosz, P.; Stępień, M.; Golke, A.; Dzieciatkowski, T., Challenges of the Immunotherapy: Perspectives and Limitations of the Immune Checkpoint Inhibitor Treatment. *Int J Mol Sci* **2022**, *23* (5).
85. Tang, J.; Pearce, L.; O'Donnell-Tormey, J.; Hubbard-Lucey, V. M., Trends in the global immuno-oncology landscape. *Nat Rev Drug Discov* **2018**, *17* (11), 783-784.
86. Weinmann, H., Cancer Immunotherapy: Selected Targets and Small-Molecule Modulators. *ChemMedChem* **2016**, *11* (5), 450-66.
87. Yue, E. W.; Sparks, R.; Polam, P.; Modi, D.; Douty, B.; Wayland, B.; Glass, B.; Takvorian, A.; Glenn, J.; Zhu, W.; Bower, M.; Liu, X.; Leffet, L.; Wang, Q.; Bowman, K. J.; Hansbury, M. J.; Wei, M.; Li, Y.; Wynn, R.; Burn, T. C.; Koblisch, H. K.; Fridman, J. S.; Emm, T.; Scherle, P. A.; Metcalf, B.; Combs, A. P., INCB24360 (Epacadostat), a Highly Potent and Selective Indoleamine-2,3-dioxygenase 1 (IDO1) Inhibitor for Immuno-oncology. *ACS Med Chem Lett* **2017**, *8* (5), 486-491.
88. Siu, L.; Gelmon, K.; Chu, Q.; Pachynski, R.; Alese, O.; Basciano, P.; Walker, J.; Mitra, P.; Zhu, L.; Phillips, P.; Hunt, J.; Desai, J., BMS-986205, an optimized indoleamine 2,3-dioxygenase 1 (IDO1) inhibitor, is well tolerated with potent pharmacodynamic (PD) activity, alone and in combination with nivolumab (nivo) in advanced cancers in a phase 1/2a trial. *Cancer Research* **2017**, *77*, CT116-CT116.
89. Xu, X.; Ren, J.; Ma, Y.; Liu, H.; Rong, Q.; Feng, Y.; Wang, Y.; Cheng, Y.; Ge, R.; Li, Z.; Bian, J., Discovery of cyanopyridine scaffold as novel indoleamine-2,3-dioxygenase 1 (IDO1) inhibitors through virtual screening and preliminary hit optimisation. *Journal of enzyme inhibition and medicinal chemistry* **2019**, *34* (1), 250-263.
90. U.S. National Library of Medicine. [clinicaltrials.gov](https://clinicaltrials.gov) (accessed 28.03.2023).
91. Brincks, E. L.; Adams, J.; Wang, L.; Turner, B.; Marcinowicz, A.; Ke, J.; Essmann, M.; Mautino, L. M.; Allen, C. V.; Kumar, S.; Vahanian, N.; Link, C.; Mautino, M. R., Indoximod opposes the immunosuppressive effects mediated by IDO and TDO via modulation of AhR function and activation of mTORC1. *Oncotarget* **2020**, *11* (25), 2438-2461.
92. Prendergast, G. C.; Malachowski, W. P.; DuHadaway, J. B.; Muller, A. J., Discovery of IDO1 Inhibitors: From Bench to Bedside. *Cancer Res* **2017**, *77* (24), 6795-6811.

## References

93. Kumar, S.; Jaipuri, F. A.; Waldo, J. P.; Potturi, H.; Marcinowicz, A.; Adams, J.; Van Allen, C.; Zhuang, H.; Vahanian, N.; Link, C.; Brincks, E. L.; Mautino, M. R., Discovery of indoximod prodrugs and characterization of clinical candidate NLG802. *Eur J Med Chem* **2020**, *198*, 112373.
94. Gomes, B.; Driessens, G.; Bartlett, D.; Cai, D.; Cauwenberghs, S.; Crosignani, S.; Dalvie, D.; Denies, S.; Dillon, C. P.; Fantin, V. R.; Guo, J.; Letellier, M.-C.; Li, W.; Maegley, K.; Marillier, R.; Miller, N.; Pirson, R.; Rabolli, V.; Ray, C.; Streiner, N.; Torti, V. R.; Tsaparikos, K.; Van den Eynde, B. J.; Wythes, M.; Yao, L.-C.; Zheng, X.; Tumang, J.; Kraus, M., Characterization of the Selective Indoleamine 2,3-Dioxygenase-1 (IDO1) Catalytic Inhibitor EOS200271/PF-06840003 Supports IDO1 as a Critical Resistance Mechanism to PD-(L)1 Blockade Therapy. *Mol Cancer Ther* **2018**, *17* (12), 2530-2542.
95. Dorsey, F. C.; Benhadji, K. A.; Sams, L. L.; Young, D. A.; Schindler, J. F.; Huss, K. L.; Nikolayev, A.; Carpenito, C.; Clawson, D.; Jones, B.; Faber, A. L.; Thomas, J. E.; Haney, S. A.; Zhao, G.; McMillen, W. T.; Smeal, T.; Sall, D. J.; Kalos, M. D.; Geeganage, S.; Henry, J. R., Abstract 5245: Identification and characterization of the IDO1 inhibitor LY3381916. *Canc Res* **2018**, *78* (13\_Supplement), 5245-5245.
96. Fujiwara, Y.; Kato, S.; Nesline, M. K.; Conroy, J. M.; DePietro, P.; Pabla, S.; Kurzrock, R., Indoleamine 2, 3-dioxygenase (IDO) inhibitors and cancer immunotherapy. *Canc Treat Rev* **2022**, 102461.
97. Opitz, C. A.; Somarribas Patterson, L. F.; Mohapatra, S. R.; Dewi, D. L.; Sadik, A.; Platten, M.; Trump, S., The therapeutic potential of targeting tryptophan catabolism in cancer. *Br J Cancer* **2020**, *122* (1), 30-44.
98. Röhrig, U. F.; Reynaud, A.; Majjigapu, S. R.; Vogel, P.; Pojer, F.; Zoete, V., Inhibition Mechanisms of Indoleamine 2,3-Dioxygenase 1 (IDO1). *J Med Chem* **2019**.
99. de Almeida, V. M.; Santos-Filho, O. A., Identification of Potential Allosteric Site Binders of Indoleamine 2,3-Dioxygenase 1 from Plants: A Virtual and Molecular Dynamics Investigation. *Pharmaceuticals (Basel, Switzerland)* **2022**, *15* (9).
100. Hu, M.; Zhou, W.; Wang, Y.; Yao, D.; Ye, T.; Yao, Y.; Chen, B.; Liu, G.; Yang, X.; Wang, W.; Xie, Y., Discovery of the first potent proteolysis targeting chimera (PROTAC) degrader of indoleamine 2,3-dioxygenase 1. *APSB* **2020**, *10* (10), 1943-1953.
101. Zhai, L.; Ladomersky, E.; Lenzen, A.; Nguyen, B.; Patel, R.; Lauing, K. L.; Wu, M.; Wainwright, D. A., IDO1 in cancer: a Gemini of immune checkpoints. *Cell Mol Immunol* **2018**, *15* (5), 447-457.
102. Van den Eynde, B. J.; van Baren, N.; Baurain, J.-F., Is There a Clinical Future for IDO1 Inhibitors After the Failure of Epcadostat in Melanoma? *Ann Rev Cancer Biol* **2019**, *4* (1).
103. Tang, K.; Wu, Y.-H.; Song, Y.; Yu, B., Indoleamine 2,3-dioxygenase 1 (IDO1) inhibitors in clinical trials for cancer immunotherapy. *J Hematol Oncol* **2021**, *14* (1), 68.
104. Komiya, T.; Huang, C. H., Updates in the Clinical Development of Epcadostat and Other Indoleamine 2,3-Dioxygenase 1 Inhibitors (IDO1) for Human Cancers. *Front Oncol* **2018**, *8*.
105. Crans, D. C., Grand challenges in chemical biology: Past, present and future. *Front Chem Biol* **2022**, *1*.
106. The Nobel Prize in Chemistry 2020 - Press Release. <https://www.nobelprize.org/prizes/chemistry/2020/press-release/> (accessed 31.05.2023).
107. The Nobel Prize in Chemistry 2022 - Press Release. <https://www.nobelprize.org/prizes/chemistry/2022/press-release/> (accessed 31.05.2023).
108. Kawasumi, M.; Nghiem, P., Chemical Genetics: Elucidating Biological Systems with Small-Molecule Compounds. *JID* **2007**, *127* (7), 1577-1584.
109. Spring, D. R., Chemical genetics to chemical genomics: small molecules offer big insights. *Chem Soc Rev* **2005**, *34* (6), 472-482.
110. Lipinski, C. A.; Lombardo, F.; Dominy, B. W.; Feeney, P. J., Experimental and computational approaches to estimate solubility and permeability in drug discovery and development settings. *Adv Drug Deliv Rev* **1997**, *23* (1), 3-25.

## References

111. Lipinski, C. A., Lead- and drug-like compounds: the rule-of-five revolution. *Drug Discov Today Technol* **2004**, 1 (4), 337-341.
112. Atanasov, A. G.; Zotchev, S. B.; Dirsch, V. M.; Orhan, I. E.; Banach, M.; Rollinger, J. M.; Barreca, D.; Weckwerth, W.; Bauer, R.; Bayer, E. A.; Majeed, M.; Bishayee, A.; Bochkov, V.; Bonn, G. K.; Braidy, N.; Bucar, F.; Cifuentes, A.; D'Onofrio, G.; Bodkin, M.; Diederich, M.; Dinkova-Kostova, A. T.; Efferth, T.; El Bairi, K.; Arkells, N.; Fan, T.-P.; Fiebich, B. L.; Freissmuth, M.; Georgiev, M. I.; Gibbons, S.; Godfrey, K. M.; Gruber, C. W.; Heer, J.; Huber, L. A.; Ibanez, E.; Kijjoo, A.; Kiss, A. K.; Lu, A.; Macias, F. A.; Miller, M. J. S.; Mocan, A.; Müller, R.; Nicoletti, F.; Perry, G.; Pittalà, V.; Rastrelli, L.; Ristow, M.; Russo, G. L.; Silva, A. S.; Schuster, D.; Sheridan, H.; Skalicka-Woźniak, K.; Skaltsounis, L.; Sobarzo-Sánchez, E.; Bredt, D. S.; Stuppner, H.; Sureda, A.; Tzvetkov, N. T.; Vacca, R. A.; Aggarwal, B. B.; Battino, M.; Giampieri, F.; Wink, M.; Wolfender, J.-L.; Xiao, J.; Yeung, A. W. K.; Lizard, G.; Popp, M. A.; Heinrich, M.; Berindan-Neagoe, I.; Stadler, M.; Daglia, M.; Verpoorte, R.; Supuran, C. T.; the International Natural Product Sciences, T., Natural products in drug discovery: advances and opportunities. *Nat Rev Drug Discov* **2021**, 20 (3), 200-216.
113. Schreiber, S. L., Molecular diversity by design. *Nature* **2009**, 457, 153-154.
114. Schreiber, S. L., Molecular diversity by design. *Nature* **2009**, 457 (7226), 153-154.
115. Wetzelsch, S.; Bon, R. S.; Kumar, K.; Waldmann, H., Biology-Oriented Synthesis. *Angew Chem Int Ed* **2011**, 50 (46), 10800-10826.
116. Karageorgis, G.; Foley, D. J.; Laraia, L.; Waldmann, H., Principle and design of pseudo-natural products. *Nat Chem* **2020**, 12 (3), 227-235.
117. Karageorgis, G.; Foley, D. J.; Laraia, L.; Brakmann, S.; Waldmann, H., Pseudo Natural Products-Chemical Evolution of Natural Product Structure. *Angew Chem Int Ed Engl* **2021**, 60 (29), 15705-15723.
118. Schenone, M.; Dančik, V.; Wagner, B. K.; Clemons, P. A., Target identification and mechanism of action in chemical biology and drug discovery. *Nat Chem Biol* **2013**, 9 (4), 232-40.
119. Ji, K.-Y.; Liu, C.; Liu, Z.-Q.; Deng, Y.-F.; Hou, T.-J.; Cao, D.-S., Comprehensive assessment of nine target prediction web services: which should we choose for target fishing? *Brief Bioinformatics* **2023**, 24 (2).
120. Swinney, D. C.; Anthony, J., How were new medicines discovered? *Nat Rev Drug Discov* **2011**, 10 (7), 507-519.
121. Vincent, F.; Loria, P.; Pregel, M.; Stanton, R.; Kitching, L.; Nocka, K.; Doyonnas, R.; Steppan, C.; Gilbert, A.; Schroeter, T.; Peakman, M.-C., Developing predictive assays: The phenotypic screening "rule of 3". *Sci Transl Med* **2015**, 7 (293), 293ps15-293ps15.
122. Laraia, L.; Garivet, G.; Foley, D. J.; Kaiser, N.; Müller, S.; Zinken, S.; Pinkert, T.; Wilke, J.; Corkery, D.; Pahl, A.; Sievers, S.; Janning, P.; Arenz, C.; Wu, Y.; Rodriguez, R.; Waldmann, H., Image-Based Morphological Profiling Identifies a Lysosomotropic, Iron-Sequestering Autophagy Inhibitor. *Angew Chem Int Ed* **2020**, 59 (14), 5721-5729.
123. Talevi, A., Multi-target pharmacology: possibilities and limitations of the "skeleton key approach" from a medicinal chemist perspective. *Front Pharmacol* **2015**, 6, 205.
124. Pushpakom, S.; Iorio, F.; Eyers, P. A.; Escott, K. J.; Hopper, S.; Wells, A.; Doig, A.; Guilliams, T.; Latimer, J.; McNamee, C.; Norris, A.; Sanseau, P.; Cavalla, D.; Pirmohamed, M., Drug repurposing: progress, challenges and recommendations. *Nat Rev Drug Discov* **2019**, 18 (1), 41-58.
125. Reddy, A. S.; Zhang, S., Polypharmacology: drug discovery for the future. *Expert review of clinical pharmacology* **2013**, 6 (1), 41-7.
126. Kabir, A.; Muth, A., Polypharmacology: The science of multi-targeting molecules. *Pharmacol Res* **2022**, 176, 106055.
127. Bolognesi, M. L.; Cavalli, A., Multitarget Drug Discovery and Polypharmacology. *ChemMedChem* **2016**, 11 (12), 1190-1192.
128. Proschak, E.; Stark, H.; Merk, D., Polypharmacology by Design: A Medicinal Chemist's Perspective on Multitargeting Compounds. *J Med Chem* **2019**, 62 (2), 420-444.

## References

129. Comess, K. M.; McLoughlin, S. M.; Oyer, J. A.; Richardson, P. L.; Stöckmann, H.; Vasudevan, A.; Warder, S. E., Emerging Approaches for the Identification of Protein Targets of Small Molecules - A Practitioners' Perspective. *J Med Chem* **2018**, *61* (19), 8504-8535.
130. Yang, S.-Q.; Zhang, L.-X.; Ge, Y.-J.; Zhang, J.-W.; Hu, J.-X.; Shen, C.-Y.; Lu, A.-P.; Hou, T.-J.; Cao, D.-S., In-silico target prediction by ensemble chemogenomic model based on multi-scale information of chemical structures and protein sequences. *J Cheminform* **2023**, *15* (1), 48.
131. Doudna, J. A.; Charpentier, E., The new frontier of genome engineering with CRISPR-Cas9. *Science* **2014**, *346* (6213), 1258096.
132. Mayor-Ruiz, C.; Bauer, S.; Brand, M.; Kozicka, Z.; Siklos, M.; Imrichova, H.; Kaltheuner, I. H.; Hahn, E.; Seiler, K.; Koren, A.; Petzold, G.; Fellner, M.; Bock, C.; Müller, A. C.; Zuber, J.; Geyer, M.; Thomä, N. H.; Kubicek, S.; Winter, G. E., Rational discovery of molecular glue degraders via scalable chemical profiling. *Nat Chem Biol* **2020**, *16* (11), 1199-1207.
133. Paananen, J.; Fortino, V., An omics perspective on drug target discovery platforms. *Brief Bioinformatics* **2019**, *21* (6), 1937-1953.
134. Santos, R.; Ursu, O.; Gaulton, A.; Bento, A. P.; Donadi, R. S.; Bologa, C. G.; Karlsson, A.; Al-Lazikani, B.; Hersey, A.; Oprea, T. I.; Overington, J. P., A comprehensive map of molecular drug targets. *Nat Rev Drug Discov* **2017**, *16* (1), 19-34.
135. Meissner, F.; Geddes-McAlister, J.; Mann, M.; Bantscheff, M., The emerging role of mass spectrometry-based proteomics in drug discovery. *Nat Rev Drug Discov* **2022**, *21* (9), 637-654.
136. Reckzeh, E. S.; Brockmeyer, A.; Metz, M.; Waldmann, H.; Janning, P., Target Engagement of Small Molecules: Thermal Profiling Approaches on Different Levels. *Methods Mol Biol* **2019**, *1888*, 73-98.
137. Molina, D. M.; Jafari, R.; Ignatushchenko, M.; Seki, T.; Larsson, E. A.; Dan, C.; Sreekumar, L.; Cao, Y.; Nordlund, P., Monitoring Drug Target Engagement in Cells and Tissues Using the Cellular Thermal Shift Assay. *Science* **2013**, *341* (6141), 84-87.
138. Ziegler, S.; Sievers, S.; Waldmann, H., Morphological profiling of small molecules. *Cell Chem Biol* **2021**, *28* (3), 300-319.
139. Bray, M.-A.; Singh, S.; Han, H.; Davis, C. T.; Borgeson, B.; Hartland, C.; Kost-Alimova, M.; Gustafsdottir, S. M.; Gibson, C. C.; Carpenter, A. E., Cell Painting, a high-content image-based assay for morphological profiling using multiplexed fluorescent dyes. *Nat Protoc* **2016**, *11* (9), 1757-1774.
140. Gustafsdottir, S. M.; Ljosa, V.; Sokolnicki, K. L.; Anthony Wilson, J.; Walpita, D.; Kemp, M. M.; Petri Seiler, K.; Carrel, H. A.; Golub, T. R.; Schreiber, S. L.; Clemons, P. A.; Carpenter, A. E.; Shamji, A. F., Multiplex Cytological Profiling Assay to Measure Diverse Cellular States. *PLOS ONE* **2013**, *8* (12), e80999.
141. Axel, P.; Beate, S.; Marion, R.; Marc, D.; Christian, H.; Adam, N.; Sonja, S.; Herbert, W.; Slava, Z., Morphological Subprofile Analysis for Bioactivity Annotation of Small Molecules. *bioRxiv* **2022**, 2022.08.15.503944.
142. Axel, P.; Jie, L.; Sohan, P.; Soheila Rezaei, A.; Beate, S.; Jens, W.; Jana, B.; Sandra, K.; Sonja, S.; Slava, Z.; Herbert, W., Illuminating Dark Chemical Matter using the Cell Painting Assay. *bioRxiv* **2023**, 2023.05.31.542818.
143. Akbarzadeh, M.; Deipenwisch, I.; Schoelermann, B.; Pahl, A.; Sievers, S.; Ziegler, S.; Waldmann, H., Morphological profiling by means of the Cell Painting assay enables identification of tubulin-targeting compounds. *Cell Chem Biol* **2022**, *29* (6), 1053-1064.e3.
144. Schölermann, B.; Bonowski, J.; Grigalunas, M.; Burhop, A.; Xie, Y.; Hooch, J. G. F.; Liu, J.; Dow, M.; Nelson, A.; Nowak, C.; Pahl, A.; Sievers, S.; Ziegler, S., Identification of Dihydroorotate Dehydrogenase Inhibitors Using the Cell Painting Assay. *Chembiochem* **2022**, *23* (22), e202200475.
145. Burhop, A.; Bag, S.; Grigalunas, M.; Woitalla, S.; Bodenbinder, P.; Brieger, L.; Strohmam, C.; Pahl, A.; Sievers, S.; Waldmann, H., Synthesis of Indofulvin Pseudo-Natural Products Yields a New Autophagy Inhibitor Chemotype. *Adv Sci (Weinh)* **2021**, *8* (19), e2102042.

## References

146. Schneidewind, T.; Brause, A.; Scholermann, B.; Sievers, S.; Pahl, A.; Sankar, M. G.; Winzker, M.; Janning, P.; Kumar, K.; Ziegler, S.; Waldmann, H., Combined morphological and proteome profiling reveals target-independent impairment of cholesterol homeostasis. *Cell Chem Biol* **2021**.
147. Pahl, A.; Schölermann, B.; Rusch, M.; Dow, M.; Hedberg, C.; Nelson, A.; Sievers, S.; Waldmann, H.; Ziegler, S., Morphological Subprofile Analysis for Bioactivity Annotation of Small Molecules. *bioRxiv* **2022**, 2022.08.15.503944.
148. Schneidewind, T.; Brause, A.; Pahl, A.; Burhop, A.; Mejuch, T.; Sievers, S.; Waldmann, H.; Ziegler, S., Morphological profiling identifies a common mode of action for small molecules with different targets. *ChemBioChem* **2020**, *21* (22), 3197-3207.
149. Gally, J.-M.; Pahl, A.; Waldmann, H., Identifying bioactivity of pseudo-natural products using the Cell Painting assay. *ARKIVOC* **2020**, 2021 (4), 89-104.
150. Blake, R. A., Target validation in drug discovery. *Methods Mol Biol* **2007**, *356*, 367-77.
151. Palmer, A. C.; Kishony, R., Opposing effects of target overexpression reveal drug mechanisms. *Nat Commun* **2014**, *5*, 4296.
152. Smith, C., Drug target validation: Hitting the target. *Nature* **2003**, *422* (6929), 342-345.
153. Wyatt, P. G.; Gilbert, I. H.; Read, K. D.; Fairlamb, A. H., Target validation: linking target and chemical properties to desired product profile. *Current topics in medicinal chemistry* **2011**, *11* (10), 1275-83.
154. Sim, D. S.; Kauser, K., In Vivo Target Validation Using Biological Molecules in Drug Development. In *New Approaches to Drug Discovery*, Nielsch, U.; Fuhrmann, U.; Jaroch, S., Eds. Springer International Publishing: Cham, 2016; pp 59-70.
155. Hennes, E.; Lampe, P.; Dötsch, L.; Bruning, N.; Pulvermacher, L. M.; Sievers, S.; Ziegler, S.; Waldmann, H., Cell-Based Identification of New IDO1 Modulator Chemotypes. *Angew Chem Int Ed Engl* **2021**, *60* (18), 9869-9874.
156. Baell, J., Observations on screening-based research and some concerning trends in the literature. *Future Med Chem* **2010**, *2* (10), 1529-1546.
157. Baell, J.; Walters, M. A., Chemistry: Chemical con artists foil drug discovery. *Nature* **2014**, *513* (7519), 481-483.
158. Baell, J. B.; Holloway, G. A., New Substructure Filters for Removal of Pan Assay Interference Compounds (PAINS) from Screening Libraries and for Their Exclusion in Bioassays. *J Med Chem* **2010**, *53* (7), 2719-2740.
159. Dahlin, J. L.; Nissink, J. W.; Strasser, J. M.; Francis, S.; Higgins, L.; Zhou, H.; Zhang, Z.; Walters, M. A., PAINS in the assay: chemical mechanisms of assay interference and promiscuous enzymatic inhibition observed during a sulfhydryl-scavenging HTS. *J Med Chem* **2015**, *58* (5), 2091-113.
160. Saubern, S.; Guha, R.; Baell, J. B., KNIME Workflow to Assess PAINS Filters in SMARTS Format. Comparison of RDKit and Indigo Cheminformatics Libraries. *Mol Inf* **2011**, *30* (10), 847-850.
161. Klockow, J. L.; Glass, T. E., Development of a Fluorescent Chemosensor for the Detection of Kynurenine. *Org Lett* **2013**, *15* (2), 235-237.
162. Theate, I.; van Baren, N.; Pilotte, L.; Moulin, P.; Larrieu, P.; Renauld, J. C.; Herve, C.; Gutierrez-Roelens, I.; Marbaix, E.; Sempoux, C.; Van den Eynde, B. J., Extensive profiling of the expression of the indoleamine 2,3-dioxygenase 1 protein in normal and tumoral human tissues. *Cancer Immunol Res* **2015**, *3* (2), 161-72.
163. Dückert, H.; Pries, V.; Khedkar, V.; Menninger, S.; Bruss, H.; Bird, A. W.; Maliga, Z.; Brockmeyer, A.; Janning, P.; Hyman, A.; Grimme, S.; Schürmann, M.; Preut, H.; Hübel, K.; Ziegler, S.; Kumar, K.; Waldmann, H., Natural product-inspired cascade synthesis yields modulators of centrosome integrity. *Nat Chem Biol* **2012**, *8* (2), 179-184.
164. Grigalunas, M.; Burhop, A.; Zinken, S.; Pahl, A.; Gally, J. M.; Wild, N.; Mantel, Y.; Sievers, S.; Foley, D. J.; Scheel, R.; Strohmam, C.; Antonchick, A. P.; Waldmann, H., Natural product fragment combination to performance-diverse pseudo-natural products. *Nat Commun* **2021**, *12* (1), 1883.

## References

165. Sentein, P., Action of nocodazole on the mechanisms of segmentation mitosis. *Cell Biol Int Rep* **1977**, *1* (6), 503-509.
166. Sohaskey, C. D.; Barbour, A. G., Esterases in Serum-Containing Growth Media Counteract Chloramphenicol Acetyltransferase Activity In Vitro. *Antimicrob Agents Chemother* **1999**, *43* (3), 655-660.
167. Takahashi, M.; Hirota, I.; Nakano, T.; Kotani, T.; Takani, D.; Shiratori, K.; Choi, Y.; Haba, M.; Hosokawa, M., Effects of steric hindrance and electron density of ester prodrugs on controlling the metabolic activation by human carboxylesterase. *Drug metabolism and pharmacokinetics* **2021**, *38*, 100391.
168. Santhekadur, P. K.; Kumar, D. P., RISC assembly and post-transcriptional gene regulation in Hepatocellular Carcinoma. *Genes & diseases* **2020**, *7* (2), 199-204.
169. Bhutia, Y. D.; Babu, E.; Ganapathy, V., Interferon-gamma induces a tryptophan-selective amino acid transporter in human colonic epithelial cells and mouse dendritic cells. *Biochim Biophys Acta* **2015**, *1848* (2), 453-62.
170. Ikotun, O. F.; Marquez, B. V.; Huang, C.; Masuko, K.; Daiji, M.; Masuko, T.; McConathy, J.; Lapi, S. E., Imaging the L-Type Amino Acid Transporter-1 (LAT1) with Zr-89 ImmunoPET. *PLOS ONE* **2013**, *8* (10), e77476.
171. Boyd, Y. K. C. A., Characterisation of L-tryptophan transporters in human placenta: a comparison of brush border and basal membrane vesicles. *J Physiol* **2001**, *531* (2), 405-416.
172. Wang, Q.; Holst, J., L-type amino acid transport and cancer: targeting the mTORC1 pathway to inhibit neoplasia. *Am J Cancer Res* **2015**, *5* (4), 1281-94.
173. Jin, M., Unique roles of tryptophanyl-tRNA synthetase in immune control and its therapeutic implications. *Exp Mol Med* **2019**, *51* (1), 1-10.
174. Miyanokoshi, M.; Yokosawa, T.; Wakasugi, K., Tryptophanyl-tRNA synthetase mediates high-affinity tryptophan uptake into human cells. *J Biol Chem* **2018**, *293* (22), 8428-8438.
175. Paley, E. L., Tryptamine-Induced Tryptophanyl-tRNA trp Deficiency in Neurodifferentiation and Neurodegeneration Interplay: Progenitor Activation with Neurite Growth Terminated in Alzheimer's Disease Neuronal Vesicularization and Fragmentation. *J Alzheimers Dis* **2011**, *26*, 263-298.
176. Yokosawa, T.; Sato, A.; Wakasugi, K., Tryptophan Depletion Modulates Tryptophanyl-tRNA Synthetase-Mediated High-Affinity Tryptophan Uptake into Human Cells. *Genes* **2020**, *11* (12), 1423.
177. Magnusson, A. O.; Szekrenyi, A.; Joosten, H. J.; Finnigan, J.; Charnock, S.; Fessner, W. D., nanoDSF as screening tool for enzyme libraries and biotechnology development. *The FEBS journal* **2019**, *286* (1), 184-204.
178. Panda, S.; Roy, A.; Deka, S. J.; Trivedi, V.; Manna, D., Fused Heterocyclic Compounds as Potent Indoleamine-2,3-dioxygenase 1 Inhibitors. *ACS Med Chem Lett* **2016**, *7* (12), 1167-1172.
179. Lewis-Ballester, A.; Forouhar, F.; Kim, S.-M.; Lew, S.; Wang, Y.; Karkashon, S.; Seetharaman, J.; Batabyal, D.; Chiang, B.-Y.; Hussain, M.; Correia, M. A.; Yeh, S.-R.; Tong, L., Molecular basis for catalysis and substrate-mediated cellular stabilization of human tryptophan 2,3-dioxygenase. *Sci Rep* **2016**, *6* (1), 35169.
180. Zhai, L.; Spranger, S.; Binder, D. C.; Gritsina, G.; Lauing, K. L.; Giles, F. J.; Wainwright, D. A., Molecular Pathways: Targeting IDO1 and Other Tryptophan Dioxygenases for Cancer Immunotherapy. *Clin Cancer Res* **2015**, *21* (24), 5427-33.
181. Pantouris, G.; Serys, M.; Yuasa, H. J.; Ball, H. J.; Mowat, C. G., Human indoleamine 2,3-dioxygenase-2 has substrate specificity and inhibition characteristics distinct from those of indoleamine 2,3-dioxygenase-1. *Amino Acids* **2014**, *46* (9), 2155-2163.
182. Sono, M.; Roach, M. P.; Coulter, E. D.; Dawson, J. H., Heme-Containing Oxygenases. *Chem Rev* **1996**, *96* (7), 2841-2888.
183. O'Connell, J. D.; Paulo, J. A.; O'Brien, J. J.; Gygi, S. P., Proteome-Wide Evaluation of Two Common Protein Quantification Methods. *J Proteome Res* **2018**, *17* (5), 1934-1942.
184. Goedhart, J.; Luijsterburg, M. S., VolcanoR is a web app for creating, exploring, labeling and sharing volcano plots. *Sci Rep* **2020**, *10* (1), 20560.

## References

185. VolcaNoseR - Exploring volcano plots. <https://huygens.science.uva.nl/VolcaNoseR/>.
186. (GOC), G. O. C., The Gene Ontology resource: enriching a GOld mine. *Nucleic Acids Res* **2021**, 49 (D1), D325-d334.
187. Ashburner, M.; Ball, C. A.; Blake, J. A.; Botstein, D.; Butler, H.; Cherry, J. M.; Davis, A. P.; Dolinski, K.; Dwight, S. S.; Eppig, J. T.; Harris, M. A.; Hill, D. P.; Issel-Tarver, L.; Kasarskis, A.; Lewis, S.; Matese, J. C.; Richardson, J. E.; Ringwald, M.; Rubin, G. M.; Sherlock, G., Gene ontology: tool for the unification of biology. The Gene Ontology Consortium. *Nature genetics* **2000**, 25 (1), 25-9.
188. BioJupies. <https://maayanlab.cloud/biojupies/> (accessed 03.03.2021).
189. Torre, D.; Lachmann, A.; Ma'ayan, A., BioJupies: Automated Generation of Interactive Notebooks for RNA-Seq Data Analysis in the Cloud. *Cell Syst* **2018**, 7 (5), 556-561.e3.
190. Reactome Pathway Browser. <https://reactome.org/> (accessed 03.03.2021).
191. Fabregat, A.; Jupe, S.; Matthews, L.; Sidiropoulos, K.; Gillespie, M.; Garapati, P.; Haw, R.; Jassal, B.; Korninger, F.; May, B.; Milacic, M.; Roca, C. D.; Rothfels, K.; Sevilla, C.; Shamovsky, V.; Shorser, S.; Varusai, T.; Viteri, G.; Weiser, J.; Wu, G.; Stein, L.; Hermjakob, H.; D'Eustachio, P., The Reactome Pathway Knowledgebase. *Nucleic Acids Res* **2018**, 46 (D1), D649-d655.
192. Chen, E. Y.; Tan, C. M.; Kou, Y.; Duan, Q.; Wang, Z.; Meirelles, G. V.; Clark, N. R.; Ma'ayan, A., Enrichr: interactive and collaborative HTML5 gene list enrichment analysis tool. *BMC Bioinform* **2013**, 14, 128.
193. Kuleshov, M. V.; Jones, M. R.; Rouillard, A. D.; Fernandez, N. F.; Duan, Q.; Wang, Z.; Koplev, S.; Jenkins, S. L.; Jagodnik, K. M.; Lachmann, A.; McDermott, M. G.; Monteiro, C. D.; Gundersen, G. W.; Ma'ayan, A., Enrichr: a comprehensive gene set enrichment analysis web server 2016 update. *Nucleic Acids Res* **2016**, 44 (W1), W90-7.
194. Lad, L.; Schuller, D. J.; Shimizu, H.; Friedman, J.; Li, H.; Ortiz de Montellano, P. R.; Poulos, T. L., Comparison of the heme-free and -bound crystal structures of human heme oxygenase-1. *J Biol Chem* **2003**, 278 (10), 7834-43.
195. Walther, T. C.; Alves, A.; Pickersgill, H.; Loiodice, I.; Hetzer, M.; Galy, V.; Hülsmann, B. B.; Köcher, T.; Wilm, M.; Allen, T.; Mattaj, I. W.; Doye, V., The conserved Nup107-160 complex is critical for nuclear pore complex assembly. *Cell* **2003**, 113 (2), 195-206.
196. Lin, D. H.; Stuwe, T.; Schilbach, S.; Rundlet, E. J.; Perriches, T.; Mobbs, G.; Fan, Y.; Thierbach, K.; Huber, F. M.; Collins, L. N.; Davenport, A. M.; Jeon, Y. E.; Hoelz, A., Architecture of the symmetric core of the nuclear pore. *Science* **2016**, 352 (6283), aaf1015.
197. Bertino, J. R.; Waud, W. R.; Parker, W. B.; Lubin, M., Targeting tumors that lack methylthioadenosine phosphorylase (MTAP) activity: current strategies. *Cancer biology & therapy* **2011**, 11 (7), 627-32.
198. Morisseau, C.; Hammock, B. D., Impact of soluble epoxide hydrolase and epoxyeicosanoids on human health. *Annual review of pharmacology and toxicology* **2013**, 53, 37-58.
199. Hashimoto, K., Role of Soluble Epoxide Hydrolase in Metabolism of PUFAs in Psychiatric and Neurological Disorders. *Front Pharmacol* **2019**, 10.
200. Contaminant Repository for Affinity Purification (CRAPome). <https://reprint-apms.org/?q=reprint-home> (accessed 16.03.2023).
201. Mellacheruvu, D.; Wright, Z.; Couzens, A. L.; Lambert, J. P.; St-Denis, N. A.; Li, T.; Miteva, Y. V.; Hauri, S.; Sardi, M. E.; Low, T. Y.; Halim, V. A.; Bagshaw, R. D.; Hubner, N. C.; Al-Hakim, A.; Bouchard, A.; Faubert, D.; Fermin, D.; Dunham, W. H.; Goudreault, M.; Lin, Z. Y.; Badillo, B. G.; Pawson, T.; Durocher, D.; Coulombe, B.; Aebersold, R.; Superti-Furga, G.; Colinge, J.; Heck, A. J.; Choi, H.; Gstaiger, M.; Mohammed, S.; Cristea, I. M.; Bennett, K. L.; Washburn, M. P.; Raught, B.; Ewing, R. M.; Gingras, A. C.; Nesvizhskii, A. I., The CRAPome: a contaminant repository for affinity purification-mass spectrometry data. *Nat Methods* **2013**, 10 (8), 730-6.
202. Similarity Ensemble Approach (SEA) Target Prediction. <https://sea.bkslab.org/> (accessed 03.05.2023).



## References

203. Keiser, M. J.; Roth, B. L.; Armbruster, B. N.; Ernsberger, P.; Irwin, J. J.; Shoichet, B. K., Relating protein pharmacology by ligand chemistry. *Nature biotechnology* **2007**, *25* (2), 197-206.
204. SwissTargetPrediction. <http://www.swisstargetprediction.ch/> (accessed 03.05.2023).
205. Daina, A.; Michielin, O.; Zoete, V., SwissTargetPrediction: updated data and new features for efficient prediction of protein targets of small molecules. *Nucleic Acids Res* **2019**, *47* (W1), W357-W364.
206. SuperPred. <https://prediction.charite.de/index.php> (accessed 03.05.2023).
207. Nickel, J.; Gohlke, B.-O.; Erehman, J.; Banerjee, P.; Rong, W. W.; Goede, A.; Dunkel, M.; Preissner, R., SuperPred: update on drug classification and target prediction. *Nucleic Acids Res* **2014**, *42* (W1), W26-W31.
208. Munro, S.; Thomas, K. L.; Abu-Shaar, M., Molecular characterization of a peripheral receptor for cannabinoids. *Nature* **1993**, *365* (6441), 61-65.
209. Latek, D.; Kolinski, M.; Ghoshdastider, U.; Debinski, A.; Bombolewski, R.; Plazinska, A.; Jozwiak, K.; Filipek, S., Modeling of ligand binding to G protein coupled receptors: cannabinoid CB1, CB2 and adrenergic  $\beta$ 2AR. *J Mol Model* **2011**, *17* (9), 2353-2366.
210. Sophocleous, A.; Marino, S.; Kabir, D.; Ralston, S. H.; Idris, A. I., Combined deficiency of the Cnr1 and Cnr2 receptors protects against age-related bone loss by osteoclast inhibition. *Aging cell* **2017**, *16* (5), 1051-1061.
211. Gautheron, J.; J eru, I., The Multifaceted Role of Epoxide Hydrolases in Human Health and Disease. *Int J Mol Sci* **2021**, *22* (1), 13.
212. Sun, C.-P.; Zhang, X.-Y.; Morisseau, C.; Hwang, S. H.; Zhang, Z.-J.; Hammock, B. D.; Ma, X.-C., Discovery of Soluble Epoxide Hydrolase Inhibitors from Chemical Synthesis and Natural Products. *J Med Chem* **2021**, *64* (1), 184-215.
213. Hwang, H. W.; Lee, J. R.; Chou, K. Y.; Suen, C. S.; Hwang, M. J.; Chen, C.; Shieh, R. C.; Chau, L. Y., Oligomerization is crucial for the stability and function of heme oxygenase-1 in the endoplasmic reticulum. *J Biol Chem* **2009**, *284* (34), 22672-9.
214. Wilks, A.; Black, S. M.; Miller, W. L.; Ortiz de Montellano, P. R., Expression and characterization of truncated human heme oxygenase (hHO-1) and a fusion protein of hHO-1 with human cytochrome P450 reductase. *Biochemistry* **1995**, *34* (13), 4421-7.
215. Sebasti an, V. P.; Salazar, G. A.; Coronado-Arr azola, I.; Schultz, B. M.; Vallejos, O. P.; Berkowitz, L.;  lvarez-Lobos, M. M.; Riedel, C. A.; Kalergis, A. M.; Bueno, S. M., Heme Oxygenase-1 as a Modulator of Intestinal Inflammation Development and Progression. *Front Immunol* **2018**, *9*.
216. Feng, S.; Liu, D.; Feng, W.; Feng, G., Allyl Fluorescein Ethers as Promising Fluorescent Probes for Carbon Monoxide Imaging in Living Cells. *Anal Chem* **2017**, *89* (6), 3754-3760.
217. Turcanu, V.; Dhouib, M.; Poindron, P., Determination of Heme Oxygenase Activity in Murine Macrophages for Studying Oxidative Stress Inhibitors. *Anal Biochem* **1998**, *263* (2), 251-253.
218. The Human Protein Atlas: HMOX1. <https://www.proteinatlas.org/ENSG00000100292-HMOX1> (accessed 09.05.2023).
219. Wolf, N. M.; Morisseau, C.; Jones, P. D.; Hock, B.; Hammock, B. D., Development of a high-throughput screen for soluble epoxide hydrolase inhibition. *Anal Biochem* **2006**, *355* (1), 71-80.
220. Morisseau, C.; Sahdeo, S.; Cortopassi, G.; Hammock, B. D., Development of an HTS assay for EPHX2 phosphatase activity and screening of nontargeted libraries. *Anal Biochem* **2013**, *434* (1), 105-11.
221. Chen, D.; Whitcomb, R.; MacIntyre, E.; Tran, V.; Do, Z. N.; Sabry, J.; Patel, D. V.; Anandan, S. K.; Gless, R.; Webb, H. K., Pharmacokinetics and Pharmacodynamics of AR9281, an Inhibitor of Soluble Epoxide Hydrolase, in Single- and Multiple-Dose Studies in Healthy Human Subjects. *Journal of clinical pharmacology* **2012**, *52* (3), 319-328.
222. Podolin, P. L.; Bolognese, B. J.; Foley, J. F.; Long, E.; Peck, B.; Umbrecht, S.; Zhang, X.; Zhu, P.; Schwartz, B.; Xie, W.; Quinn, C.; Qi, H.; Sweitzer, S.; Chen, S.;

## References

- Galop, M.; Ding, Y.; Belyanskaya, S. L.; Israel, D. I.; Morgan, B. A.; Behm, D. J.; Marino, J. P.; Kurali, E.; Barnette, M. S.; Mayer, R. J.; Booth-Genthe, C. L.; Callahan, J. F., In vitro and in vivo characterization of a novel soluble epoxide hydrolase inhibitor. *Prostaglandins & other lipid mediators* **2013**, *104-105*, 25-31.
223. Hammock, B. D.; McReynolds, C. B.; Wagner, K.; Buckpitt, A.; Cortes-Puch, I.; Croston, G.; Lee, K. S. S.; Yang, J.; Schmidt, W. K.; Hwang, S. H., Movement to the Clinic of Soluble Epoxide Hydrolase Inhibitor EC5026 as an Analgesic for Neuropathic Pain and for Use as a Nonaddictive Opioid Alternative. *J Med Chem* **2021**, *64* (4), 1856-1872.
224. Kramer, J. S.; Woltersdorf, S.; Dufлот, T.; Hiesinger, K.; Lillich, F. F.; Knöll, F.; Wittmann, S. K.; Klingler, F.-M.; Brunst, S.; Chaikuad, A.; Morisseau, C.; Hammock, B. D.; Buccellati, C.; Sala, A.; Rovati, G. E.; Leuillier, M.; Fraineau, S.; Rondeaux, J.; Hernandez-Olmos, V.; Heering, J.; Merk, D.; Pogoryelov, D.; Steinhilber, D.; Knapp, S.; Bellien, J.; Proschak, E., Discovery of the First in Vivo Active Inhibitors of the Soluble Epoxide Hydrolase Phosphatase Domain. *J Med Chem* **2019**, *62* (18), 8443-8460.
225. Lu, Q.; Cai, Y.; Xiang, C.; Wu, T.; Zhao, Y.; Wang, J.; Wang, H.; Zou, L., Ebselen, a multi-target compound: its effects on biological processes and diseases. *Expert Rev Mol Med* **2021**, *23*, e12.
226. Terentis, A. C.; Freewan, M.; Sempértegui Plaza, T. S.; Raftery, M. J.; Stocker, R.; Thomas, S. R., The Selenazal Drug Ebselen Potently Inhibits Indoleamine 2,3-Dioxygenase by Targeting Enzyme Cysteine Residues. *Biochemistry* **2010**, *49* (3), 591-600.
227. Zhang, X.; Selvaraju, K.; Saei, A. A.; D'Arcy, P.; Zubarev, R. A.; Arnér, E. S.; Linder, S., Repurposing of auranofin: Thioredoxin reductase remains a primary target of the drug. *Biochimie* **2019**, *162*, 46-54.
228. Ren, X.; Zou, L.; Lu, J.; Holmgren, A., Selenocysteine in mammalian thioredoxin reductase and application of ebselen as a therapeutic. *Free Radic Biol Med* **2018**, *127*, 238-247.
229. Chadda, R.; Robertson, J. L., Chapter Three - Measuring Membrane Protein Dimerization Equilibrium in Lipid Bilayers by Single-Molecule Fluorescence Microscopy. In *Meth Enzymol*, Spies, M.; Chemla, Y. R., Eds. Academic Press: 2016; Vol. 581, pp 53-82.
230. Rigobello, M. P.; Scutari, G.; Folda, A.; Bindoli, A., Mitochondrial thioredoxin reductase inhibition by gold(I) compounds and concurrent stimulation of permeability transition and release of cytochrome c. *Biochem Pharmacol* **2004**, *67* (4), 689-96.
231. Uhlén, M.; Björling, E.; Agaton, C.; Szgyarto, C. A.; Amini, B.; Andersen, E.; Andersson, A. C.; Angelidou, P.; Asplund, A.; Asplund, C.; Berglund, L.; Bergström, K.; Brumer, H.; Cerjan, D.; Ekström, M.; Elobeid, A.; Eriksson, C.; Fagerberg, L.; Falk, R.; Fall, J.; Forsberg, M.; Björklund, M. G.; Gumbel, K.; Halimi, A.; Hallin, I.; Hamsten, C.; Hansson, M.; Hedhammar, M.; Hercules, G.; Kampf, C.; Larsson, K.; Lindskog, M.; Lodewyckx, W.; Lund, J.; Lundberg, J.; Magnusson, K.; Malm, E.; Nilsson, P.; Odling, J.; Oksvold, P.; Olsson, I.; Oster, E.; Ottosson, J.; Paavilainen, L.; Persson, A.; Rimini, R.; Rockberg, J.; Runeson, M.; Sivertsson, A.; Skölleremo, A.; Steen, J.; Stenvall, M.; Sterky, F.; Strömberg, S.; Sundberg, M.; Tegel, H.; Tourle, S.; Wahlund, E.; Waldén, A.; Wan, J.; Wernérus, H.; Westberg, J.; Wester, K.; Wrethagen, U.; Xu, L. L.; Hober, S.; Pontén, F., A human protein atlas for normal and cancer tissues based on antibody proteomics. *Molecular & cellular proteomics : MCP* **2005**, *4* (12), 1920-32.
232. Uhlén, M.; Fagerberg, L.; Hallström, B. M.; Lindskog, C.; Oksvold, P.; Mardinoglu, A.; Sivertsson, Å.; Kampf, C.; Sjöstedt, E.; Asplund, A.; Olsson, I.; Edlund, K.; Lundberg, E.; Navani, S.; Szgyarto, C. A.-K.; Odeberg, J.; Djureinovic, D.; Takanen, J. O.; Hober, S.; Alm, T.; Edqvist, P.-H.; Berling, H.; Tegel, H.; Mulder, J.; Rockberg, J.; Nilsson, P.; Schwenk, J. M.; Hamsten, M.; von Feilitzen, K.; Forsberg, M.; Persson, L.; Johansson, F.; Zwahlen, M.; von Heijne, G.; Nielsen, J.; Pontén, F., Tissue-based map of the human proteome. *Science* **2015**, *347* (6220), 1260419.
233. Meirer, K.; Steinhilber, D.; Proschak, E., Inhibitors of the Arachidonic Acid Cascade: Interfering with Multiple Pathways. *Basic Clin Pharmacol Toxicol* **2014**, *114* (1), 83-91.

## References

234. Shao, J.; Wang, H.; Yuan, G.; Chen, Z.; Li, Q., Involvement of the arachidonic acid cytochrome P450 epoxygenase pathway in the proliferation and invasion of human multiple myeloma cells. *PeerJ* **2016**, *4*, e1925.
235. Liu, X.; Qian, Z. Y.; Xie, F.; Fan, W.; Nelson, J. W.; Xiao, X.; Kaul, S.; Barnes, A. P.; Alkayed, N. J., Functional screening for G protein-coupled receptor targets of 14,15-epoxyeicosatrienoic acid. *Prostag Oth Lipid Mediat* **2017**, *132*, 31-40.
236. Wagner, B. K.; Schreiber, S. L., The Power of Sophisticated Phenotypic Screening and Modern Mechanism-of-Action Methods. *Cell Chem Biol* **2016**, *23* (1), 3-9.
237. Tan, M. H.; Nowak, N. J.; Loor, R.; Ochi, H.; Sandberg, A. A.; Lopez, C.; Pickren, J. W.; Berjian, R.; Douglass, H. O.; Chu, T. M., Characterization of a New Primary Human Pancreatic Tumor Line. *Cancer Investig* **1986**, *4* (1), 15-23.
238. Jin, J.; Wu, X.; Yin, J.; Li, M.; Shen, J.; Li, J.; Zhao, Y.; Zhao, Q.; Wu, J.; Wen, Q.; Cho, C. H.; Yi, T.; Xiao, Z.; Qu, L., Identification of Genetic Mutations in Cancer: Challenge and Opportunity in the New Era of Targeted Therapy. *Front Oncol* **2019**, *9*.
239. Croitoru-Lamoury, J.; Lamoury, F. M.; Caristo, M.; Suzuki, K.; Walker, D.; Takikawa, O.; Taylor, R.; Brew, B. J., Interferon-gamma regulates the proliferation and differentiation of mesenchymal stem cells via activation of indoleamine 2,3 dioxygenase (IDO). *PLoS One* **2011**, *6* (2), e14698.
240. Gocher, A. M.; Workman, C. J.; Vignali, D. A. A., Interferon- $\gamma$ : teammate or opponent in the tumour microenvironment? *Nat Rev Immunol* **2022**, *22* (3), 158-172.
241. Liu, M.; Wang, X.; Wang, L.; Ma, X.; Gong, Z.; Zhang, S.; Li, Y., Targeting the IDO1 pathway in cancer: from bench to bedside. *J Hematol Oncol* **2018**, *11* (1), 100.
242. Prendergast, G. C.; Smith, C.; Thomas, S.; Mandik-Nayak, L.; Laury-Kleintop, L.; Metz, R.; Muller, A. J., Indoleamine 2,3-dioxygenase pathways of pathogenic inflammation and immune escape in cancer. *Cancer Immunol Immunother* **2014**, *63* (7), 721-35.
243. Opitz, C. A.; Somarribas Patterson, L. F.; Mohapatra, S. R.; Dewi, D. L.; Sadik, A.; Platten, M.; Trump, S., The therapeutic potential of targeting tryptophan catabolism in cancer. *Br J Cancer* **2019**.
244. Bekki, S.; Hashimoto, S.; Yamasaki, K.; Komori, A.; Abiru, S.; Nagaoka, S.; Saeki, A.; Suehiro, T.; Kugiyama, Y.; Beppu, A.; Kuroki, T.; Nakamura, M.; Ito, M.; Yatsushashi, H., Serum kynurenine levels are a novel biomarker to predict the prognosis of patients with hepatocellular carcinoma. *PLoS One* **2020**, *15* (10), e0241002.
245. Mandarano, M.; Orecchini, E.; Bellezza, G.; Vannucci, J.; Ludovini, V.; Baglivo, S.; Tofanetti, F. R.; Chiari, R.; Loreti, E.; Puma, F.; Sidoni, A.; Belladonna, M. L., Kynurenine/Tryptophan Ratio as a Potential Blood-Based Biomarker in Non-Small Cell Lung Cancer. *Int J Mol Sci* **2021**, *22* (9).
246. Ariëns, E. J., Stereochemistry, a basis for sophisticated nonsense in pharmacokinetics and clinical pharmacology. *Eur J Clin Pharmacol* **1984**, *26* (6), 663-668.
247. Smith, S. W., Chiral Toxicology: It's the Same Thing...Only Different. *Toxicol Sci* **2009**, *110* (1), 4-30.
248. Teo, S. K.; Colburn, W. A.; Tracewell, W. G.; Kook, K. A.; Stirling, D. I.; Jaworsky, M. S.; Scheffler, M. A.; Thomas, S. D.; Laskin, O. L., Clinical Pharmacokinetics of Thalidomide. *Clin Pharmacokinet* **2004**, *43* (5), 311-327.
249. U.S. Food and Drug Administration. <https://www.fda.gov/regulatory-information/search-fda-guidance-documents/development-new-stereoisomeric-drugs> (accessed 03.04.2023).
250. Huttunen, K. M.; Raunio, H.; Rautio, J., Prodrugs--from serendipity to rational design. *Pharmacological reviews* **2011**, *63* (3), 750-71.
251. Dafferner, A. J.; Lushchekina, S.; Masson, P.; Xiao, G.; Schopfer, L. M.; Lockridge, O., Characterization of butyrylcholinesterase in bovine serum. *Chemico-biological interactions* **2017**, *266*, 17-27.
252. Ray, S.; Kreitler, D. F.; Gulick, A. M.; Murkin, A. S., The Nitro Group as a Masked Electrophile in Covalent Enzyme Inhibition. *ACS Chem Biol* **2018**, *13* (6), 1470-1473.
253. Rusinov, V. L.; Sapozhnikova, I. M.; Ulomskii, E. N.; Medvedeva, N. R.; Egorov, V. V.; Kiselev, O. I.; Deeva, E. G.; Vasin, A. V.; Chupakhin, O. N., Nucleophilic substitution of

## References

- nitro group in nitrotriazolotriazines as a model of potential interaction with cysteine-containing proteins. *Chem Heterocycl Comp* **2015**, *51* (3), 275-280.
254. Nepali, K.; Lee, H.-Y.; Liou, J.-P., Nitro-Group-Containing Drugs. *J Med Chem* **2019**, *62* (6), 2851-2893.
255. Yue, E. W.; Douty, B.; Wayland, B.; Bower, M.; Liu, X.; Leffet, L.; Wang, Q.; Bowman, K. J.; Hansbury, M. J.; Liu, C.; Wei, M.; Li, Y.; Wynn, R.; Burn, T. C.; Koblish, H. K.; Fridman, J. S.; Metcalf, B.; Scherle, P. A.; Combs, A. P., Discovery of potent competitive inhibitors of indoleamine 2,3-dioxygenase with in vivo pharmacodynamic activity and efficacy in a mouse melanoma model. *J Med Chem* **2009**, *52* (23), 7364-7.
256. Ortiz-Meoz, R. F.; Wang, L.; Matico, R.; Rutkowska-Klute, A.; De la Rosa, M.; Bedard, S.; Midgett, R.; Strohmmer, K.; Thomson, D.; Zhang, C.; Mebrahtu, M.; Guss, J.; Totoritis, R.; Consler, T.; Campobasso, N.; Taylor, D.; Lewis, T.; Weaver, K.; Muelbaier, M.; Seal, J.; Dunham, R.; Kazmierski, W.; Favre, D.; Bergamini, G.; Shewchuk, L.; Rendina, A.; Zhang, G., Characterization of Apo-Form Selective Inhibition of Indoleamine 2,3-Dioxygenase\*. *ChemBioChem* **2021**, *22* (3), 516-522.
257. Ortiz-Meoz, R. e. a., Characterization of novel inhibition of indoleamine 2,3-dioxygenase by targeting its apo form. *bioRxiv* **2018**.
258. Nelp, M. T.; Kates, P. A.; Hunt, J. T.; Newitt, J. A.; Balog, A.; Maley, D.; Zhu, X.; Abell, L.; Allentoff, A.; Borzilleri, R.; Lewis, H. A.; Lin, Z.; Seitz, S. P.; Yan, C.; Groves, J. T., Immune-modulating enzyme indoleamine 2,3-dioxygenase is effectively inhibited by targeting its apo-form. *Proc Natl Acad Sci U S A* **2018**, *115* (13), 3249-3254.
259. Atamna, H.; Brahmabhatt, M.; Atamna, W.; Shanower, G. A.; Dhahbi, J. M., ApoHRP-based assay to measure intracellular regulatory heme. *Metallomics : integrated biometal science* **2015**, *7* (2), 309-21.
260. Sun, L., Advances in the discovery and development of selective heme-displacing IDO1 inhibitors. *Expert Opin Drug Discov* **2020**, *15* (10), 1223-1232.
261. Davies, C.; Dötsch, L.; Ciulla, M. G.; Hennes, E.; Yoshida, K.; Gasper, R.; Scheel, R.; Sievers, S.; Strohmman, C.; Kumar, K.; Ziegler, S.; Waldmann, H., Identification of a Novel Pseudo-Natural Product Type IV IDO1 Inhibitor Chemotype. *Angew Chem Int Ed* **2022**, *61* (40), e202209374.
262. Vivoli, M.; Novak, H. R.; Littlechild, J. A.; Harmer, N. J., Determination of protein-ligand interactions using differential scanning fluorimetry. *Journal of visualized experiments : JoVE* **2014**, (91), 51809.
263. Niebling, S.; Burastero, O.; Bürgi, J.; Günther, C.; Defelipe, L. A.; Sander, S.; Gattkowski, E.; Anjanappa, R.; Wilmanns, M.; Springer, S.; Tidow, H.; García-Alai, M., FoldAffinity: binding affinities from nDSF experiments. *Scientific Reports* **2021**, *11* (1), 9572.
264. Röhrig, U. F.; Michielin, O.; Zoete, V., Structure and Plasticity of Indoleamine 2,3-Dioxygenase 1 (IDO1). *J Med Chem* **2021**, *64* (24), 17690-17705.
265. Bakmiwewa, S. M.; Fatokun, A. A.; Tran, A.; Payne, R. J.; Hunt, N. H.; Ball, H. J., Identification of selective inhibitors of indoleamine 2,3-dioxygenase 2. *Bioorganic Med Chem Lett* **2012**, *22* (24), 7641-7646.
266. He, X.; He, G.; Chu, Z.; Wu, H.; Wang, J.; Ge, Y.; Shen, H.; Zhang, S.; Shan, J.; Peng, K.; Wei, Z.; Zou, Y.; Xu, Y.; Zhu, Q., Discovery of the First Potent IDO1/IDO2 Dual Inhibitors: A Promising Strategy for Cancer Immunotherapy. *J Med Chem* **2021**, *64* (24), 17950-17968.
267. Zhang, Z.; Wang, Y.; Chen, X.; Song, X.; Tu, Z.; Chen, Y.; Zhang, Z.; Ding, K., Characterization of an aromatic trifluoromethyl ketone as a new warhead for covalently reversible kinase inhibitor design. *Bioorg Med Chem* **2021**, *50*, 116457.
268. HPP Progress To Date (The Human Proteome Organization). <https://www.hupo.org/hpp-progress-to-date> (accessed 14.04.2023).
269. Shuken, S. R., An Introduction to Mass Spectrometry-Based Proteomics. *J Proteome Res* **2023**, *22* (7), 2151-2171.
270. Jiang, L.; Wang, M.; Lin, S.; Jian, R.; Li, X.; Chan, J.; Dong, G.; Fang, H.; Robinson, A. E.; Aguet, F.; Anand, S.; Ardlie, K. G.; Gabriel, S.; Getz, G.; Graubert, A.; Hadley, K.; Handsaker, R. E.; Huang, K. H.; Kashin, S.; MacArthur, D. G.; Meier, S. R.;

## References

- Nedzel, J. L.; Nguyen, D. Y.; Segrè, A. V.; Todres, E.; Balliu, B.; Barbeira, A. N.; Battle, A.; Bonazzola, R.; Brown, A.; Brown, C. D.; Castel, S. E.; Conrad, D.; Cotter, D. J.; Cox, N.; Das, S.; de Goede, O. M.; Dermitzakis, E. T.; Engelhardt, B. E.; Eskin, E.; Eulalio, T. Y.; Ferraro, N. M.; Flynn, E.; Fresard, L.; Gamazon, E. R.; Garrido-Martín, D.; Gay, N. R.; Guigó, R.; Hamel, A. R.; He, Y.; Hoffman, P. J.; Hormozdiari, F.; Hou, L.; Im, H. K.; Jo, B.; Kasela, S.; Kellis, M.; Kim-Hellmuth, S.; Kwong, A.; Lappalainen, T.; Li, X.; Liang, Y.; Mangul, S.; Mohammadi, P.; Montgomery, S. B.; Muñoz-Aguirre, M.; Nachun, D. C.; Nobel, A. B.; Oliva, M.; Park, Y.; Park, Y.; Parsana, P.; Reverter, F.; Rouhana, J. M.; Sabatti, C.; Saha, A.; Skol, A. D.; Stephens, M.; Stranger, B. E.; Strober, B. J.; Teran, N. A.; Viñuela, A.; Wang, G.; Wen, X.; Wright, F.; Wucher, V.; Zou, Y.; Ferreira, P. G.; Li, G.; Melé, M.; Yeger-Lotem, E.; Barcus, M. E.; Bradbury, D.; Krubit, T.; McLean, J. A.; Qi, L.; Robinson, K.; Roche, N. V.; Smith, A. M.; Sobin, L.; Tabor, D. E.; Undale, A.; Bridge, J.; Brigham, L. E.; Foster, B. A.; Gillard, B. M.; Hasz, R.; Hunter, M.; Johns, C.; Johnson, M.; Karasik, E.; Kopen, G.; Leinweber, W. F.; McDonald, A.; Moser, M. T.; Myer, K.; Ramsey, K. D.; Roe, B.; Shad, S.; Thomas, J. A.; Walters, G.; Washington, M.; Wheeler, J.; Jewell, S. D.; Rohrer, D. C.; Valley, D. R.; Davis, D. A.; Mash, D. C.; Branton, P. A.; Barker, L. K.; Gardiner, H. M.; Mosavel, M.; Siminoff, L. A.; Flicek, P.; Haeussler, M.; Juettemann, T.; Kent, W. J.; Lee, C. M.; Powell, C. C.; Rosenbloom, K. R.; Ruffier, M.; Sheppard, D.; Taylor, K.; Trevanion, S. J.; Zerbino, D. R.; Abell, N. S.; Akey, J.; Chen, L.; Demanelis, K.; Doherty, J. A.; Feinberg, A. P.; Hansen, K. D.; Hickey, P. F.; Jasmine, F.; Kaul, R.; Kibriya, M. G.; Li, J. B.; Li, Q.; Linder, S. E.; Pierce, B. L.; Rizzardi, L. F.; Smith, K. S.; Stamatoyannopoulos, J.; Tang, H.; Carithers, L. J.; Guan, P.; Koester, S. E.; Little, A. R.; Moore, H. M.; Nierras, C. R.; Rao, A. K.; Vaught, J. B.; Volpi, S.; Snyder, M. P., A Quantitative Proteome Map of the Human Body. *Cell* **2020**, *183* (1), 269-283.e19.
271. Rusinova, I.; Forster, S.; Yu, S.; Kannan, A.; Masse, M.; Cumming, H.; Chapman, R.; Hertzog, P. J., Interferome v2.0: an updated database of annotated interferon-regulated genes. *Nucleic Acids Res* **2013**, *41* (Database issue), D1040-6.
272. Hertzog, P.; Forster, S.; Samarajiwa, S., Systems biology of interferon responses. *Journal of interferon & cytokine research : the official journal of the International Society for Interferon and Cytokine Research* **2011**, *31* (1), 5-11.
273. McNab, F.; Mayer-Barber, K.; Sher, A.; Wack, A.; O'Garra, A., Type I interferons in infectious disease. *Nat Rev Immunol* **2015**, *15* (2), 87-103.
274. Parkin, J.; Cohen, B., An overview of the immune system. *The Lancet* **2001**, *357* (9270), 1777-1789.
275. Croitoru-Lamoury, J.; Lamoury, F. M. J.; Caristo, M.; Suzuki, K.; Walker, D.; Takikawa, O.; Taylor, R.; Brew, B. J., Interferon- $\gamma$  Regulates the Proliferation and Differentiation of Mesenchymal Stem Cells via Activation of Indoleamine 2,3 Dioxygenase (IDO). *PLOS ONE* **2011**, *6* (2), e14698.
276. Ostler, N.; Britzen-Laurent, N.; Liebl, A.; Naschberger, E.; Lochnit, G.; Ostler, M.; Forster, F.; Kunzelmann, P.; Ince, S.; Supper, V.; Praefcke, G. J.; Schubert, D. W.; Stockinger, H.; Herrmann, C.; Stürzl, M., Gamma interferon-induced guanylate binding protein 1 is a novel actin cytoskeleton remodeling factor. *Mol Cell Biol* **2014**, *34* (2), 196-209.
277. Tecalco-Cruz, A. C.; Macías-Silva, M.; Ramírez-Jarquín, J. O.; Méndez-Ambrosio, B., Identification of genes modulated by interferon gamma in breast cancer cells. *Biochemistry and biophysics reports* **2021**, *27*, 101053.
278. Bonam, S. R.; Bayry, J.; Tschan, M. P.; Muller, S., Progress and Challenges in The Use of MAP1LC3 as a Legitimate Marker for Measuring Dynamic Autophagy In Vivo. *Cells* **2020**, *9* (5).
279. Baeken, M. W.; Weckmann, K.; Diefenthaler, P.; Schulte, J.; Yusifli, K.; Moosmann, B.; Behl, C.; Hajieva, P., Novel Insights into the Cellular Localization and Regulation of the Autophagosomal Proteins LC3A, LC3B and LC3C. *Cells* **2020**, *9* (10).
280. Redhead, M.; Satchell, R.; McCarthy, C.; Pollack, S.; Unitt, J., Thermal Shift as an Entropy-Driven Effect. *Biochemistry* **2017**, *56* (47), 6187-6199.

## References

281. Campbell, N. K.; Fitzgerald, H. K.; Dunne, A., Regulation of inflammation by the antioxidant haem oxygenase 1. *Nat Rev Immunol* **2021**, *21* (7), 411-425.
282. Gottlieb, Y.; Truman, M.; Cohen, L. A.; Leichtmann-Bardoogo, Y.; Meyron-Holtz, E. G., Endoplasmic reticulum anchored heme-oxygenase 1 faces the cytosol. *Haematologica* **2012**, *97* (10), 1489-93.
283. Dunn, L. L.; Midwinter, R. G.; Ni, J.; Hamid, H. A.; Parish, C. R.; Stocker, R., New insights into intracellular locations and functions of heme oxygenase-1. *Antioxidants & redox signaling* **2014**, *20* (11), 1723-42.
284. Marjon, K.; Cameron, Michael J.; Quang, P.; Clasquin, Michelle F.; Mandley, E.; Kunii, K.; McVay, M.; Choe, S.; Kernytsky, A.; Gross, S.; Konteatis, Z.; Murtie, J.; Blake, Michelle L.; Travins, J.; Dorsch, M.; Biller, Scott A.; Marks, Kevin M., MTAP Deletions in Cancer Create Vulnerability to Targeting of the MAT2A/PRMT5/RIOK1 Axis. *Cell Rep* **2016**, *15* (3), 574-587.
285. Strobl, C. D.; Henrich, F.; Singer, K.; Peter, K.; Kreutz, M.; Kremer, A.; Mackensen, A.; Aigner, M., MTA-mediated inhibition of human T cells: Mechanism and MTAP overexpression as putative overcoming strategy. *Canc Res* **2017**, *77* (13\_Supplement), 3971-3971.
286. González-Aguilera, C.; Askjaer, P., Dissecting the NUP107 complex: multiple components and even more functions. *Nucleus (Austin, Tex.)* **2012**, *3* (4), 340-8.
287. Senger, S.; Csokmay, J.; Akbar, T.; Jones, T. I.; Sengupta, P.; Lilly, M. A., The nucleoporin Seh1 forms a complex with Mio and serves an essential tissue-specific function in Drosophila oogenesis. *Development* **2011**, *138* (10), 2133-2142.
288. Gill, S. S.; Hammock, B. D.; Yamamoto, I.; Casida, J. E., PRELIMINARY CHROMATOGRAPHIC STUDIES ON THE METABOLITES AND PHOTODECOMPOSITION PRODUCTS OF THE JUVENOID 1-(4'-ETHYLPHENOXY)-6,7-EPOXY-3,7-DIMETHYL-2-OCTENE. In *Insect Juvenile Hormones: Chemistry and Action*, Menn, J. J.; Beroza, M., Eds. Academic Press: 1972; pp 177-189.
289. Hammock, B. D.; Gill, S. S.; Stamoudis, V.; Gilbert, L. I., Soluble mammalian epoxide hydratase: action on juvenile hormone and other terpenoid epoxides. *Comp Biochem Physiol* **1976**, *53B*, 263-265.
290. Morisseau, C.; Hammock, B. D., EPOXIDE HYDROLASES: Mechanisms, Inhibitor Designs, and Biological Roles. *Annu Rev Pharmacol* **2005**, *45* (1), 311-333.
291. Imig, J. D.; Zhao, X.; Capdevila, J. H.; Morisseau, C.; Hammock, B. D., Soluble Epoxide Hydrolase Inhibition Lowers Arterial Blood Pressure in Angiotensin II Hypertension. *Hypertension* **2002**, (39), 690-694.
292. Khadir, A.; Kavalakatt, S.; Madhu, D.; Cherian, P.; Al-Mulla, F.; Abubaker, J.; Tiss, A., Soluble Epoxide Hydrolase 2 Expression Is Elevated in Obese Humans and Decreased by Physical Activity. *Int J Mol Sci* **2020**, *21* (6), 2056.
293. Liu, M.-S.; Zhao, H.; Xu, C.-X.; Xie, P.-B.; Wang, W.; Yang, Y.-Y.; Lee, W.-H.; Jin, Y.; Zhou, H.-Q., Clinical significance of EPHX2 deregulation in prostate cancer. *Asian J Androl* **2021**, *23* (1), 109-115.
294. Reisdorf, W. C.; Xie, Q.; Zeng, X.; Xie, W.; Rajpal, N.; Hoang, B.; Burgert, M. E.; Kumar, V.; Hurle, M. R.; Rajpal, D. K.; O'Donnell, S.; MacDonald, T. T.; Vossenkämper, A.; Wang, L.; Reilly, M.; Votta, B. J.; Sanchez, Y.; Agarwal, P., Preclinical evaluation of EPHX2 inhibition as a novel treatment for inflammatory bowel disease. *PLoS One* **2019**, *14* (4), e0215033.
295. Kim, I.-H.; Heitzler, F. R.; Morisseau, C.; Nishi, K.; Tsai, H.-J.; Hammock, B. D., Optimization of Amide-Based Inhibitors of Soluble Epoxide Hydrolase with Improved Water Solubility. *J Med Chem* **2005**, *48* (10), 3621-3629.
296. Morisseau, C.; Goodrow, M. H.; Dowdy, D.; Zheng, J.; Greene, J. F.; Sanborn, J. R.; Hammock, B. D., Potent urea and carbamate inhibitors of soluble epoxide hydrolases. *Proc Natl Acad Sci U S A* **1999**, *96* (16), 8849-54.
297. Hefke, L.; Hiesinger, K.; Zhu, W. F.; Kramer, J. S.; Proschak, E., Computer-Aided Fragment Growing Strategies to Design Dual Inhibitors of Soluble Epoxide Hydrolase and LTA4 Hydrolase. *ACS Medicinal Chemistry Letters* **2020**, *11* (6), 1244-1249.

## References

298. Hwang, S. H.; Weckler, A. T.; Wagner, K.; Hammock, B. D., Rationally designed multitarget agents against inflammation and pain. *Curr Med Chem* **2013**, *20* (13), 1783-99.
299. Amrein, B. A.; Bauer, P.; Duarte, F.; Janfalk Carlsson, Å.; Naworyta, A.; Mowbray, S. L.; Widersten, M.; Kamerlin, S. C. L., Expanding the Catalytic Triad in Epoxide Hydrolases and Related Enzymes. *ACS Catalysis* **2015**, *5* (10), 5702-5713.
300. Borhan, B.; Jones, A. D.; Pinot, F.; Grant, D. F.; Kurth, M. J.; Hammock, B. D., Mechanism of Soluble Epoxide Hydrolase: FORMATION OF AN  $\alpha$ -HYDROXY ESTER-ENZYME INTERMEDIATE THROUGH Asp-333 (\*). *J Biol Chem* **1995**, *270* (45), 26923-26930.
301. Nagy-Grócz, G.; Zádor, F.; Dvorácskó, S.; Bohár, Z.; Benyhe, S.; Tömböly, C.; Párdutz, Á.; Vécsei, L., Interactions between the Kynurenine and the Endocannabinoid System with Special Emphasis on Migraine. *Int J Mol Sci* **2017**, *18* (8), 1617.
302. Jenny, M.; Santer, E.; Pirich, E.; Schennach, H.; Fuchs, D.,  $\Delta$ 9-Tetrahydrocannabinol and cannabidiol modulate mitogen-induced tryptophan degradation and neopterin formation in peripheral blood mononuclear cells in vitro. *J Neuroimmunol* **2009**, *207* (1), 75-82.
303. Minegishi, S.; Yumura, A.; Miyoshi, H.; Negi, S.; Taketani, S.; Motterlini, R.; Foresti, R.; Kano, K.; Kitagishi, H., Detection and Removal of Endogenous Carbon Monoxide by Selective and Cell-Permeable Hemoprotein Model Complexes. *JACS* **2017**, *139* (16), 5984-5991.
304. Rock, R. B.; Hu, S.; Deshpande, A.; Munir, S.; May, B. J.; Baker, C. A.; Peterson, P. K.; Kapur, V., Transcriptional response of human microglial cells to interferon-gamma. *Genes and immunity* **2005**, *6* (8), 712-9.
305. Tassioulas, I.; Hu, X.; Ho, H.; Kashyap, Y.; Paik, P.; Hu, Y.; Lowell, C. A.; Ivashkiv, L. B., Amplification of IFN-alpha-induced STAT1 activation and inflammatory function by Syk and ITAM-containing adaptors. *Nat Immunol* **2004**, *5* (11), 1181-9.
306. Gibbs, P. E.; Miralem, T.; Maines, M. D., Characterization of the human biliverdin reductase gene structure and regulatory elements: promoter activity is enhanced by hypoxia and suppressed by TNF-alpha-activated NF-kappaB. *FASEB journal : official publication of the Federation of American Societies for Experimental Biology* **2010**, *24* (9), 3239-54.
307. Singh, V.; Evans, G. B.; Lenz, D. H.; Mason, J. M.; Clinch, K.; Mee, S.; Painter, G. F.; Tyler, P. C.; Furneaux, R. H.; Lee, J. E.; Howell, P. L.; Schramm, V. L., Femtomolar Transition State Analogue Inhibitors of 5'-Methylthioadenosine/S-Adenosylhomocysteine Nucleosidase from *Escherichia coli*\*. *J Biol Chem* **2005**, *280* (18), 18265-18273.
308. Singh, V.; Shi, W.; Evans, G. B.; Tyler, P. C.; Furneaux, R. H.; Almo, S. C.; Schramm, V. L., Picomolar Transition State Analogue Inhibitors of Human 5'-Methylthioadenosine Phosphorylase and X-ray Structure with MT-Immucillin-A. *Biochemistry* **2004**, *43* (1), 9-18.
309. Basu, I.; Cordovano, G.; Das, I.; Belbin, T. J.; Guha, C.; Schramm, V. L., A transition state analogue of 5'-methylthioadenosine phosphorylase induces apoptosis in head and neck cancers. *J Biol Chem* **2007**, *282* (29), 21477-86.
310. Bzówka, M.; Mitusińska, K.; Hopko, K.; Góra, A., Computational insights into the known inhibitors of human soluble epoxide hydrolase. *Drug Discov Today* **2021**, *26* (8), 1914-1921.
311. Tolvanen, T. A., Current Advances in CETSA. *Frontiers in molecular biosciences* **2022**, *9*, 866764.
312. Mullin, C. A.; Hammock, B. D., Chalcone oxides—potent selective inhibitors of cytosolic epoxide hydrolase. *Arch Biochem Biophys* **1982**, *216* (2), 423-439.
313. Kim, I.-H.; Park, Y.-K.; Hammock, B. D.; Nishi, K., Structure–Activity Relationships of Cycloalkylamide Derivatives as Inhibitors of the Soluble Epoxide Hydrolase. *J Med Chem* **2011**, *54* (6), 1752-1761.
314. Yu, Z.; Xu, F.; Huse, L. M.; Morisseau, C.; Draper, A. J.; Newman, J. W.; Parker, C.; Graham, L.; Engler, M. M.; Hammock, B. D.; Zeldin, D. C.; Kroetz, D. L., Soluble epoxide hydrolase regulates hydrolysis of vasoactive epoxyeicosatrienoic acids. *Circulation research* **2000**, *87* (11), 992-8.

## References

315. Imig, J. D.; Zhao, X.; Capdevila, J. H.; Morisseau, C.; Hammock, B. D., Soluble epoxide hydrolase inhibition lowers arterial blood pressure in angiotensin II hypertension. *Hypertension* **2002**, *39* (2), 690-694.
316. Kim, I.-H.; Morisseau, C.; Watanabe, T.; Hammock, B. D., Design, synthesis, and biological activity of 1, 3-disubstituted ureas as potent inhibitors of the soluble epoxide hydrolase of increased water solubility. *J Med Chem* **2004**, *47* (8), 2110-2122.
317. Jones, P. D.; Tsai, H.-J.; Do, Z. N.; Morisseau, C.; Hammock, B. D., Synthesis and SAR of conformationally restricted inhibitors of soluble epoxide hydrolase. *Bioorg Med Chem Lett* **2006**, *16* (19), 5212-5216.
318. Burmistrov, V.; Morisseau, C.; Danilov, D.; Harris, T. R.; Dalinger, I.; Vatsadze, I.; Shkineva, T.; Butov, G. M.; Hammock, B. D., 1, 3-Disubstituted and 1, 3, 3-trisubstituted adamantyl-ureas with isoxazole as soluble epoxide hydrolase inhibitors. *Bioorg Med Chem Lett* **2015**, *25* (23), 5514-5519.
319. Hwang, S. H.; Tsai, H.-J.; Liu, J.-Y.; Morisseau, C.; Hammock, B. D., Orally bioavailable potent soluble epoxide hydrolase inhibitors. *J Med Chem* **2007**, *50* (16), 3825-3840.
320. Anandan, S.-K.; Do, Z. N.; Webb, H. K.; Patel, D. V.; Gless, R. D., Non-urea functionality as the primary pharmacophore in soluble epoxide hydrolase inhibitors. *Bioorg Med Chem Lett* **2009**, *19* (4), 1066-1070.
321. Banerjee, S., An insight into the interaction between  $\alpha$ -ketoamide- based inhibitor and coronavirus main protease: A detailed in silico study. *Biophysical chemistry* **2021**, *269*, 106510.
322. Robello, M.; Barresi, E.; Baglini, E.; Salerno, S.; Taliani, S.; Settimo, F. D., The Alpha Keto Amide Moiety as a Privileged Motif in Medicinal Chemistry: Current Insights and Emerging Opportunities. *J Med Chem* **2021**, *64* (7), 3508-3545.
323. Zhang, L.; Lin, D.; Sun, X.; Curth, U.; Drosten, C.; Sauerhering, L.; Becker, S.; Rox, K.; Hilgenfeld, R., Crystal structure of SARS-CoV-2 main protease provides a basis for design of improved  $\alpha$ -ketoamide inhibitors. *Science* **2020**, *368* (6489), 409-412.
324. Lazaar, A. L.; Yang, L.; Boardley, R. L.; Goyal, N. S.; Robertson, J.; Baldwin, S. J.; Newby, D. E.; Wilkinson, I. B.; Tal-Singer, R.; Mayer, R. J.; Cheriyan, J., Pharmacokinetics, pharmacodynamics and adverse event profile of GSK2256294, a novel soluble epoxide hydrolase inhibitor. *British journal of clinical pharmacology* **2016**, *81* (5), 971-9.
325. Hallenbeck, K. K.; Turner, D. M.; Renslo, A. R.; Arkin, M. R., Targeting Non-Catalytic Cysteine Residues Through Structure-Guided Drug Discovery. *Current topics in medicinal chemistry* **2017**, *17* (1), 4-15.
326. Winzker, M. Biological characterization of farnesyl-mediated protein-protein interactions. Technische Universität Dortmund, 2019.
327. Kotecki, M.; Reddy, P. S.; Cochran, B. H., Isolation and characterization of a near-haploid human cell line. *Experimental cell research* **1999**, *252* (2), 273-80.
328. Gatto, F.; Miess, H.; Schulze, A.; Nielsen, J., Flux balance analysis predicts essential genes in clear cell renal cell carcinoma metabolism. *Sci Rep* **2015**, *5* (1), 10738.
329. Zhou, Y.; Li, X.; Guan, A.; Zhou, H.; Zhu, Y.; Wang, R.; Li, R., EPHX2 Inhibits Colon Cancer Progression by Promoting Fatty Acid Degradation. *Front Oncol* **2022**, *12*, 870721.
330. Raina, K.; Lu, J.; Qian, Y.; Altieri, M.; Gordon, D.; Rossi, A. M. K.; Wang, J.; Chen, X.; Dong, H.; Siu, K.; Winkler, J. D.; Crew, A. P.; Crews, C. M.; Coleman, K. G., PROTAC-induced BET protein degradation as a therapy for castration-resistant prostate cancer. *PNAS* **2016**, *113* (26), 7124-7129.
331. Kuhn, D. J.; Chen, Q.; Voorhees, P. M.; Strader, J. S.; Shenk, K. D.; Sun, C. M.; Demo, S. D.; Bennett, M. K.; van Leeuwen, F. W. B.; Chanan-Khan, A. A.; Orlowski, R. Z., Potent activity of carfilzomib, a novel, irreversible inhibitor of the ubiquitin-proteasome pathway, against preclinical models of multiple myeloma. *Blood* **2007**, *110* (9), 3281-3290.
332. Kreiß, M.; Oberlis, J. H.; Seuter, S.; Bischoff-Kont, I.; Sürün, D.; Thomas, D.; Göbel, T.; Schmid, T.; Rådmark, O.; Brandes, R. P.; Fürst, R.; Häfner, A. K.; Steinhilber,



## References

- D., Human 5-lipoxygenase regulates transcription by association to euchromatin. *Biochem Pharmacol* **2022**, *203*, 115187.
333. Nguyen, N. T.; Nakahama, T.; Le, D. H.; Van Son, L.; Chu, H. H.; Kishimoto, T., Aryl hydrocarbon receptor and kynurenine: recent advances in autoimmune disease research. *Front Immunol* **2014**, *5*, 551.
334. Chiaro, C. R.; Patel, R. D.; Perdeu, G. H., 12(R)-Hydroxy-5(Z),8(Z),10(E),14(Z)-eicosatetraenoic acid [12(R)-HETE], an arachidonic acid derivative, is an activator of the aryl hydrocarbon receptor. *Mol Pharmacol* **2008**, *74* (6), 1649-56.
335. Rojas, I. Y.; Moyer, B. J.; Ringelberg, C. S.; Wilkins, O. M.; Pooler, D. B.; Ness, D. B.; Coker, S.; Tosteson, T. D.; Lewis, L. D.; Chamberlin, M. D.; Tomlinson, C. R., Kynurenine-Induced Aryl Hydrocarbon Receptor Signaling in Mice Causes Body Mass Gain, Liver Steatosis, and Hyperglycemia. *Obesity* **2021**, *29* (2), 337-349.
336. Eric, A. E.; Rozenn, N. L.; Nona, S.; Sina, A. G.; Rheem, A. T., CYP2J2 Expression in Adult Ventricular Myocytes Protects Against Reactive Oxygen Species Toxicity. *Drug Metab Disp* **2018**, *46* (4), 380.
337. Park, B.; Sardar Pasha, S. P. B.; Sishtla, K.; Corson, T. W., AAV8 mediated expression of shRNA targeting soluble epoxide hydrolase suppresses choroidal neovascularization. *Invest Ophthalmol Vis Sci* **2020**, *61* (7), 4343-4343.
338. Abraham, N. G.; Singh, S. P.; Bellner, L.; Bamshad, D.; Drummond, G., Abstract 079: Hmox1 Activation Reprograms White Fat to Beige Adipose Tissue Through Recruitment of Cyp2C44-derived EET, pAMPK-PGC1 $\alpha$  That Enhances Mitochondrial Mfn2 and Opa1. *Hypertension* **2016**, *68* (suppl\_1), A079-A079.
339. Wang, B.; Wu, L.; Chen, J.; Dong, L.; Chen, C.; Wen, Z.; Hu, J.; Fleming, I.; Wang, D. W., Metabolism pathways of arachidonic acids: mechanisms and potential therapeutic targets. *Sig Transduct Target Ther* **2021**, *6* (1), 94.
340. Baron, J. A., Aspirin and NSAIDs for the prevention of colorectal cancer. *Cancer Prev II* **2009**, 223-229.
341. Zhao, Y.-s.; Zhu, S.; Li, X.-w.; Wang, F.; Hu, F.-l.; Li, D.-d.; Zhang, W.-c.; Li, X., Association between NSAIDs use and breast cancer risk: a systematic review and meta-analysis. *Breast Cancer Res Treat* **2009**, *117*, 141-150.
342. Knox, C.; Law, V.; Jewison, T.; Liu, P.; Ly, S.; Frolkis, A.; Pon, A.; Banco, K.; Mak, C.; Neveu, V.; Djoumbou, Y.; Eisner, R.; Guo, A. C.; Wishart, D. S., DrugBank 3.0: a comprehensive resource for 'omics' research on drugs. *Nucleic Acids Res* **2011**, *39* (Database issue), D1035-41.
343. Law, V.; Knox, C.; Djoumbou, Y.; Jewison, T.; Guo, A. C.; Liu, Y.; Maciejewski, A.; Arndt, D.; Wilson, M.; Neveu, V.; Tang, A.; Gabriel, G.; Ly, C.; Adamjee, S.; Dame, Z. T.; Han, B.; Zhou, Y.; Wishart, D. S., DrugBank 4.0: shedding new light on drug metabolism. *Nucleic Acids Res* **2014**, *42* (Database issue), D1091-7.
344. Wishart, D. S.; Feunang, Y. D.; Guo, A. C.; Lo, E. J.; Marcu, A.; Grant, J. R.; Sajed, T.; Johnson, D.; Li, C.; Sayeeda, Z.; Assempour, N.; Iynkkaran, I.; Liu, Y.; Maciejewski, A.; Gale, N.; Wilson, A.; Chin, L.; Cummings, R.; Le, D.; Pon, A.; Knox, C.; Wilson, M., DrugBank 5.0: a major update to the DrugBank database for 2018. *Nucleic Acids Res* **2018**, *46* (D1), D1074-d1082.
345. Wishart, D. S.; Knox, C.; Guo, A. C.; Cheng, D.; Shrivastava, S.; Tzur, D.; Gautam, B.; Hassanali, M., DrugBank: a knowledgebase for drugs, drug actions and drug targets. *Nucleic Acids Res* **2008**, *36* (Database issue), D901-6.
346. Wishart, D. S.; Knox, C.; Guo, A. C.; Shrivastava, S.; Hassanali, M.; Stothard, P.; Chang, Z.; Woolsey, J., DrugBank: a comprehensive resource for in silico drug discovery and exploration. *Nucleic Acids Res* **2006**, *34* (Database issue), D668-72.
347. Griñán-Ferré, C.; Codony, S.; Pujol, E.; Yang, J.; Leiva, R.; Escolano, C.; Puigoriol-Illamola, D.; Companys-Aleman, J.; Corpas, R.; Sanfeliu, C.; Pérez, B.; Loza, M. I.; Brea, J.; Morisseau, C.; Hammock, B. D.; Vázquez, S.; Pallàs, M.; Galdeano, C., Pharmacological Inhibition of Soluble Epoxide Hydrolase as a New Therapy for Alzheimer's Disease. *Neurotherapeutics* **2020**, *17* (4), 1825-1835.

## References

348. Barnes, N. A.; Stephenson, S. J.; Tooze, R. M.; Doody, G. M., Amino acid deprivation links BLIMP-1 to the immunomodulatory enzyme indoleamine 2,3-dioxygenase. *J Immunol* **2009**, *183* (9), 5768-77.
349. Hahn, S.; Achenbach, J.; Buscató, E.; Klingler, F.-M.; Schroeder, M.; Meirer, K.; Hieke, M.; Heering, J.; Barbosa-Sicard, E.; Loehr, F.; Fleming, I.; Doetsch, V.; Schubert-Zsilavecz, M.; Steinhilber, D.; Proschak, E., Complementary Screening Techniques Yielded Fragments that Inhibit the Phosphatase Activity of Soluble Epoxide Hydrolase. *ChemMedChem* **2011**, *6* (12), 2146-2149.
350. Petrovic, A.; Mosalaganti, S.; Keller, J.; Mattiuzzo, M.; Overlack, K.; Krenn, V.; De Antoni, A.; Wohlgemuth, S.; Cecatiello, V.; Pasqualato, S.; Raunser, S.; Musacchio, A., Modular assembly of RWD domains on the Mis12 complex underlies outer kinetochore organization. *Mol Cell* **2014**, *53* (4), 591-605.
351. Pfaffl, M. W., A new mathematical model for relative quantification in real-time RT-PCR. *Nucleic Acids Res* **2001**, *29* (9), e45-e45.
352. Littlejohn, T. K.; Takikawa, O.; Skylas, D.; Jamie, J. F.; Walker, M. J.; Truscott, R. J., Expression and purification of recombinant human indoleamine 2, 3-dioxygenase. *Protein Expr Purif* **2000**, *19* (1), 22-9.
353. Kabsch, W., XDS. *Acta Crystallogr D Biol Crystallogr* **2010**, *66* (Pt 2), 125-132.
354. McCoy, A. J.; Grosse-Kunstleve, R. W.; Adams, P. D.; Winn, M. D.; Storoni, L. C.; Read, R. J., Phaser crystallographic software. *J Appl Cryst* **2007**, *40* (4), 658-674.
355. Liebschner, D.; Afonine, P. V.; Baker, M. L.; Bunkoczi, G.; Chen, V. B.; Croll, T. I.; Hintze, B.; Hung, L.-W.; Jain, S.; McCoy, A. J.; Moriarty, N. W.; Oeffner, R. D.; Poon, B. K.; Prisant, M. G.; Read, R. J.; Richardson, J. S.; Richardson, D. C.; Sammito, M. D.; Sobolev, O. V.; Stockwell, D. H.; Terwilliger, T. C.; Urzhumtsev, A. G.; Videau, L. L.; Williams, C. J.; Adams, P. D., Macromolecular structure determination using X-rays, neutrons and electrons: recent developments in Phenix. *Acta Crystallogr D Biol Crystallogr* **2019**, *75* (10), 861-877.
356. Afonine, P. V.; Grosse-Kunstleve, R. W.; Echols, N.; Headd, J. J.; Moriarty, N. W.; Mustyakimov, M.; Terwilliger, T. C.; Urzhumtsev, A.; Zwart, P. H.; Adams, P. D., Towards automated crystallographic structure refinement with phenix.refine. *Acta Crystallogr D Biol Crystallogr* **2012**, *68* (Pt 4), 352-367.
357. Emsley, P.; Lohkamp, B.; Scott, W. G.; Cowtan, K., Features and development of Coot. *Acta Crystallogr D Biol Crystallogr* **2010**, *66* (Pt 4), 486-501.
358. Tyanova, S.; Temu, T.; Carlson, A.; Sinitcyn, P.; Mann, M.; Cox, J., Visualization of LC-MS/MS proteomics data in MaxQuant. *Proteomics* **2015**, *15* (8), 1453-6.
359. Cox, J.; Mann, M., MaxQuant enables high peptide identification rates, individualized p.p.b.-range mass accuracies and proteome-wide protein quantification. *Nature biotechnology* **2008**, *26* (12), 1367-72.
360. Tyanova, S.; Temu, T.; Sinitcyn, P.; Carlson, A.; Hein, M. Y.; Geiger, T.; Mann, M.; Cox, J., The Perseus computational platform for comprehensive analysis of (prote)omics data. *Nat Methods* **2016**, *13* (9), 731-740.
361. Tyanova, S.; Cox, J., Perseus: A Bioinformatics Platform for Integrative Analysis of Proteomics Data in Cancer Research. *Methods Mol Biol* **2018**, *1711*, 133-148.

## Abbreviations

### 10 Abbreviations

<b>Abbreviation</b>	<b>Meaning</b>
1-MT	1-methyl-L-tryptophan
3-HANA	3-hydroxyanthranilic acid
3-HK	3-hydroxykynurenine
AA	arachidonic acid
Ac/N	N-terminal acetylation
AhR	aryl hydrocarbon receptor
APC	antigen-presenting cell
APOL	apolipoprotein L
APS	ammonium persulfate
ARE	antioxidant response element
ASR	age-standardized incidence rate
ATL2	atlastin-2
ATP	adenosine triphosphate
BBT	2'-(2-benzothiazoyl)-6'-hydroxybenzothiazole
BBPT	2'-(2-benzothiazoyl)-6'-hydroxybenzothiazole phosphate
BIOS	biology-oriented synthesis
BIS-TRIS	bis(2-hydroxyethyl)amino-tris(hydroxymethyl)methane
Bn	benzyl
Boc	<i>tert</i> -Butyloxycarbonyl
BSA	bovine serum albumin
BVR	biliverdin reductase
CAR	chimeric antigen receptor
CETSA	cellular thermal shift assay
CMV	cytomegalovirus
COMAS	compound management and screening center
COVID-19	coronavirus disease 2019
COX	cyclooxygenase
CPA	cell painting assay
CRISPR	Clustered Regularly Interspaced Short Palindromic Repeats
CRS	cytokine release syndrome
CST3	cystatin-C
CTL	cytotoxic T lymphocyte
CTLA-4	CTL-associated protein 4
CTSS	cathepsin S
CXCL	C-X-C motif chemokine
CYP	cytochrome P450
DAPI	4',6-Diamidine-2'-phenylindole dihydrochloride
DC	dendritic cell
DHET	dihydroxyeicosatrienoic acid
DMSO	dimethyl sulfoxide
DNA	deoxyribonucleic acid
DOS	diversity-oriented synthesis
DSF	differential scanning fluorimetry
DTE	dithioerythritol
DTNB	5,5'-dithiobis-(2-nitrobenzoic acid)
DTT	dithiotreitol
ECM	extracellular matrix
ECS	Elongin-Cullin-SOCS
EDTA	ethylenediaminetetraacetic acid
EET	epoxyeicosatrienoic acid

## Abbreviations

<b>Abbreviation</b>	<b>Meaning</b>
eGFP	enhanced green fluorescent protein
EGTA	ethylene glycol-bis( $\beta$ -aminoethyl ether)-tetraacetic acid
em	emission
ER	endoplasmic reticulum
ESI	electrospray ionization
Et	ethyl
EtOH	ethanol
EWG	electron-withdrawing group
ex	excitation
FABP3	fatty acid-binding protein 3
FBS	fetal bovine serum
FDA	US Food and Drug Administration
Fluc	firefly luciferase
FOSL1	Fos-related antigen 1
FOXP3	forkhead box p3
GAS	gamma interferon activation site
GBP	guanylate-binding protein
GCN2	general control nonderepressible 2
GM2A	ganglioside GM2 activator
GO	gene ontology
GPCR	G protein-coupled receptor
HCD	high-energy collision-dissociation
HMOX	heme oxygenase
HPLC	high performance liquid chromatography
HRMS	high resolution mass spectrometry
HSBP	heat shock factor-binding protein
HTS	high-throughput screening
IC50	half-maximal inhibitory concentration
IDO	indoleamine 2,3-dioxygenase
IFIT	interferon-induced protein with tetratricopeptide repeat
IFN	interferon
IFRD	interferon-related developmental regulator
IL	interleukin
IPTG	isopropyl $\beta$ -d-1-thiogalactopyranoside
IRG	IFN-regulated gene
ITIM	immunoreceptor tyrosine-based inhibitory motif
JAK	janus kinase
KAT	kynurenine aminotransferase
KMO	kynurenine 3-monooxygenase
KO	knockout
Kyn	kynurenine
KYNU	kynureninase
LAMB3	laminin subunit $\beta$ -3
LAT	system L-type amino acid transporter
LFQ	label-free quantification
LPS	lipopolysaccharides
LOX	lipoxygenase
<i>m</i>	meta
mAbs	monoclonal antibodies
MAP1LC3	microtubule-associated proteins 1A/1B light chain 3
MAPK	mitogen-activated protein kinase
MDSC	myeloid-derived suppressor cells
Me	methyl
MeOH	methanol

## Abbreviations

<b>Abbreviation</b>	<b>Meaning</b>
MESNA	2-mercaptoethanesulfonate
miRNA	micro RNA
MMOA	molecular mode-of-action
mRNA	messenger RNA
MS	mass spectrometry
MTAP	methylthioadenosine phosphorylase
MTAP	methylthioadenosine
MT-DADMe-ImmA	methylthio-DADMe-Immucillin A
mTORC1	mammalian target of rapamycin complex 1
MTR-1-P	5-methylthioribose-1-phosphate
NAD	nicotinamide adenine dinucleotide
NEAA	non-essential amino acids
NF	nuclear factor
NK cell	natural killer cell
NP	natural product
<i>o</i>	ortho
<i>p</i>	para
PAINS	pan-assay interference
PBS	phosphate-buffered saline
PD-1	programmed cell death protein 1
pdb	protein data bank
PDE $\delta$	phosphodiesterase 6 $\delta$
<i>p</i> -DMAB	<i>para</i> -dimethylaminobenzaldehyde
PEG	polyethylene glycol
PGE	prostaglandin
Phe	phenyl
PHOME	(3-phenyl-oxiranyl)-acetic acid cyano-(6-methoxy-naphthalen-2-yl)-methyl ester
PIPES	piperazine- <i>N,N'</i> -bis(2-ethanesulfonic acid)
PK	pharmacokinetics
PLTP	phospholipid transfer protein
PNP	pseudo-natural product
PPI	protein-protein interaction
PRMT5	protein arginine N-methyltransferase 5
PROTAC	proteolysis-targeting chimera
PTM	posttranslational modification
PUFA	polyunsaturated fatty acid
RFU	relative fluorescence units
RGA	reporter gene assay
RISC	RNA-induced silencing complex
Rluc	<i>Renilla</i> luciferase
RNA	ribonucleic acid
ROS	reactive oxygen species
RT-qPCR	reverse transcriptase quantitative polymerase chain reaction
SAR	structure-activity relationship
SD	standard deviation
SDS	sodium dodecyl sulfate
SDS-PAGE	polyacrylamide gelelectrophoresis
sEH	soluble epoxide hydrolase
SEH1L	SEH1 like nucleoporin
sEH-H	hydrolyse domain of sEH
sEH-P	phosphatase domain of sEH
SERF2	small EDRK-rich factor 2

## Abbreviations

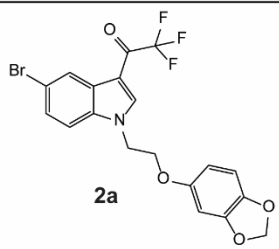
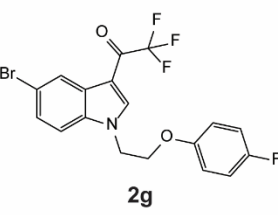
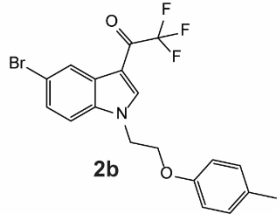
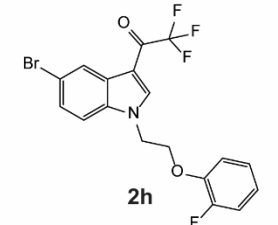
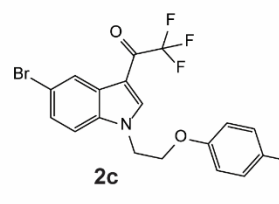
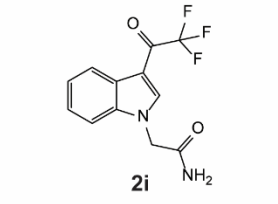
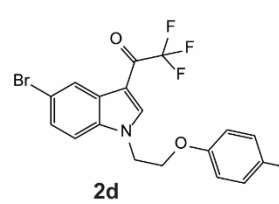
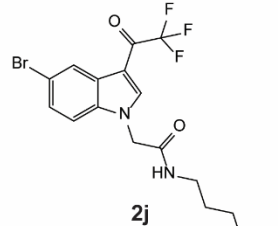
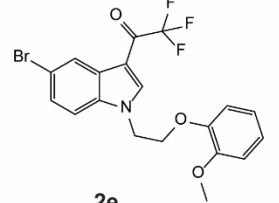
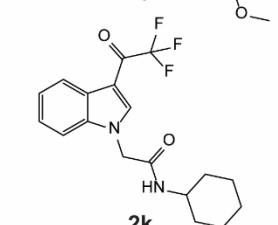
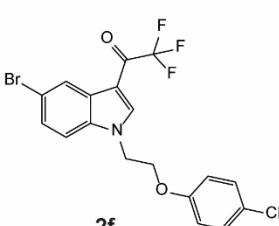
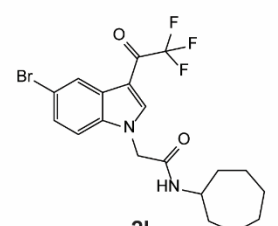
<b>Abbreviation</b>	<b>Meaning</b>
SESTD1	SEC14 domain and spectrin repeat-containing protein 1
SH2	Src homology region 2
SHP	SH2 domain-containing phosphatase
siRNA	small interfering RNA
SOCS3	suppressor of cytokine signaling 3
STAT	signal transducers and activators of transcription
StRE	stress response element
SURF1	surfeit locus protein 1
targetID	target identification
<i>t</i> -AUCB	<i>trans</i> -4-[4-(3-adamantan-1-ylureido)cyclohexyloxy]benzoic acid
<i>t</i> -Bu	tert-butyl
TCA	trichloroacetic acid
TCEAL4	transcription elongation factor A protein-like 4
TDO	tryptophan 2,3-dioxygenase
TEAB	triethylammonium bicarbonate
TEMED	tetramethylethylenediamine
TFA	trifluoroacetic acid
TGF	transforming growth factor
Th	T helper cells
THP	tetrahydropyridine
TME	tumor microenvironment
TMS	transmembrane segment
TMT	tandem mass tag
TNF	tumor necrosis factor
TPP	thermal proteome profiling
Treg	T regulatory cell
TRIS	tris(hydroxymethyl)aminomethane
tRNA	transfer RNA
Trp	L-tryptophan
TrpRS	tryptophanyl-tRNA synthetase
TrxR	thioredoxin reductase
TSA	thermal shift assay
TSP	tumor stroma percentage
Ub	ubiquitin
UBL5	ubiquitin-like protein 5
wt	wildtype
ZFAND6	AN1-type zinc finger protein 6

## 11 Appendix

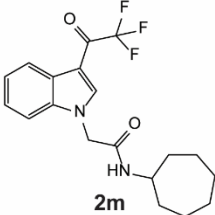
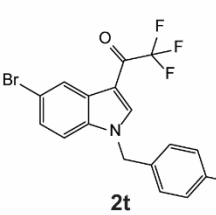
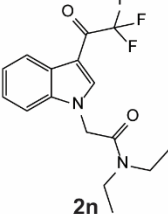
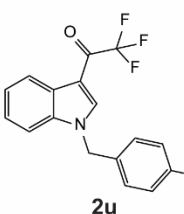
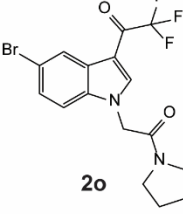
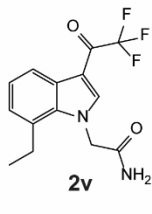
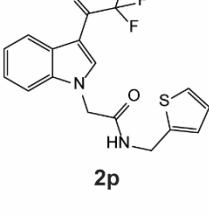
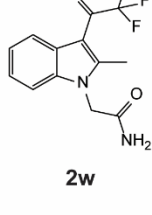
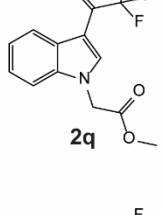
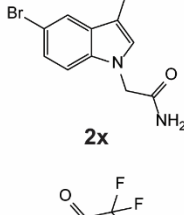
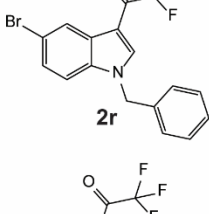
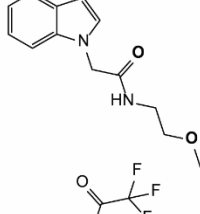
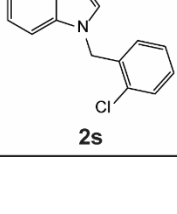
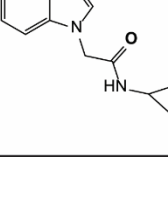
## 11.1 Supplementary Data

## 11.1.1 Supplementary Tables

**Table S1:** Structures and structure-activity relationship (SAR) of epoxykynins for reduction of Kyn levels (related to Table 2). IC<sub>50</sub> and % inhibition values were determined in BxPC-3 cells using the automated Kyn assay. Kyn assay inhibition values were determined as a single point measurement at 7.1 μM. Table is continued on following pages.

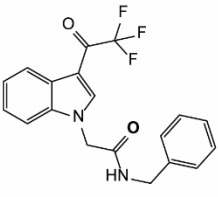
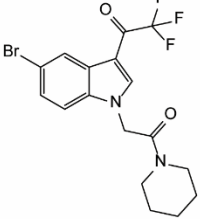
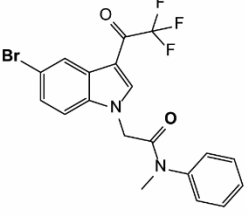
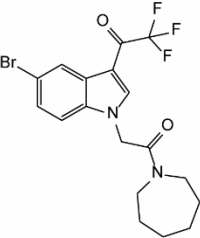
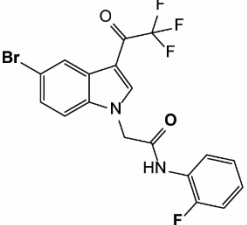
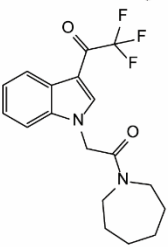
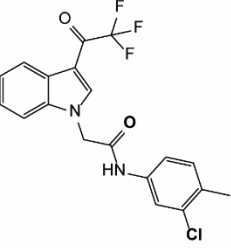
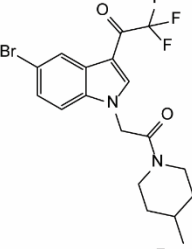
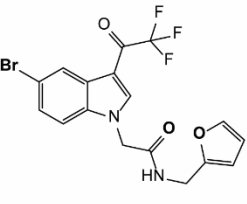
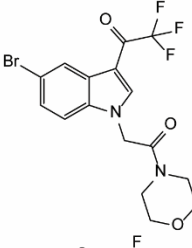
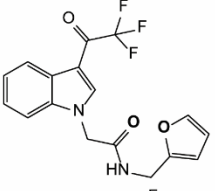
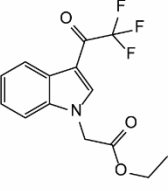
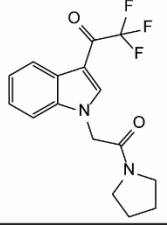
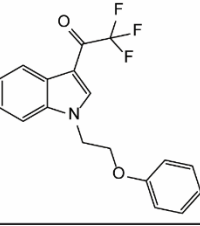
entry	Kyn assay IC <sub>50</sub> [μM]	Kyn assay inhibition [%]	entry	Kyn assay IC <sub>50</sub> [μM]	Kyn assay inhibition [%]
 <b>2a</b>	0.09 ± 0.03	95	 <b>2g</b>	3.05 ± 0.25	100
 <b>2b</b>	0.103 ± 0.02	83	 <b>2h</b>	0.097 ± 0.025	99
 <b>2c</b>	3.01 ± 0.8	20	 <b>2i</b>	0.045 ± 0.001	112
 <b>2d</b>	>10	12	 <b>2j</b>	0.402 ± 0.10	95
 <b>2e</b>	5.43 ± 0.6	54	 <b>2k</b>	3.49 ± 0.3	41
 <b>2f</b>	0.05 ± 0.017	98	 <b>2l</b>	0.036 ± 0.015	98

## Appendix

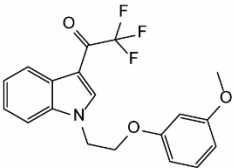
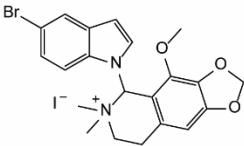
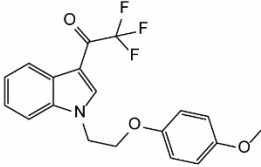
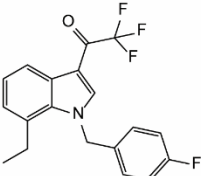
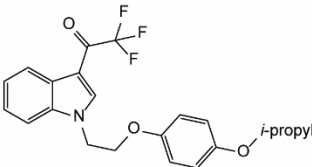
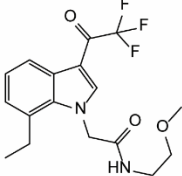
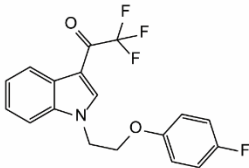
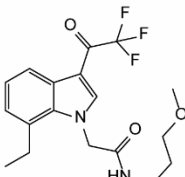
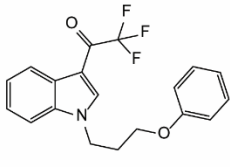
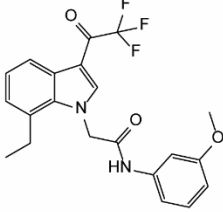
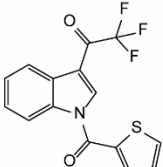
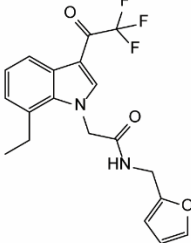
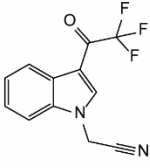
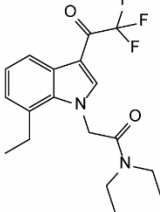
entry	Kyn assay IC <sub>50</sub> [μM]	Kyn assay inhibition [%]	entry	Kyn assay IC <sub>50</sub> [μM]	Kyn assay inhibition [%]
	1.73 ± 0.1	55		0.767 ± 0.41	67
	>10	0		>10	28
	1.94 ± 0.2	70		>10	2
	7.24 ± 3.8	49		>10	-36
	>10	-7		>10	-3
	>10	12		>10	0
	>10	11		>10	45



## Appendix

entry	Kyn assay IC <sub>50</sub> [μM]	Kyn assay inhibition [%]	entry	Kyn assay IC <sub>50</sub> [μM]	Kyn assay inhibition [%]
	>10	3		1.43 ± 0.2	88
	6.65 ± 2.6	12		1.23 ± 0.2	88
	2.27 ± 0.6	52		>10	16
	0.753 ± 0.4	85		0.343 ± 0.04	96
	0.564 ± 0.12	93		>10	-8
	9.12 ± 1.1	34		>10	-9
	>10	-23		1.18 ± 0.7	84

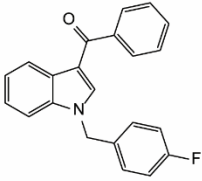
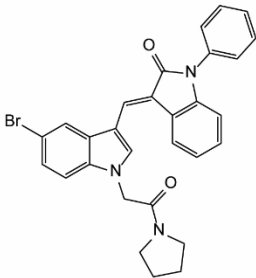
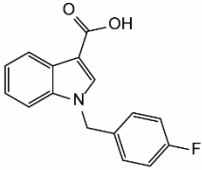
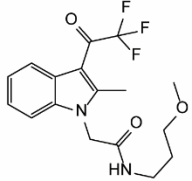
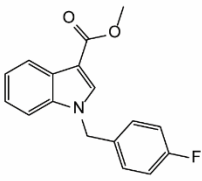
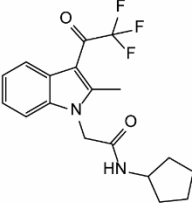
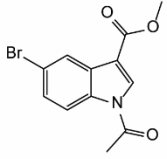
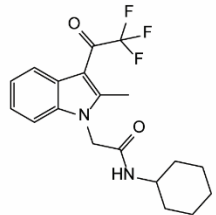
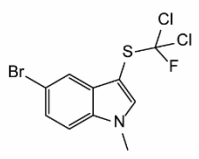
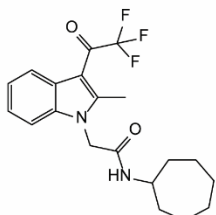
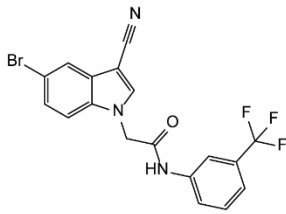
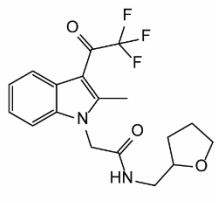
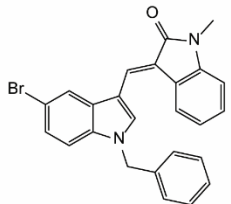
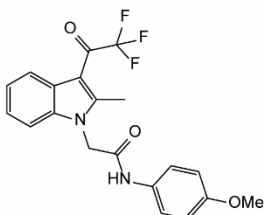
## Appendix

entry	Kyn assay IC <sub>50</sub> [μM]	Kyn assay inhibition [%]	entry	Kyn assay IC <sub>50</sub> [μM]	Kyn assay inhibition [%]
	>10	-11		not determined	3
	>10	18		>10	-4
	0.493 ± 0.12	96		>10	-9
	2.05 ± 0.1	108		>10	-23
	>10	10		>10	-13
	not determined	1		>10	37
	inactive	10		>10	4

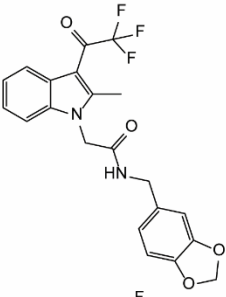
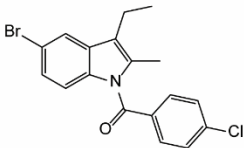
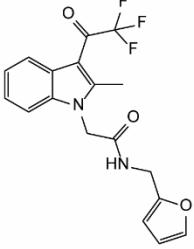
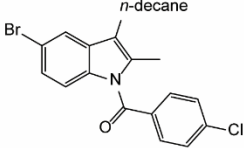
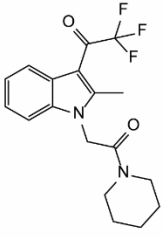
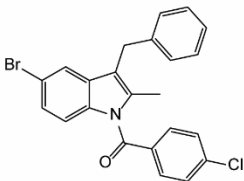
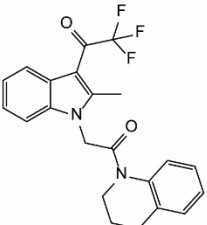
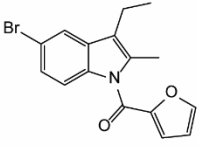
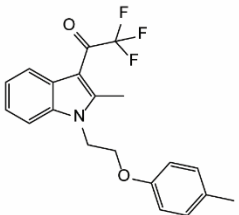
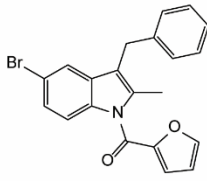
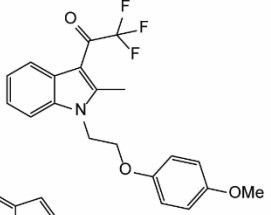
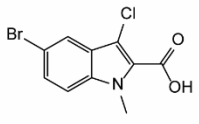
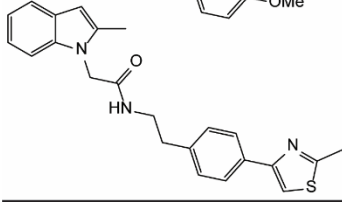
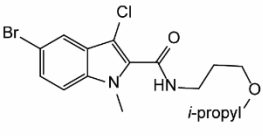
## Appendix

entry	Kyn assay IC <sub>50</sub> [μM]	Kyn assay inhibition [%]	entry	Kyn assay IC <sub>50</sub> [μM]	Kyn assay inhibition [%]
	>10	23		not determined	-22
	1.12 ± 0.4	77		>10	-11
	>10	47		>10	-18
	3.89 ± 2.4	74		2.14 ± 0.1	70
	>10	-14		7.18 ± 1.4	59
	not determined	-19		>10	-7
	1.99 ± 0.4	71		3.94 ± 0.7	21

## Appendix

entry	Kyn assay IC <sub>50</sub> [μM]	Kyn assay inhibition [%]	entry	Kyn assay IC <sub>50</sub> [μM]	Kyn assay inhibition [%]
	>10	0		not determined	36
	>10	7		>10	-2
	9.32 ± 1.0	42		4.29 ± 1.6	63
	not determined	-18		4.4 ± 0.4	12
	not determined	42		1.7 ± 0.1	82
	not determined	-30		>10	1
	not determined	23		>10	-2

## Appendix

entry	Kyn assay IC <sub>50</sub> [μM]	Kyn assay inhibition [%]	entry	Kyn assay IC <sub>50</sub> [μM]	Kyn assay inhibition [%]
	>10	-4		not determined	-7
	>10	23		not determined	2
	>10	-1		not determined	12
	>10	-15		not determined	18
	>10	-22		>10	42
	0.275 ± 0.08	97		not determined	4
	1.6 ± 0	87		not determined	-4

## Appendix

**Table S2:** Global proteome profiling analysis. Gene names of proteins that were upregulated upon treatment with IFN- $\gamma$  (DMSO+IFN- $\gamma$  vs. DMSO-IFN- $\gamma$ , N=3). Related to Figure 31A.

gene name	significance (-log(p))	fold change	gene name	significance (-log(p))	fold change
SH3TC2	2.62	9.78	SP110	4.87	3.38
SLC12A7	3.27	9.60	DTX3L	6.10	3.35
IDO1	5.17	7.80	LAP3	4.44	3.33
GBP1	2.86	7.15	APOL2	2.90	3.23
WARS	3.34	6.61	GOLM1	6.72	3.16
GBP2	4.81	6.42	CXCL10	2.87	3.12
GBP4	6.60	6.32	DDX58	4.16	3.10
XAF1	4.47	5.97	IFIT5	2.81	3.10
UBE2L6	2.67	5.44	FOSL1	4.19	3.03
APOL3	4.97	5.26	SERPING1	3.88	3.02
IFRD1	3.26	4.91	TYMP	3.33	3.02
GBP5	4.15	4.88	RFX5	2.98	2.99
MAP1LC3B	3.34	4.47	IL1B	3.29	2.98
AKAP12	3.89	4.36	HSPA5	2.33	2.96
LAMB3	4.28	4.26	NT5C3A	2.52	2.95
IFIT3	5.77	4.16	SERPINB2	2.71	2.81
NMI	3.52	4.13	PARP9	3.55	2.78
SAMHD1	4.89	4.09	TRIM21	3.18	2.77
BACH1	5.01	3.91	GCH1	2.06	2.66
IFI35	4.36	3.86	CD55	3.74	2.63
STAT1	3.19	3.84	ISG15	2.62	2.62
CXCL9	2.34	3.74	CTSS	3.55	2.59
TRIM22	5.10	3.58	IFIT2	3.22	2.57
ICAM1	3.86	3.51	LAMC2	2.71	2.56
IL1A	3.56	3.49	RNF114	5.60	2.52

**Table S3:** Global proteome profiling analysis. Gene names of proteins that were downregulated upon treatment with IFN- $\gamma$  (DMSO+IFN- $\gamma$  vs. DMSO-IFN- $\gamma$ , N=3). Related to Figure 31A.

gene name	significance (-log(p))	fold change	gene name	significance (-log(p))	fold change
ECT2	3.59	-2.51	CROT	2.46	-3.22
MAP3K6	2.39	-2.51	CHEK1	4.01	-3.42
SERINC3	2.32	-2.58	SESTD1	2.94	-3.48
PDCD4	2.73	-2.58	AES	2.47	-3.49
UQCRC2	2.71	-2.62	PLTP	3.00	-3.50
HSBP1	2.86	-2.67	GM2A	2.47	-3.54
PARP2	2.48	-2.71	ZNF706	2.74	-3.70
ATL2	2.97	-2.76	CKS1B	4.75	-3.73
DHFR	4.13	-2.81	TCEAL4	2.56	-3.82
SECISBP2	2.07	-2.84	CETN3	2.61	-4.01
N/A	3.70	-2.88	HIST1H3A	3.20	-4.03
UNG	3.40	-2.89	UBE2C	5.12	-4.19
NUSAP1	3.57	-2.90	SERF2	2.96	-4.26
CST3	3.13	-2.95	DHCR24	2.45	-4.29
FAM83D	4.58	-3.00	UBL5	3.41	-4.41
MELK	3.65	-3.01	ASF1B	2.20	-4.51
TPX2	2.76	-3.11	SKP2	4.51	-4.76

## Appendix

**Table S4:** Global proteome profiling analysis. Gene names of proteins that were upregulated upon treatment with epoxykynin (epoxykynin+IFN- $\gamma$  vs. DMSO+IFN- $\gamma$ , N=3). Related to Figure 31B.

gene name	significance ( $-\log(p)$ )	fold change	gene name	significance ( $-\log(p)$ )	fold change
CXCL9	3.83	10.28	CXorf38	3.40	3.20
GM2A	2.15	6.14	CETN3	2.44	3.19
PLTP	2.45	5.49	COL6A1	2.30	3.14
PLAU	2.35	5.18	ESPN	2.18	3.02
HSBP1	2.65	5.17	APOBEC3C	2.05	3.02
C15orf57	2.32	4.96	RIMKLB	2.12	3.02
ZFAND6	2.22	4.49	CTNNBIP1	2.46	3.01
PREPL	2.99	4.10	PAIP2	2.73	2.91
CST3	4.60	4.09	HMGCS1	3.03	2.83
SERF2	4.58	3.68	GBP2	3.62	2.81
CA2	2.43	3.59	IVNS1ABP	2.70	2.79
CXCL10	3.17	3.56	MAP3K6	2.36	2.67
UBL5	2.13	3.55	CDC123	3.49	2.65
DUSP7	2.21	3.55	OAS1	2.13	2.65
APOL3	3.85	3.54	EPST11	2.88	2.64
RFX5	2.03	3.50	ATL2	2.30	2.61
TCEAL4	2.99	3.42	RPAP2	2.41	2.58
SHKBP1	2.17	3.36	RALGPS2	2.30	2.55
SESTD1	2.75	3.34	KCTD5	3.25	2.55
GBP5	2.86	3.26	TRIM16	2.39	2.52
CTSS	4.06	3.21	SPINT2	2.62	2.51

**Table S5:** Global proteome profiling analysis. Gene names of proteins that were downregulated upon treatment with epoxykynin (epoxykynin+IFN- $\gamma$  vs. DMSO+IFN- $\gamma$ , N=3). Related to Figure 31B.

gene name	significance ( $-\log(p)$ )	fold change	gene name	significance ( $-\log(p)$ )	fold change
IL1B	3.59	-2.88	IL1A	3.73	-4.95
KRT18	3.10	-2.94	IFRD1	4.55	-6.38
CTH	3.40	-2.94	MAP1LC3B	2.69	-7.50
FOSL1	3.71	-2.98	S100A12	3.45	-7.57
LAMB3	3.15	-3.76	S100A8	2.77	-12.67

## Appendix

**Table S6:** Affinity-based chemical proteomics (pulldown). Enriched proteins on affinity probe **3b** as identified by HRMS (n=2, N=4, FDR 0.01). Proteins that were identified in both experimental replicates are highlighted in grey. Table is continued on the next pages. Related to Figure 36.

gene name	n1, N=4		n2, N=4	
	significance (-log(p))	difference (log <sub>2</sub> (3b-4b))	significance (-log(p))	difference (log <sub>2</sub> (3b-4b))
EPHX2	2.14	1.99	4.74	2.54
HIBCH			4.47	1.11
HPCAL1;HPCA			3.54	1.63
LYPLA2			4.32	1.14
MTAP	6.47	2.34	4.65	1.04
RPL31			1.88	1.46
SEH1L	5.77	2.38	8.38	3.31
TRA2B	4.44	2.36		

**Table S7:** Affinity-based chemical proteomics (pulldown). Enriched proteins on control probe **4b** as identified by HRMS (n=2, N=4, FDR 0.01). Proteins that were identified in both experimental replicates are highlighted in grey. Table is continued on the next pages. Related to Figure 36.

gene name	n1, N=4		n2, N=4	
	significance (-log(p))	difference (log <sub>2</sub> (3b-4b))	significance (-log(p))	difference (log <sub>2</sub> (3b-4b))
ABCB7			3.99	-1.10
ADK	3.63	-2.53	8.27	-2.29
AKAP8			1.95	-4.07
ALG5			2.87	-1.30
APOO			5.01	-1.54
ARL6IP5			4.54	-1.40
ARL8B;ARL8A			3.03	-1.47
ATL3			6.25	-1.26
ATP1B3			2.16	-1.22
ATP5EP2;ATP5E			1.06	-2.06
ATP5F1			4.90	-1.08
ATP5J	1.99	-2.04		
ATP5J2;ATP5J2-			4.92	-1.08
PTCD1				
ATP5L			4.75	-1.05
BCAP31			4.09	-1.71
BET1;DKFZp781C0425			1.61	-1.71
BST2			4.99	-1.48
C1GALT1			4.11	-1.56
CCDC134			1.98	-1.64
CD44			5.52	-1.38
CD97			4.32	-1.08
CDC42			3.03	-1.19
CERS2			1.23	-1.78
CHCHD3			4.86	-1.25
CISD1			5.84	-1.59
CISD2			5.47	-1.79
CLPTM1L			5.41	-1.34
COMT			4.56	-1.18
COX4I1			4.13	-1.46
COX5A			4.64	-1.11
CSE1L			5.70	-1.04



## Appendix

gene name	n1, N=4		n2, N=4	
	significance (-log(p))	difference (log <sub>2</sub> (3b-4b))	significance (-log(p))	difference (log <sub>2</sub> (3b-4b))
CYB5R3			4.03	-1.14
DAD1			2.98	-1.72
DEGS1			3.87	-1.27
DHCR7			5.03	-1.17
DHRS1			5.12	-1.39
DHRS3			1.78	-1.73
EDIL3			4.63	-1.13
ELOVL1			1.52	-1.73
ELOVL5			4.25	-1.24
EPHX1			5.28	-1.33
ERGIC1			5.45	-1.18
FADS1			6.51	-1.37
FADS2			5.42	-1.08
FAM105A			3.82	-1.31
FKBP11	2.29	-2.35	3.88	-1.09
FUNDC2	3.94	-2.88	3.25	-2.34
GALNT2			4.70	-1.22
GLUD1; GLUD2	5.49	-1.67		
GNB2			4.58	-1.47
GNG5			3.32	-2.39
GPR89A;GPR89B			4.26	-1.52
GPX8	1.74	-2.91	5.58	-1.27
HCCS			4.07	-1.51
HEATR1			4.34	-1.08
HEBP1	5.95	-2.58	7.07	-1.71
HLA-A			5.18	-1.12
HLA-B			5.85	-1.21
HLA-C;HLA-Cw			6.13	-1.09
HMOX2			2.90	-1.19
IKBIP			3.59	-1.09
IMMT			5.80	-1.54
ITPA	7.11	-2.85		
LCLAT1			4.33	-1.19
LMAN1			5.19	-1.07
LMAN2			4.80	-1.93
LMAN2L			3.30	-1.41
LMF2			5.73	-1.19
MAGT1			3.07	-1.27
MBOAT7			3.91	-1.07
MCU			4.73	-1.13
MGST1			7.32	-1.55
MLEC			2.87	-1.49
MPC1;BRP44L			3.22	-1.41
MPC2			2.09	-2.13
MPDU1			5.77	-1.38
MRRF	1.72	-2.19		
MT-ATP8			3.10	-1.76
MTCH2			4.98	-1.12
MT-CO2			5.61	-1.26
MTOR			4.15	-1.45
MTX1			3.19	-1.68
NDC1			5.47	-1.10
NDUFA8			1.71	-2.00
NDUFAF2			3.64	-1.78
NDUFB11			3.56	-2.54
NDUFB3			2.91	-1.38

## Appendix

gene name	n1, N=4		n2, N=4	
	significance (-log(p))	difference (log <sub>2</sub> (3b-4b))	significance (-log(p))	difference (log <sub>2</sub> (3b-4b))
NDUFB5			2.58	-1.33
NT5C3B			4.26	-2.45
PDCD6			4.93	-1.04
PFDN6	2.68	-2.03		
PGM3			1.60	-1.89
PGRMC1			2.03	-1.66
PGRMC2	5.25	-2.35	5.06	-1.35
PIGS			4.47	-1.31
PIGT			3.43	-1.68
PITPNB	3.07	-1.85		
POR			2.96	-1.15
PRKDC			6.33	-1.04
PSMD8	1.60	-2.76		
PTGES2	2.46	-1.91	4.52	-1.10
PTRH2			3.44	-2.13
RAB10			5.76	-1.54
RAB11B;RAB11A			4.73	-1.57
RAB14			4.70	-1.27
RAB18			4.35	-2.48
RAB1A			2.32	-1.98
RAB1B			5.56	-1.10
RAB21			6.51	-1.78
RAB2A			4.94	-1.55
RAB31;RAB22A			4.19	-1.76
RAB5A			1.75	-1.80
RAB5C			5.12	-1.35
RAB6A; RAB6B	3.54	-1.75		
RAB7A			5.39	-1.45
RAB8A			4.36	-1.10
RAP1B; RAP1A	5.15	-3.86	4.61	-1.80
RDH11			5.07	-1.16
RETSAT			2.60	-1.31
RFT1			3.56	-1.83
RHOA			1.44	-1.98
RHOG			3.93	-2.42
S100A10			2.24	-2.67
SACM1L			4.85	-1.26
SAMM50			6.98	-1.74
SAR1A			2.86	-1.74
SCAMP3	4.90	-2.82		
SCARB1			4.86	-2.93
SCCPDH	3.90	-1.94	2.87	-1.17
SCPEP1	3.14	-2.01		
SEC11A			6.78	-1.37
SEC22B			4.69	-1.43
SEC61B			6.41	-1.59
SEC61G			5.67	-1.83
SEC63			1.62	-2.21
SECTM1			1.95	-2.08
SIGMAR1			2.04	-2.18
SLC30A7			2.68	-1.65
SMPD4			2.01	-1.41
SOAT1			4.68	-1.17
SPCS2			4.77	-1.24
SPCS3			4.57	-1.17
SPR			6.49	-1.58

## Appendix

gene name	n1, N=4		n2, N=4	
	significance (-log(p))	difference (log <sub>2</sub> (3b-4b))	significance (-log(p))	difference (log <sub>2</sub> (3b-4b))
SSR3			1.19	-1.65
STT3A			5.09	-1.01
SYPL1			2.75	-1.36
TAMM41			2.34	-1.24
TAPBP			3.64	-1.41
TBL2	4.26	-1.49	4.86	-1.15
TM9SF1			3.10	-1.19
TM9SF2			5.99	-1.03
TM9SF3			4.62	-1.12
TM9SF4			2.22	-1.71
TMED2			3.30	-1.38
TMED7-			4.25	-1.18
TICAM2;TMED7				
TMEM109			1.98	-1.97
TMEM205			1.66	-2.06
TMPO			4.49	-1.16
TOMM20			1.36	-2.28
TOMM7			4.28	-1.26
TOR1AIP1			3.54	-1.08
TPP1			1.83	-1.41
TSPO			4.84	-1.35
TUBGCP4			2.45	-1.20
VAPA			4.92	-1.51
VAPB			2.70	-1.28
VDAC1			5.11	-1.31
VMP1			1.88	-1.51
XPO7			6.26	-1.04
YIF1A			3.68	-1.24
ZMPSTE24			5.52	-1.69

## Appendix

**Table S8:** Affinity-based chemical proteomics (pulldown). LFQ intensities for proteins selectively enriched by affinity probe **3b** in comparison to control probe **4b** (n1, N=4).

gene name	affinity probe 3b				control probe 4b			
	LFQ1	LFQ2	LFQ3	LFQ4	LFQ1	LFQ2	LFQ3	LFQ4
EPHX2	7352600	6270200	6809100	6688400	0	0	0	0
MTAP	13678000	16810000	18212000	16267000	3253500	3132500	2994100	3442400
SEH1L	75267000	88492000	108110000	80662000	15245000	18745000	16230000	17053000

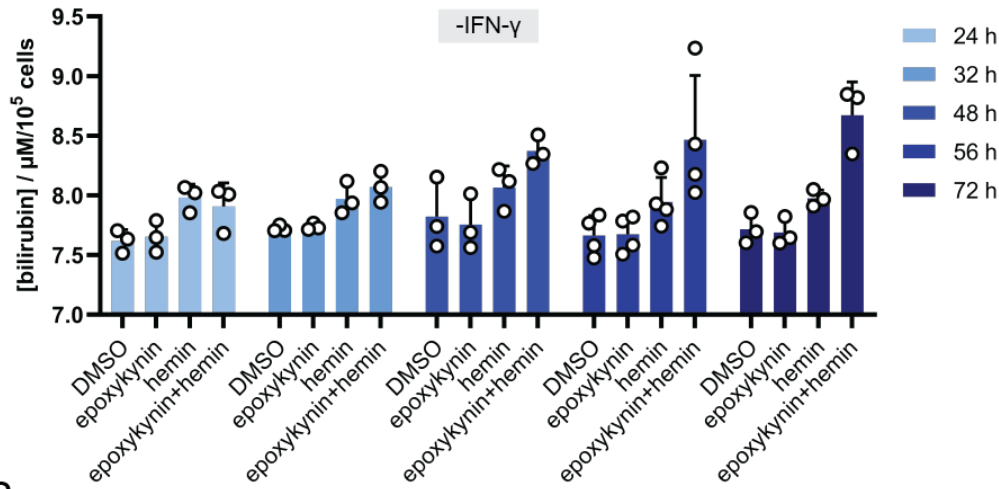
**Table S9:** Affinity-based chemical proteomics (pulldown). LFQ intensities for proteins selectively enriched by affinity probe **3b** in comparison to control probe **4b** (n2, N=4).

gene name	affinity probe 3b				control probe 4b			
	LFQ1	LFQ2	LFQ3	LFQ4	LFQ1	LFQ2	LFQ3	LFQ4
EPHX2	23157000	15787000	15518000	21115000	0	0	0	0
MTAP	17151000	20828000	17404000	18929000	9893700	8366300	8462400	9450700
SEH1L	281169984	254340000	262070000	260070000	24289000	25395000	28607000	28273000

## Appendix

### 11.1.2 Supplementary Figures

A



B

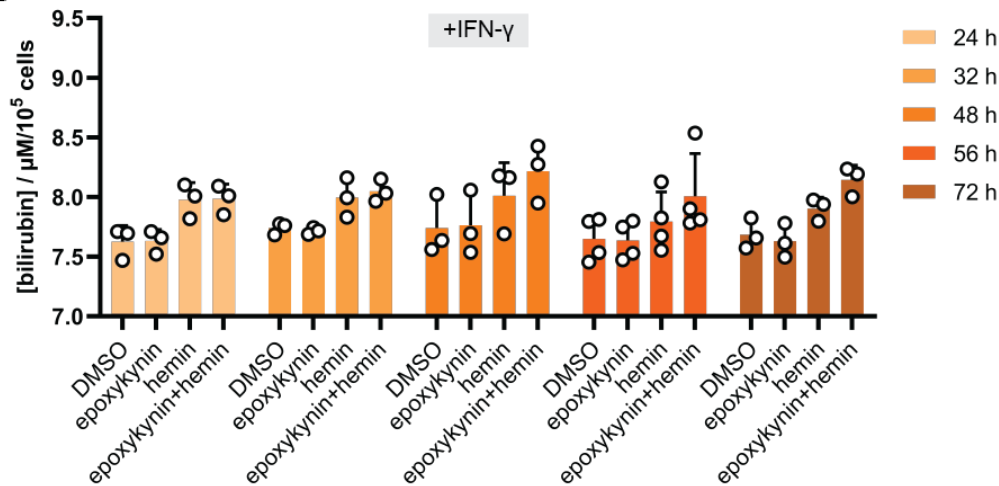
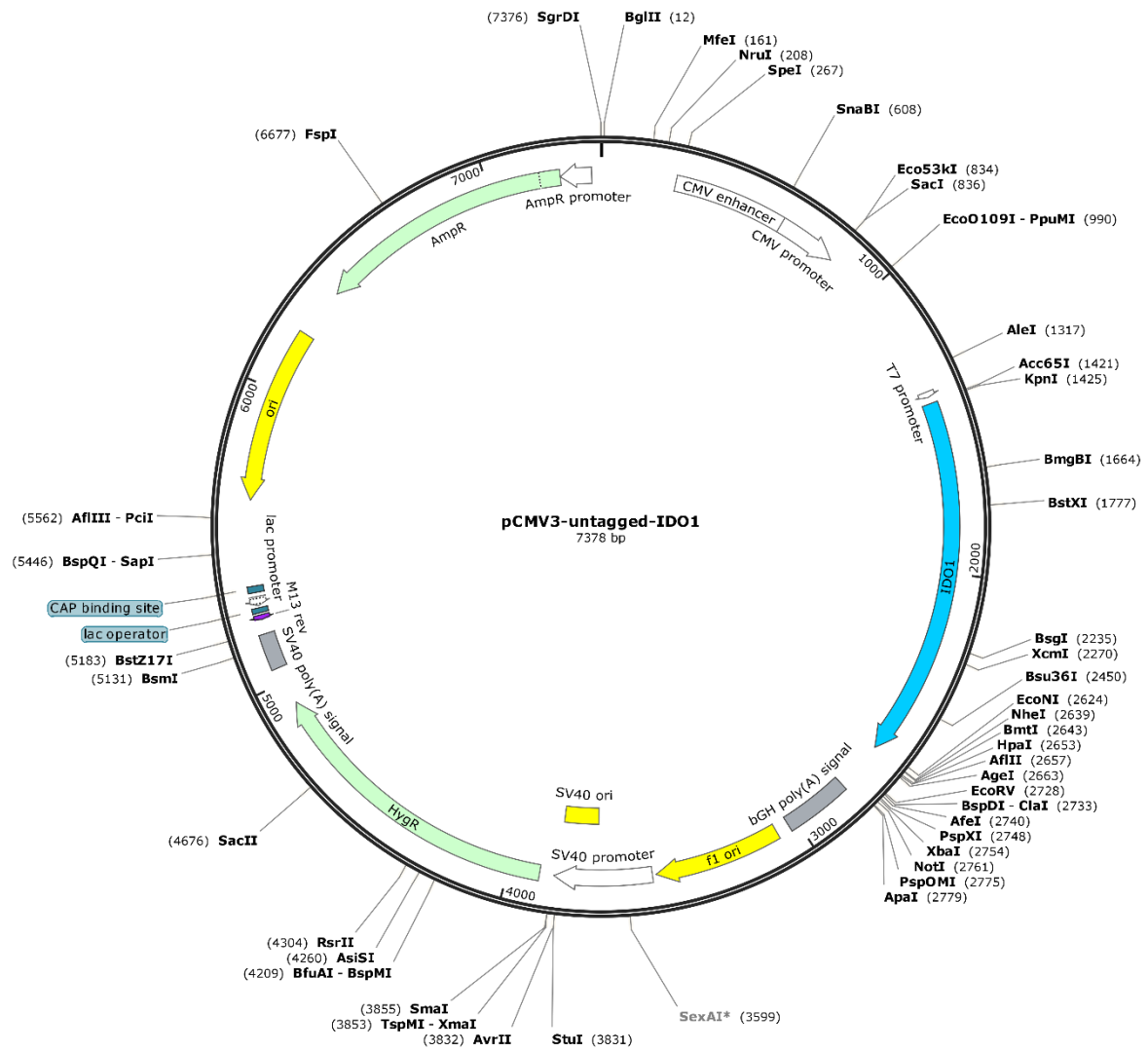


**Figure S1:** Bilirubin quantification in SKOV-3 cells. Cells were treated with 10  $\mu$ M epoxykyrin and 100  $\mu$ M hemin A) in the absence or B) presence of IFN- $\gamma$  and incubated for up to 72 h. Bilirubin was extracted from the cell culture supernatant with benzene and quantified by absorbance using the molar attenuation coefficient of bilirubin dissolved in benzene<sup>217</sup> (mean values $\pm$ SD, n=3). Related to Figure 47.

# Appendix

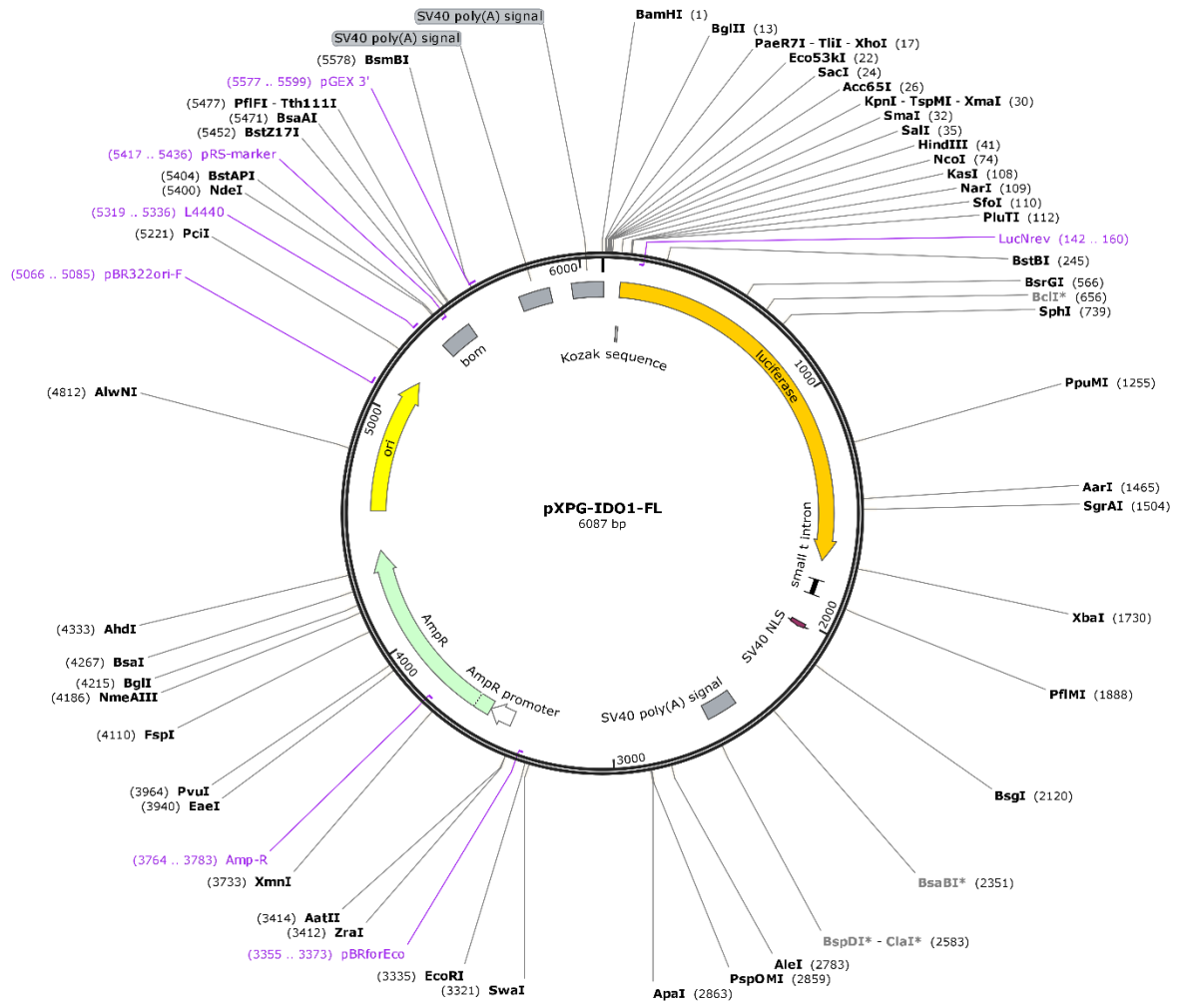
## 11.1.3 Vector Maps

Created with SnapGene®



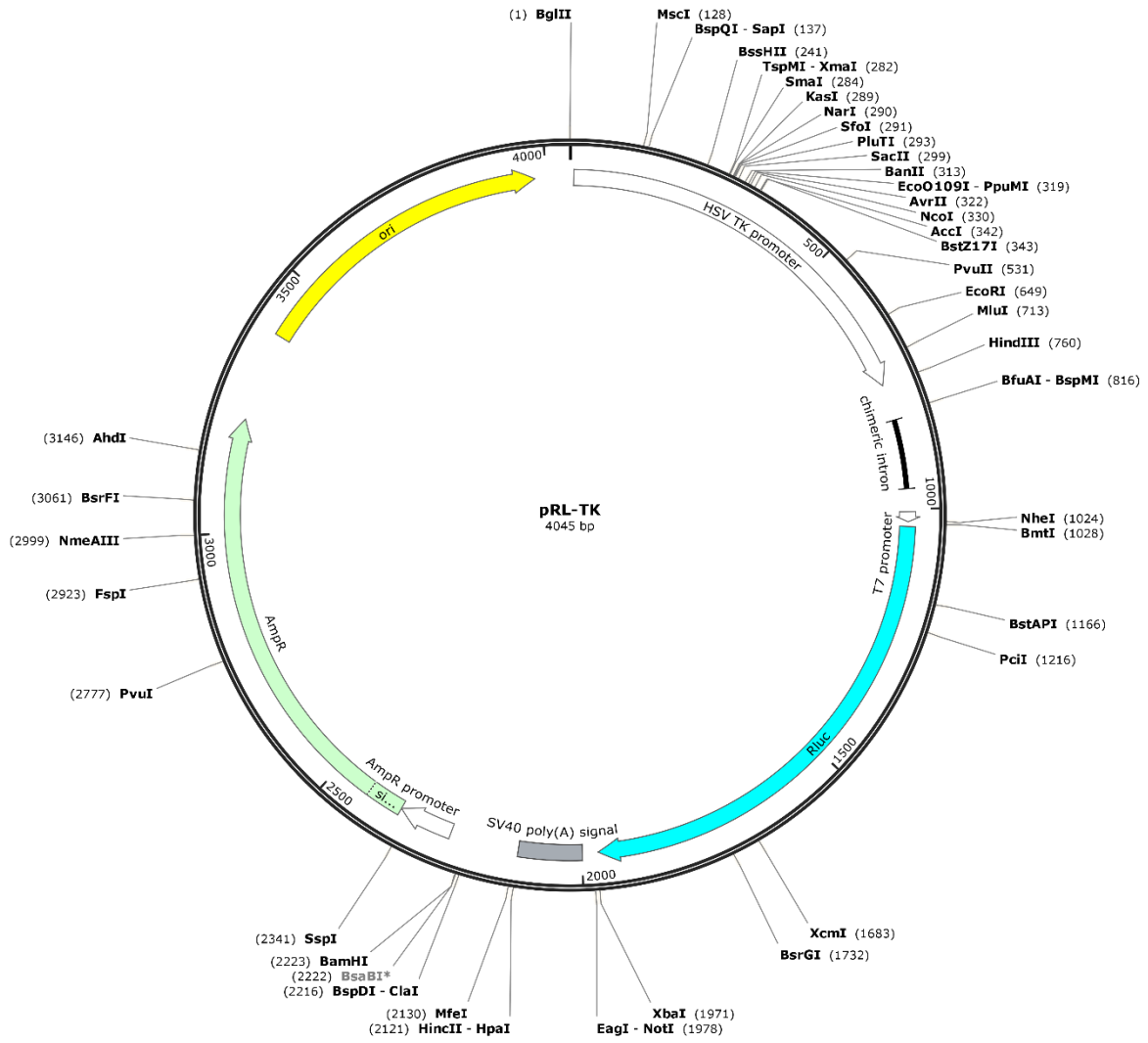
# Appendix

Created with SnapGene®



# Appendix

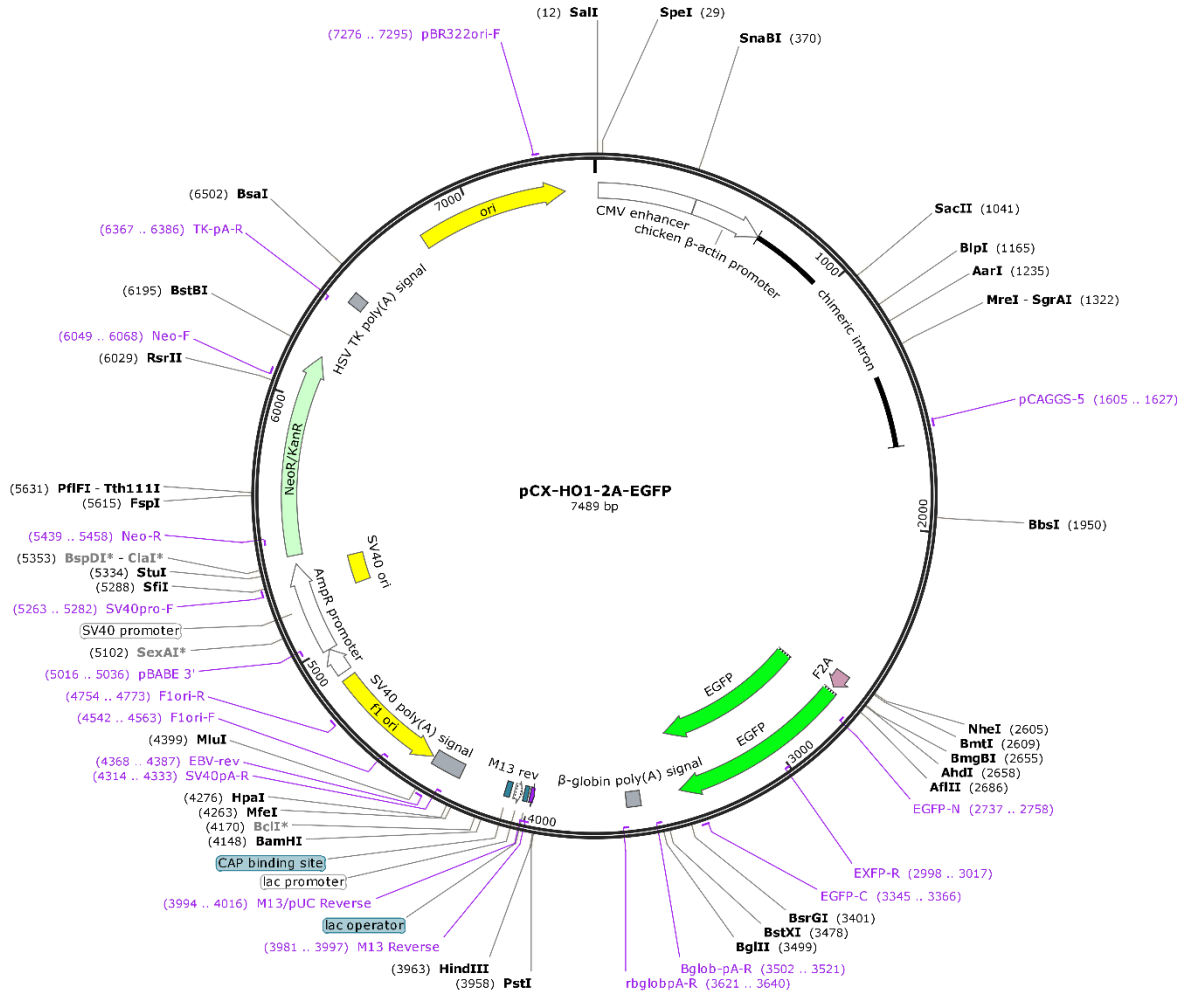
Created with SnapGene®





# Appendix

Created with SnapGene®



### 11.2 Acknowledgements

*“No one who achieves success does so without acknowledging the help of others.”*

-Alfred North Whitehead

First of all, I would like to express my deepest gratitude to my supervisor Prof. Herbert Waldmann for the opportunity to pursue my doctoral degree in his department. I highly appreciate the excellent scientific environment and equipment, the possibility to work both independently, but also collaboratively and the incredible knowledge and experience provided by Prof. Waldmann. I am also deeply thankful for the support of my direct supervisor Dr. Slava Ziegler. She always advised me with constructive ideas and suggestions and promoted my projects. Moreover, I value her open and kind nature which made her approachable for all sort of questions. Both of my supervisors tremendously shaped my scientific view and helped me to become the junior scientist I am today.

I would like to extend my sincere thanks to Prof. Carsten Watzl for taking the responsibility as my second examiner.

I would like to thank Dr. Elisabeth Hennes and Dr. Caitlin Davies in particular who collaborated with me on both of my projects. Elisabeth did incredible work with the establishment of the Kyn assay which paved the way for my projects. Furthermore, she shared her knowledge with me and was always available for fruitful discussions. Secondly, I am deeply grateful to Caitlin who performed all the chemistry work for my projects. It was amazing to not only work together with a colleague, but with a true friend. We complemented each other in the best possible ways.

Special thanks also go to Aylin Binici and Dr. Sarah Zinken. Together with Caitlin, you two have been there almost the entire time of my PhD and without you, this journey would not have been possible. I enjoyed our little tea times and girl nights and most of all, the fun we had together. Sarah's calm and steady personality is as inspiring as Aylin's passionate way to see things.

I would also like to express my sincere thanks to Dr. Jana Flegel, Dr. Michael Winzker, Siska Führer and Sandra Koska. They all contributed to the great working atmosphere and were always open for scientific discussions. Especially Jana taught me to be critical when looking at my own results and Micha became a mentor for me from the time I started my work in this department.

Additionally, I would like to thank Christine Nowak and Dr. Gang Xue. Both of them not only made working in the lab extremely pleasant and fun, but provided unmatched expertise in

## Appendix

biology fields less familiar to me. Moreover, I learned a lot from them about different cultures and my inability to pronounce certain things.

I would like to acknowledge all group members who supported my work, the COMAS, especially Dr. Sonja Sievers, Dr. Axel Pahl, Dr. Claude Ostermann and Christiane Pfaff, the HRMS team around Dr. Petra Janning and Dr. Raphael Gasper's crystallography and biophysics facility. I would also like to recognize some colleagues who have made my time in this department memorable, namely Jens Warmers, Dr. Adrian Krzyzanowski, Dr. Annina Burhop, Dr. Tabea Schneidewind, Eric Ogel, Caiming Wang, Dr. Michael Grigalunas, Dr. Ruirui Zhang, Dr. Xiufen Cheng, Dr. Alexandra Friese, Dr. Belén Lucas, Sasikala Thavam, Beate Schölermann and Brigitte Rose. Furthermore, I would like to thank my students Yasmin Jelali and Laura Dragun, as well as my trainees Elena Schwendich, Kimberly Wohde, Karolina Kubat and Celine da Cruz Lopes Guita for their help in the lab.

Lastly, I am deeply grateful to my family and friends. I am extremely thankful for the continued support of Stefan Schmeing, Patrick Günther, Alexandra Brause, Raphael Gasper and David Yurt. And most importantly, I would like to thank my parents. They always supported me in every possible way and served as my role models for ambitiously pursuing my goals. Ihr alle wart abseits des Instituts immer für mich da und habt mich auf eure persönliche Art dabei unterstützt, meinen Weg zu gehen. Danke dafür!

## Appendix

### 11.3 Publication List

Xue<sup>+</sup>, G.; Xie<sup>+</sup>, J.; Hinterndorfer, M.; Cigler, M.; Dötsch, L.; Imrichova, H.; Lampe, P.; Cheng, X.; Rezai Adariani, S.; Winter, G.; Waldmann, H., Discovery of a Drug-like, Natural Product-Inspired DCAF11 Ligand Chemotype. *Nat Comm*, under revision.

Flegel, J.; Shaaban<sup>+</sup>, S.; Jia<sup>+</sup>, Z. J.; Schulte, B.; Lian, Y.; Krzyzanowski, A.; Metz, M.; Schneidewind, T.; Wesseler, F.; Flegel, A.; Reich, A.; Brause, A.; Xue, G.; Zhang, M.; Dötsch, L.; Stender, I. D.; Hoffmann, J.-E.; Scheel, R.; Janning, P.; Rastinejad, F.; Schade, D.; Strohmam, C.; Antonchick, A. P.; Sievers, S.; Moura-Alves, P.; Ziegler, S.; Waldmann, H., The Highly Potent AhR Agonist Picoberin Modulates Hh-Dependent Osteoblast Differentiation. *J Med Chem* **2022**, *65* (24), 16268-16289.

Davies<sup>+</sup>, C.; Dötsch<sup>+</sup>, L.; Ciulla, M. G.; Hennes, E.; Yoshida, K.; Gasper, R.; Scheel, R.; Sievers, S.; Strohmam, C.; Kumar, K.; Ziegler, S.; Waldmann, H., Identification of a Novel Pseudo-Natural Product Type IV IDO1 Inhibitor Chemotype. *Angew Chem Int Ed* **2022**, *61* (40), e202209374.

Hennes, E.; Lampe, P.; Dötsch, L.; Bruning, N.; Pulvermacher, L. M.; Sievers, S.; Ziegler, S.; Waldmann, H., Cell-Based Identification of New IDO1 Modulator Chemotypes. *Angew Chem Int Ed Engl* **2021**, *60* (18), 9869-9874.

Karatas, H.; Akbarzadeh, M.; Adihou, H.; Hahne, G.; Pobbati, A. V.; Yihui Ng, E.; Guéret, S. M.; Sievers, S.; Pahl, A.; Metz, M.; Zinken, S.; Dötsch, L.; Nowak, C.; Thavam, S.; Friese, A.; Kang, C.; Hong, W.; Waldmann, H., Discovery of Covalent Inhibitors Targeting the Transcriptional Enhanced Associate Domain Central Pocket. *Journal of Medicinal Chemistry* **2020**, *63* (20), 11972-11989.

Škopić, M. K.; Salamon, H.; Bugain, O.; Jung, K.; Gohla, A.; Doetsch, L. J.; Santos, D. d.; Bhat, A.; Wagner, B.; Brunschweiger, A., Acid- and Au(i)-mediated synthesis of hexathymidine-DNA-heterocycle chimeras, an efficient entry to DNA-encoded libraries inspired by drug structures. *Chem Sci* **2017**, *8* (5), 3356-3361.

<sup>+</sup>These authors contributed equally to this work.

## Appendix

# Eidesstattliche Versicherung (Affidavit)

Name, Vorname  
(Surname, first name)

Matrikel-Nr.  
(Enrolment number)

Belehrung:

Wer vorsätzlich gegen eine die Täuschung über Prüfungsleistungen betreffende Regelung einer Hochschulprüfungsordnung verstößt, handelt ordnungswidrig. Die Ordnungswidrigkeit kann mit einer Geldbuße von bis zu 50.000,00 € geahndet werden. Zuständige Verwaltungsbehörde für die Verfolgung und Ahndung von Ordnungswidrigkeiten ist der Kanzler/die Kanzlerin der Technischen Universität Dortmund. Im Falle eines mehrfachen oder sonstigen schwerwiegenden Täuschungsversuches kann der Prüfling zudem exmatrikuliert werden, § 63 Abs. 5 Hochschulgesetz NRW.

Die Abgabe einer falschen Versicherung an Eides statt ist strafbar.

Wer vorsätzlich eine falsche Versicherung an Eides statt abgibt, kann mit einer Freiheitsstrafe bis zu drei Jahren oder mit Geldstrafe bestraft werden, § 156 StGB. Die fahrlässige Abgabe einer falschen Versicherung an Eides statt kann mit einer Freiheitsstrafe bis zu einem Jahr oder Geldstrafe bestraft werden, § 161 StGB.

Die oben stehende Belehrung habe ich zur Kenntnis genommen:

Official notification:

Any person who intentionally breaches any regulation of university examination regulations relating to deception in examination performance is acting improperly. This offence can be punished with a fine of up to EUR 50,000.00. The competent administrative authority for the pursuit and prosecution of offences of this type is the chancellor of the TU Dortmund University. In the case of multiple or other serious attempts at deception, the candidate can also be unenrolled, Section 63, paragraph 5 of the Universities Act of North Rhine-Westphalia.

The submission of a false affidavit is punishable.

Any person who intentionally submits a false affidavit can be punished with a prison sentence of up to three years or a fine, Section 156 of the Criminal Code. The negligent submission of a false affidavit can be punished with a prison sentence of up to one year or a fine, Section 161 of the Criminal Code.

I have taken note of the above official notification.

Ort, Datum  
(Place, date)

Unterschrift  
(Signature)

Titel der Dissertation:  
(Title of the thesis):

---

---

---

Ich versichere hiermit an Eides statt, dass ich die vorliegende Dissertation mit dem Titel selbstständig und ohne unzulässige fremde Hilfe angefertigt habe. Ich habe keine anderen als die angegebenen Quellen und Hilfsmittel benutzt sowie wörtliche und sinngemäße Zitate kenntlich gemacht.

Die Arbeit hat in gegenwärtiger oder in einer anderen Fassung weder der TU Dortmund noch einer anderen Hochschule im Zusammenhang mit einer staatlichen oder akademischen Prüfung vorgelegen.

I hereby swear that I have completed the present dissertation independently and without inadmissible external support. I have not used any sources or tools other than those indicated and have identified literal and analogous quotations.

The thesis in its current version or another version has not been presented to the TU Dortmund University or another university in connection with a state or academic examination.\*

**\*Please be aware that solely the German version of the affidavit ("Eidesstattliche Versicherung") for the PhD thesis is the official and legally binding version.**

Ort, Datum  
(Place, date)

Unterschrift  
(Signature)